SEDIMENTATION IN A FJORD-HEAD DELTA, BELLA COOLA, BRITISH COLUMBIA

By

© RAY KOSTASCHUK

A Thesis

Submitted to the School of Graduate Studies

in Partial Fulfilment of the Requirements

for the Degree

Doctor of Philosophy

McMaster University

1984

SEDIMENTATION IN A FJORD-HEAD DELTA, BELLA COOLA, BRITISH COLUMBIA

Imagine a river, wide and majestic, which flows for miles and miles between strong embankments, where the land is firm. At a certain point, the river, out of weariness, because its flow has taken up too much time and too much space, because it is approaching the sea, which annihilates all rivers within itself, no longer knows what it is, loses its identity. It becomes its own delta. A major branch may remain, but many break off from it in every direction, and some flow together again, into one another, and you can't tell what begets what, and sometimes you can't tell what is still river and what is already sea...

(Umberto Eco: The Name of the Rose)

For the Walrus

STRAWBERRY FIELDS FOREVER

Let me take you down cause I'm going to
Strawberry Fields,
Nothing is real,
And nothing to get hung about,
Strawberry Fields forever.

Living is easy with eyes closed,
Misunderstanding all you see,
Its getting hard to be someone
But it all works out,
It doesn't matter much to me.

No one I think is in my tree,
I mean it must be high or low,
That is you can't you know tune in
But its all right,
That is I think its not too bad.

Always no sometimes think its me,
But you know I know when its a dream,
I think its not for me ah yes
But its all wrong,
That is I think I disagree.

(John Lennon, 1967)

DOCTOR OF PHILOSOPHY (1984) McMASTER UNIVERSITY

(Geography Department) Hamilton, Ontario

TITLE: Sedimentation in a Fjord-Head Delta, Bella Coola, British Columbia

AUTHOR: Ray Kostaschuk, B.A. (Simon Fraser University)
M.Sc. (University of Calgary)

SUPERVISOR: Dr. S.B. McCann
Dr. J.J. Drake
Dr. G.V. Middleton

NUMBER OF PAGES: 298

ABSTRACT

The Bella Coola delta is a laterally confined, steep-fronted, coarse-grained fjord-head delta in North Bentinck Arm in the Coast Mountains of British Columbia. River mouth morphodynamics are directly related to the large tidal range (3.9 m mean range; 5.9 m large range). The tide changes the location and nature of the zone of marine-riverine interaction, producing a high tide and a low tide outlet. Frictional forces dominate at high tide as the effluent disperses over the delta plain through four morphodynamic zones and a radial bar. During low tide, frictional, inertial and buoyant forces and an internal hydraulic jump control the formation of five morphodynamic zones and a lunate-middle ground bar.

The subaqueous delta consists of a sandy delta front with slopes of 2.2 to 15° and a silt-clay prodelta sloping at 0.5 to 2.2°. Debris flow or turbidity current chutes and their depositional zones, shallow- and deep-seated rotational slides, growth faults and folds are the primary morphologic components. Sediment instability and deformation are mainly a result of gravitational forces, earthquake loading, retrogression, oversteepening of distributary mouth bar fronts, and excess pore pressures produced by gas generation, depositional loading and rapid tidal drawdown.

The sediment package of the Bella Coola delta and North Bentinck

Arm consists of two seismic sequence units, a lower probably Pleistocene sequence and an upper delta - related sequence. A glacial moraine facies and a glaciomarine facies characterizes the lower unit. The upper sequence delta plain sediments are well stratified sands and gravels deposited by distributary channels, with some rippled sands and peat. Delta front sediments probably consist of sand and mud laminae deposited from suspension, debris flow sands and gravels, graded sand and silt associated with turbidity currents and undisturbed bedding in slide blocks. Massive silts and clays deposited from suspension and graded sand and silt turbidities compose the prodelta. Rotational slides, growth faults with displaced beds and roll-over anticlines, and folds related to creep processes have deformed prodelta sediments.

ACKNOWLEDGEMENTS

There are a number of individuals and organizations who aided in the completion of my thesis.

My supervisor, Dr. S.B. McCann, provided direction and advice at all stages of the project, from planning to the final product. Thanks are also due to Dr. J.J. Drake and Dr. G.V. Middleton for their guidance and assistance.

At the Pacific Geoscience Centre of the Geological Survey of Canada, I would like to thank Dr. J.L. Luternauer and Dr. C.J. Yorath for their efforts in arranging the Parizeau cruise into Bella Coola. Captain B.L. Newton and the crew of the C.S.S. Parizeau, Dr. B.D. Bornhold, Ivan Frydecky, Trudy Forbes, and Gail Jewsbury also provided invaluable assistance.

Special thanks to Heather Field and Rod Kostaschuk for assisting with the Bella Coola based field operations, Phil Matsushita for proofreading text, and to Moe Howard, Jerome ('Curly') Howard and Larry Fine for being a never ending source of inspiration.

Financial support was provided by the National Research Council of Canada operating grant A5082 to S.B. McCann and a Natural Sciences and Engineering Research Council Postgraduate Scholarship to the author.

TABLE OF CONTENTS

LIST OF TABLES

LIST OF FIGURES

SECTION I - INTRODUCTORY MATERIAL

CHAPTER 1

INTRODUCTION

The main goal of this thesis is to examine sedimentation in the Bella Coola delta, a fjord-head delta being deposited by the Bella Coola River into North Bentinck Arm on the fjord coastline of British Columbia. The thesis is divided into four sections. Section I provides introductory material and includes two chapters. Chapter 1 defines deltas and fjord deltas and presents a brief history of delta studies in general and a summary of the literature on fjord deltas in particular. The second chapter describes the characteristics of the drainage basin, receiving basin and subaerial delta plain of the Bella Coola delta.

Sections II and III examine the Bella Coola delta in terms of two recent and important delta research themes: river mouth form and process, and subaqueous delta and fjord sedimentology, morphology and sediment stability. Chapters 3 to 6 comprise section II. Chapter 3 provides the framework for the river mouth process section and is based on a review of literature. Chapter 4 analyzes the effects of tides and waves in Bella Coola distributary mouths and chapter 5 describes the morphodynamics at the mouth of the main Bella Coola distributary, the

North Channel. Chapter 6 is a comparison of the Bella Coola results with the morphodynamic models outlined in chapter 3.

Section III consists of four chapters. Chapter 7 presents a literature-review framework for the examination of the Bella Coola subaqueous delta and fjord. The seismic stratigraphy of North Bentinck Arm is outlined in chapter 8. Seismic facies, morphology, geotechnical character and sediment instabilities are examined for the delta front in chapter 9 and the prodelta in chapter 10. Section IV consists of chapter 11, which summarizes the previous sections and provides details on the delta-fjord sediment package.

1.1 Definitions of Deltas and Fjord Deltas

Deltas can be defined as coastal accumulations, both subaqueous and subaerial, adjacent to, or in close proximity to, the stream source, including the deposits that have been secondarily molded by various marine agents such as waves, currents, or tides. (Wright, 1978). Thus deltas can occur wheneyer a stream debouches into a receiving basin; the receiving basin may be an ocean, gulf, inland sea, bay, estuary or lake. Fjord deltas, as the name implies, are deltas prograding into fjords. Fjords are long, narrow and deep basins of glacial origin that are located on mountainous, high relief coastlines.

1.2 Trends in Delta Research

The studies by G.K. Gilbert (1885) on raised Pleistocene deltas

in Lake Bonneville mark the beginning of modern delta research and dominated thinking on the subject for many years. Johnston's (1922) thorough investigation of the Fraser delta was the first detailed sedimentologic-morphologic examination of a modern delta, but his work had little impact on subsequent research. The Mississippi delta is the most intensely studied delta in the world (e.g. Trowbridge 1930; Fisk, 1944, 1947, 1955, 1960; Coleman and Gagliano, 1964; Wright and Coleman, 1971; Prior and Coleman, 1978), causing it to succeed Gilbert deltas as the delta model. By 1970, investigators began to realize that a single delta model was inappropriate, and proposed a number of delta models based on the dominance of river or basin influence (Fisher et al., 1969; Wright and Coleman, 1973; Coleman and Wright, 1975; Galloway, 1975).

Most of the early work on deltas stressed delta morphology and depositional framework, largely ignoring the processes involved. In the last 15 years, however, process-oriented studies have been undertaken on the Mississippi and other deltas. These investigations fall into two main groups: one concerned with river mouth processes and the other with subaqueous slope processes. L.D. Wright has been in the vanguard of river mouth studies, examining effluent mechanics and deposition in river-dominated (Wright and Coleman, 1971, 1974), wave- dominated (Wright, 1977), and tidally-dominated (Wright et al., 1973) situations. More recently, the trend has been towards the delineation and modelling of subaqueous slope forms and processes, with the Mississippi delta as the primary focus of attention (e.g. Prior and Coleman, 1978a, b, 1979; Prior et al., 1981).

1.3 Fjord Deltas

Fjord deltas are the most important Holocene depositional environment in temperate fjords. In British Columbia, fjord deltas are of three types (Figure 1). The most common are the deltas associated with large rivers debouching into the heads of fjords. The second type are produced by large rivers entering the fjord along the wall, usually from tributary valleys. Small, steep fan deltas associated with high energy streams along fjord walls comprise the third group. The characteristics of each of these groups are described below.

1.3.1 Fjord-Head Deltas

Fjord-head deltas, of which the Bella Coola is an example, are the best known of the three groups. Examples of this type include the Squamish Delta (Bell, 1975), the Kitimat Delta (Bell, 1976; Luternauer and Swan, 1978; Prior et al., 1983) and the Klinaklini and Homathko deltas (Syvitski and Farrow, 1983). The rivers feeding these deltas are coarse-grained (sand and gravel) bedload streams with a meandering (Squamish, Kitimat, Homathko), wandering (Bella Coola) or braided (Klinaklini) morphology. Stream discharges are low in fall and winter, rising in the spring in response to snowmelt and remaining high in summer due to glacier melt.

Intertidal positions of fjord-head deltas are typically composed of salt marsh in proximal areas and sand flats in distal zones, both of which are dissected by distributary channels. Channel positions may be

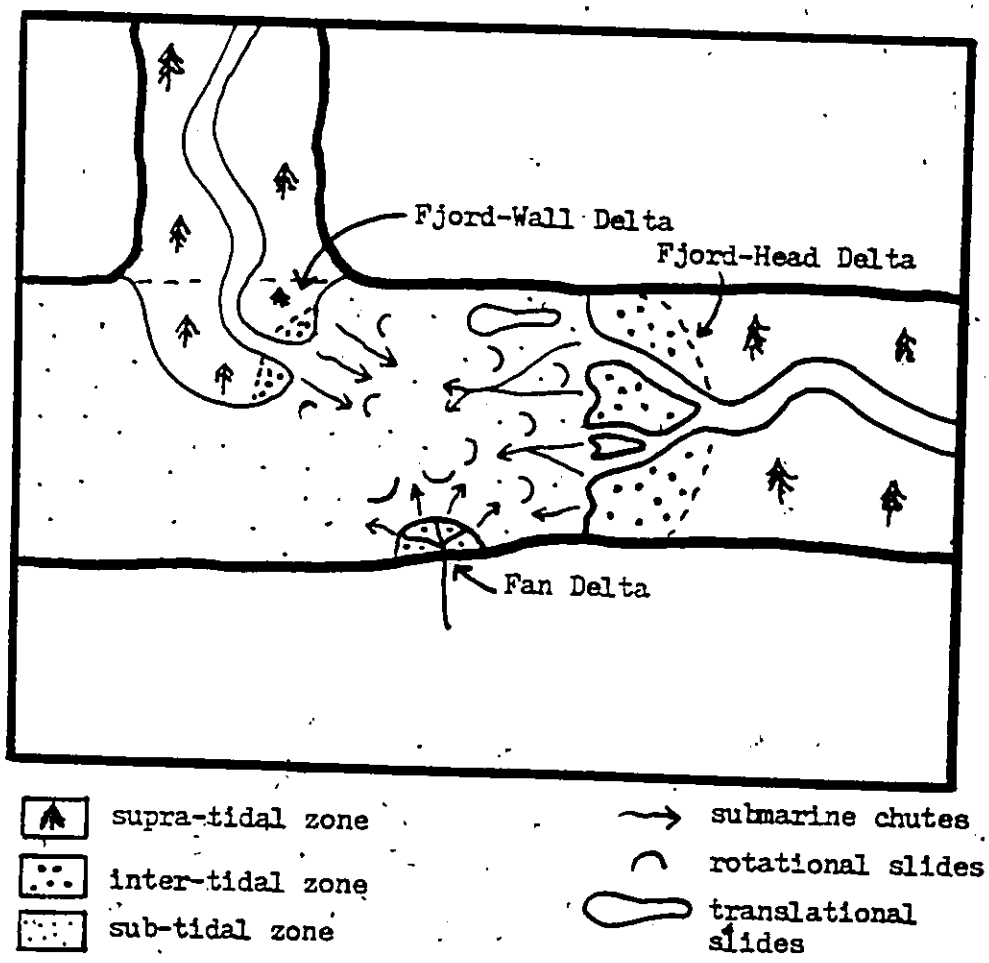

Figure 1. Three main types of fjord deltas.

laterally stable (Homathko) or unstable (Klinaklini) over time. Intertidal sediments are coarse-textured, ranging from sand and gravel near distributary channels to sand and mud in off channel areas. Bedforms vary from wave-generated bars and ripples to unidirectional flow features produced by tidal and fluvial currents, such as ripples and megaripples.

Subtidal (delta front and prodelta) slopes of fjord head deltas and high near distributary mouths (9-45°) decreasing offshore to values less than 1°. The deltas are rapidly prograding, with average rates of 6.5 ma^{-1} at 18 m depths on the Squamish delta (Bell, 1975). Sediment textures generally fine from sand to mud in an offshore direction, and display size variations across the subaqueous slope.

The morphology of subtidal areas of fjord head deltas is dominated by two types of features: channels (chutes) and slides. Channels have been described from submersible observations of the Homathko and Klinaklini deltas (Syvitski and Farrow, 1983). The channels originate at distributary mouths or as arcuate slumps at the seaward edge of the intertidal zones, and may coalesce downslope. Channels are flanked by levees and beds are rippled. At the downslope terminations of some channels hummocky depositional zones occur. Prior et al. (1981) suggest that debris-flows or slides are the main processes involved in generation of these channels. A major submarine slide occurred on the Kitimat Delta in 1975 (Luternauer and Swan, 1978; Prior et al., 1983). The slide began as a number of shallow rotational slides on upslope areas, becoming translational downslope and extending more than 4 km down

fjord. The channels noted on the Homathko and Klinaklini deltas were not described on the Kitimat. The Kitimat delta is somewhat finer-grained and slopes are lower, suggesting that these characteristics may restrict channel formation.

1.3.2 Fjord-Wall Deltas

There is very little information on the less common fjord-wall deltas, examples of which include the Dean River and Talheomey River deltas. The following discussion of the Dean delta is based on preliminary results of an investigation by McCann et al. (in preparation). The Dean River is a meandering or wandering gravel bedload stream debouching into Dean Channel. Stream discharge is controlled by spring snowmelt, with low flows in summer, fall and winter.

The subaerial Dean delta has a lobate form, as in Figure 1, projecting into and across the fjord. Much of the delta is presently inactive and forest covered with deposition being restricted to a small area near the river mouth. The intertidal zone has a morphology similar to intertidal areas of fjord-head deltas, with a number of distributary channels dissecting salt marsh and sand and gravel flats.

The subaqueous delta is featureless and composed of mud in inactive areas. The active portion of the delta is composed of sand in proximal areas, grading to mud offshore. Submarine channels (chutes), shallow, arcuate rotational slides and large, deep-seated rotational slides are the most important subaqueous features.

1.3.3 Fan Deltas

Fan deltas are very common along fjord walls. The streams responsible for these features drain steep wall slopes, are high energy and transport very coarse cobble to boulder-sized bedload. Delta distributaries are usually braided and the intertidal areas limited in extent and composed of cobbles and gravels.

Observations have been made on subaqueous portions of fan-deltas near the Squamish (Terzaghi, 1956; Prior et al., 1981) and Homathko and Klinaklini (Syvitski and Farrow, 1983) River deltas. Subaqueous slopes are extremely steep, averaging 15 to 25° to the fjord floor, and consist of cobbles and boulders partly imbedded and covered by bottom mud. These slopes are very unstable, as indicated by a recent (1955) slide on the Squamish fan delta. Submarine channels and large base-of-slope rotational slide (slump) blocks have also been described.

1.3.4 Summary

The following points summarize the features and processes of fjord deltas:

1 the high drainage basin relief and associated hydrologic and climatologic regimes cause high sediment yields and bedload dominance in contributing rivers and delta distributaries;

2 The long, narrow and deep morphology of the fjord receiving basin causes deposition on deltas to be laterally confined;

intertidal zones grade from salt marsh to sand and gravel flats offshore and are dissected by distributary channels;

subaqueous slopes are steep and coarse-grained proximally becoming more gently sloping and finer offshore and are marked by deformational features such as translational and rotational slides and submarine channels or chutes.

CHAPTER 2

STUDY AREA AND DELTA PLAIN

2.1 Introduction

Morphologic and depositional patterns on deltas are functions of the characteristics of the contributing drainage basin and receiving basin of the delta. Chapter 2 examines the drainage and receiving basins of the Bella Coola delta and provides a brief discussion of the subaerial delta plain. The Bella Coola delta is situated in North Bentinck Arm in the fjord coastline of British Columbia (Figure 2).

2.2 Drainage Basin

The drainage basin of the Bella Coola river is shown in Figure 3. The following discussion describes the physiography and bedrock geology, late Quaternary deposits and history, climatology, hydrology and fluvial system of the basin.

Physiography and Bedrock Geology

The western part of the Bella Coola basin is located within the Coast Mountains on the north flank of the highest part of the range. Monarch Mountain, on the southern edge of the basin is the highest point

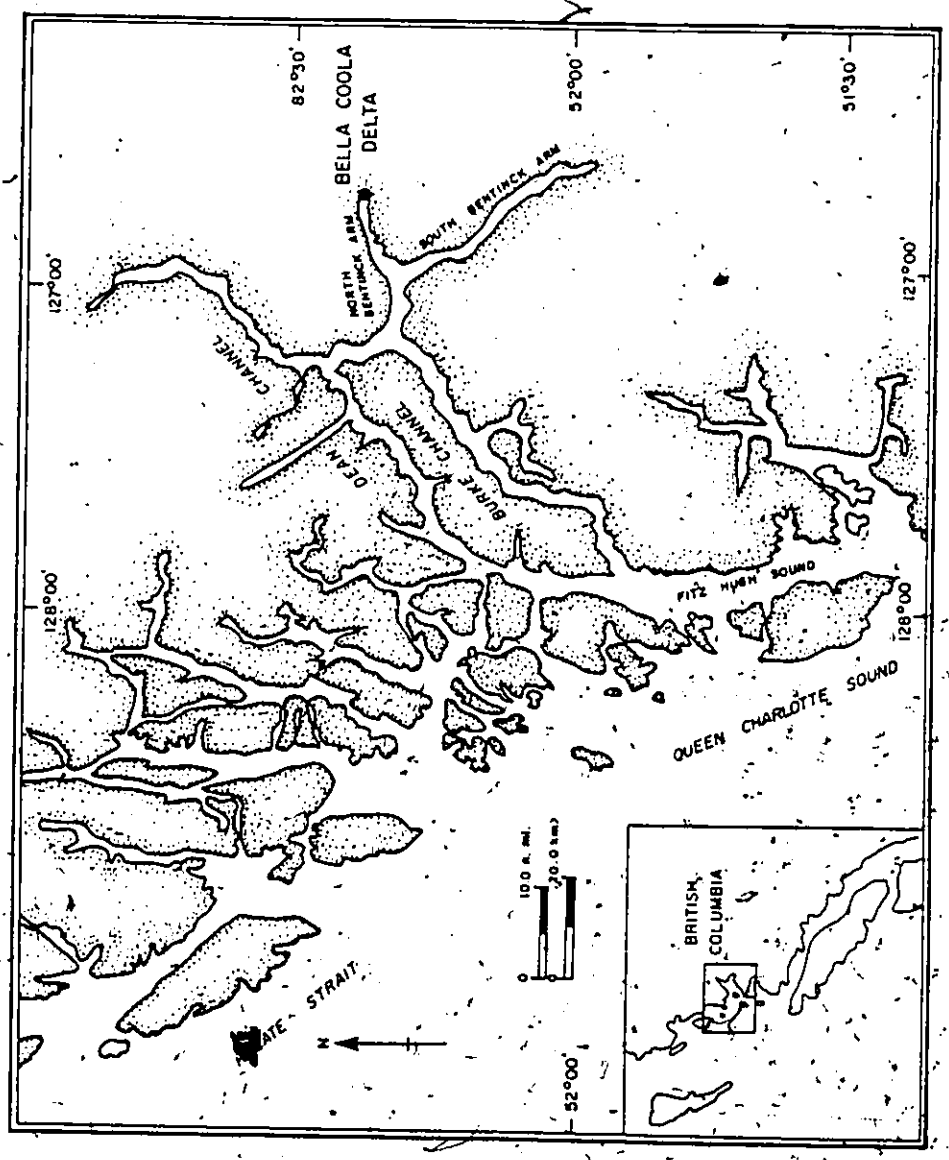

Figure 2. Location of study area.

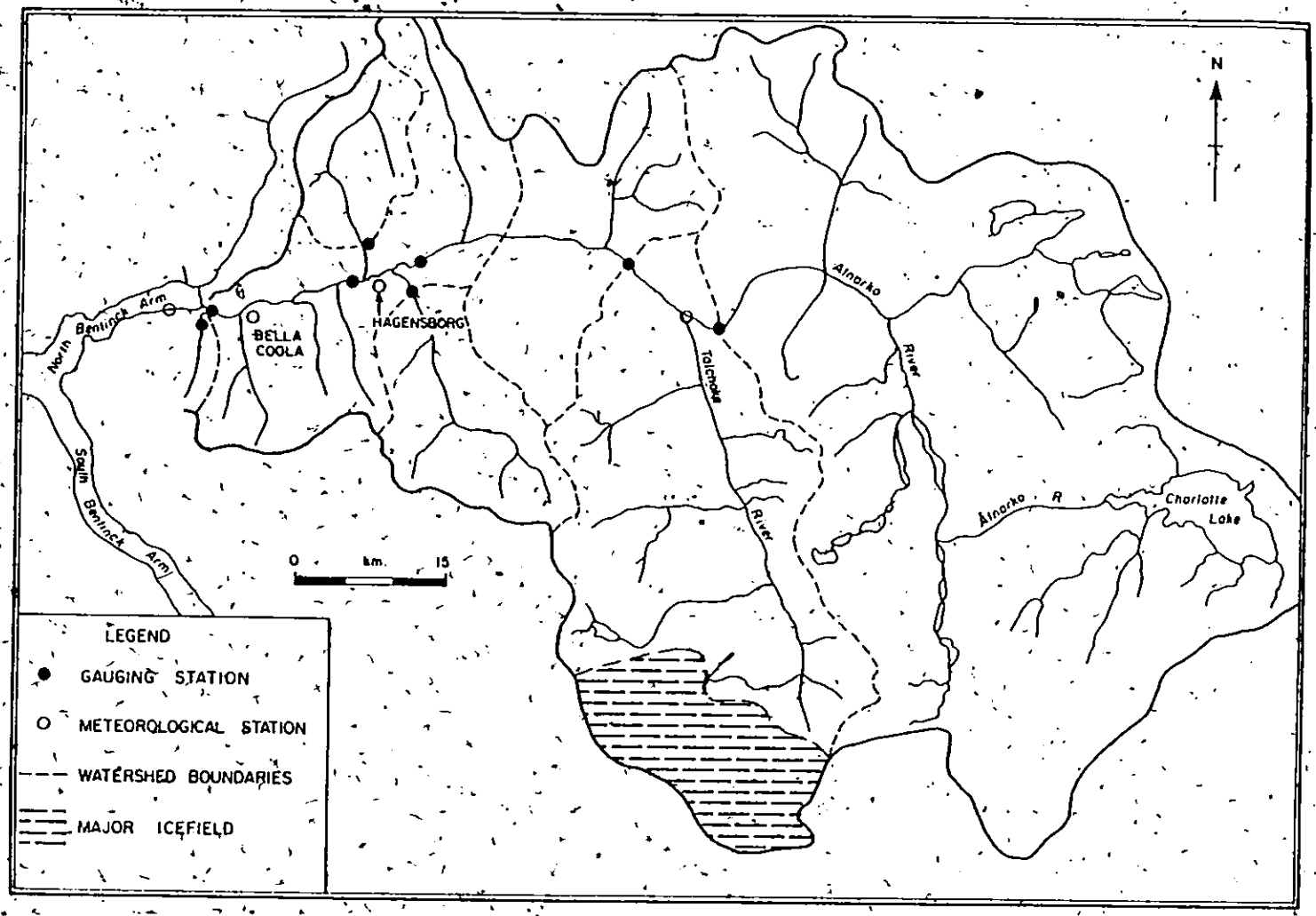

Figure 3. Drainage basin of the Bella Coola River (from Tempest, 1974).

at 3523 m. Peak elevations of the order of 2250 m occur north of the Bella Coola River, and the mountains rise to 3000 m to the south. The mountains have been heavily glaciated, resulting in deep, straight, glacial troughs between high craggy ridges. Bare rock faces are common, with moraine, cobble-gravel river deposits, and boulder cobble alluvial fans in the valley (Church and Russell, 1977).

The eastern part of the basin lies on the north part of the Fraser Plateau. The upland surface has elevations in the range 1500-2000 m. The drainage area in the plateau comprises 1/3 of the total for the Bella Coola River. On the plateau, ground moraine and dead ice topography (glacio-fluvial gravels) form the surface (Church and Russell, 1977). There are nineteen different bedrock types in the area, the main types being granitic plutonic rocks and metasedimentary and volcanic rocks (Hart, 1981).

Late Quaternary Deposits and History

The Bella Coola valley was glaciated repeatedly during the Pleistocene Epoch. During the most recent glaciation, the Fraser glaciation, most of the study area was covered by ice. The glacier ice flowed west and southwest from central British Columbia, through the mountain passes and towards the Pacific Ocean (Leaney and Morris, 1981). The ice achieved elevations of 1800 to 2000 m along valley walls (Hart, 1981), and scoured the fjord bottom well below the sea level of the time.

Deglaciation of the outer islands of the fjord coast commenced about 12,400 B.P. and was probably complete at Bella Coola 10,500-11,000 B.P. (Andrews and Retherford, 1978). Till was deposited locally at lower elevations, and outwash was deposited along the valley walls as ice contact terraces and in the valley centre as irregularly shaped masses of ice contact debris (Leaney and Morris, 1981).

During and shortly after deglaciation, the sea level was higher relative to the land in the Bella Coola Valley than it is at present. The limit of marine inundation, as indicated by the topsets of raised deltas and marine sand and clay, extended to about 17 m above present sea level in the area. As isostatic rebound began to raise the land relative to the sea during the Holocene, prominent sedimentary terraces of outwash, deltaic, and ancestral Bella Coola River deposits were left on the valley sides. Present sea levels were attained by 7,000-8,000 B.P., with a subsequent fluctuation to a level of -4 m more than 1,000 years ago (Andrews and Retherford, 1978).

Climatology

Long, cool, relatively wet summers and short, mild and wet winters characterize the climate of the Bella Coola area. Temperature and precipitation values are summarized on Figure 4. Temperature variations at Bella Coola are controlled primarily by the Pacific Ocean, but with distance inland the ocean effect decreases, and mean annual temperatures decrease. Altitude also effects temperature, the latter decreasing with increasing elevation (Leaney and Morris, 1981).

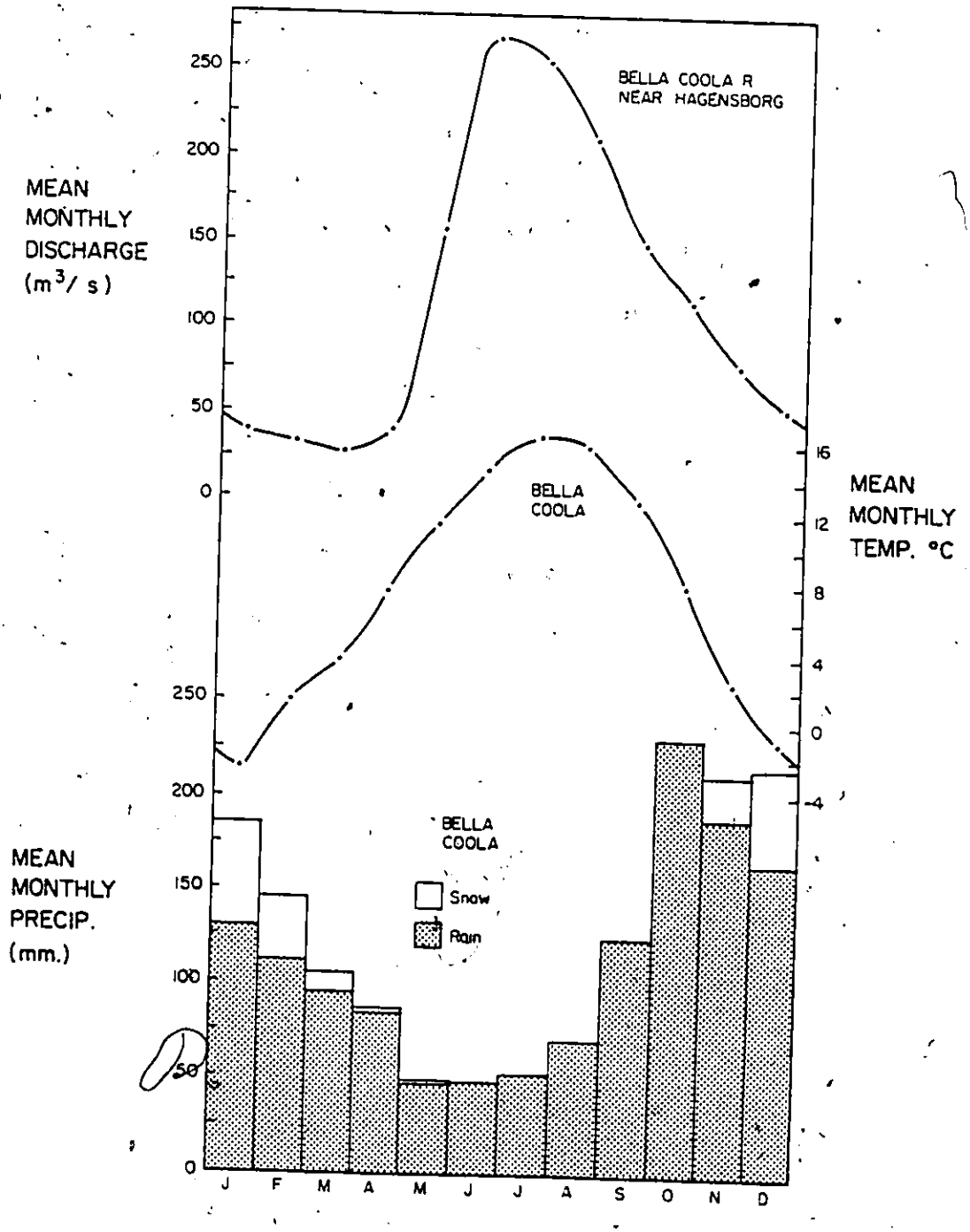

Figure 4. Bella Coola hydrologic and climatic data (from Hart, 1981).

Most precipitation falls from fall and winter storms impinging onto the coast from the Pacific, with the least amount of precipitation occurring during July and August. Much of this precipitation is in the form of rain at lower elevations, snow at higher elevations. Precipitation amounts decrease inland from Bella Coola (Leaney and Morris, 1981).

No wind data is available from the study area, but some qualitative comments can be made. Prevailing winds in the area are oriented by the long axis of North Bentinck Arm and the Bella Coola Valley, and are thus in an east-west direction. Winds are predominantly from the west during the spring, summer and fall, due to the prevailing Westerlies. In winter, winds are from the east in response to the flow of cold air from the interior plateau. The westerly winds generally set in around 10:00 a.m., blowing fresh until sunset when they usually fall calm. Winter east winds can blow with gale force.

Hydrology

The Bella Coola River system drains an area of 6,480 km^2, which extends from the Interior Plateau through the Coast Mountains to North Bentinck Arm. The Bella Coola River is formed by the confluence of the Atnarko and Talchako Rivers, 64.3 km east of the tidal water. The Atnarko River arises from Charolotte Lake at the eastern edge of the watershed, while the Talchako River orginates from the Talchako glacier in the Coast Mountains. The Atnarko river drains 3250 km^2, and the Talchako river has a drainage basin of 1,100 km^2. Glacier ice covers

33% of the drainage basin of the Talchako River, or 7% of the total Bella Coola basin. Numerous other smaller streams flow into the Bella Coola River (Leaney and Morris, 1981).

The Bella Coola River has a mean annual discharge of 181 $m^3 s^{-1}$. Streamflow in the Bella Coola is low in autumn and winter and increases through May with snowmelt and rain, rising to a June peak and remaining high through July, the period of peak glaciermelt (Figure 4) (Hart, 1981). The maximum monthly discharge from the two major tributaries does not occur at the same time. In the Atnarko River maximum mean monthly flows occur during June, owing to heavy rain, while in the Talchako River peak flows occur in July as a result of glaciermelt. Seventy-five percent of the discharge of the Bella Coola occurs between May and September (Leaney and Morris, 1981). These trends, however, mask the importance of fall and winter rains which, particularly if supplied through the range of elevation to a ripe snowpack, could produce a maximum probable flood (Hart, 1981). Peak flows during a flood in January 1968 attained values of 1500 $m^3 sec^{-1}$ in the Bella Coola River. These fall and winter flows are short lived, extremely intense, and vary from year to year, while the spring and summer floods are more consistent from year to year, less extreme, and of longer duration (Church and Russell, 1977).

Bella Coola River Fluvial System

The Bella Coola River has been described by Church and Russell (1977) and Church (1981) as a "wandering gravel bedload river". Gravels

are entrained by the river from its banks and are delivered from tributaries. Sediment storage in the main channel is located principally in a series of sedimentation zones where the river is laterally unstable.

Sedimentation zones usually occur upstream from tributary alluvial fans where the river gradient is locally reduced, although in the lower 25 km of river sedimentation zones have a regular spacing of 4 km which may reflect the sporadic step like transport of coarse material produced by high flows. A series of maps shows that the locus of lateral instability has progressed downstream from km 25 in 1900, to near the mouth today. This pattern is believed to be related to the passage of a 'slug' of gravel downstream through the successive sedimentation zones. Average movement would be about 0.25 km yr^{-1}. The probable explanation for this effect is the introduction of unusual volumes of sediment into the main channel by the erosion of Neoglacial (18th and 19th century) moraines of alpine glaciers (Church, 1981).

The sediment load of the lower Bella Coola River can thus be divided into 2 major components, suspended load and bedload. Suspended sediment concentrations are relatively low in the spring, autumn and winter, (< 10 mg ℓ^{-1}) increasing as fine grained material from soil erosion is entrained during flood conditions. During extreme floods, sediment as coarse as medium sand may be placed into intermittent suspension. Most of the suspended load carried by the river is a result of glaciermelt in the summer months. Glacial 'flour' from the icefield in the Talchako basin is carried downstream and concentrations exceed 100 mg ℓ^{-1}. This material is largely silt sized.

Bedload is transported during floods, including those in spring and summer, but most importantly those floods that occur in the fall and winter due to major rainstorms on the snowpack. In addition, the bedload 'slug' discussed by Church (1981) has probably reached as far downstream as the delta. A major winter flood occurred in December 1980 and material as coarse as very coarse sand and fine gravel was deposited on overbank areas in the lower reaches of the river. This indicates that large amounts of bedload were in transit at this time.

Annual quantities of sediment transported by the Bella Coola River to the delta have been estimated by Western Canada Hydraulic Laboratories (1976) to be about 13,600 metric tonnes (15,000 tons). Much of this weight would be sand and gravel transported as bedload.

2.3 Receiving Basin

The receiving basin of the Bella Coola delta, North Bentinck Arm, is described in terms of basin morphology, tides, waves and currents, all of which affect sedimentation on the delta.

Basin Morphology

North Bentinck Arm is a narrow elongate fjord basin that is approximately 15 km long and 2.6 to 3.0 km wide (Figure 5). The subaerial slopes of the Arm are extremely steep, rising rapidly to elevations greater than 1,000 m above sea level, with the mountains becoming higher towards the head of the Arm. North Bentinck Arm, as is typical

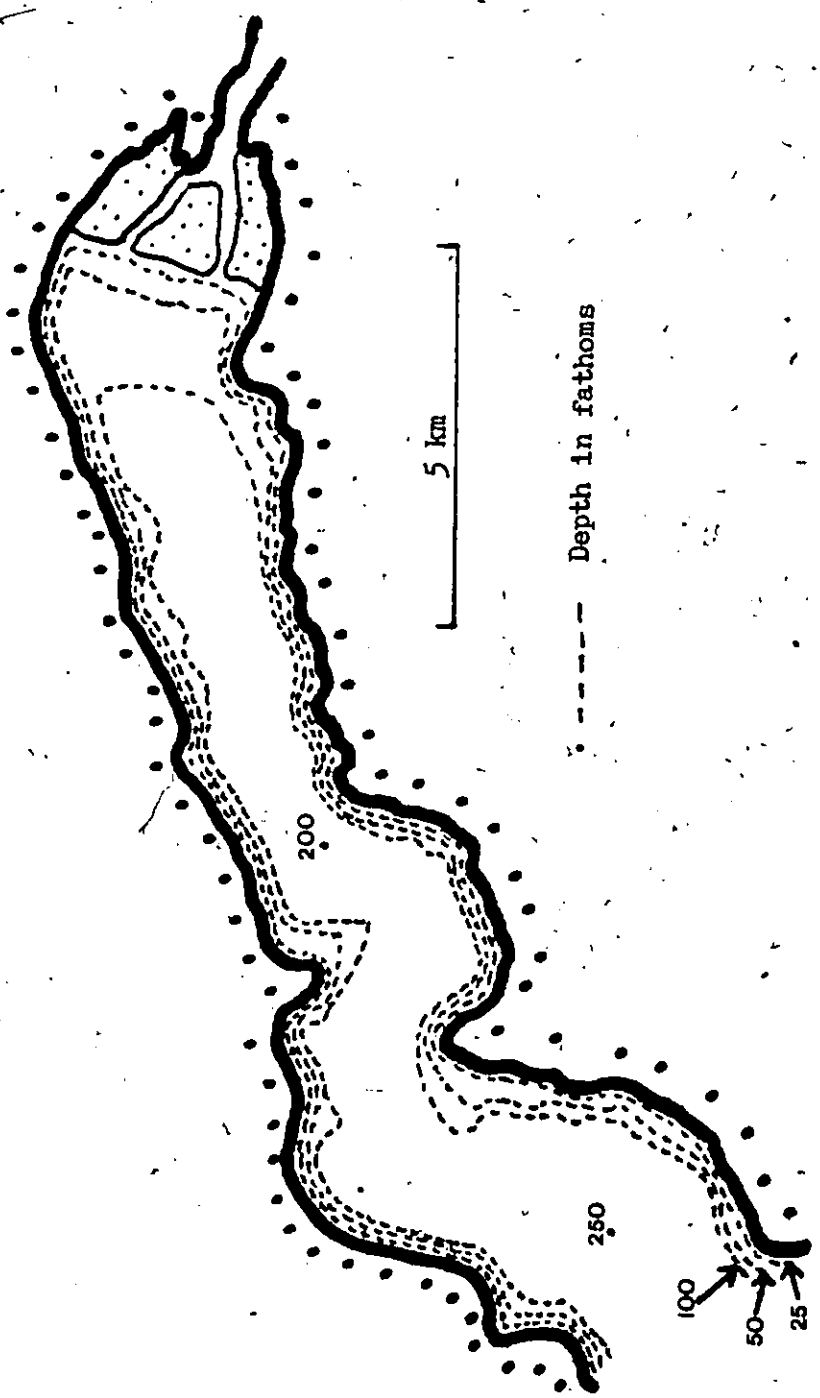

Figure 5. North Bentinck Arm bathymetry.

of fjords in B.C., is very deep, with a mean depth of 400 m, and a maximum depth of 550 m. Subaqueous wall slopes are also very steep, with the 100 fathom (183 m) contour lying only 360 m from shore.

Tides

The tides in North Bentinck Arm are of the mixed, semidiurnal type, with 2 complete tidal oscillations daily with inequalities both in height and time, reaching their greatest values when the declination of the moon has passed its maximum. Bella Bella, about 31 km northwest of Bella Coola, is the Reference Port for tidal predictions at Bella Coola. There are only 6 and 5-minute delays in times of higher high and lower low waters respectively, between Bella Bella and Bella Coola, suggesting that the tides approximate a standing wave in the basin. Tidal data for Bella Coola were recorded during 1909, 1950-1957, and 1964-1967. The mean water level at Bella Coola is 2.9 m, mean tidal range is 3.9 m, and large tidal range is 5.9 m. Meteorological conditions can produce a departure from predicted tide heights (Leaney and Morris, 1981).

Waves

Waves in North Bentinck Arm are locally generated, there is no evidence for long period sewells penetrating from the open ocean. The various bends in the fjord system reduce the fetch. The characteristics of waves in North Bentinck Arm are discussed in Section II of this thesis.

Currents

There are three forces that generate currents in North Bentinck Arm: 1. tides, 2. river runoff and 3. winds. Tidal effects on currents were determined for the Whiskey Bay area (Figure 5) by Dodimead and Herlinveaux (1968). Surface and 1 meter currents responded to the tide midway between high and low water, and a peak outflowing surface current of 100 cm sec^{-1} was recorded on the ebb tide. Currents at 15 m were about 30 cm sec^{-1} and at 25 m around 15 cm sec^{-1}. As is discussed in Section II, tidal currents are much weaker at the head of the fjord. River runoff currents occur on the surface of North Bentinck Arm and are examined in detail in Section II.

Winds have pronounced effect on currents in North Bentinck Arm, in some cases up-inlet winds of 32 km hr^{-1} were able to reverse the flow of the ebbing tide. Up inlet winds tend to be strongest along the northern shore, and the outflowing ebb is also strongest there (Leaney and Morris, 1981).

It was concluded by Leaney and Morris (1981) that in North Bentinck Arm, a surface down-channel flow persists until at least the mid-flood period under conditions of low runoff. If relatively strong up-inlet winds prevail, the flow may reverse before the mid-flood stage of the tide. Under most tidal conditions and up-inlet winds, the surface water moves from mid-channel into Whiskey Bay and up-channel along the southern shore.

2.4 Delta Plain

The Bella Coola Delta can be divided into two major components: a gently sloping subaerial (supra and intertidal) delta plain and a subaqueous (subtidal) delta composed of the delta front and prodelta (Figure 6). The subaqueous delta is examined in detail in Section III. The delta plain consists of a tree covered upper delta plain and a lower delta plain composed of salt marsh grading seaward into sand flats (Figure 7). Major and minor distributary and tidal channels flanked by gravel bars cross the delta plain.

Upper Delta Plain

The upper delta plain is the supratidal area to the east of the active delta (Figure 7). Vegetation in this zone is willows nearer the active delta blending into mixed coniferous forest eastward (Leaney and Morris, 1981). Sedimentation is primarily a result of overbank deposition during high magnitude floods of the Bella Coola River.

Lower Delta Plain

The major components of the lower deltaic plain are the salt marsh and the sand flats. The salt marsh is subdivided into two zones, the high marsh and the low marsh. The high marsh has the high tide limit as an upper boundary, and is less frequently inundated than the low marsh. The main high marsh species is Elocharis palustris. The low marsh is more frequently inundated and is composed primarily of Hippuris

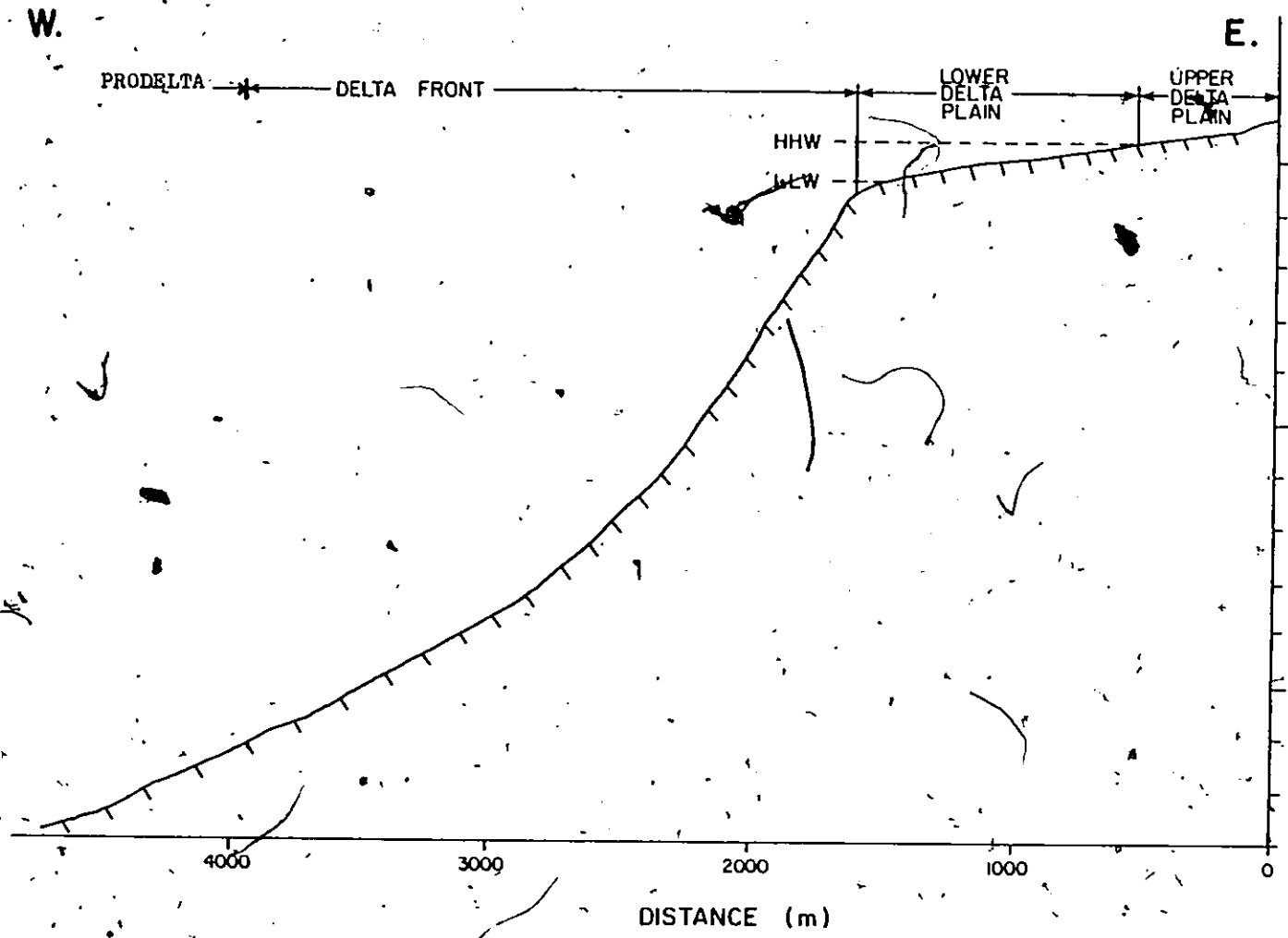

Figure 6. Components of the Bella Coola delta.

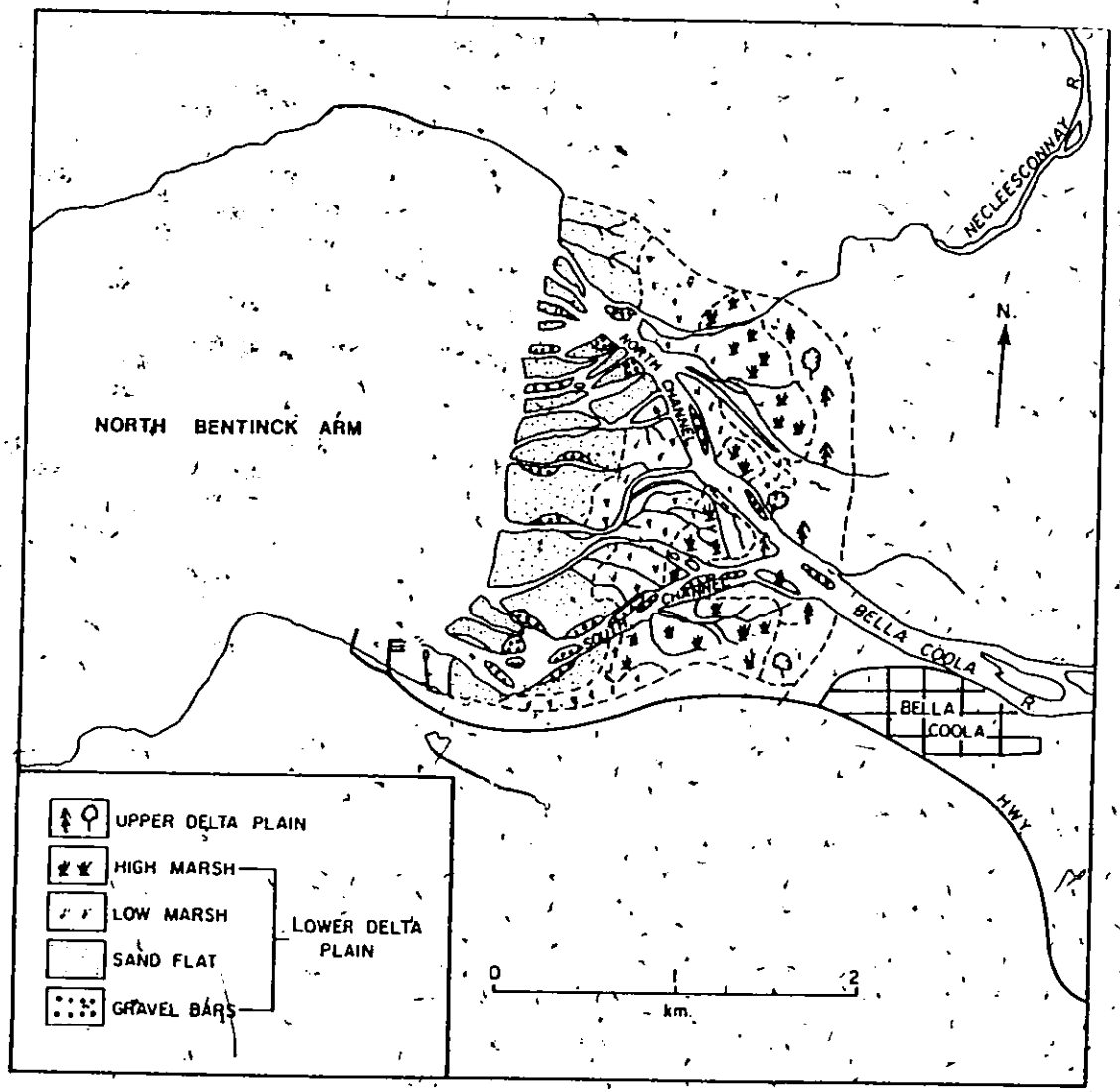

Figure 7. Environments of the subaerial delta plain.

tetraphylla and Plantago maritima (Leanney and Morris, 1981). The major roles of the salt marsh on sedimentation on the delta are to stabilize the surface against erosion by tides and distributaries and to trap fine-grained sediment ordinarily removed by ebbing tides.

Sand flats occupy much of the interdistributary areas of the seaward portion of the lower delta plain. The surface of the sand flats is composed almost entirely of medium-grained sand covered by long, straight crested, symmetrical to slightly assymetrical low amplitude ripples with wavelength 3-5 cm produced by wave action during high tide conditions. There appears to be little grain size variation onshore or laterally on the flats. Sand flat sediments are exposed by migrating channels. Alternating layers of 3-5 cm thick finer and coarser sand are combined with organic (peat) horizons of 1-2 cm thickness. Ripple marks oriented in both flood and ebb directions are located within sand layers. The organic horizons are probably related to the deposition of plant matter during falling tides. The peat serves as a useful 'tracer' for examination of low tide distributary mouth sediment plumes as it produces a dark gray to black colour in the water.

Channels

There are three main channel types on the delta plain: distributary channels carrying primarily fluvial discharge, tidal channels originating in the high salt marsh and related to tidal drainage, and tidal-distributary channels which have significant tidal and fluvial components. In many cases the tidal channels join the distributary

system. Examples of these channel types and morphometric analyses are presented in Section II.

There are two main distributary channels, the North Channel and the South Channel (Figure 7). Discharge measurements on July 4, 1981 showed that the North Channel carries approximately 80% of the total river discharge, and the South Channel 20%. Of the total annual sediment load of 13,600 metric tonnes (15,000 tons) supplied to the delta by the Bella Coola River, the South Channel carries 2,700 to 3,600 metric tonnes (3,000 to 4,000 tons) or 20-26% of the load and the North Channel carries 10,000-10,900 metric tonnes (11,000-12,000 tons) or 74-80% of the total load (Western Canada Hydraulics, 1976).

The South Channel is a shallow, inefficient distributary, choked by sediment and containing numerous gravel bars. In contrast, the North Channel is deeper, swifter, and has fewer gravel bars. Gravel on the delta plain is restricted to areas near distributary channel margins, in association with distributary mouth bars and within distributary channels. Some of the smaller channels are laterally migrating rapidly, incising into sand flat deposits and transporting sand to the delta front.

Small distributary channels occur as the result of crevassing of levees in the upper areas of the North and South Channels. As the North Channel crosses the delta plain in its lower reaches, a number of small, shallow channels break off and flow over the sand flats. Most of the discharge from the North Channel, however, enters North Bentinck Arm via

the main branch of the North Channel, and the smaller distributaries account for only a small portion of the total discharge. Similar channel bifurcations occurs on the South Channel near the low tide limit.

Tidal channels are not a major component of the delta plain. They are limited in extent, heading on the high salt marsh and merging a short distance seaward with small distributary channels. The tidal-distributary channels that result usually pass over the sand flats to the edge of the delta plain. Tidal channel banks are stabilized by salt marsh vegetation and beds are muddy. In contrast, tidal-distributary channel banks are composed of easily eroded sand flat sediments and beds are sandy.

SECTION II - RIVER MOUTH PROCESSES AND RESPONSES

List of Symbols

a: buoyancy coefficient

b_o: outlet width (m)

C: Chezy coefficient

C_g: group wave velocity (ms^{-1})

c: individual wave velocity (ms^{-1})

E_j: volume of salt water entrained over interval j (m^3)

F: Froude Number

F': Densimetric Froude Number

f: Darcy-Weisbach friction factor

g: acceleration due to gravity (ms^{-2})

H: deep water wave height (m)

H': shallow water wave height (m)

h: water depth (m)

h': depth of the density interface (m)

h_o: outlet depth (m).

$\bar{h}$: mean water depth over x (m)

I: similarity integral

K: friction coefficient

L: deep water wavelength (m)

L': shallow water wavelength (m)

ℓ: upstream distance of channel affected by tide (m)

n: Manning coefficient

P: total wave power per unit crest width (W)

P': nearshore wave power per unit crest width (W)

P_r: tidal prism (m^3)

Q: discharge ($m^3 s^{-1}$)

Q_o: outlet discharge ($m^3 s^{-1}$)

R_o: outlet Reynolds Number

r: correlation coefficient

T: wave period (s)

U: velocity (ms^{-1})

U_e: entrainment velocity (ms^{-1})

U_j: average velocity over interval j (ms^{-1})

U_{max}: centreline velocity (ms^{-1})

U_n: mean velocity at section n (ms^{-1})

U_o: outlet velocity (ms^{-1})

U_*: shear velocity (ms^{-1})

W: particle settling velocity (ms^{-1})

w_o: channel width at mouth (m)

w_x: channel width at distance x upstream of mouth (m)

x: distance seaward or landward of outlet (m)

x_j: downcurrent distance over interval j (m)

γ: density ratio

δ_w: horizontal convergence coefficient

ε: rate of jet expansion

Ω: buoyancy coefficient

ν: kinematic viscosity ($m^2 s^{-1}$)

ρ_f: fresh water density ($kg\ m^{-3}$)

ρ_s: salt water density ($kg\ m^{-3}$)

ϕ: weight per unit volume of sea water ($N\ m^{-3}$)

σ_T: density ($kg\ m^{-3}$)

τ_o: boundary shear stress at outlet (Pa)

ω: stream power ($N\ m^{-1} s^{-1}$)

CHAPTER 3

FRAMEWORK

3.1 Introduction

Section II considers river mouth processes (effluent dynamics) and the associated process-response interactions which occur when a channel debouches into ambient basin water. It consists of four chapters. Chapter 3 provides the framework for the section, based on a review of literature. Chapter 4 analyses the effects of tides and waves on the Bella Coola delta, and chapter 5 describes the morphodynamics at the mouth of the North Channel. Chapter 6 is a comparison of the results from Bella Coola with the morphodynamic models of Wright (1977) and Bates (1953) and provides a section summary.

The major synthesis by Wright (1977) has provided a starting point for this section. Some of the more important field, laboratory and theoretical river mouth process studies include those of Axelson (1967), Bates (1953), Bondar (1970), Bonham-Carter and Sutherland (1968), Borichansky and Mikhailov (1966), Crickmay and Bates (1955), Garvine (1974, 1975), Gilbert (1884), Jopling (1963), Kashiwamura and Yoshida (1967, 1969, 1971), Komar (1973), Scruton (1956, 1970), Wright (1970, 1971), Wright and Coleman (1971, 1972, 1973, 1974) and Wright et

al. (1973). Wright (1977) concluded that:

1. river mouth form-process variability can be best understood by considering river mouth systems as the result of three primary and two modifying forces:

Primary forces:
1. inertia and associated turbulent diffusion
2. turbulent bed friction
3. buoyancy

Secondary forces:
4. tides
5. waves

2. the relative importance of the three primary forces depends on four factors:

a. discharge and outflow velocity of the stream
b. water depths in and seaward of the river mouth
c. the amount and grain size of the sediment load
d. density contrasts between river and basin waters

3. dominance by each of the primary and secondary forces results in six morphodynamic models of river mouth sedimentation:

(i) inertia dominated -- axial jet
(ii) friction dominated - plane jet
(iii) buoyancy dominated - buoyant jet

(iv) buoyancy dominated - plane jet

(v) tide dominated

(vi) wave dominated

These models are discussed below. It must be stressed at the outset that the models represent idealized situations and most river mouths probably reflect a combination of these forces.

3.2 Homopycnal and Hypopycnal Flows

Bates' (1953) distinction between homopycnal and hypopycnal outflows is a basic component of morphodynamic models based on the dominance of primary forces. In homopycnal outflow there is only a small density contrast between issuing and ambient waters; in hypopycnal situations the issuing water flows over denser, usually saline, basin water. The inertia dominated and friction dominated models usually apply to homopycnal situations, and the buoyancy dominated models to hypopycnal situations. A third, and rare, type of outflow is hyperpycnal, where issuing river water is denser than basin water and enters the basin as an underflow.

3.2.1 Homopycnal Outflows

For homopycnal outflows the structure of the effluent jet depends on the ratio of inertial to viscous forces as indexed by the outlet Reynolds number R_o:

$$R_o = U_o[h_o(b_o/2)]^{1/2})/\nu \qquad (1)$$

where U_o is the mean outlet velocity, b_o is the width of the outlet, h_o is the depth of the outlet and ν is the kinematic viscosity. The terms in this and the following equations are illustrated on Figure 8. When R_o exceeds a value of 3,000, inertial forces dominate and the jet becomes fully turbulent (Pearce, 1966).

The drag per unit area of the boundary at the outlet can be described by the boundary shear stress τ_o:

$$\tau_o = \rho_f U_*^2 \qquad (2)$$

where U_* is the shear velocity:

$$U_* = \frac{k \quad (U_1 - U_2)}{2.3 \ (\log y_1 - \log y_2)} \qquad (3)$$

where U_1 and U_2 are velocities at y_1 and y_2, it is assumed that the velocity profile is logarithmic and the Von Kármán coefficient k has a clear water value of 0.4 (Gray, 1970).

3.2.2 Hypopycnal Outflows

For hypopycnal outflows the ratio of inertial to buoyant forces is provided by the densimetric Froude number F':

$$F' = U/(\gamma g h')^{1/2} \qquad (4)$$

where U is the mean outflow velocity of the issuing river water; γ is the density ratio:

$$\gamma = 1 - (\rho_f/\rho_s) \qquad (5)$$

where ρ_f is the density of the issuing river water and ρ_s is the density of the ambient basin sea water; g is the acceleration due to gravity, and h' is the depth of the density interface (Wright and Coleman, 1971; Wright, 1977). Values of F' less than 1 indicate a dominance of buoyancy and a suppression of inertia and turbulence, values greater than 1 indicate an increasing importance of turbulence with the jet becoming fully turbulent when F' exceeds 16.1 (Hayashi and Shuto, 1967, 1968).

In the subsequent discussion, lines of equal density are expressed in terms of σ_t values, where σ_t is related to the density $\rho(g\ cm^{-3})$ by:

$$\sigma_t = 10^3(\rho - 1). \qquad (6)$$

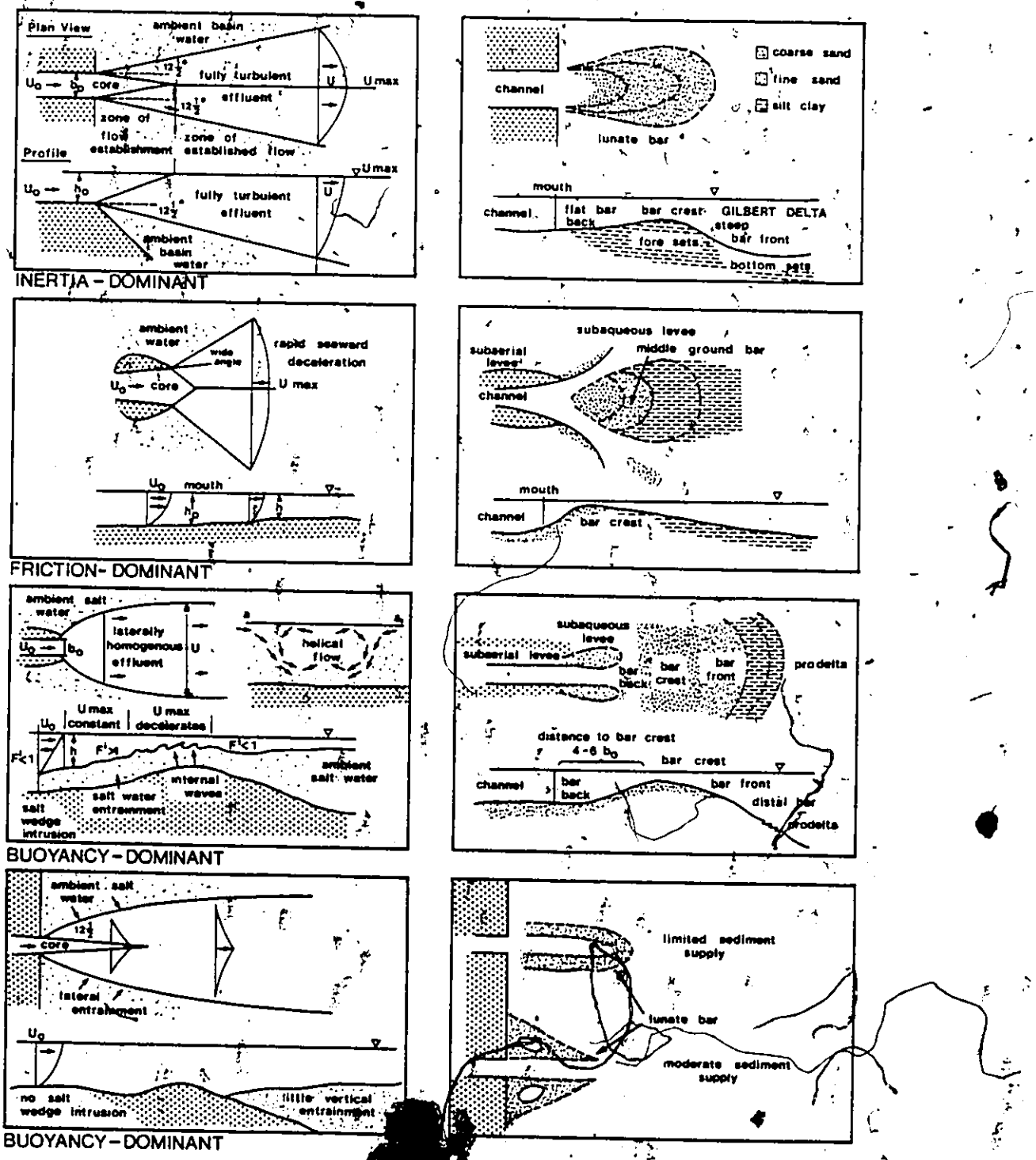

Figure 8. River mouth morphodynamic models associated with primary forces (from Wright, 1977; Bates, 1953).

3.3 Morphodynamic Models Related to Primary Forces

3.3.1 Inertia Dominated

Inertia dominated effluents are associated with homopycnal outflows, where sufficiently deep water allows vertical and lateral effluent expansion, and are termed axial jets (Figure 8a). The effluent is fully turbulent, with values of R_o exceeding 3,000.

Diffusion results as eddies are generated at the effluent boundaries and produce effluent expansion, mixing and deceleration. The axial jet is characterized by a zone of flow establishment with a seaward-diminishing core of constant velocity which extends 6.2 b_o seaward of the outlet, and a zone of established flow dominated by turbulent eddies with progressively seaward decelerating centreline flow (Wright, 1977). The flow deceleration is represented by:

$$U_{max}/U_o = h_o(b_o/2)/\varepsilon Ix \qquad (7)$$

where U_{max} is the centreline velocity, x is the distance seaward of the outlet, I is a similarity integral = 0.316, and ε is the rate of jet expansion:

$$\varepsilon = \frac{dh}{dx} = 0.22 \qquad (8)$$

which is equivalent to an angle of separation between the centreline and

jet boundaries of 12 1/2° in both the vertical and horizontal (Stozenbach and Harleman, 1973). The plan-form velocity profile has a normal distribution, values of F' exceed 16.1 and τ_o is moderately large (Wright, 1977, 1978).

The distributary mouth bar associated with an inertial effluent is the lunate bar (Figure 8a). In response to low spreading angles of the axial jet, the lateral dispersion of sediments is restricted to a narrow zone which extends gradually seaward and then falls off more steeply beyond the bar crest (Wright 1978; Bonham-Carter and Sutherland, 1968). The experiments of Jopling (1963) displayed a similar pattern. Deltas related to inertial effluents would include high-energy glaciolacutrine 'Gilbert' types (eg., Gilbert, 1884).

3.3.2 Friction Dominated

Friction dominated effluents occur in homopycnal situations where depths seaward of the outlet are shallow and turbulent bed friction becomes important (Figure 8b). Values of $R_o > 3{,}000$ and the effluent is fully turbulent. Plane jet diffusion exists in this situation because jet expansion is limited to the horizontal by the bed. Friction and plane jet diffusion cause rapid increases in lateral spreading and deceleration as compared to axial jets (Wright, 1977). Through theoretical considerations, Borichansky and Mikhailov (1966) have shown that flow deceleration is expressed by:

$$U_{max}/U_o = e^{-K(x/h)} \tag{9}$$

where K is a function of the Chezy coefficient C:

$$K = g/C^2 \tag{10}$$

where g is the acceleration due to gravity. According to Giles (1977), C can be related to the better known Manning coefficient n by:

$$C = R^{1/6}/n \tag{11}$$

where R is the hydraulic radius, or to the Darcy-Weisbach friction factor f by:

$$C = \sqrt{8g/f} \tag{12}$$

Increases in width b seaward of the outlet are given by:

$$b/b_o = (h_o/\bar{h})e^{K(x/h)} \tag{13}$$

where $\bar{h}$ is the mean water depth over x (Mikhailov, 1966). A normal transverse velocity distribution should exist seaward of the core region and values of τ_o should be very large (Wright, 1977).

There is a distinct pattern of bar and subaqueous levee developments related to friction dominated effluents. In early stages a broad

radial distributary mouth bar (Coleman, 1976) develops. As deposition continues subaqueous levees develop along the flanks of the effluent and channelization occurs along the inner banks of the levees. The result is a triangular middle ground bar separating diverging channels (Figure 8b) (Wright, 1978). Examples of middle ground bars can be found at the mouths of crevasses on the Mississippi Delta (Coleman et al., 1964).

3.3.3 Buoyancy Dominated - Buoyant Jet

When a salt wedge intrusion occurs in distributary channels the outflow spreads as a buoyant plume above the saline basin water (Figure 8c) and a value of $F' \propto 1$ is maintained at the outlet (Wright and Coleman, 1971; Wright, 1977). High river mouth depth-width values, which are a direct result of fine grained sediment loads and low tidal range promote intrusion of a salt wedge into the channel (Wright, 1977). Entrainment of saline basin water occurs primarily vertically, across the density interface where F' values exceed 1. Super-elevation of the effluent in response to buoyant forces produces a secondary circulation and helical flow pattern in the jet (Wright and Coleman, 1971). Velocity values are similar across the effluent in plan (Figure 8c) and not normally distributed as in axial or plane jets. Wright and Coleman (1971) have shown that the seaward velocity U (averaged over the cross section) decreases with increasing vertical entrainment of salt water such that at any section n:

$$U_n = (Q\rho_f)_{n-1} / [(Q\rho_f)_{n-1} + (E_j \rho_s)] \qquad (14)$$

where Q_{n-1} is the volume of water discharged per unit time at the previous section and the subscripts f and s refer to the fresh and salt water layers respectively, and E_j is the volume of salt water entrained over the interval j having a downcurrent distance x_j with unit width:

$$E_j = U_e(x_j / \langle U_j \rangle) \qquad (15)$$

where $\langle U_j \rangle$ is the average velocity over the interval and the entrainment velocity U_e is:

$$U_e = 3.5 \times 10^{-4}(U - 1.15(gh\gamma)^{1/2}). \qquad (16)$$

The lateral expansion of the buoyant effluent is given by Bondar (1970) as

$$b/b_o = (1 + ax)^{2/3} \qquad (17)$$

and the change in thickness, h', of the plume above the density interface:

$$h'/h_o = 1/(1 + ax)^{2/3} \qquad (18)$$

where:

$$a = \frac{3}{2}\left[\frac{\Omega\, h_o'(h_o')^{1/2}}{Q_o}\right] \qquad (19)$$

where Q_o is the outlet discharge rate and:

$$\Omega = \frac{4}{3}(2g\gamma)^{1/2}(1 - \frac{\gamma}{2}). \qquad (20)$$

Equations (17) to (19) assume a constant seaward velocity and no vertical entrainment.

In the model described above, the effluent in the region between the mouth and 4 to 6 channel widths (b_o) seaward expands as a homogenous layer a result of hydrostatic pressure produced by buoyancy. This expansion rate is usually greater than axial jets but less than friction dominated plane jets. As the effluent spreads laterally in this region it thins vertically as seaward velocities remain constant (Wright, 1977). Values of τ_o should be very low.

The depositional pattern associated with buoyancy dominated effluents is shown on Figure 8c. Straight subaqueous levees occur seaward of subaerial levees as a result of flow convergence near the bed, and produce straight distributaries with high depth-width ratios and a small number of bifurcations. The distributary mouth bar crest is situated 4 to 6 channel widths seaward of the outlet and is composed of the coarsest bar sediment. On the bar front the sediment fines seaward, eventually grading into the clays of the prodelta zone (Wright, 1977; Wright and Coleman, 1974). Examples of buoyancy dominated effluents and sedimentation patterns include the major distributaries of the

Mississippi (Wright, 1970, 1971; Wright and Coleman, 1971, 1974), the Po (Nelson, 1970) and the Danube (Bondar, 1970).

3.3.4 Buoyancy Dominated - Plane Jet

Bates (1953) suggested that a salt wedge intrusion into the lower reaches of a distributary channel was an 'unnatural' phenomenon resulting from dredging activity at the river mouth. He suggested that in natural situations the effluent would flow out over the basin water as plane jet with the density interface acting as a rigid boundary (Figure 8d). In his model entrainment of basin water was primarily lateral, with little entrainment vertically across the density interface. Deceleration rates for the jet are noted by Bates (1953) as being similar to the two-dimensional (plane jet) experimental results of Albertson, et al. (1950) defined by:

$$U_{max}/U_o = 2.28\ x/b_o \qquad (21)$$

for the zone of established flow. The angle of separation would be initially large (35°), decreasing to 8° in the zone of established flow, with a normally distributed velocity profile in plan and a parabolic shape. Bates, (1953) suggests that a lunate distributary mouth bar would develop in conjunction with plane jet diffusion (Figure 8d). Straight levees develop along the flanks of the jet in conjunction with deposition of a transverse bar beyond the core region where flow begins to decelerate at 4 to 8 channel widths seaward of the outlet. The

transverse bar joins the levees to produce the lunate morphology. Bates (1953) cites various Mississippi distributaries as examples of this type of plane jet diffusion and related deposition.

3.4 Morphodynamic Models Related to Modifying Marine Forces

Modifying marine forces include tides, waves, coastal currents, various frequencies of internal waves, biologic and chemical processes and sea ice and thermal processes. The marine forces exert 2 main types of influence: (1) they directly modify the outflow processes by promoting more rapid mixing and momentum exchange between effluent and ambient waters and by redirecting the sediment transport flows, and (2) they redistribute and remold the river mouth deposits following their initial desposition (Wright, 1977). Waves and tides are the most important modifying factors and are the two considered by Wright (1977).

3.4.1 Tide Dominated

Strong tides have three basic effects: (1) tidal mixing obliterates vertical density gradients, subduing the effects of buoyancy; (2) for at least part of the year, tides may account for a greater fraction of the sediment transporting energy than does the river, causing bidirectional sediment transport; and (3) the range of positions of the land-sea interface and of the zone of marine-riverine interactions is greatly extended, both vertically and horizontally (Wright, 1977). Wright et al. (1973) have shown that for tidal processes to dominate over riverine processes the tidal prism, defined as the total volume of

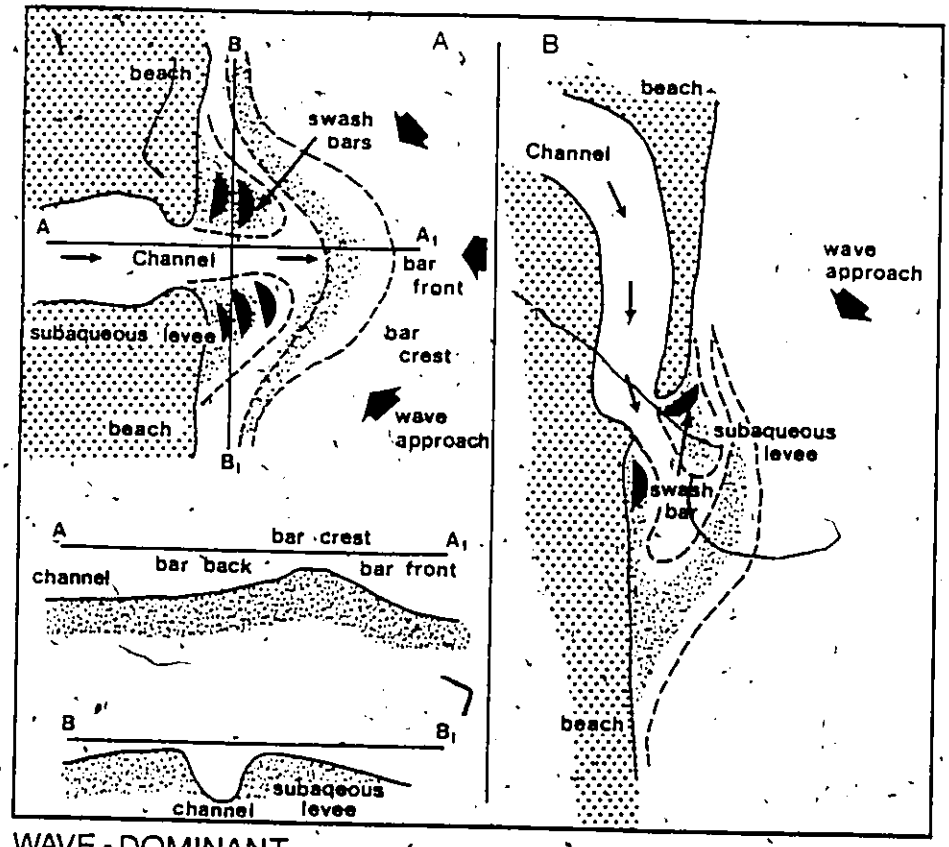

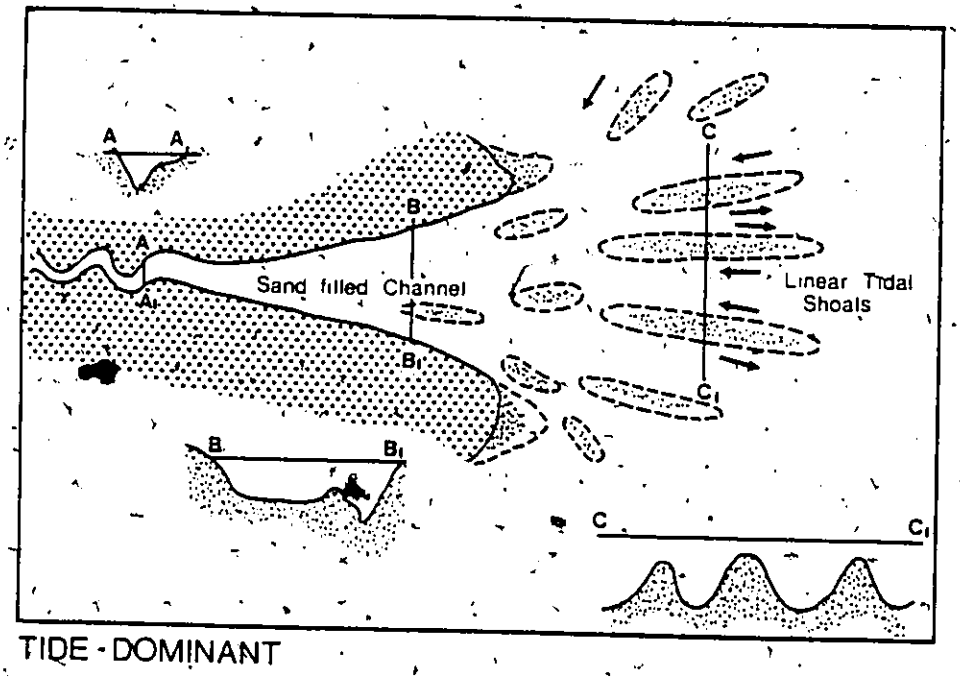

Figure 9. River mouth morphologies associated with modifying marine forces (from Wright, 1977).

water exchanged past any section by tidal transport during one tidal cycle, must exceed river discharge during that cycle.

Distributary channels experiencing strong standing wave tidal influence tend to display a "funnel-shape" or exponentially upstream-converging widths, w, expressed in dimensionless form as:

$$w_x/w_o = e^{-\delta_w(x/\ell)} \qquad (22)$$

where δ_w is the horizontal convergence coefficient and ℓ is the upstream distance from the mouth affected by the tide (Wright et al., 1973). Tidal currents can produce linear subaqueous ridges (Wright et al., 1975) and bidirectional sediment transport within channels can result in preservation of both flood and ebb-oriented bedforms and sedimentary structures (Wright, 1977). Figure 9a summarizes the morphology of tide-dominated river mouths.

3.4.2 Wave Dominated

Waves can directly modify the expansion and deceleration patterns of river mouth effluents. Outflow from river mouths refracts and steepens incident waves causing the waves to break in water depths greater than the normally breaking depth and enhancing the mixing and momentum exchange between effluent and ambient waters. This effect, plus wave-induced set-up opposing the outflow, causes very rapid deceleration and loss of sediment transporting ability within short

distances of the outlet (Wright, 1970, 1977). The relationship between wave and river power can be expressed by the discharge effectiveness ratio, the ratio of average river discharge per unit channel width to the nearshore wave power per unit crest width. Total wave power per unit crest width, P, for any given set of wave characteristics is given by:

$$P = \emptyset H^2 C_g / 8 \qquad (23)$$

where $\emptyset$ is the weight per unit volume of seawater, H is the deep-water wave height, and C_g is the group velocity (celerity) of the wave given by:

$$C_g = 1/2\ c = 1/2(g/2\pi\ T) \qquad (24)$$

where c is the individual wave velocity (celerity) and T is the period. Deep-water wavelength (L) can be calculated from

$$c = L/T \qquad (25)$$

(Wright and Coleman, 1973; Komar, 1976). In most instances the wave power near shore (P'), due to shallow-water wave attenuation, is much less than the deep water power (P) and this loss of power must be accounted for. Shallow-water attenuation affects wave height (H) and wavelength (L), producing shallow-water wave height (H') and wavelength (L') according to relationships provided by Russell and MacMillan

(1952). The value of H' then replaces H in the power equation (equation 23) and the nearshore wave power (P') calculated.

The depositional patterns characteristic of river mouths influenced by strong wave activity are summarized on Figure 9b. A crescentic bar forms at a short distance from the mouth and pronounced subaqueous levees develop which have the form of broad shoals. Shoaling waves produce swash bars on the levee-shoals.

3.5 Summary

The primary intention behind Chapter 3 is to establish a framework for subsequent chapters in this section by discussing the morphodynamic models proposed by Wright (1977) and Bates (1953). The models are based on the dominance of three primary forces: (i) inertia, (ii) friction, (iii) buoyancy, and two secondary forces: (iv) tides and (v) waves. Again, it must be stressed that the models are idealized and the actual morphodynamics at most river mouths probably reflect a combination of these forces.

Data collection and the field program related to river mouth processes and responses were designed in the context of the models just discussed. Chapters 4 and 5 present the results of the data collection in Bella Coola and chapter 6 compares these results with the models.

CHAPTER 4

TIDAL AND WAVE PROCESSES AND RESPONSES

4.1 Introduction

This chapter examines the effects of the two major modifying marine forces, tides and waves, on the Bella Coola Delta. As will be discussed below, in terms of Wright's (1977) tide and wave dominated models, the effects of these processes are relatively minor. However, tidal forces, as expressed in mixed semi-diurnal tidal cycles, have a major impact on river mouth processes by changing the location and nature of the zone of marine-riverine interaction. The result is two distinct outlets for each distributary, a low tide outlet and a high tide outlet.

4.2 The Tides as a Shifter of Outlet Position

During periods of low tide the outlets of the main distributaries are located near the break in slope between delta plain and delta front. During high tide conditions the outlets are shifted up channel to the east and are located on the surface of the delta plain. In addition, each of these end positions migrate about a mean location with the lunar tidal cycles. Locations of high and low tide outlets for the

North Channel are shown in Figure 10. The confining effect of levees on the upper portion of the channel causes the mean high water outlet to be situated near the lower high water position.

Each of the high and low tide outlets remain stationary for approximately one hour on either side of slack water. The rise or fall of the tide between periods of slack water causes the outlet position to migrate continuously up or down channel. The effluent sweeps over the delta plain as the outlet migrates between slack water positions. The morphologic effects produced by the sweeping of the effluent are not apparent in the field. The subsequent discussion in this section focuses on the morphodynamics related to the slack water high and low tide outlets.

4.3 Tidal Forces

As discussed in chapter 3, Wright et al. (1973) suggest that influence of tides on distributary channels can be assessed in two ways: (1) by comparing tidal prism and river discharge, and (2) through channel morphometry. The following is an attempt to apply the criteria for tidal influence proposed by Wright et al. (1973) to the Bella Coola Delta.

4.3.1 Tidal Prism vs. River Discharge

Wright et al. (1973) suggest that for tidal processes to dominate over riverine processes the tidal prism passing through the channel

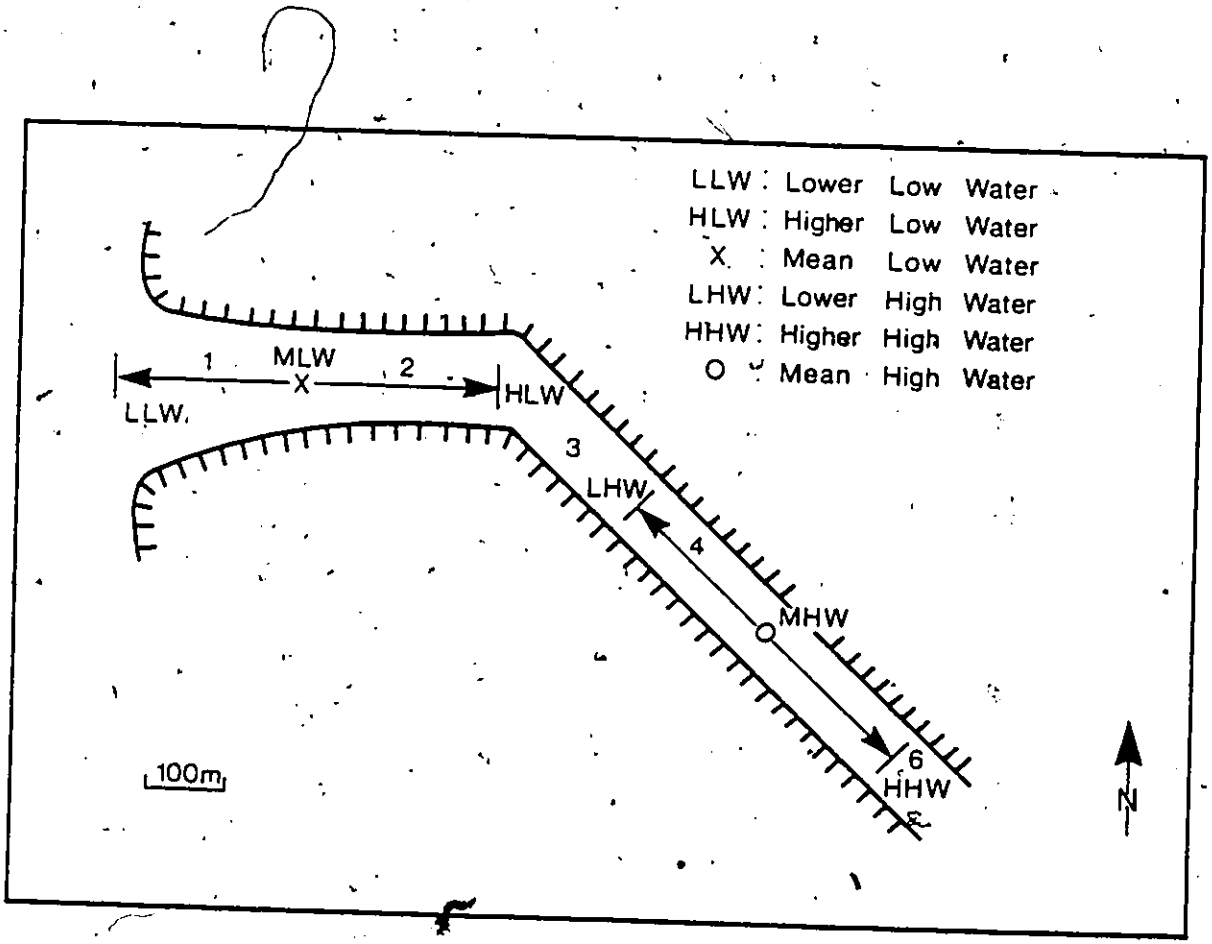

Figure 10. Locations of high and low tide outlets for the North Channel.

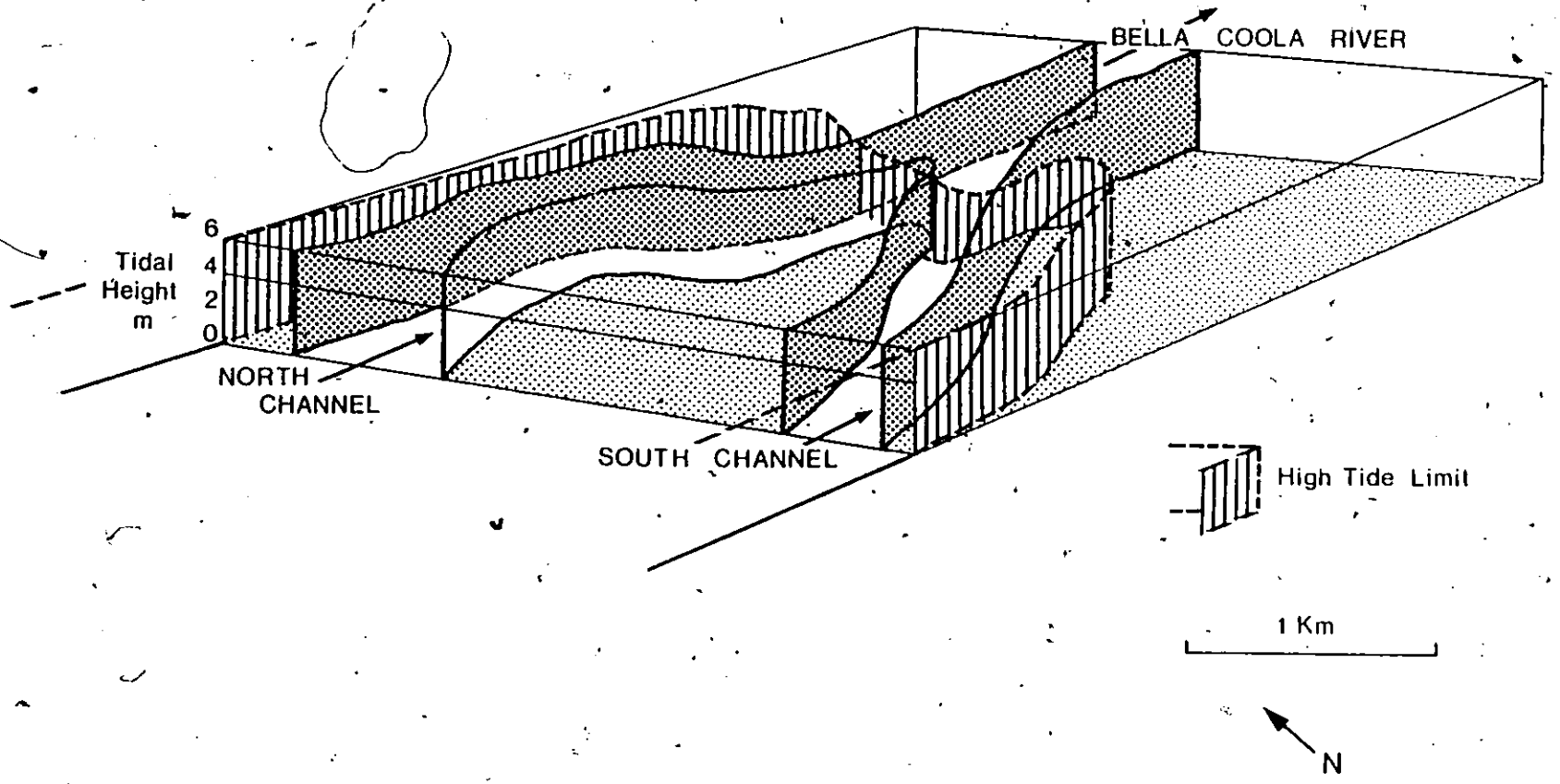

Figure 11. Tidal prisms over the delta plain.

must exceed river discharge. Such a comparison is straight-forward for distributary channels with well-defined banks that remain subaerial or slightly subaqueous during flood tides. However, the situation in Bella Coola is complicated by the existence of two distinct distributary outlets and the fact that the delta plain is flooded over its entire area during high tide and low tide channels disappear.

Lacking well defined subaerial banks to aid in estimation of tidal prism within the distributary channels, the tidal prism over the North and South Channel widths was determined for the mean tidal range (3.9 m) and the spring tidal range (5.9 m) (Figure 11). The prism, Pr, over each channel during a rise or fall of the tide, then is the volume of a wedge with a height h of 3.9 or 5.9 m at the low tide end, a width, w, equivalent to the distributary channel width and a length, ℓ, determined by the distance between the low tide limit (the break in slope between delta plain and delta front) and the high tide limit (here assumed to be the landward extent of the high salt marsh for spring tides and 3.9/5.9 times that distance for mean tides). Thus:

$$Pr = 2(1/2\ h\ \ell)w = (h\ell)w \qquad (26)$$

Values of Pr for mean and spring tides for the North and South channels are summarized on Table 1 as well as a value of Pr for the lower delta plain. This method of calculating Pr for the channels may be an underestimate of the actual value because flood tides will occupy the topographically lower channels preferentially as the tide rises and ebbing

NORTH CHANNEL				
Tide (m)	h (m)	l (m)	w (m)	Pr (m^3)x 10^5
3.9	3.9	1074	110	4.6
5.9	5.9	1625	110	10.5
SOUTH CHANNEL				
Tide (m)	h (m)	l (m)	w (m)	Pr (m^3)x 10^5
3.9	3.9	1033	120	4.8
5.9	5.9	1563	120	11.1
DELTA PLAIN				
Tide (m)	h (m)	l (m)	w (m)	Pr (m^3)x 10^5
3.9	3.9	925	2300	83.0
5.9	5.9	1400	2300	190.0

Table 1. Tidal Prisms for the North and South Channel and the Lower Delta Plain.

tides will drain from topographically higher off-channel areas into channels.

During the highest period of discharge in May and June (260 $m^3 s^{-1}$) the volume of river water discharged over a 12 hour tidal cycle is approximately 0.11×10^6 m^3, a value less than the total spring tide prism on the lower delta plain but larger than the mean tide prism. During the period of lowest discharge in winter (30 $m^3 s^{-1}$) the volume of river water discharged would be 1.3×10^6 m^3, a value considerably less than both spring and mean tide prisms.

The North Channel carries approximately 80% of the river discharge, and as such during the period of highest discharge would transport $8.9 \times 10^6 m^3$ of water in 12 hrs. This value is around 8 times larger than the spring tide prism over the North Channel, and 20 times larger than the mean tide prism. During the period of lowest discharge the North Channel transports 10×10^6 m^3 of water, a value similar to the spring tide prism and twice that of the mean tide prism.

The South Channel, carrying 20% of the river discharge, transports 2.3×10^6 m^3 of water in 12 hrs. during the period of highest discharge. This value is twice the spring tide prism and 5 times that of the mean tide prism. During the period of lowest river discharge the South Channel transports 0.26×10^6 m^3 of water. In this case the spring tide prism is 4 times that of the volume transported by the channel, and the mean tide prism around twice the channel value.

It is unlikely that the comparison of prism over the entire delta plain has any value in determining the relative importance of tidal and river processes for the two main distributary channels on the delta. The comparison of prism over each channel versus channel discharge, however, is probably valid. These results indicate that in the North Channel river discharge exceeds or equals both spring and mean tide prism during the entire year, suggesting a dominance of riverine forces. In the South Channel the river discharge exceeds tidal prism during periods of high river discharge, but tidal prism exceeds discharge during periods of low river discharge. This indicates tidal processes may be important in the South Channel during low river discharge.

4.3.2 Channel Morphometry

In order to determine whether channels on the delta had a "funnel shape", Equation (22) was used to determine values of δ_w for the North Channel, the South Channel, a 'purely' tidal channel originating in the high salt marsh and a tidal-distributary channel which, on aerial photographs, appears to have significant tidal and riverine discharges. Measurements were obtained from air photos (B.C. 80 146-005; B.C. 79 190-188) and the results are shown in Figure 12. All of the relationships, except the South Channel ($r = 0.53$) are statistically significant ($r > 0.90$). The values of δ_w, the slope of the regression lines on Figure 12, show considerable range, from 0.249 for the South Channel to 2.832 for the tidal channel.

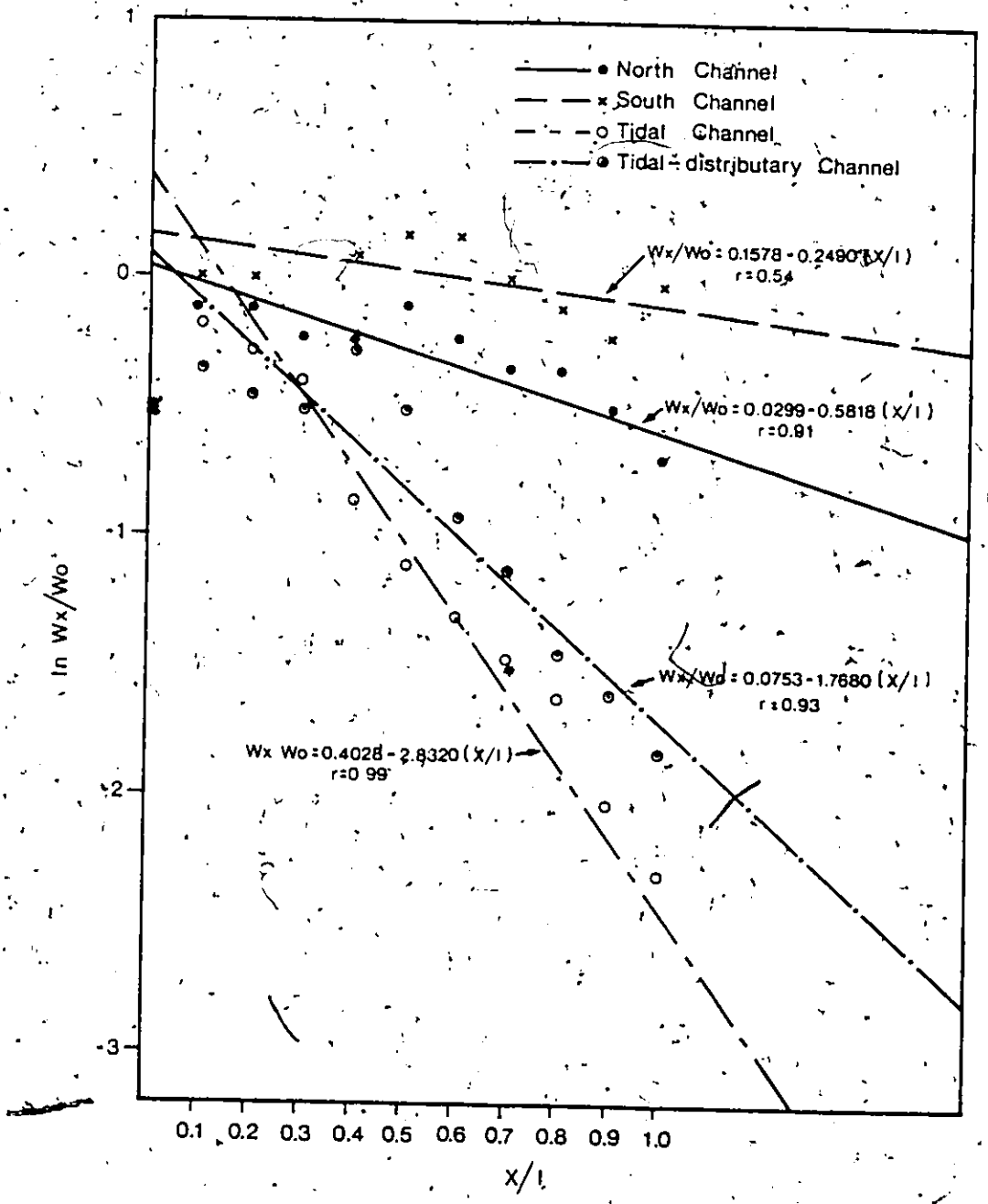

Figure 12. Delta plain channel morphometry. The term w_x is the channel width at x, w_o is the width at the outlet and l is the upstream distance affected by the tide.

Table 2 shows values of δ_w from this study and five channels examined by Wright et al. (1973). The only value of δ_w from Bella Coola comparable to the exponentially convergent channels examined by Wright et al. (1973) is that of the tidal channel ($\delta_w = -2.83$), similar to values from the Hooghly and Cua Soirap rivers.

The morphometric results suggest that the North Channel, the tidal channel and the tidal-distributary channel converge exponentially, while on the South Channel this tendency is not as clearly developed. The low value of δ_w and r for the South Channel may be related to the deposition of a large gravel bar on the north side of the mid-reaches of the channel, which results in a localized widening.

The values of δ_w for these channels suggests that the tidal influence is greater in the tidal channel (as would be expected), decreasing in the tidal-distributary and North Channel and South Channels respectively as river processes become more dominant. It must be pointed out that some horizontal expansion in the lower reaches of these channels may be related to a lack of bank vegetation as the channel passes over the sand flats, causing the channel to widen and shallow.

4.4 Wave Forces

4.4.1 Wave Characteristics

No wind record is available for the Bella Coola area, so

CHANNEL	Bella Coola Delta				Wright et al. (1973)				
	North Channel	South Channel	Tidal channel	Tidal distributary	Ord	Khor Abdullah	Irrawaddy	Hooghly	Cua Soirap
MEAN TIDAL RANGE (m)	3.9	3.9	3.9	3.9	5.1	2.6	2.0	4.2	2.6
ε_w	-0.58	-0.25	-2.83	-1.77	-4.28	-4.40	-3.54	-2.83	-2.80

Table 2. Channel Convergence Coefficients for the Bella Coola and Other Deltas.

WAVE CONDITIONS	T = 1 s H = 0.5 m H'= 0.5 m	T = 2 s H = 0.9 m H'= 0.5 m	T = 4 s H = 1.5 m H'= 1.35 m
WAVE POWER (W)	0.10	0.64	.90
RIVER DISCHARGE (m^3s^{-1})	1.02	1.02	1.02
DISCHARGE EFFECTIVENESS (m^3s^{-1}/W)	10.2	1.59	0.54

DEPTH, d = 2 m

WAVE CONDITIONS	T = 1 s H = 0.5 m H'= 0.5 m	T = 2 s H = 0.9 m H'= 0.81 m	T = 4 2 H = 1.5 m H'= 1.5 m
WAVE POWER (W)	0.10	0.42	1.67
RIVER DISCHARGE (m^3s^{-1})	1.02	1.02	1.02
DISCHARGE EFFECTIVENESS (m^3s^{-1}/W)	10.2	2.43	0.62

DEPTH, d = 1 m

Wave Processes at the High Tide Outlet

WAVE CONDITIONS	T = 1 s H = 0.5 m	T = 2 s H = 0.9 m	T = 4 s H = 1.5 m
WAVE POWER (W)	0.10	0.64	3.52
RIVER DISCHARGE (m^3s^{-1})	1.02	1.02	1.02
DISCHARGE EFFECTIVENESS (m^3s^{-1}/W)	10.2	1.59	0.29

Wave Processes at the Low Tide Outlet

Table 3. Wave Processes at the High and Low Tide Outlets.

hindcasting techniques cannot be used to generate wave data. Observations have been made, however, on wind patterns and resultant wave generation in the delta area. During summer (July and August) westerly, up-inlet, winds generally set in around 10 a.m., blowing fresh until sunset when they usually fall calm. Waves observed near the break in slope between delta plain and delta front tend to be steep and short period (2-4 s) with maximum wave heights of 0.9 to 1.5 m. Mean periods and heights are on the order of 1.0 s and 0.5 m respectively. In the winter winds blow primarily from the east, and waves thus produced have little impact on the delta. At no time of the year do long period swells penetrate from the open ocean.

4.4.2 Wave Power

Using Equations (23) and (24) the total wave power per unit crest width, P, can be calculated for the high and low tide outlets during summer wave conditions. For the low tide outlet, the steep offshore slopes produced little wave attenuation and hence no change in wave power (Table 3).

At the high tide outlet, shoaling of waves over the delta plain during flood tides must be accounted for. Table 3 summarizes values of P' for deep water wave heights (H) of 0.5, 0.9 and 1.5 m, and periods of 1, 2 and 4 s respectively for the high tide outlet. The values of attenuated wave height (H') and wavelength (L') were determined for water depths of 2 m and 1 m from Russell and Macmillans (1952) relation-

ships. As can be seen on Table 3, for d = 2 m, H' and hence P' were reduced somewhat from H and P only for the most intense wave conditions (T = 4 s, H = 1.5 m), and were essentially unchanged for more moderate conditions. (T = 2 s, H = 0.9 m; T = 1 s, H = 0.5 m). For a depth (d) of 1 m, P was reduced for H = 0.9 m and T = 2 s and H = 1.5 m and T = 4 s conditions and unchanged for H = 0.5 m and T = 1.0 s. In general, then, wave attenuation has had considerable effect on wave power reaching the high tide outlet.

4.4.3 Discharge Effectiveness

The average river discharge per unit channel width during the summer can be obtained by dividing the mean discharge at this time (~ 250 $m^3 s^{-1}$) by the total width of the two main distributary channels, a value of 1.02 $m^3 s^{-1}$ (Table 3). These results show that during the summer when both discharge and wave power are at high values, river processes dominate except during maximum wave conditions. It is unlikely that maximum or even mean wave conditions persists on a daily basis, in fact many calm days occur. As a result, the values of P and P' are probably considerably overestimated. During the remaining 10 months of the year when easterly winds either alternate with or predominate over the westerlies, the discharge effectiveness is undoubtedly much higher.

4.4.4 Morphology

There is no morphologic evidence on the Bella Coola Delta for any of the depositional patterns related to wave-dominated river mouths (Figure 9), nor other wave-generated features such as beach ridges, barriers or spits that are found on wave-influenced deltas. Waves, however, achieve some reworking of sediment on the sand flats of the delta plain during periods of high tide when the flats are flooded. Symmetric to slightly asymmetric, rounded, straight crested wave-generated ripples cover most of the sand flat zone (Figure 13). On the northern edge of the sand flats a series of subtle, shore-parallel intertidal wave-formed bars has developed (Figure 14). There are 6 bars, with bars farthest offshore having the greatest spacing (wavelength) at 90 m and greatest amplitudes at 30 cm. Both bar spacing (Figure 15) and amplitude decrease in an onshore direction. The dominant bedforms on the bars are wave-formed ripples, and small-scale stratification associated with the ripples is the primary sedimentary structure within the bars. In the troughs between bars the dominant bedforms are small current ripples produced by ebb-drainage and (discussed below) high tide effluent currents running roughly parallel to the troughs. This bar and trough system best corresponds to the 'ridge and runnel' type of intertidal wave-formed bars described originally by King and Williams (1949) and more recently by Hale and McCann (1982).

Figure 13. Wave-formed ripples on the sand flats.

Figure 14. Ridge and runnel wave-formed bars on the sand flats.

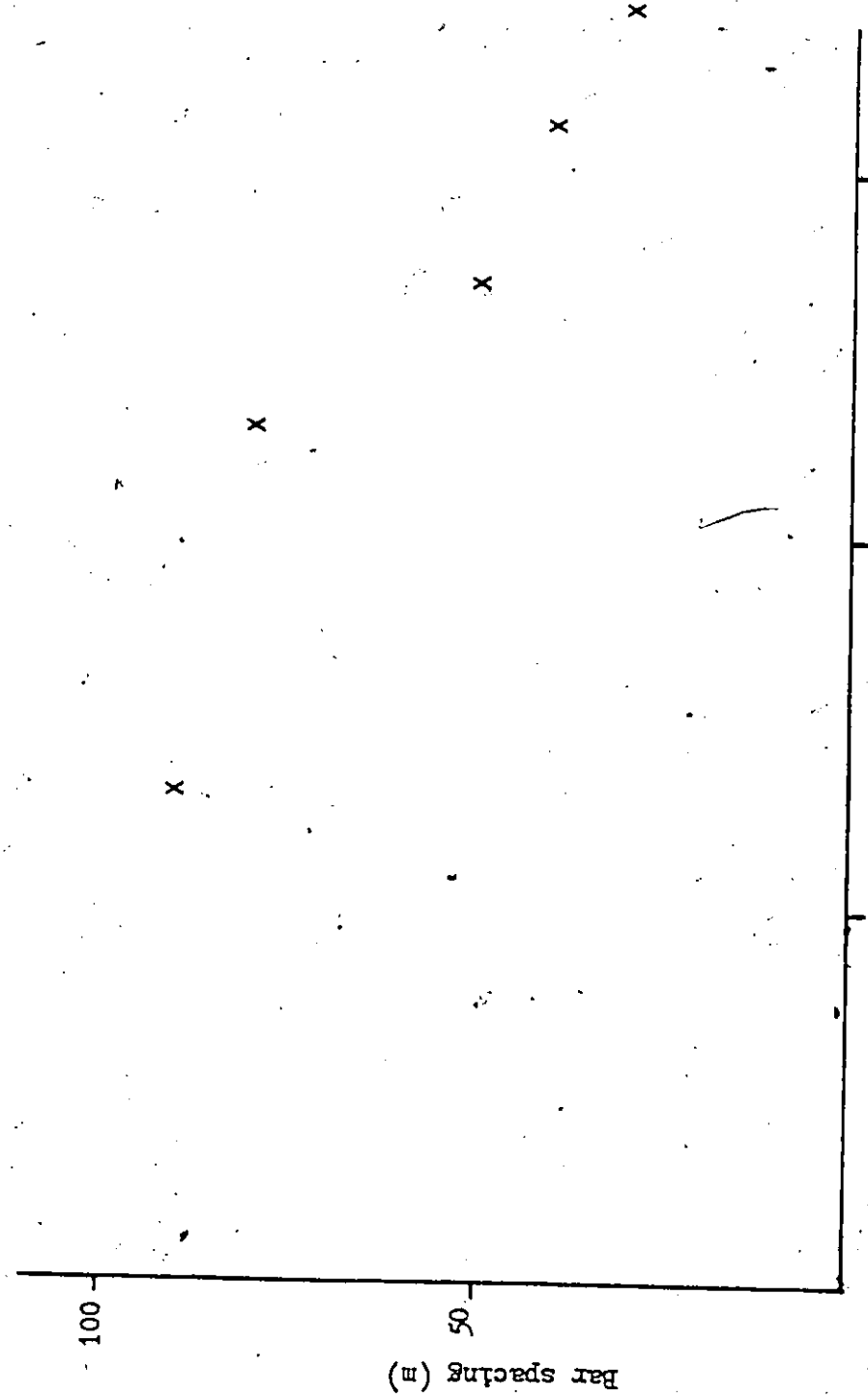

Figure 15. Ridge and runnel bar spacing versus distance onshore.

4.5 Summary

The main influence of the tide on the Bella Coola Delta is to change the location and nature of the zone of marine-riverine interaction, producing a low tide and high tide outlet for each distributary. As discussed in the following chapter, this shift in outlets produces two distinct river mouth dynamic and morphologic responses. The comparison of tidal prism and river discharge for the North and South Channels suggests that tidal processes are likely to dominate over river processes only during periods of low river discharge, and that overall, river processes dominate over tidal. The morphometric analysis supports this conclusion, indicating a small tidal component in channel shape. Morphometry indicates a strong tidal influence in purely tidal channels, a weaker influence in tidal-distributary channels.

Onshore (westerly) summer winds generate short, steep waves that impinge on the delta. The power generated by these waves is insufficient to overwhelm river discharge and as such river processes dominate over wave processes. Waves have achieved some reworking of sediment on the sand flats and have created a series of 'ridge and runnel' bars and extensive zones of wave-generated ripples.

CHAPTER 5

PROCESSES AND RESPONSES ASSOCIATED WITH THE NORTH CHANNEL EFFLUENT

5.1 Introduction

This chapter discusses the morphodynamics associated with primary effluent forces at the high and low tide outlets of the North Channel. The dynamics are examined first, followed by a discussion of suspended sediment concentrations within the effluents and in North Bentinck Arm. Next the morphology of channel mouths and distributary mouth bars is described. Finally, the relationships between effluent dynamics and associated morphologies, sediment transport and bedforms are discussed.

5.2 Effluent Dynamics

The effluent dynamics of the high and low tide outlets were examined during periods of high summer discharge in 1981 and 1982. Discharges in the North Channel were considerably higher in 1981 (200-210 $m^3 s^{-1}$) than in 1982 (70-108 $m^3 s^{-1}$), although the fresh water surface layer in North Bentinck Arm was twice as thick in the latter year (6 m vs 3 m). Measurements at the high tide outlet were taken during 2 hr. periods at high slack water and at the low tide outlet

during 2 hr. periods at low slack water. Velocities were determined with a Marsh-McBirney Model 201 current meter, water temperature and salinity with a YSI Model 33 salinometer, and positions assessed from horizontal sextant angles.

5.2.1 High Tide Outlet

The effluent plume during the high discharges of 1981 (210 $m^3 s^{-1}$) is shown on Figure 16, which represents the portion of the plume from the outlet at point A to 150 m downplume at A'. A more detailed analysis of the effluent, based on data obtained in 1982 during somewhat lower discharges (70-80 $m^3 s^{-1}$) is presented on Figure 17. As discussed earlier, the position of the outlet will vary slightly throughout the lunar tidal cycle.

Five dynamic zones can be identified in the high tide effluent (Figures 17a and 17b). In zones 0-3 the effluent is in contact with the bed and forces of friction are important. Zone 0 is located within the distributary channel landward of the outlet and is dominated by channel processes. Values of R_o at the outlet are very large ($2.9 - 3.3 \times 10^6$), indicating that the effluent is fully turbulent. Large values of τ_o (3.3 N m^{-2} on July 15, 1982) at the outlet also occur. Velocities are higher in the central portion of the outlet, decreasing towards the banks.

Zone 1 extends from the outlet to 3-3.5 channel widths (b_o)

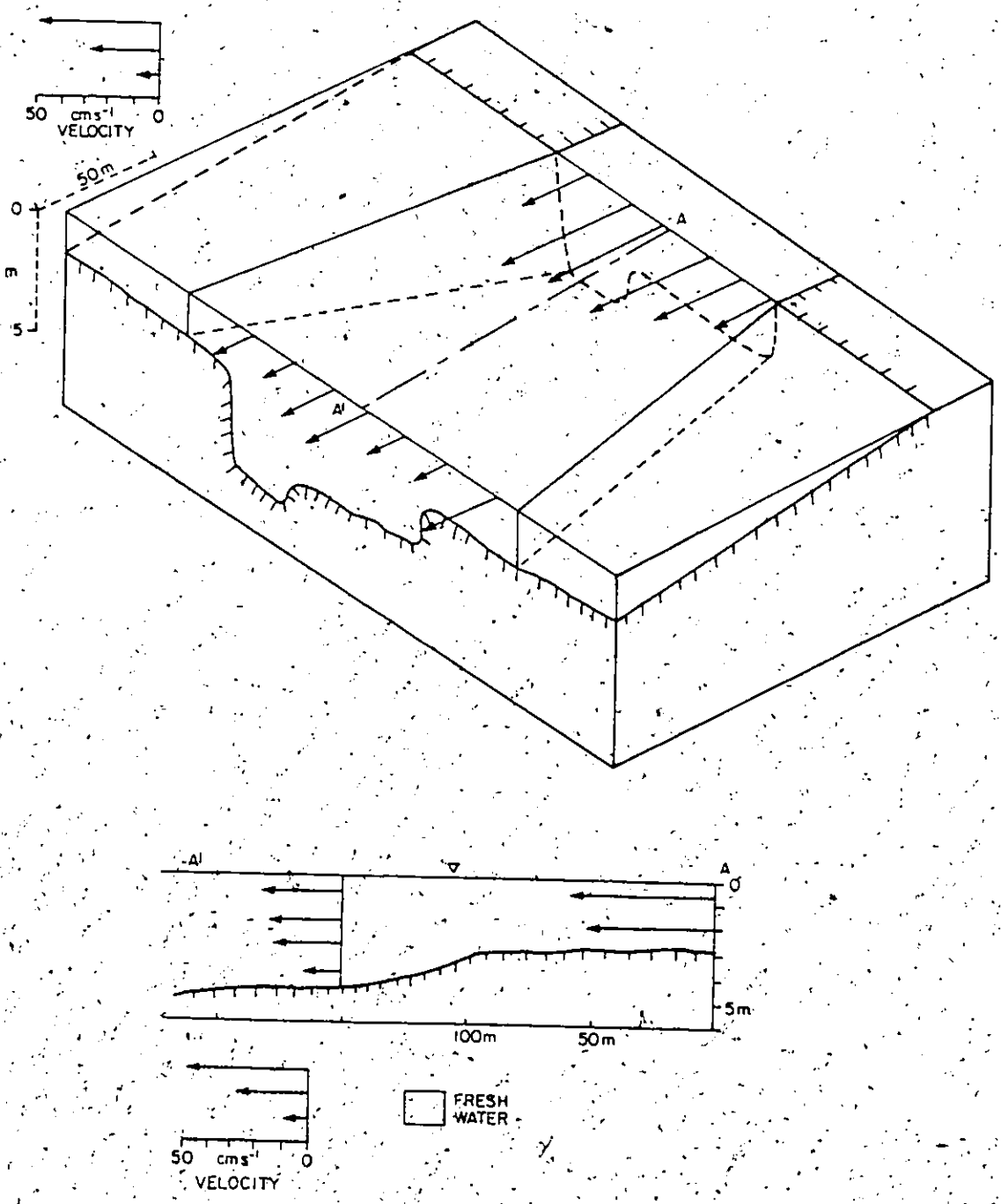

Figure 16. Effluent plume at the high tide outlet in 1981.

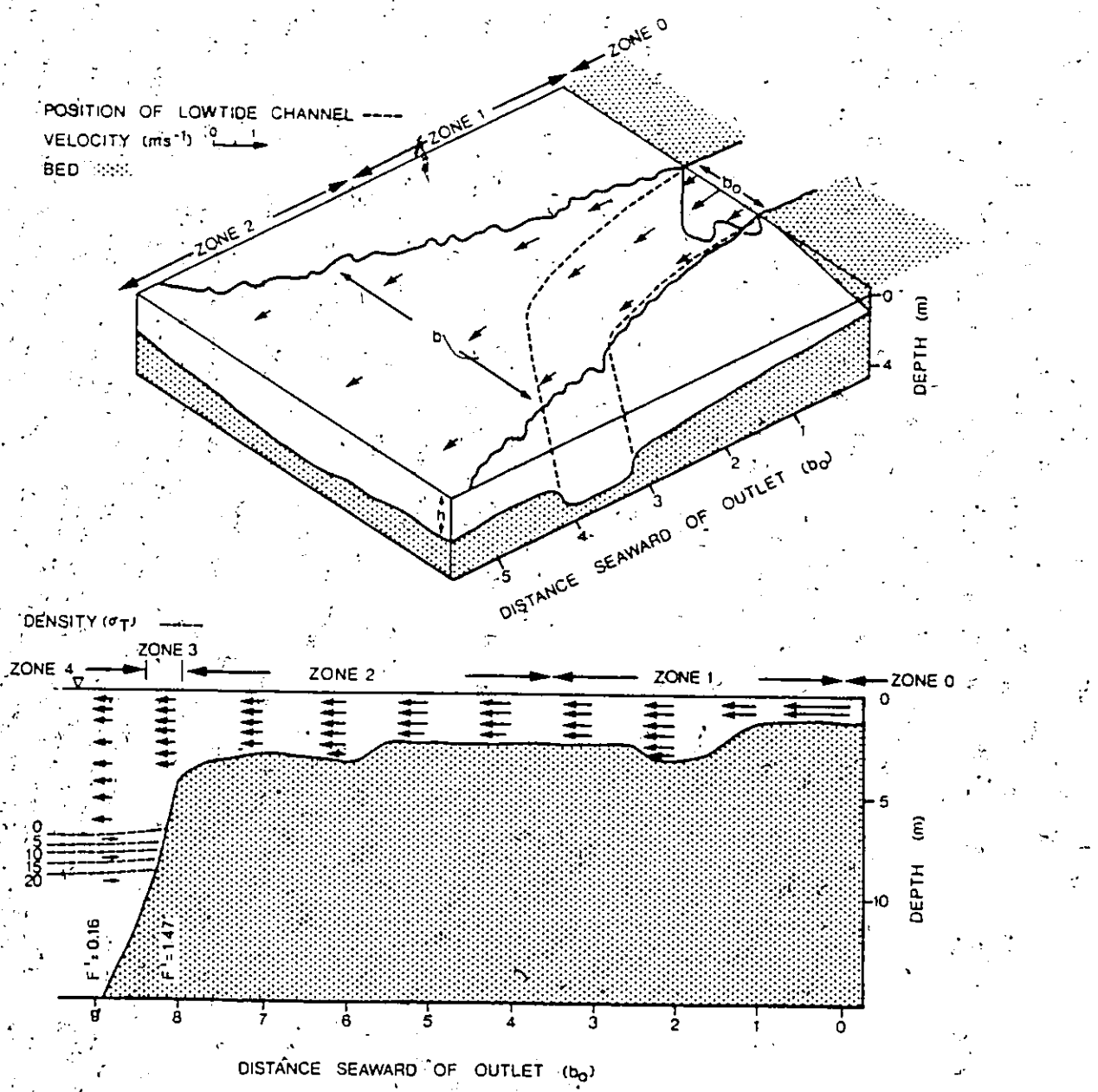

Figure 17. Effluent plume at the high tide outlet in 1982.

downstream. The primary control in this zone is the presence of the low tide distributary channel (Figure 17a). The distributary tends to channelize the effluent, restricting horizontal expansion and reducing the spreading angles to 5° - 8°. Mean velocities decrease towards the boundaries between effluent and ambient waters (Figures 16, 17a) and also downstream, especially where depths (h) increase between 2 and 3.5 b_o (Figure 17b). The boundary between effluent and ambient fresh water is marked by numerous eddies up to 5 m. in diamter.

Zone 2 extends from 3.5 b_o to the break in slope between the delta plain and the delta front at 9.0 b_o from the outlet. The effluent is no longer confined by the low tide channel in this zone and as a result expands more rapidly laterally at a higher spreading angle of 16-17°. There is a marked seaward and lateral decrease in velocity (Figure 17b) and, as in Zone 1, the effluent boundary is marked by eddies.

Zone 3 is very short and is the area between 8 b_o and 8.2 b_o (Figure 17b). As the effluent passes beyond the break in slope it debouches into the fresh water surface layer overlying saline basin water. Density differences are very small between ambient and effluent waters and the outflow is essentially homopycnal in this zone. Values of F' exceed 1, turbulent diffusion becomes important and a reverse circulation develops. At the seaward edge of Zone 3 buoyancy increases in importance and F' decreases through the critical value of unity.

In Zone 4, beyond 8.2 b_o, the effluent flows over saline basin

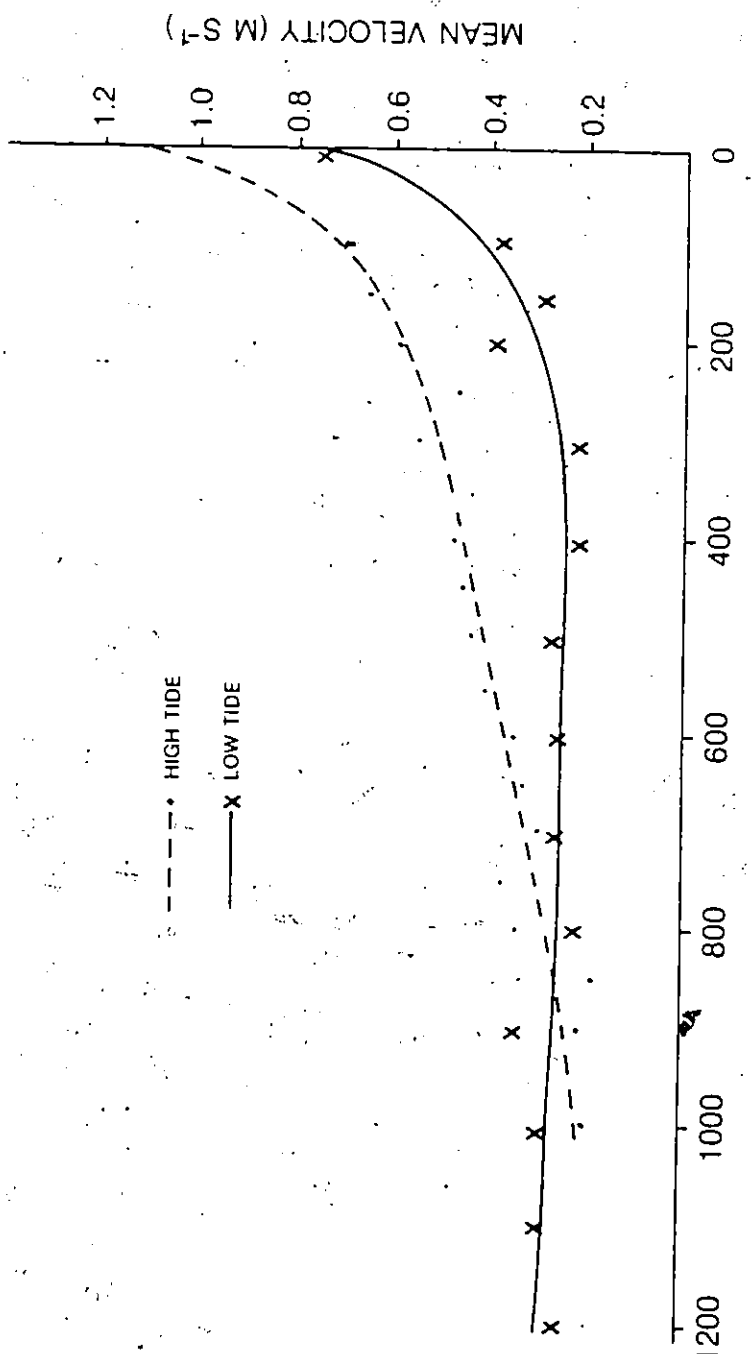

Figure 18. Decrease in mean centreline effluent velocities with distance from high and low tide outlets in 1982.

water, buoyancy becomes dominant and there is little mixing across the interface ($F' << 1$). Effluent expansion beyond the delta plain is discussed in some detail in the following section on low tide dynamics.

Centreline velocities in the effluent decrease rapidly seaward of the outlet (Figure 18). This rapid deceleration reflects the influence of bed friction.

5.2.2 Low Tide Outlet

The position of the low tide outlet varies with the height of low tide. The outlet is situated at the break in slope between delta plain and delta front during lower low water, and up to 2 b_o to the west on the delta plain during higher low water.

The effluent jet for 1981 is summarized on Figure 19 ($Q = 200$ $m^3 s^{-1}$) and for 1982 on Figure 20 ($Q = 108$ $m^3 s^{-1}$). The outlet positions on these diagrams are representative of moderately low tides (0.5 m), during higher low tides (2-2.5 m) the outlet position is shifted landward (E.) on the delta plain. During extremely low tides (-0.5 m) portions of the distributary mouth bar crest are exposed subaerially, subdividing the channel at the mouth and producing a number of smaller sub-plumes for the effluent. The long sections on Figures 20b and 20c were measured during extremely low tides with a reduced outlet width of 50 m on the north side of the outlet.

Six dynamic zones may be identified for the low tide effluent

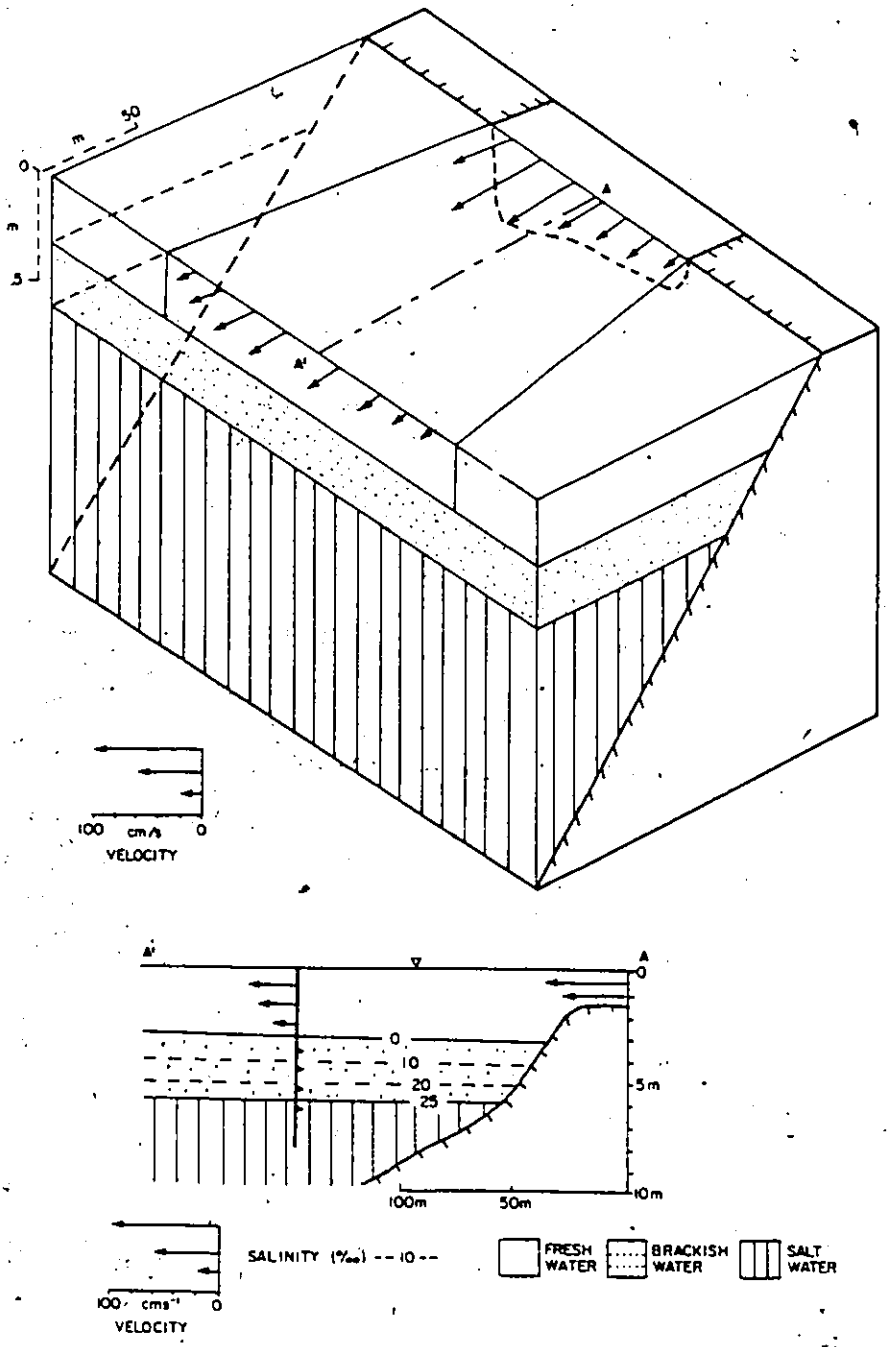

Figure 19. Effluent plume at the low tide outlet in 1981.

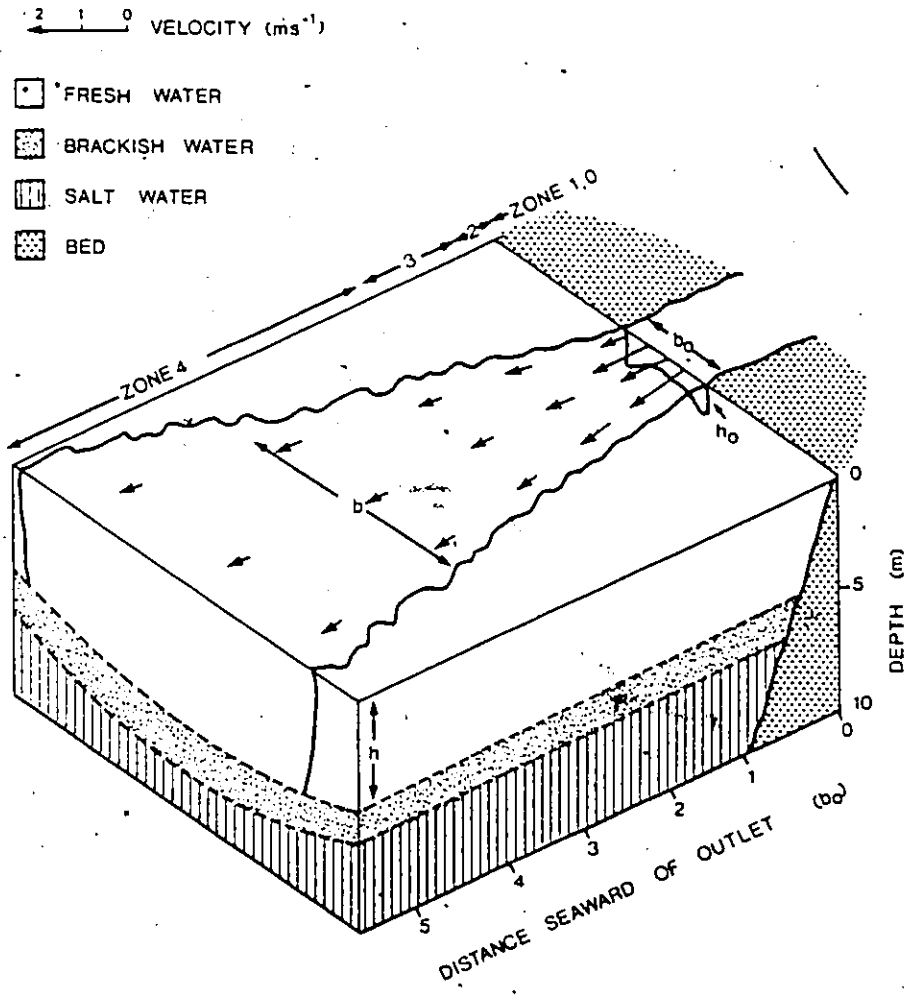

a

Figure 20. Effluent plume at the low tide outlet in 1982.

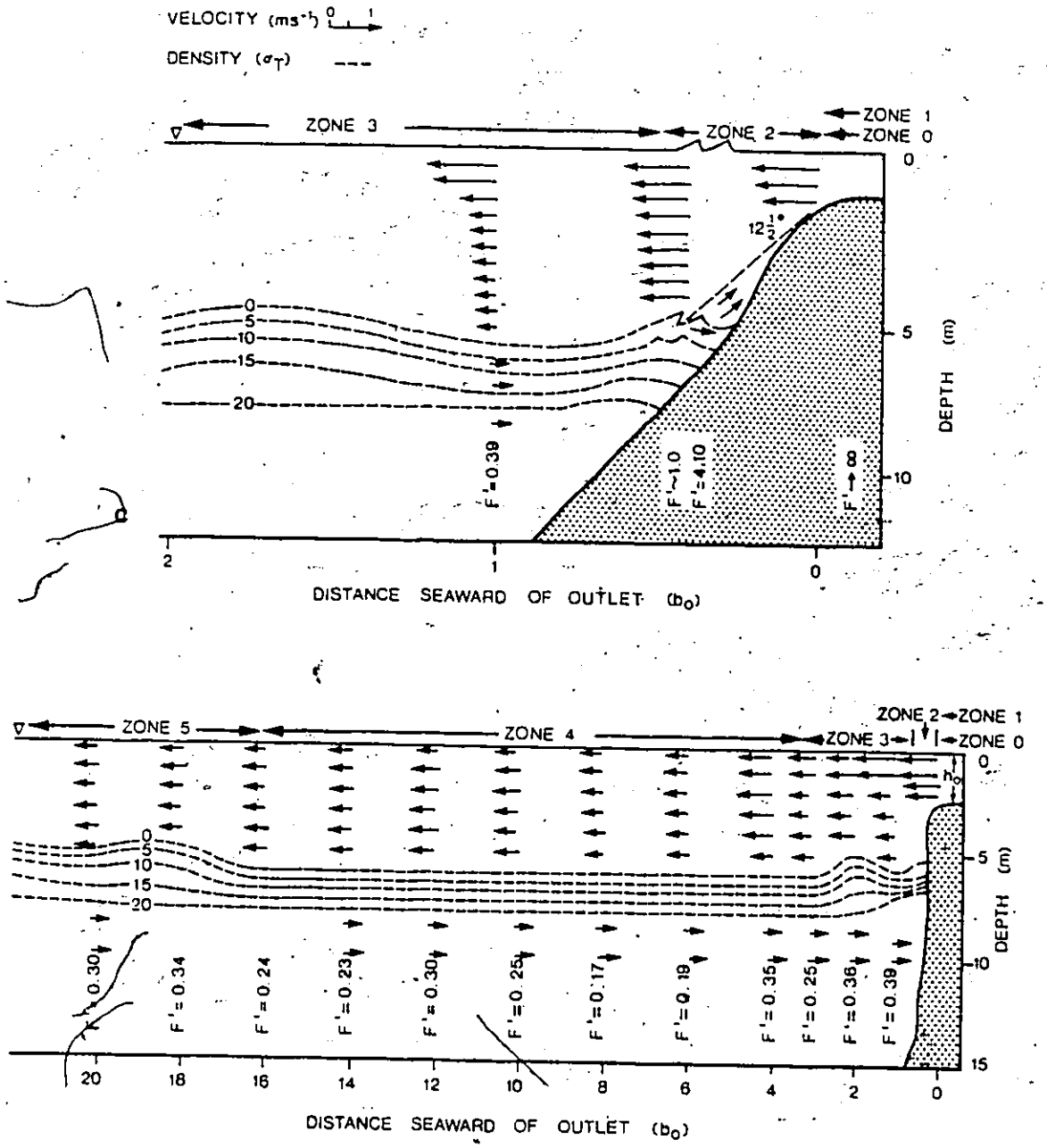

Figure 20 (continued)

(Figure 20, a,b,c). Zone 0 extends landward from the outlet and is dominated by fluvial processes. Zone 1 exists during conditions of higher low water and occupies the area between the outlet and the break in slope between delta plain and delta front. The effluent tends to be channelized by the low tide distributary channel in Zone 1 and lateral effluent expansion is restricted to an angle of approximately 5° (Figure 21). In Zone 1 the effluent is in contact with the bed and friction is important.

Zone 2 is short, extending from the outlet to 0.2-0.5 b_o seaward as the effluent passes beyond the break in slope between delta plain and delta front and into the fresh water surface layer (Figure 20c). There is very little density difference between effluent and ambient waters vertically and laterally (homopycnal), and values of F' exceed 1 (4.01). There is strong vertical mixing, characterized by rapid fluctuations in isopycnal positions, and a dominance of inertial forces and turbulent diffusion. A very strong return flow occurs below the outflow within the fresh water and upper brackish layers and a small scale circulation system develops. The air-water interface in this zone is broken by standing waves. An internal hydraulic jump occurs at the seaward edge of Zone 2 as values of F' pass from supercritical ($F' > 1$) to subcritical ($F' < 1$). A considerable amount of flow deceleration is associated with this zone. Mean velocities are highest on either side of the centre of the outlet, decreasing towards the centre and towards channel banks. Lateral effluent boundaries contain numerous small-scale eddies (1 m diameter) as velocities near the boundaries are large enough to cause shear and considerable lateral entrainment. For Zone 2 seaward

Figure 21. Aerial photograph of the low tide effluent in 1979 (BC79-190 No. 188).

lateral expansion occurs at an angle of 11-13°.

Zone 3 occupies the area between 0.2-0.5 b_o and 3 b_o. The effluent is now debouching over saline basin water at the base (hypopycnal flow) and is in contact with ambient fresh water on the flanks. Values of F' are small (< 0.7) indicating a dominance of buoyant forces and a suppression of turbulence and vertical mixing. A weak return flow has developed below the jet. Both F' and velocity are largest on either side of the plume centre; decreasing towards the centre and edges. Only a small amount of deceleration occurs in this zone. There is a surfaceward movement of the pycnocline, a decrease in effluent thickness from 6 m to 5 m and a decrease in the vertical density gradient across the interface. In addition, there is some fluctuation in isopycnal positions. This upward bulge may be a result of turbulence generated in Zone 2 that is passed down jet to Zone 3. Small scale eddies (1-2 m) are generated at the boundary between fresh effluent and ambient waters, and the surface of the jet is relatively smooth.

Zone 4 is situated between 3 and 16b_o from the outlet. In this zone buoyancy dominates (F' < 0.65), there is apparent acceleration, little vertical mixing, a weak return flow, and the interface is essentially horizontal. Velocity and F' vary across the plume in a manner similar to Zone 2. The seaward portion of this zone may be marked by extremely large eddies (25-50 m) along the effluent flanks. Zone 5 extends seaward of 16 b_o from the outlet. In this zone there is a decrease in effluent thickness (to 4.7-5.0 m), some deceleration and a dominance of buoyant forces (F' < 0.35). As with the seaward portion of

Zone 4, very large eddies may occur along the plume edge (Figure 21).

The seaward decrease in mean centreline velocities is shown on Figure 18. The jet decelerates rapidly immediately seaward of the outlet in Zone 2 in response to an internal hydraulic jump (discussed below). Seaward of Zone 3 there is an apparent acceleration of the effluent; possible reasons for which are examined below.

5.3 Suspended Sediment

Suspended sediment samples were taken with a Van Dorn water bottle at various depths in the high tide and low tide effluent jets in 1982, and on the surface of North Bentinck Arm in 1981. The high tide outlet was sampled during 2 hours about high slack water on July 17, and the low tide outlet jet during 2 hours about low slack water on July 23. Both of these days fall within a period of cloudy, rainy weather with reduced glaciermelt but a slight increase in discharge due to the rain. Daily integrated samples from the upper 30 cm of the river near the south bank at a location 1 km upstream of the delta, were taken during early June and late June, and July (Figure 22). The highest concentrations in the river occur in early June (86 mg ℓ^{-1}) during high discharges produced by spring snowmelt runoff. Concentrations in late June and July were lower (10-50 mg ℓ^{-1}). Glaciermelt was reduced during the remainder of July as cloudly conditions prevailed, but suspended sediment concentrations remain relatively constant, increasing towards the end of July during a period of prolonged rainfall. Jet samples were taken during this latter period. Although river and effluent water is

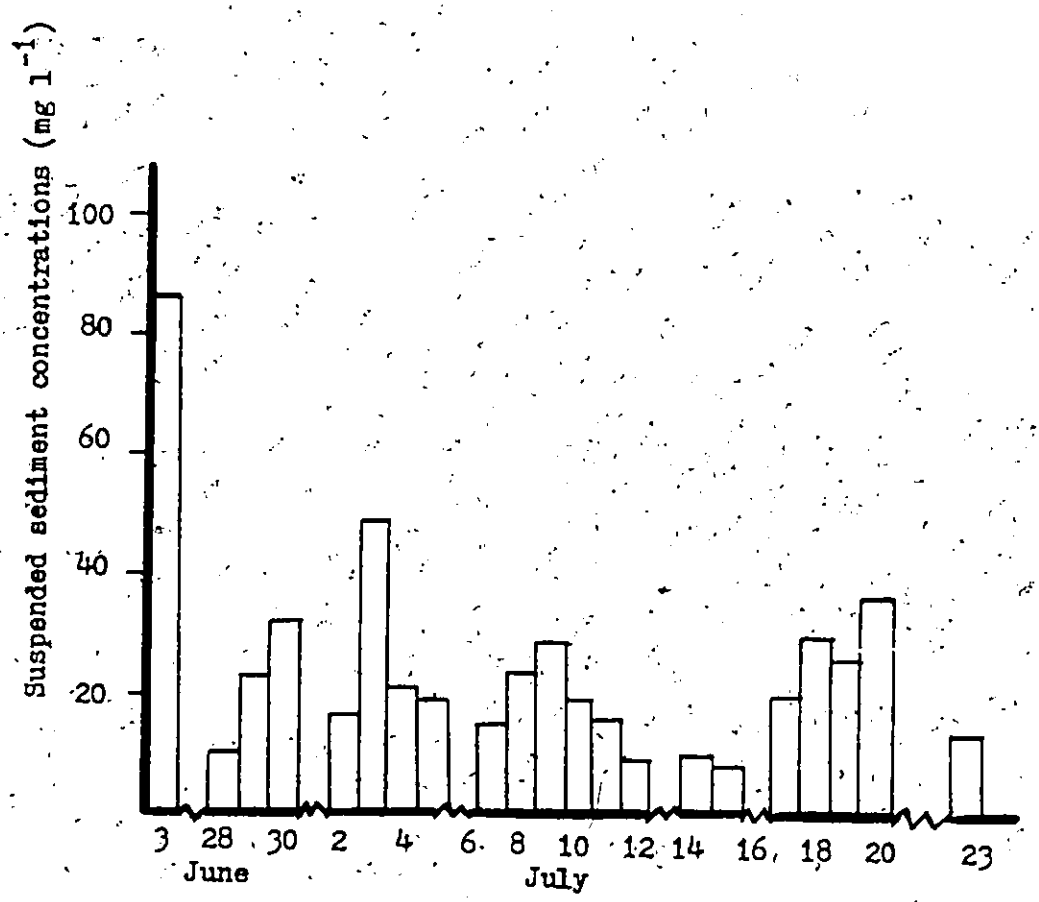

Figure 22. Suspended sediment concentrations in the Bella Coola River near the mouth in 1982.

very opaque, suspended sediment concentrations are relatively low.

5.3.1 High Tide Outlet

Vertical variations in suspended sediment concentrations along the centreline of the high tide outlet are displayed in Figure 23. In most cases concentrations are higher near the bed (15-20 mg ℓ^{-1}) decreasing toward the surface (10-20 mg ℓ^{-1}). At 2 b_o seaward of the outlet the reverse occurs, and at 7 b_o there is no vertical variation. Beyond the break in slope between delta plain and delta front, concentrations decrease slightly from the surface (16 mg ℓ^{-1}) to the pycnocline at 6 m (12 mg ℓ^{-1}), and then decrease rapidly at 8 m (2 mg ℓ^{-1}) remaining constant below this depth.

Mean concentrations are highest at the outlet centre (18 mg ℓ^{-1}), decreasing towards the sides of the outlet (9.7 and 14.4 mg ℓ^{-1}). In a downplume direction there is considerable variation in centreline concentrations (9-16 mg ℓ^{-1}) and a very slight decrease from the outlet to 9 b_o seaward. Concentrations both increase and decrease across the effluent from centreline to sides.

5.3.2 Low Tide Outlet

Centreline concentrations at the low tide outlet are greatest near the bed (22 mg ℓ^{-1}), decreasing toward the surface (16 mg ℓ^{-1}) (Figure 24). At 0.5 b_o seaward of the outlet concentrations are highest

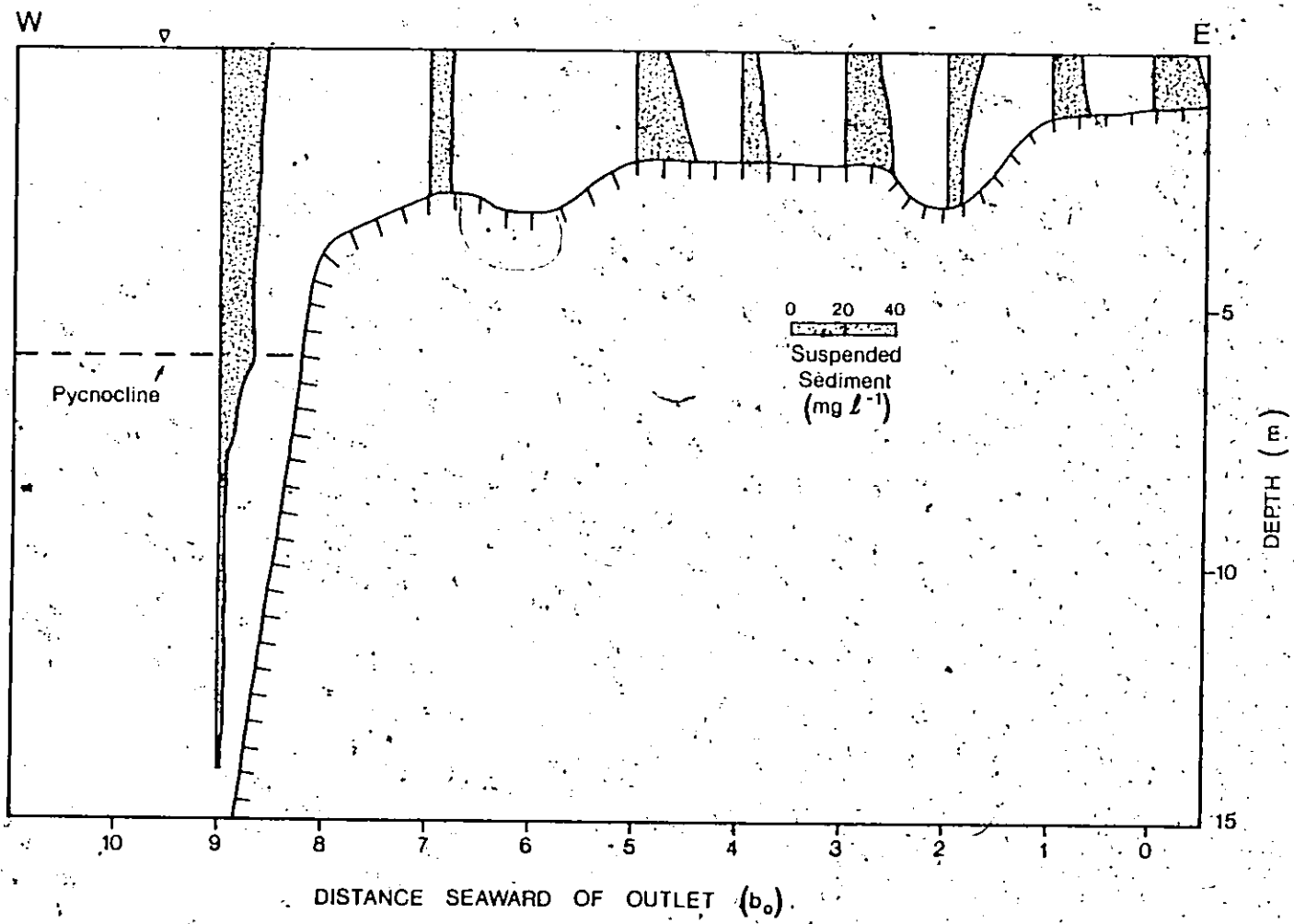

Figure 23. High tide outlet suspended sediment concentrations.

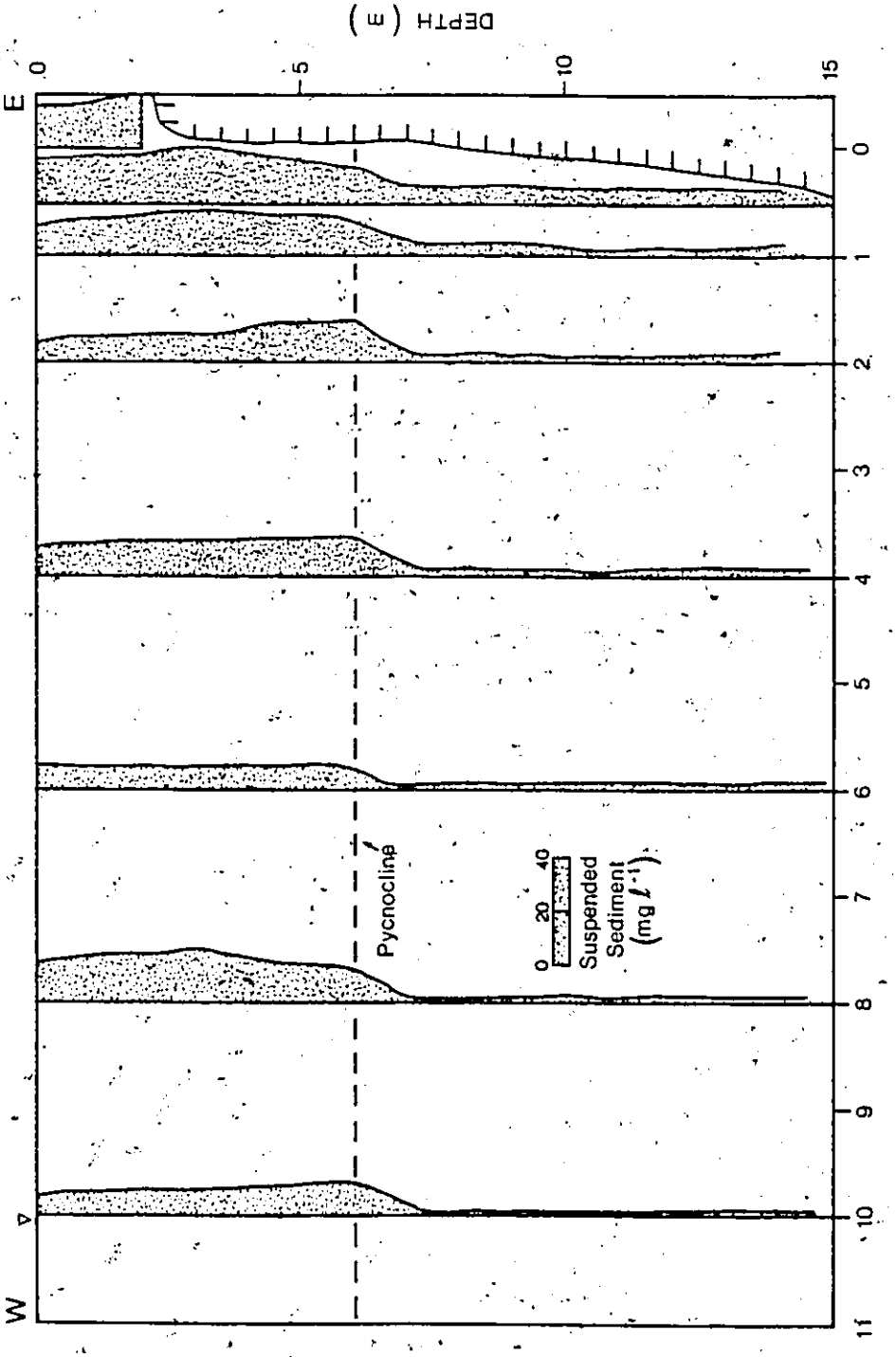

Figure 24. Low tide outlet suspended sediment concentrations.

at 3m depth (22 mg ℓ^{-1}), decreasing toward the surface (16 mg ℓ^{-1}) and to 14 m depth (4 mg ℓ^{-1}). There is a relatively abrupt break in concentrations below the pycnocline but concentrations are higher here than in similar depths farther from the outlet. Beyond 0.5 b_o concentrations are highest in the fresh water above the pycnocline (8-18 mg ℓ^{-1}), decreasing rapidly within 1 m below the pycnocline (2-3 mg ℓ^{-1}). Highest concentrations are usually found at or near the pycnocline (12-18 mg ℓ^{-1}), decreasing toward the surface (8-12 mg ℓ^{-1}). At 8 b_o the highest concentrations are found at 3 m depths, and at 6 b_o there is little vertical variation in the effluent concentrations.

Mean concentrations are highest in the centre and on the northern side of the outlet (20 mg ℓ^{-1}) and lower on the south side (15 mg ℓ^{-1}). Mean centreline concentrations in the effluent decrease from the outlet to 1 b_o seaward (15 mg ℓ^{-1}), remaining relatively constant seaward (9-15 mg ℓ^{-1}). In ambient fresh water north of the effluent mean concentrations are around 11 mg ℓ^{-1}, slightly lower than those within the outflowing effluent as some suspended sediment has settled out.

5.3.3 North Bentinck Arm

Surface suspended sediment concentrations in North Bentinck Arm were determined for the period July 10-15, 1981 (Figure 25). Highest values occur on the south side of the fjord with maximum values nearest the delta at 20 mg ℓ^{-1}. Lowest values occur near the delta on the north

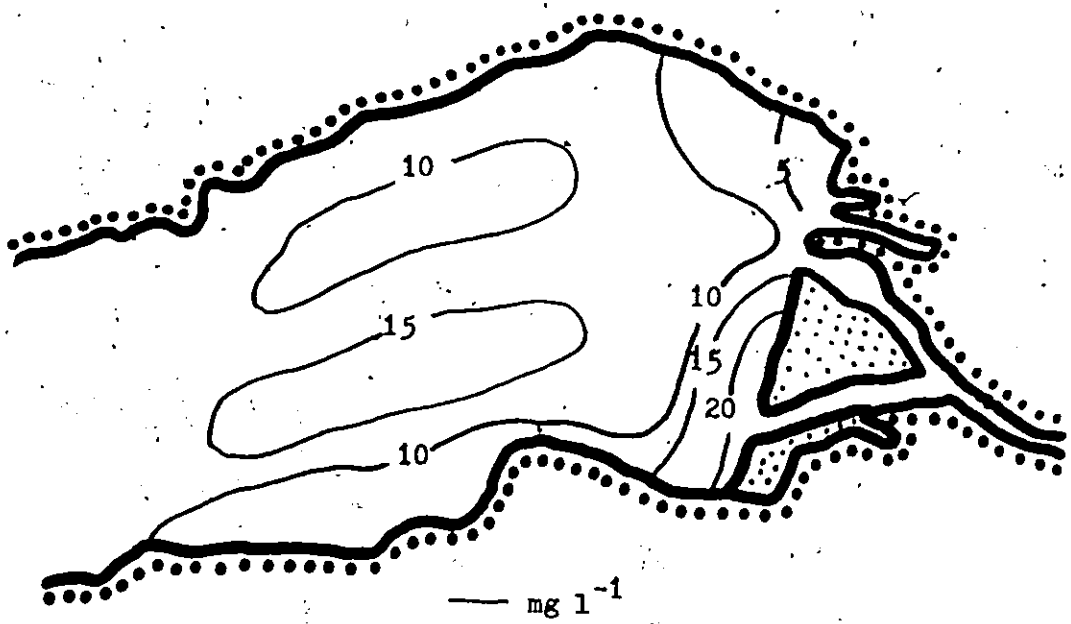

Figure 25. Suspended sediment concentrations in North Bentinck Arm.

side of the basin and are due to the input of water with little suspended sediment from the Necleetsconnay River. There is, then, a gradual decrease in surficial suspended sediment concentrations down inlet, but this decrease is quite small indicating little suspended sediment has settled out. In addition, there are two 'ridges' of higher concentrations aligned E. to W. on the fjord.

5.4 Morphology

The following is a discussion of distributary mouth channel and bar morphology associated with the high and low tide outlets. In the subsequent discussion bedforms have been classified primarily on the basis of crest to crest distance (wavelength). Ripples have characteristic lengths of 0.1 to 0.3 m, sand waves are 5 to greater than 100 m, dunes (megaripples) are 5-10 m and antidunes up to 5 m (Blatt et al., 1980). Grain size distinctions of sieve-analyzed samples are based on the Udden-Wentworth system and Folk and Wards (1957) grain size statistics.

5.4.1 High Tide Outlet

The morphology of the distributary mouth bar related to the high tide effluent is summarized on Figure 26. From the outlet to 3.5 b_o seaward the area is occupied by the low tide channel. The bed of the channel is predominantly gravel but no information is available on bedforms. There are weakly developed, sandy, subaerial levees and no subaqueous levees associated with channel and jet.

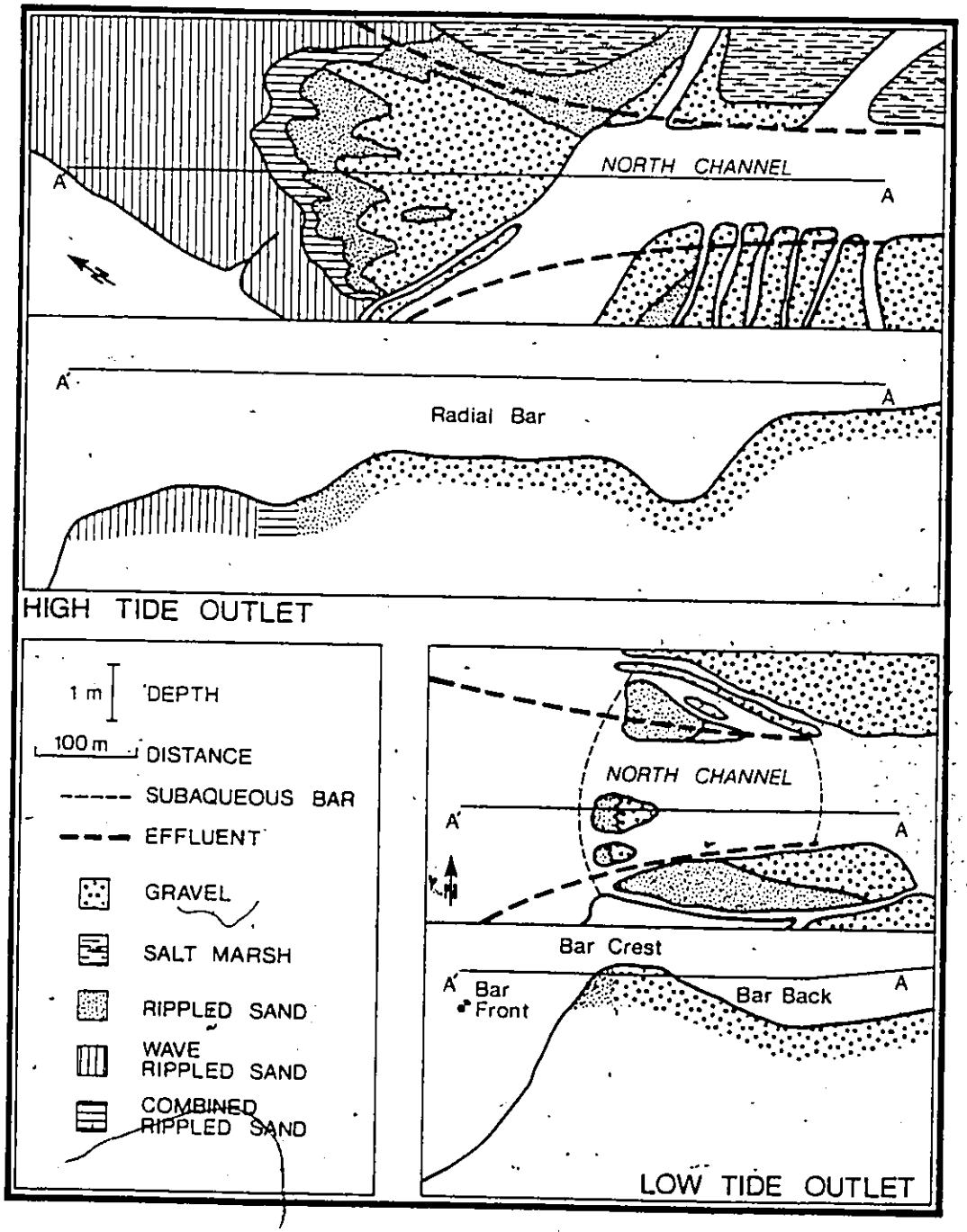

Figure 26. Distributary mouth morphology for high and low tide outlets.

Beyond 3.5 to 5.5 b_o seaward there is a large gravel sheet with a 'radial' digitate bar form. In proximal areas the bar is composed of coarse gravel to cobbles (3-6 cm) with a green algal covering on the particle surfaces. The presence of the algal mat suggests little recent movement of coarser sediment. Erosional (?) streaks 5 cm deep, 20-30 cm wide and 10 to 15 m long were noted on this portion of the bar (Figure 27). The sediment on the bar is finer (2-3 cm) and less algal covered downplume (indicating recent transport?), and in distal zones becomes a series of narrow, flow-parallel, lobes advancing over current-rippled sand (Figure 28). These distal lobes are similar in appearance to transverse bars in gravel rivers (eg. Smith, 1974). Internally the lobes range from a sand-matrix-filled gravel with no cross bedding and weakly developed normal grading, to a thin (1 to 2 particle thick) gravel veneer overlying tabular cross-bedded coarse sand with beds inclined at 5°.

As the gravel grades into sand in the extreme distal portions of the bar, a series of well developed 'transverse ribs' (McDonald and Banarjee, 1971) occur, similar to those in gravel streams (Figure 29). The ribs are located on topographic highs and oriented, as the name implies, roughly perpendicular to slightly oblique to the flow. Crest to crest distances are typically 60 to 75 cm, amplitudes range from 15 to 20 cm above the troughs, and the ribs are usually 2 to 3 m in length along the crest. In most cases the ribs are parallel to one another, but may meet at oblique angles and merge together (bifurcate?). The ribs are symmetrical in form, separated by flat bottomed troughs.

Figure 27. Erosional (?) streak on the proximal radial bar at the high tide outlet.

Figure 28. Flow-parallel lobe advancing over current-rippled sand at the high tide outlet.

Figure 29. Transverse ribs on the surface of a flow parallel lobe at high tide outlet.

Surficially the ribs are composed of clean coarse gravel to small pebble sized material, with the coarser particles located near the rib centre. Internally they consist of structureless, matrix-filled coarse sand to pebbles. Intervening rib troughs are wave rippled coarse sand at the surface and structureless coarse sand within. This coarse sand layer is usually continuous beneath the ribs and is exposed in the troughs.

Seaward and to the north of the gravel bar is a zone of current rippled sand with isolated sand waves. The sand is medium grained (0.4-0.7 mm) with a very slight decrease in grain size seaward. The majority of the ripples are straight to slightly sinuous-crested, 5 to 10 cm in amplitude and 20 to 35 cm in wavelength (Figure 30) and are oriented transverse to oblique to effluent flow. Some of the larger ripples might be classified as small dunes. Smaller ripples with wavelengths of 10 to 15 cm and amplitudes of 3 to 5 cm are usually linguoid or lunate in form. Troughs between the larger ripples may show evidence of crest-parallel tidal drainage such as lineations or small linguoid ripples. Internally the straight crested ripples are tabular cross bedded, the more irregular shaped ripples produce small-scale trough cross lamination.

Two small sand waves occur 3.5 b_o from the outlet, east of the proximal gravel bar (Figure 31). The sand waves are oriented slightly oblique to the effluent flow (to NE), are spaced 15 m apart and are 20 to 30 cm in amplitude. The backs of the sand waves are covered by sinuous crested ripples 10 to 15 cm in wavelength that are oriented oblique to the sand wave crest (to NNE). In the troughs immediately

Figure 30. Straight to slightly sinuous-crested current ripples at the high tide outlet.

Figure 31. Sandwave at high tide outlet. Flow was from left to right.

beyond the crests large straight crested ripples to small dunes, oriented perpendicular to the sand wave crests and related to tidal drainage, predominate. The sand waves were active and best defined at the end of June 1982, but destroyed as effluent discharge decreased in July. Small scale cross stratification produced by ripples occurs on the wave backs. Low angle (10°) tabular crossbeds with tangential bases characterize the sand waves.

A number of small funnel-shaped tidal drainage channels head on the distal gravel bar and flow between the gravel lobes, over the rippled sand and eventually into North Bentinck Arm. Small lunate and linguoid ripples are usually found on the beds of these channels when exposed, but standing waves (and presumably antidunes) are common as the channels drain during low tide.

Seaward of the current ripplied sand is a discontinous zone of combined ripples that grades into both the current rippled sand and wave rippled sand (Figure 32). These ripples consist of long, straight crested, rounded, symmetrical to slightly asymmetrical wave-generated forms of 6-8 cm wavelengths combined with small, 3-5 cm wavelength lunate and linguoid ripples produced by the effluent current flowing roughly transversely to the direction of wave propagation. Statification associated with these forms tends to be a chaotic mixture of small-scale single-direction foreset laminae and rarer chevron structures related to wave ripples and small-scale cross lamination produced by the current ripples. This zone does not always exist; the wave ripples may be absent when waves are not generated during the previous high tide.

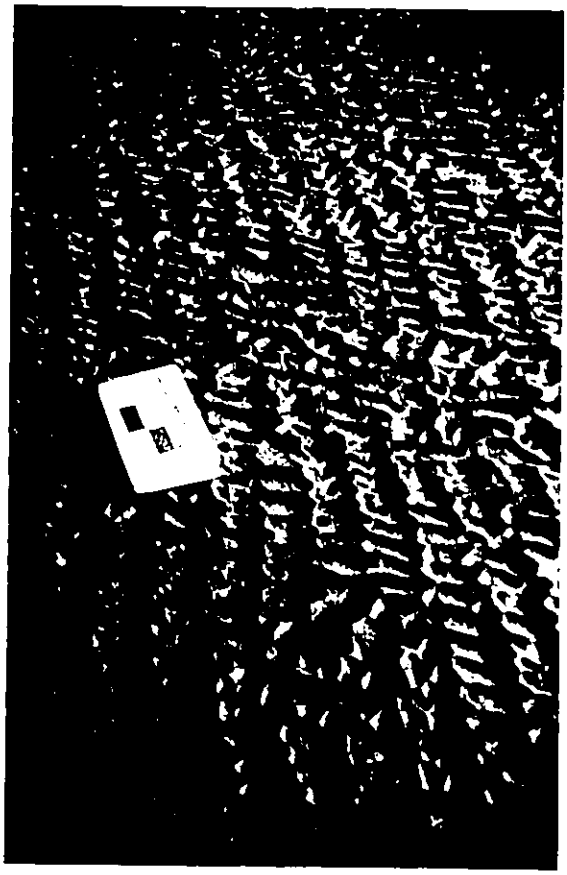

Figure 32. Combined current and wave ripples at high tide outlet.

The remaining intertidal area beneath the effluent reflects a domination by wave features, with secondary unidirectional current effects. The wave-formed bars and associated bedforms in this zone were discussed in Chapter 4 in the section on wave processes.

5.4.2 Low Tide Outlet

The distributary mouth bar associated with the low tide outlet is primarily subtidal (Figure 26) and the following description is based mainly on Raytheon Model DE 719B fathometer profiles and Eckman bottom grab samples. The small braided channels that originate on the northern and southern banks of the main channel are shallow and carry only a very small volume of the total fluvial discharge at low tide. These funnel-shaped channels are major conduits for tidal drainage and produce areas of gravel flats and rippled sand.

In plan the distributary mouth bar (Figure 26) is roughly parabolic in form, pinching out slightly landward and flaring out seaward as does the channel. The channel is deepest along the northern and southern flanks of the bar. In a landward to seaward direction (A to A' on Figure 26) the bar can be divided in four main morphologic zones: the channel, the bar back, the bar crest, and the bar front. The channel zone extends from above the higher low water outlet to the bar back and has a moderately steep seaward slope and a rectangular cross section from north to south. The bed within the channel zone is primarily gravel and cobbles (3-6 cm). The bar back is situated between the channel and bar crest zones is approximately 0.5 b_o in length and is

distinguished by a moderate landward slope and a convex-up cross section. Sediments composing the bar back are similar to the channel zone.

The bar crest is a roughly horizontal platform 0.5 b_o long with a convex up cross sectional form (Figure 19a). At extremely low tides (-0.5 m) portions of the crest are exposed as two to four bars located immediately landward of the lower low water outlet (Figure 33). The landward portion of the bar crest consists of a sheet of gravel and cobble sized material (3-6 cm) that grades into medium gravel in the central area of the crest. In the distal bar crest the gravel becomes finer and consists of a series of small lobes over sand. The extreme seaward edge of the exposed bar crest is covered by medium sand (0.4-0.6 mm) with straight to sinuous crested large ripples to small dunes (20 to 35 cm wavelengths) oriented transverse to the flow direction. The subaqueous portions of the crest on the northern and southern flanks are gravel to the break in slope between crest and bar front zones. Internally the exposed proximal cobbles and gravels are matrix-filled with no well defined structure, the distal gravels are typically a veneer over small-scale tabular cross-bedded sand.

Seaward of the bar crest is the very steeply sloping (15°) bar front, located on the upper delta front. The most distinctive features of the bar front are the erosional gullies, or 'chutes' as they are termed by Prior et al. (1981). One large chute originates in the distributary mouth bar area, beginning as a V-shaped notch 10 m deep

100 m

Figure 33. Low tide outlet of the North Channel, looking from North to South.

that has eroded back into the bar crest. The chutes are discussed in more detail in the next section.

5.5 Discussion

The following discussion examines the relationships between effluent dynamics and distributary mouth bedload transport, suspended sediment and bedforms at the high and low tide outlets of the North Channel.

5.5.1 High Tide Outlet

5.5.1.1 Bedload Transport

The well-known Shields' diagram or Hjulstrom's diagram are commonly used to determine whether a given sediment can be moved by a particular flow. The Shields' diagram was chosen for this study to determine if high and low tide outlet sediment could be entrained by measured flows. The value of τ_o was determined from the Shields diagram for quartz particles and a water temperature of 10°C (Blatt et al., 1980, p. 102). Equation (4) can then be used to determine U_*. Figure 34 shows the resulting relationship between particle size and U_* required for initiation of movement.

Samples of the channel bed near the outlet suggest a mean clast size of approximately 3 to 6 cm. On June 30 the maximum value of U_* at the outlet centre was 0.13 m sec^{-1}, capable of eroding clasts up to 1.7

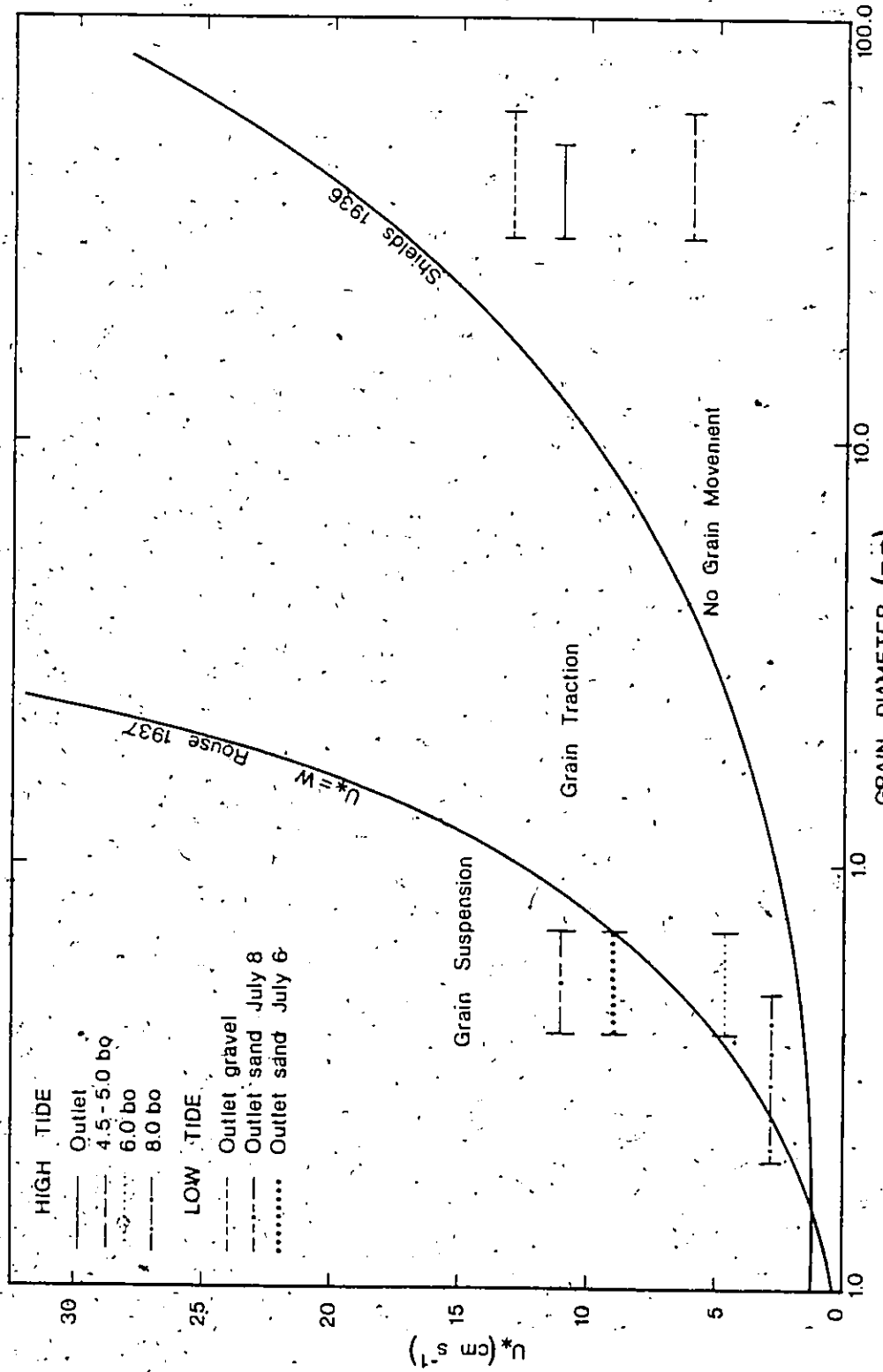

Figure 34. Criteria for particle erosion and suspension for a water temperature of 10°C.

cm. On the radial gravel bar at 4 b_o and 5 b_o the value of $U_* = 0.06$ m sec^{-1} is less than that required for movement of 2-3 cm. clasts, but capable of eroding granules up to 4 mm. Beyond the gravel bar where the bed is composed of sand at 6 b_o, a $U_* = 0.045$ m s^{-1} is capable of moving sand up to 2.4 mm in diameter. Sand sizes in this zone were generally in the medium size range (0.4-0.7 mm) and as a result the flow is competent to transport them. At 8 b_o U_* has decreased to 0.027 m s^{-1}, still capable of transporting the medium to fine sand (0.20 to 0.5 mm) in this area and of eroding sand up to 1.1 mm. It is clear from this discussion that the high tide effluent is incapable of transporting the coarser gravel and cobble sized sediment, but is competent to transport sand, and near the outlet, fine gravel. This conclusion is supported by the algal cover on much of the gravel bar, which indicates little recent movement, and by the unidirectional current bedforms on the sand which indicates that transport is occurring. The coarser material on the radial bar probably represents a lag deposit produced as the finer sizes are mobilized and transported. It must be noted that erosional capabilities of the effluent will vary to some degree depending on tidal stage. During low high water effluent depths will decrease and U_* may increase enough to erode gravel in the channel but probably not on the bar. During higher high water U_* may decrease.

Since material coarser than 4 mm cannot be transported over the radial bar during periods of high summer discharge, the question arises as to when this material can be moved. As noted earlier, high magnitude flood conditions can occur in the spring due to snowmelt, and extremely

intense storm induced floods can occur in the autumn and early winter. It is likely, then, that much of the coarser bedload fraction is transported under these flood conditions, and during the remainder of the year finer material is moved.

5.5.1.2 Suspended Sediment

For suspension of a given particle to occur, the value of U_* must be greater than or equal to W, the settling velocity of the particle (Blatt et al., 1980). Values of W were obtained from Rouse's (1937) empirical data for quartz spheres, although Graf and Acaroglu (1966) suggest that such values are not in complete agreement with natural particles of variable shape. The line $U_* = W$ is shown on Figure 34 which shows that only the finer portion of the sand present on the bed at 8 b_o would be suspended by the effluent on June 30. The actual concentrations noted on Figure 23 then, are largely a result of fine (very fine sand and silt) portions of the sediment load that are not present on the bed surface in significant quantities. Much of a given suspended sediment sample is silt-sized glacial 'flour'. The presence of this is not strongly related to hydraulic conditions in the river and might be better described as wash load (i.e., sediment not presented in any quantity on the bed; Middleton and Southard, 1977, p. 6.24).

True suspended load (i.e., material present on the bed that is swept into the main part of the flow by turbulence) decreases in concentration vertically in rivers above a known concentration near the bed, according to an equation first derived by Rouse (1937) (see Middleton

and Southard, 1977, p. 6.37-6.39, or Carson, 1971, p. 43, for details). In general, the coarser the suspended material, the steeper the rate of the vertical decrease. Insufficient data prevents a comparison of the actual values (Figure 23) in the high tide effluent with predicted values from Rouse's (1937) equation or with results from other streams, but it can be noted that in general the Bella Coola values did decrease vertically although at 2 b_o there was an increase and at 7 b_o little vertical variation. The vertical increase at 2 b_o may be a result of higher values in the upper part of the water column 'inherited' from the shallower flow at 1 b_o, and the lack of variation at 7 b_o might be related to values of $U_* < W$ (no suspension of bed material) and the suspended sediment concentration being primarily wash load.

5.5.1.3 Bedforms

Experimental work has shown that the main variables that control bedform type in a flume are grain size, mean velocity and flow depth (Middleton and Southard, 1977) and fields of stability for various bed configurations are commonly displayed on size-velocity or depth-velocity diagrams (eg. Harms et al., 1975). Maximum depths in flumes, however, are normally limited to 60 cm, and it is necessary to extrapolate phase boundaries to the much greater depths found in natural rivers (Blatt et al., 1980, p. 139). Blatt et al. (1980) suggest that in natural streams stream power, $\omega = \bar{U}\ \tau_o$ ($N\ m^{-1}\ s^{-1}$), may be used where grain size is important for lower regime bedforms that produce very little disturbance disturbance of the water surface (ripples, sand waves) or have water waves that are out of phase with the bedforms (dunes). For upper regime

bedforms, (antidunes, chutes and pools) that are in phase with water waves and depend little on grain size, they suggest that the Froude number, $F = U/\sqrt{gh} > 1$ should be used. Figure 35 relates the bedforms associated with the high tide outlet to flow conditions (ω and F) in the effluent on June 30 and July 15.

The transverse ribs at 5 b_o on the radial bar may have originated in at least two possible ways. The first possibility is that they may be unidirectional current antidune type features. The value of F at this position in the effluent during high slack water, however, is 0.10, a value much less than that required for generation of standing waves and production of antidunes. It may be that as the tide falls, the effluent shallows and accelerates to the point where super-critical conditions are achieved and the ribs created. Alternatively the ribs may be large wave ripples, produced as incoming waves interact with the outflowing effluent and by constructive interference create large standing waves which then build the ribs. These wave-effluent interaction standing waves were frequently encountered during high tide conditions on the delta plain. The presence of crest bifurcations on some ribs supports the latter hypothesis.

The sand waves noted at 8.5 b_o were positioned on the stream power versus grain size diagram (Figure 35) for ω determined from velocity profiles on the north-east edge of the effluent on July 15 (Figure 17a), and for ω in the centre of the effluent on June 30 (Figure 17b). Grain sizes varied from 0.40 to 0.55 mm. The sand waves on July 15,

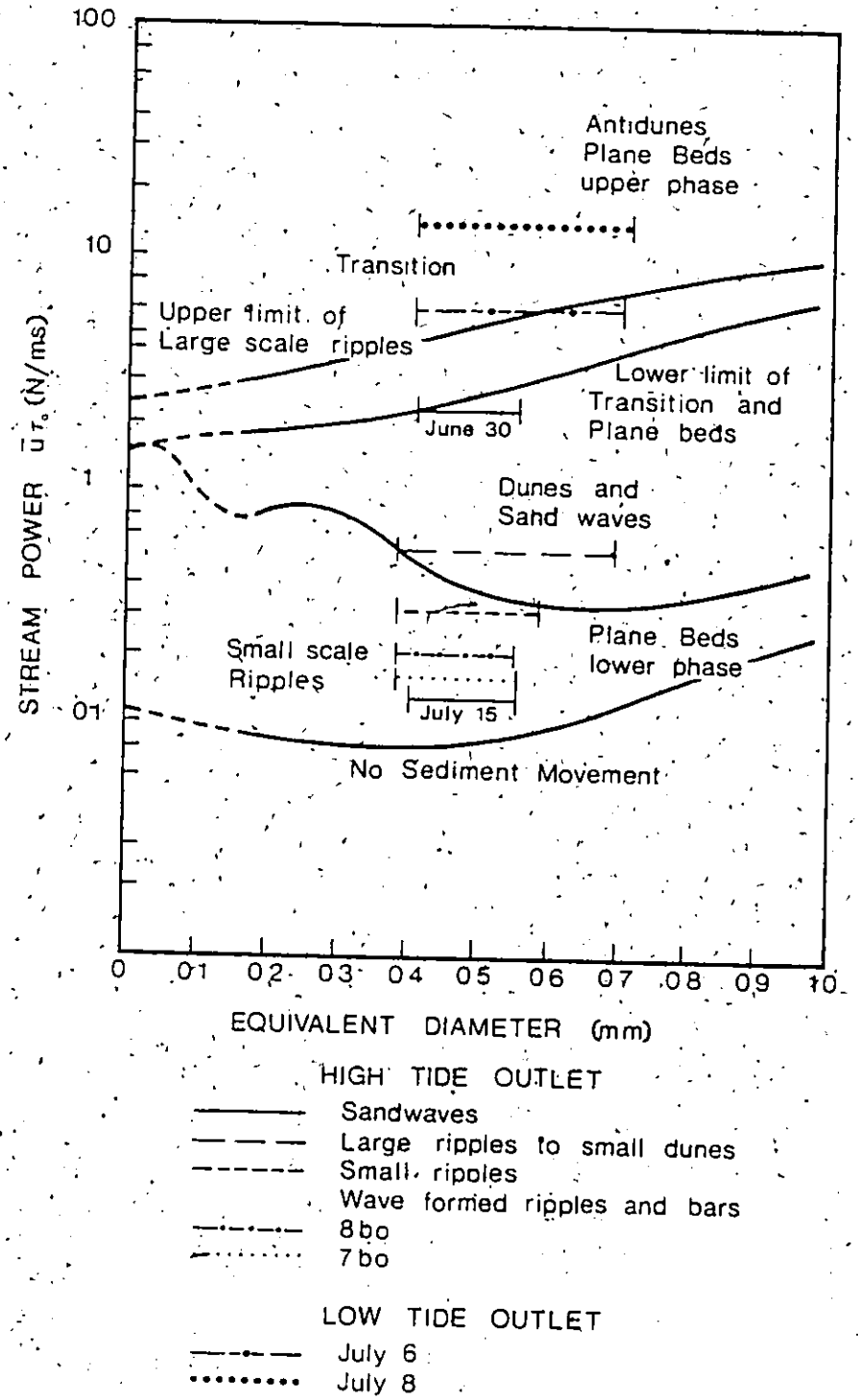

Figure 35. Hydraulic criteria for bedforms based on stream power (from Allen, 1968).

during a period of lower discharge and lower effluent velocities, fall within the zone of smaller scale ripples. As noted earlier, the sand waves during this period were inactive and were being destroyed, and the equilibrium bed phase related to the flow is the small ripples noted on the sand wave backs. If the sand waves are related to ω on June 30, they fall into the upper portion of the dunes and sand waves zone (Figure 35). Effluent velocities decrease somewhat toward the edge of the plume, and it seems reasonable to conclude that the sand waves are in equilibrium with the effluent and active during higher discharges in June, and would be positioned within the dunes and sand waves zone of Figure 35.

The straight to sinuous-crested large ripples to small dunes with grain sizes 0.4-0.7 mm at 5.5 b_o fall within the lower portion of the dunes and sand waves zone (Figure 35). Since these bedforms appear to be transitional in size between ripples and dunes, they are in equilibrium with the effluent on June 30. The small linguoid and lunate current ripples, with grain sizes 0.3-0.5 mm, in the combined zone at 6.5 b_o fall within the small scale ripple zone on June 30, as expected (Figure 35).

Within the zone of sand dominated by wave formed ripples and bars, the values of ω at 7 b_o and 8 b_o on June 30 predict small scale ripples (Figure 35). As discussed earlier, current ripples occur only in the trough between bars, while wave-ripples dominate the bar crests. It seems, then, that wave processes acting during high tide on the bar tops are able to overwhelm the currents produced by the effluent in this

zone, while the effluent (and possibly tidal drainage) dominates in the troughs. During periods of low wave activity at high tide it might be expected that the effluent would remold the entire bed into current ripples in the central portion of the plume, but current ripples were never noted on the bar tops.

5.5.2 Low Tide Outlet

5.5.2.1 Bedload Transport

The gravel clasts from the bar crest of the low tide outlet are in the range of 3 to 5 cm. On July 8 the maximum value of U_* at the outlet was 0.12 m s^{-1}, a value not competent to erode gravel, but capable of moving the medium sand on the seaward edge of the bar crest (Figure 34). It should be pointed out that the competence of the effluent over the bar crest (and bar back) will vary considerably with tidal stage. During lower tides than those on July 8, the effluent depth will decrease and U_* should increase, perhaps to the point where gravel may be transported. As depths increase during higher tides U_* should decrease. As with the high tide outlet, most of the gravel is probably transported during flood conditions.

5.5.2.2 Suspended Sediment

Maximum U_* values at the outlet on July 6 (0.08 m s^{-1}) and July 8 (0.12 m s^{-1}) are capable of placing the medium sand on the bar crest

bed into true suspension (Figure 34). Values of outlet suspended sediment concentrations near the bed on July 23 during conditions of higher low water were slightly higher (22 mg ℓ^{-1}) than those at the surface (16 mg ℓ^{-1}). Values of U_* on July 23, however, were probably not sufficient to place a large amount of sand on the bed into suspension at this time, and as with the high tide outlet, much of the suspended sediment was probably wash load.

The relatively high concentrations of suspended sediment below the pycnocline at 0.5 b_o from the outlet (Figure 24) indicate some settling out of coarser portions of the suspended load and also reflect the mixing of fresh and saline water in this zone. The lack of decrease in suspended concentrations in the surface layer seaward of the outlet reflects the fine size of the particles and indicates minor amounts of settling and vertical mixing have occurred. With time and increasing distance from the delta flocculation of clays by seawater and pelletization by zooplankton will assist particle setting (Syvitski, 1979).

5.5.2.3 Bedforms

Values of stream power were determined for July 6 and July 8 for the zone of large ripples to small dunes on the distal portion of the bar crest, and plotted on Figure 35. The July 6 values fall within the upper limit of small ripples, while the July 8 values are within the antidune-plane bed zone. Values of the Froude Number, F, are 0.15 and 0.37 on July 6 and July 8 respectively, values not large enough to

produce upper flow regime bedforms and antidune-plane bed conditions. The large ripples to small dunes noted probably represent flows similar to those recorded on July 6 during positions of moderately low water and deeper flows, or perhaps higher high water and yet deeper flows. The July 8 flows, according to stream power criteria would produce antidune-plane bed bedforms, but according to F criteria the flow would be subcritical and not capable of producing antidunes. As suggested earlier, the Froude No. criteria is probably more suitable for antidune-type bedforms and supercritical flows.

CHAPTER 6

A COMPARISON OF BELLA COOLA RIVER MOUTH MORPHODYNAMICS WITH THE MORPHODYNAMIC MODELS, AND SECTION II SUMMARY

6.1 Introduction

The first portion of this chapter compares the results of the morphodynamic analysis of the Bella Coola North Channel with the models proposed by Wright (1977) and Bates (1953). Included in this discussion are effluent expansion and deceleration and distributary mouth morphology for the high and low tide outlets. The second portion provides a brief summary of Section II of this thesis: river mouth processes and controls.

6.2 High Tide Outlet

6.2.1 Effluent Deceleration and Expansion

Since the high tide effluent is in contact with the bed over most of its length, Wright's (1977) friction-dominated model (Figure 1b) should best approximate the Bella Coola high tide outlet. Equation (9) was used to predict deceleration rates of the effluent. The value of K in the equation, which is a function of the Chezy coefficient C

(Equation 10), was determined using Manning's n (Equation 11) and the D'Arcy-Weisbach f (Equation 12). Manning's n was assigned a value of 0.03 as the North Channel has a gravel bed with no channel vegetation (see Gray, 1970, pp. 8.75-8.76), and the resulting value of C is 36. Using f calculated from values of τ_o (Equation 4) determined from velocity profiles (Equation 5) on July 15, a value of C of 37 was calculated. The values of C are almost identical, and the mean of the two was used. The value of K determined at the outlet was kept constant with distance from the outlet, although it is realized this value may change slightly when the bed composition changes from gravel to sand. The predicted and actual deceleration rates for June 30 are summarized on Figure 36.

The Bella Coola distributary mouth bar has considerable topographic variability, producing variable effluent depths over the bar. This may cause predicted deceleration rates to show some divergence from the calculated line (Figure 36). In addition, the change from gravel to rippled sand bed may introduce some error. Variation in actual values may be a result of changing depths, deviation in the position of the velocity profile from the actual line of maximum velocity and unsteady flow.

There is generally good agreement between predicted and actual deceleration rates, especially in proximal areas of the effluent (Figure 36). This proximal agreement is rather surprising in that the effluent did not expand laterally to any appreciable degree until leaving the confines of the low tide channel beyond 3.5 b_o from the outlet. Both

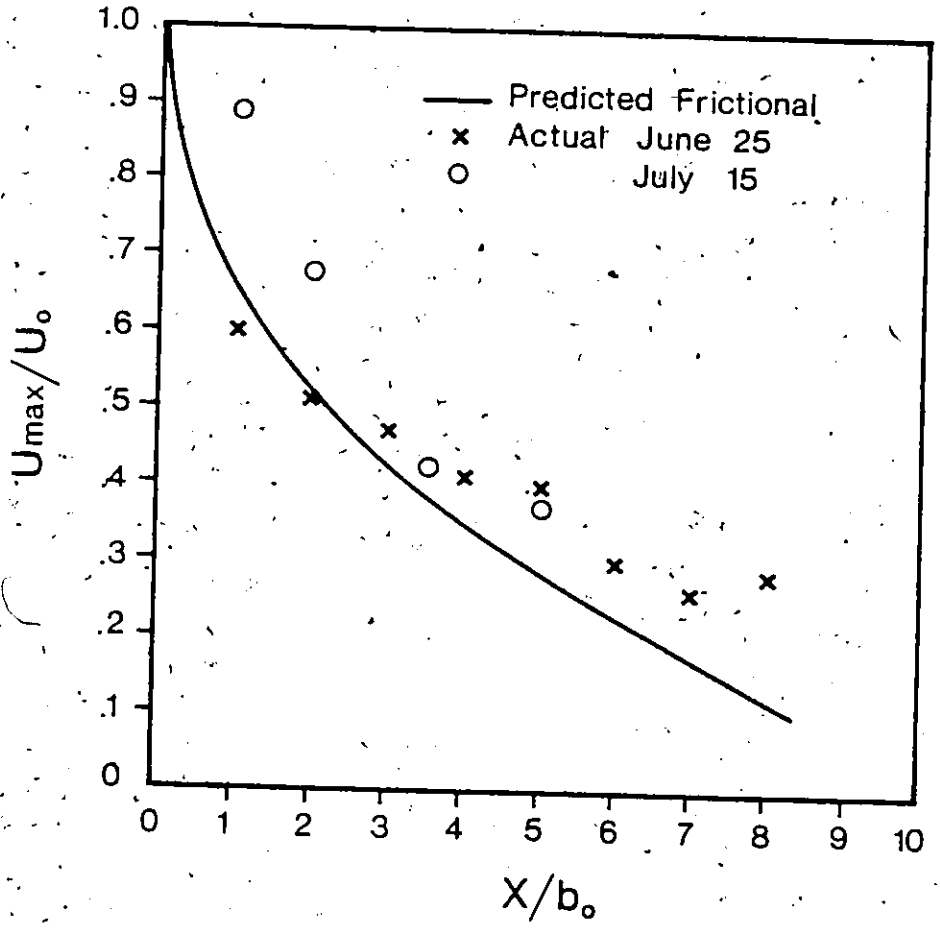

Figure 36. High tide outlet predicted and actual deceleration rates. The maximum centreline velocity is U_{max}, U_o is the velocity at the outlet, x is the distance seaward of the outlet, and b_o is outlet width.

predicted and actual values decrease very rapidly immediately downplume of the outlet area and no 'core of constant velocity' was noted. In the distal portion of the effluent there is considerable difference between predicted and actual deceleration, with the actual values being higher than predicted. This may be largely a result of the change in bed composition from proximal gravel to distal rippled sand.

Predicted and actual lateral expansion rates are shown on Figure 37. Equation (13) was used for determining the predicted values from depth data collected on July 15. Borichansky and Mikhailov (1966) note that lateral effluent expansion depends to a considerable degree on bottom configuration and roughness. The shallower the depth seaward of the outlet and the greater the roughness the greater the rate of expansion. The variability of depths over the distributary mouth bar might cause the small amount of offset in predicted values on Figure 37. The more rapid expansion rate in actual values at 5 b_o may reflect the lack of confinement of the effluent by the low tide channel beyond 3.5 b_o. Predicted and actual expansion rates show good agreement, however, indicating that the friction dominated model accurately predicts expansion rates.

6.2.2 Distributary Mouth Morphology

The high tide distributary mouth bar form is best approximated by Wright's (1977, 1978) radial bar which develops during the early stages of deposition of friction dominated effluents. At Bella Coola there is no evidence for middle ground bar development with associated

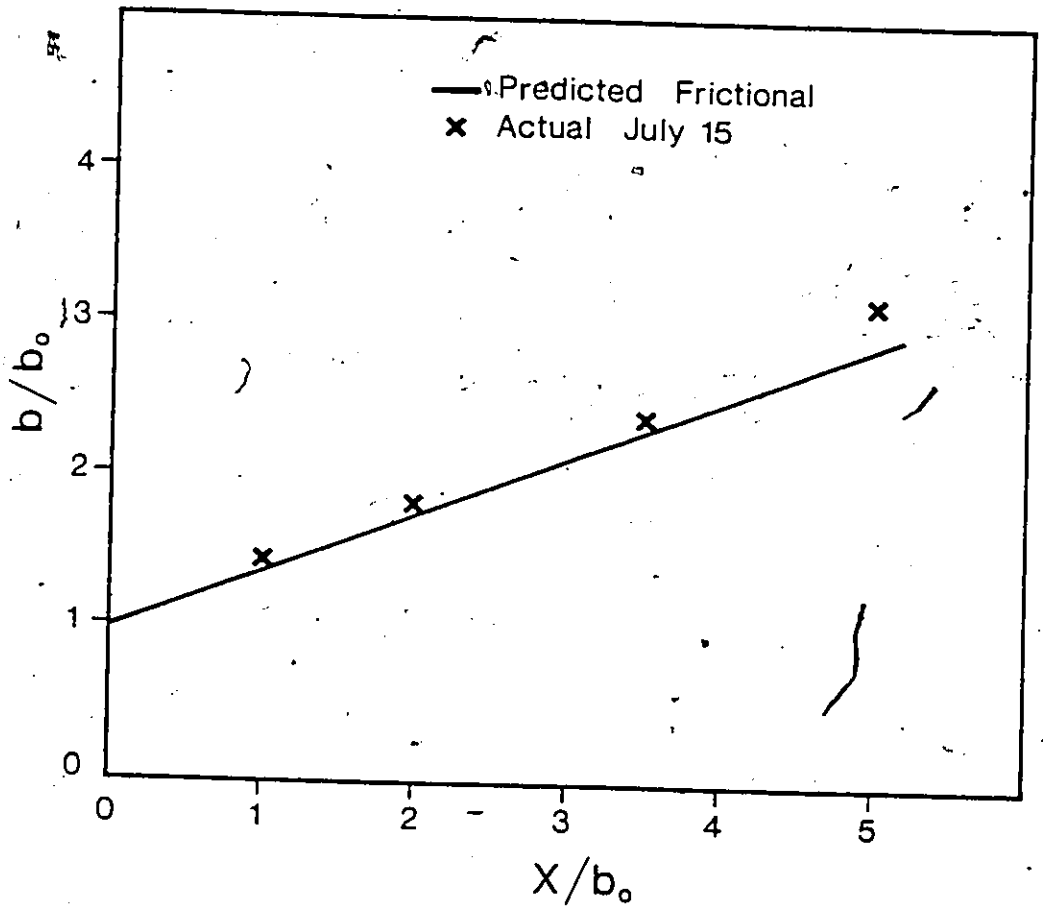

Figure 37. Lateral expansion for the high tide effluent. The width of the outlet is b_o, b is the effluent width and x is the distance from the outlet.

levees and diverging channel arms. However, the distributary pattern on the upper delta plain has a somewhat bifurcated appearance typical of patterns resulting from middle ground bars. This suggests that some manner of middle ground bar formation may occur. There are at least two reasons for the seemingly incomplete development of depositional patterns at the high tide outlet. First, the coarse nature of the sediment may restrict development of features such as subaqueous levees and hence a middle ground bar. Second, the twice daily rise and fall of the tide may not allow sufficient time for middle ground bar formation to take place, nor an equilibrium situation between effluent and deposition to establish.

6.3 Low Tide Outlet

6.3.1 Effluent Deceleration and Expansion

Friction is a factor at the low tide outlet when the outlet has shifted to the east, onto the delta plain, during higher low water conditions. Inertia and buoyancy are important seaward of the break in slope between delta plain and delta front. Deceleration and lateral expansion rates were calculated using the inertial and buoyant models.

Predicted deceleration values for inertial effluents were determined from Equations (7) and (8) for conditions on July 6 (Figure 38). The predictions show a constant velocity from the outlet to 4-5 b_o seaward (the core of constant velocity) with relatively constant deceleration seaward in the zone of established flow. These predictions

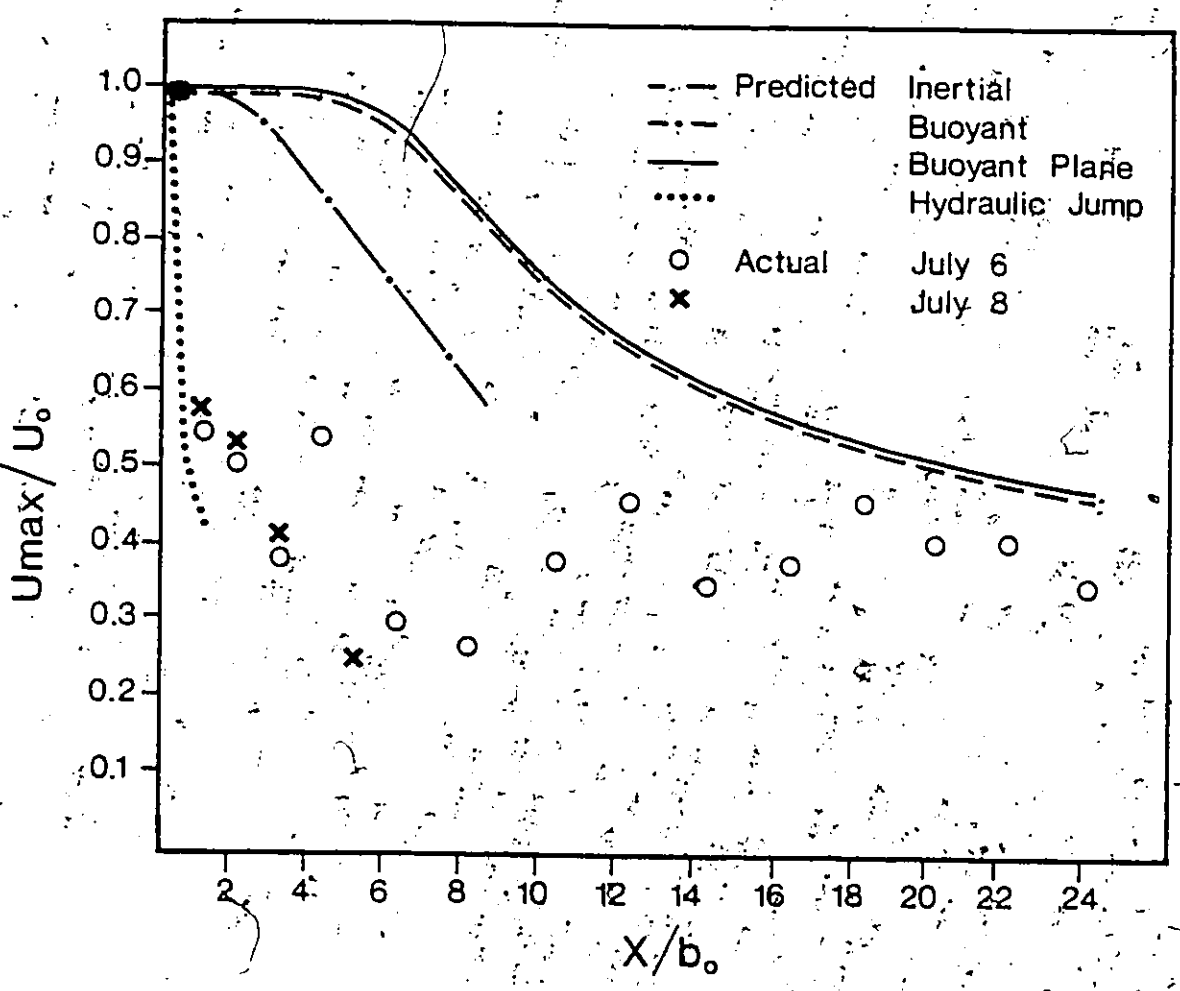

Figure 38. Low tide outlet predicted and actual deceleration rates. The maximum centreline velocity is U_{max}, U_o is the outlet velocity, x is the distance from the outlet and b_o is outlet width.

show extremely poor correspondence with actual values on July 6 (Figure 20a) and July 8 (Figure 20b, c), especially in predicting the rapid deceleration immediately seaward of the outlet. The buoyant jet deceleration curve is from Wright and Coleman's (1971, figure 7c) 'family' of curves and represents deceleration from a value of $U_o = 0.9$ m s^{-1}, similar to the mean $U_o = 0.98$ m s^{-1} for July 6 and July 8 in Bella Coola. The predicted deceleration is more rapid than the inertial model, but still shows very poor agreement with actual values.

It is clear that the deceleration models based on axial and buoyant jets do not account for the rapid seaward deceleration immediately seaward of the outlet in Bella Coola. The question that arises is what can account for the deceleration. As was noted earlier, an internal hydraulic jump takes place in the low tide effluent when values of F' decrease across the critical value of unity. Hydraulic jumps are associated with a large energy loss and rapid deceleration. Given the data collected on July 8 (Figure 20c) it is possible to use the method outlined by Streeter and Wylie (1979, p. 456-57) to predict the velocity seaward of the jump in Zone 3. The Zone 2 values of $F_1' = 4.1$, $U_1 = 0.9$ m s^{-1} and $h_1' = 5.0$ m are in the zone of the turbulent diffusion landward of the jump ($0.3\ b_o$) and $F_2 = 0.39$, $U_2 = 0.41$ m s^{-1} and $h_2' = 6.0$ m in the buoyancy dominated zone seaward of the jump ($1.0\ b_o$). To satisfy continuity it is necessary to assume:

$$U_2 h_2' = U_1 h_1' = 1.75 \qquad (27)$$

for a constant width. However, some fresh water is entrained and there is lateral expansion ($U_2 h_2 = 2.46$) so these assumptions are not absolutely valid. The value of F_2' can be predicted by:

$$F_2' = \frac{2(2)^{1/2} F_1'}{[(1 + 8 F_1'^2)^{1/2} - 1]^{3/2}} = 0.33 \qquad (28)$$

This value is similar to the actual value of 0.39; the difference is probably due to a fixed value of $h_2' = 6.0$ m, vertical entrainment, and lateral expansion. The velocity seaward of the jump is predicted by:

$$U_2 = [(F_2')^2 \gamma g U_1 h_1]^{1/3} \qquad (29)$$

The predicted value is $U_2 = 0.40$ m s^{-1} using the actual value of F_2' and 0.35 m s^{-1} using the predicted value of F_2'. These values are similar to the actual value of $U_2 = 0.41$ m s^{-1} (Figure 38).

This analysis indictes that the rapid deceleration immediately seaward of the outlet can be largely accounted for by an internal hydraulic jump occurring as flow conditions change from supercritical to subcritical values. Turbulent diffusion landward of the jump probably accounts for some deceleration, but the axial jet model predicts a core of constant velocity that does not occur in Bella Coola.

Seaward of the hydraulic jump both inertial and buoyant models

predict a constant deceleration. The actual values for July 8, however show an acceleration occurs (Figures 18, 20). Kashiwamura and Yoshida (1971) noted effluent acceleration in experiments and at the mouth of the Ishikari and Teshio Rivers in Japan. In these cases, however, the acceleration was related to seaward thinning of a salt-wedge buoyant plume. The Bella Coola effluent, however, does not thin seaward and as such the apparent acceleration cannot be explained in this manner. Possible explanations are as follows. It may be that large-scale two-cell helical flow occurs in the effluent, such as that noted by Wright and Coleman (1971) in the Mississippi. This might result in some variation in flow velocity downplume, perhaps producing higher centreline speeds in certain areas of the flow. Alternatively, the effluent may pulsate in a manner similar to that noted in density underflows (eg. Smith et al., 1982), resulting in velocity fluctuations over time not averaged out by the 6 s averages used in this study. Finally, it may be that residual tidal currents may act to increase the effluent velocity downplume. This explanation might be valid towards the fjord mouth 15 km from the delta but is unlikely to be important near the river mouth.

Lateral effluent expansion can be predicted for axial jets (12 1/2°) and for buoyant jets by Equations (17), (19) and (20). Assumptions of constant seaward velocity and no vertical entrainment are made for the buoyant jet. Predicted and actual rates are summarized on Figure 39. The axial jet expands in a linear fashion from the outlet (Figure 8a). The buoyant jet expands rapidly immediately seaward of the outlet and then lateral expansion rates decline, with a resulting parabolic shape in plan (Figure 8c). Actual values measured on July 8

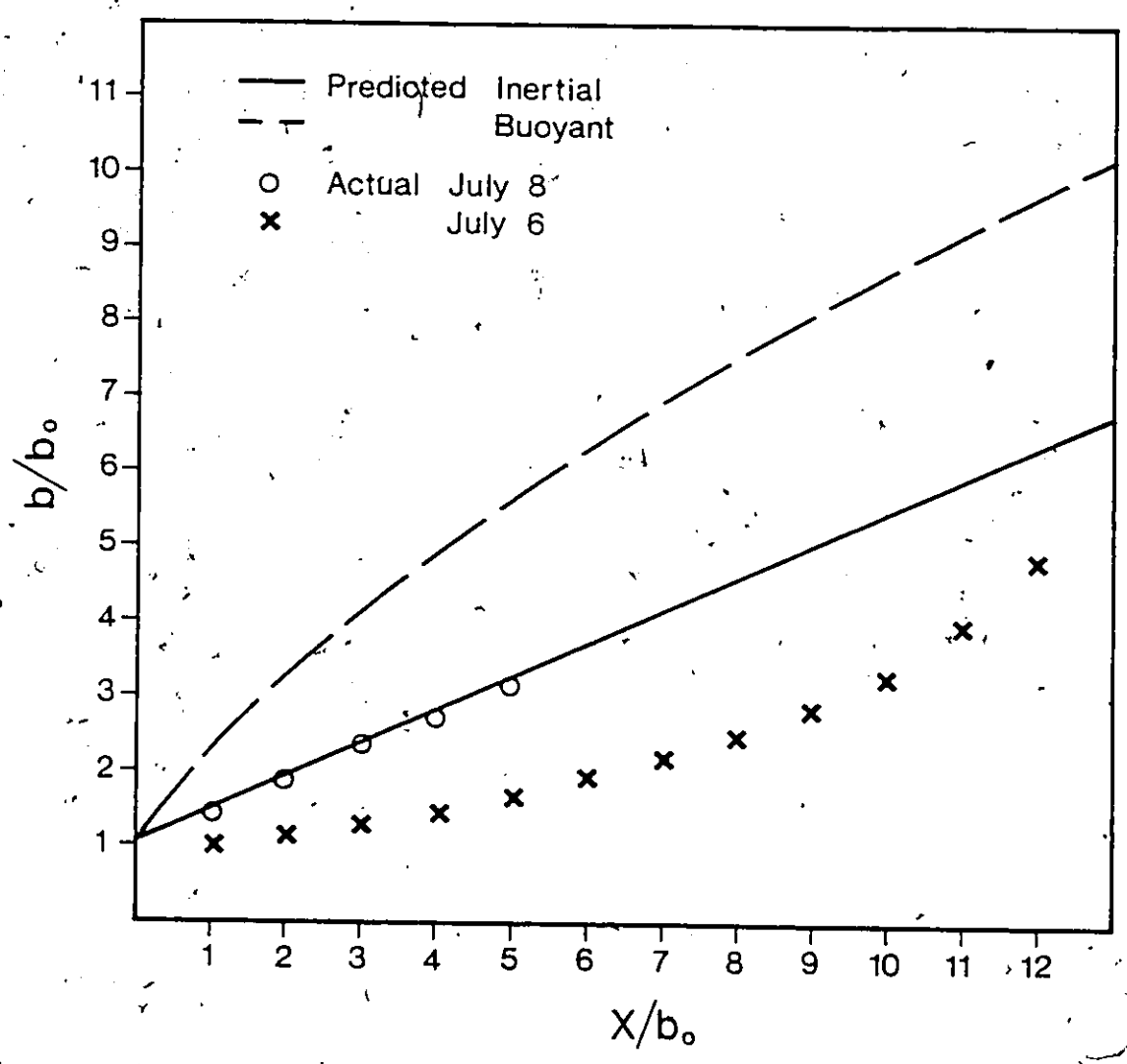

Figure 39. Lateral expansion for the low tide effluent. The width of the outlet is b_o, b is effluent width and x is the distance seaward of the outlet.

(Figure 20a) correspond very closely with predicted expansion rates. Values of August 26, 1979 were determined from an aerial photograph during a tide rising from 1.2 m (Figure 21) which places the outlet approximately 2 to 3 b_o landward of the break in slope between delta plain and front. Initial expansion rates are low, reflecting the channelization effect of the low tide channel, and then increase to 11-13°. Lateral expansion rates then, are best approximated by the axial jet model.

Vertical expansion for axial jets proceeds at 12 1/2° from the outlet, and vertical thinning for buoyant jets is predicted by Equations (18) to (20). Axial jet expansion proceeds in a linear fashion from the outlet. The buoyant jet thins rapidly at first, then maintaining a relatively constant thickness seaward. Actual values for July 6 thicken rapidly immediately seaward of the outlet, then remain constant. There is poor agreement between actual and predicted values (Figure 40). It would seem that vertical expansion in Bella Coola is not controlled by jet dynamics (except immediately beyond the break in slope where axial expansion must prevail) but rather by the thickness of the fresh water surface layer which dictates the thickness of the effluent plume.

6.3.2 Distributary Mouth Morphology

The low tide outlet channel and distributary mouth bar does not correspond with morphologies predicted by Wright's (1977) models and appears to be a combination of middle ground and lunate bars. This is hardly surprising in that frictional, inertial and buoyant forces are

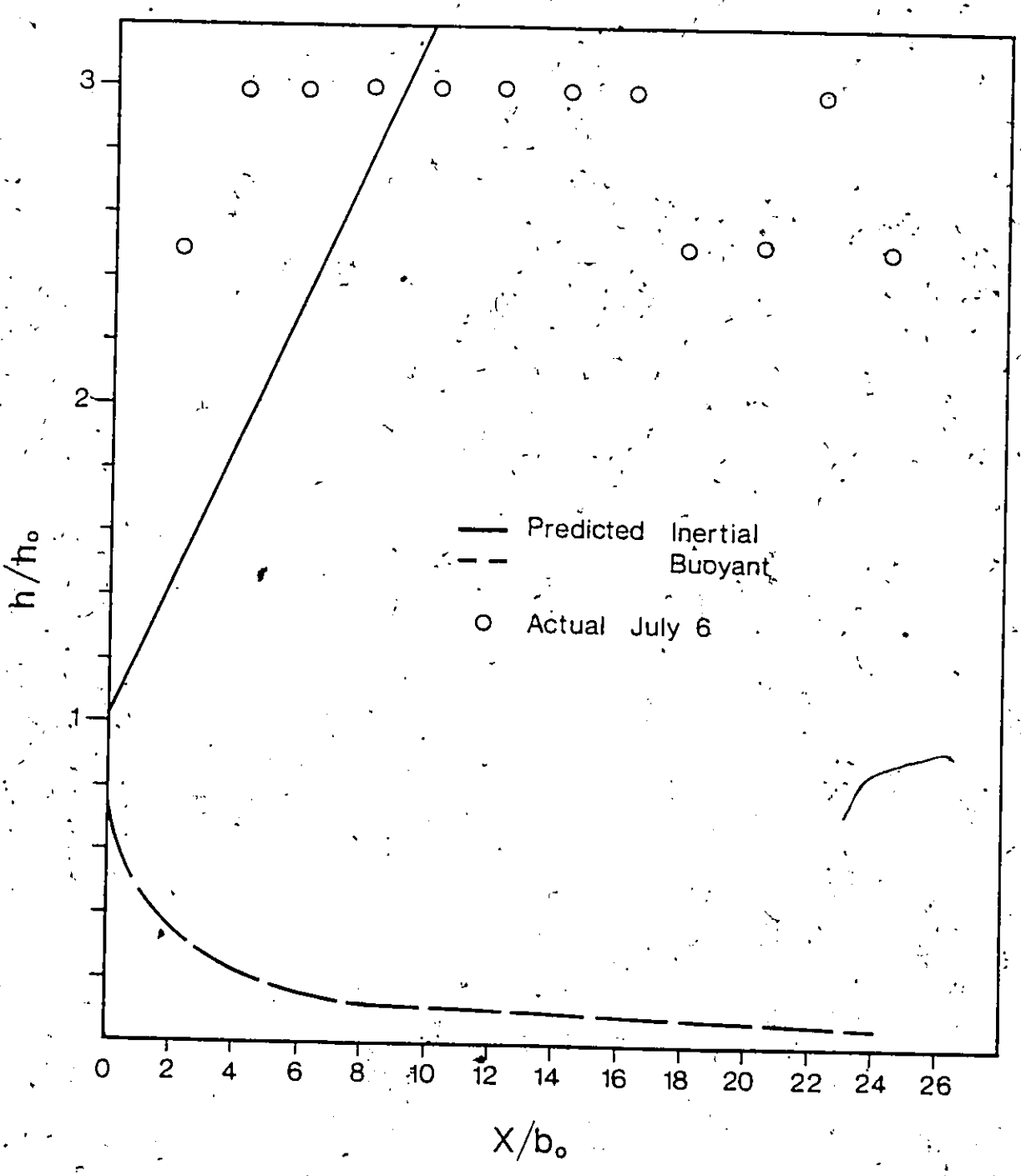

Figure 40. Vertical expansion for the low tide effluent. The outlet depth is h_o, the depth of the interface is h', the outlet width is b_o and x is the distance seaward of the outlet.

all important at this outlet. The middle ground component is reflected in diverging channel arms and a roughly triangular bar form. The bar profile, however, with a gently sloping bar back and steep bar front is typical of a lunate bar.

6.4 Summary

The more important features of the morphodynamics of the Belka Coola Delta are summarized on Figures 41 and 42.

6.4.1 High Tide Outlet

Dynamic Zone 0 is located within the channel and is dominated by channel processes. Zone 1 is dominated by friction and is associated with rapid effluent deceleration and low tide channel-confined effluent expansion of 5-8°. The channel bed and banks associated with these two dynamic zones consists of gravel to cobble sized sediment. Poorly developed sandy subaerial levees are associated with Zone 0.

Zone 2 is dominated by friction with rapid deceleration and a wide lateral spreading angle of 16-18°. Suspended sediment concentrations increase with depth within the effluent. A large radial bar is associated with this zone. The gravel portion of the bar is algal-covered gravel and cobbles in proximal areas, transverse-ribbed flow-parallel gravel lobes in distal areas. The sand portion of the bar is surfaced with current ripples and sand waves proximally, grading seaward into combined wave and current ripples. Seaward of the radial bar is a

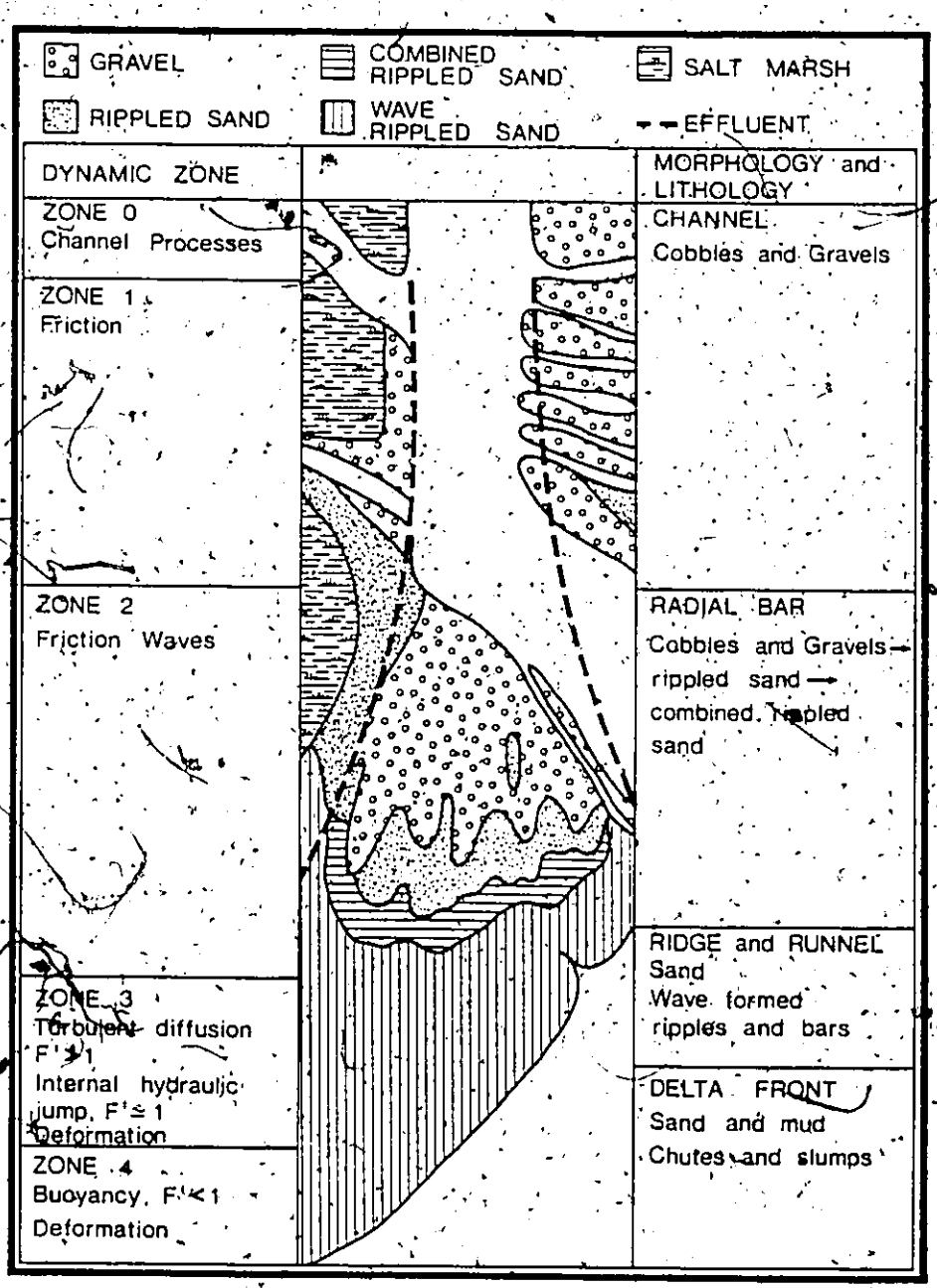

Figure 41. High tide outlet morphodynamics.

sandy area of wave-formed ridges and runnels; wave ripples on the ridges, current ripples in the runnels.

Zone 3 is narrow and situated seaward of the break in slope between delta plain and delta front and is a zone of turbulent diffusion, an internal hydraulic jump and some effluent deceleration. Zone 4 is buoyancy dominated and suspended sediment concentrations are highest in the effluent, declining below the pycnocline. The delta front is composed of sand and mud with subaqueous gullies or chutes being the main morphologic features.

The high tide outlet best corresponds with Wright's (1977) friction dominated morphodynamic model.

6.4.2 Low Tide Outlet

Dynamic Zone 0 is landward of the outlet and is dominated by channel processes. Zone 1 exists when the outlet is situated landward of the break-in slope between delta plain and delta front and is friction dominated with a confined lateral spreading angle of 5°. The distributary mouth bar back and crest are associated with these dynamic zones. The bar back slopes gently landward and is composed of gravel and cobbles. The bar crest is roughly horizontal and consists of gravel and cobbles in proximal subaerial and in subaqueous areas, and rippled sand in distal subaerial regions. Suspended sediment concentrations above the bar crest are highest near the bed, decreasing towards the surface.

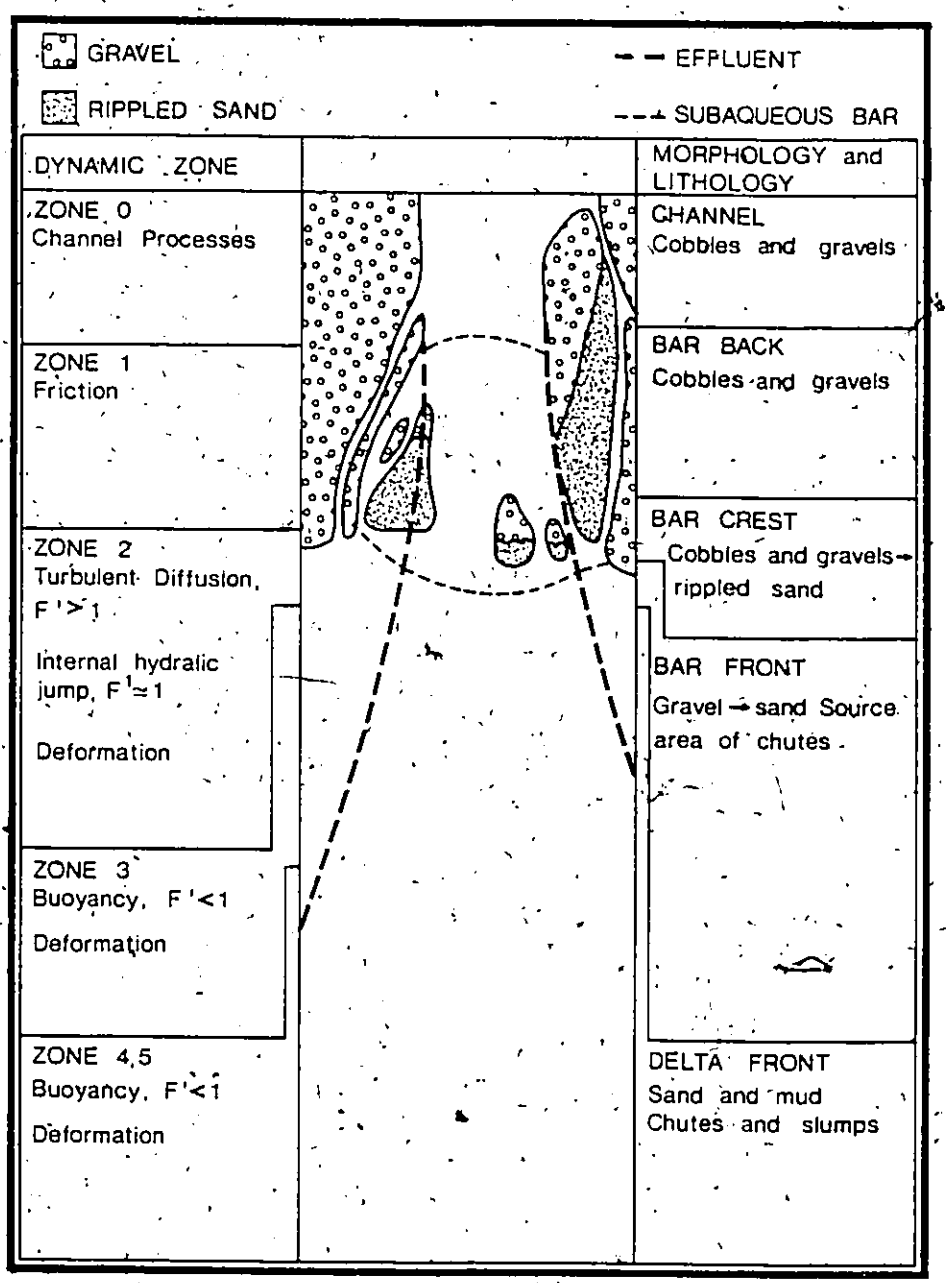

Figure 42. Low tide outlet morphodynamics.

Zone 2 is situated immediately seaward of the break in slope between delta plain and delta front and is characterized by turbulent diffusion, an internal hydraulic jump, extremely rapid deceleration and a lateral expansion angle of 11-12°. The bar front associated with this zone is oversteepened, sloping steeply seaward at 15-20°. The bar front is the primary source area for chutes and is composed of gravel, sand and mud. Suspended sediment concentrations are high above the pycnocline, decreasing to moderate values below it.

Zones 3, 4 and 5 are buoyancy dominated, display a small amount of deceleration or acceleration and expand laterally at 13°. The delta front below these zones is an area of subaqueous deposition and deformation by chutes and slumps. Suspended sediment concentrations are highest near the pycnocline, decreasing towards the surface and low below the pycnocline.

The low tide outlet does not fit Wright's (1977) inertial or buoyant models very well, and probably qualitatively is best approximated by Bates' (1953) plane jet model. Morphologically the low tide outlet is a combination of friction dominated (middle ground) and inertia dominated (lunate) patterns.

List of Symbols

A: ratio of z / h in S_L

a: half-width of debris flow chute (m)

a_x: horizontal earthquake acceleration (g)

B: ratio of $s/\gamma' Z_{max}$

b: width of sediment slice in S_R (m)

b_c: debris flow chute depth (m)

C_u: undrained shear strength (Pa)

C: cohesion (Pa)

C': effective cohesion (Pa)

d: water depth (m)

E: Young's Modulus (Pa)

F_L: fold wavelength (m)

H: wave height (m)

h: thickness of depositional load (m)

Δh: thickness of scarp sediment (m)

R: debris flow strength (Pa)

k': debris flow strength variable

k^*: debris flow strength variable

L: wavelength (m)

M_a: meander amplitude (m)

M_d: median grain size (mm or ϕ)

M_z: mean grain size (mm or ϕ)

M_α: correction factor in S_R

Δp: pressure change due to waves (Pa)

r_m: meander radius of curvature (m)

S: factor of safety for translational slides

S_E: factor of safety for translational slides affected by earthquakes

S_L: factor of safety for translational slides affected by depositional loading

S_R: factor of safety for rotational slides

S_{R_E}: factor of safety for rotational slides affected by earthquakes

s: shear strength (Pa)

u: pore water pressure (Pa)

w: chute width (m)

$\dot{w}$: debris flow plug velocity (ms^{-1})

w^*: debris flow plug velocity variable

x_o: debris flow plug half-width (m)

y_o: debris flow plug thickness (m)

Z: thickness of sediment above slip surface (m)

Z_l: thickness of sediment from scarp top to slip surface (m)

Z_{max}: maximum sediment thickness in rotational slide (m)

$\bar{Z}$: average thickness of sediment slice in S_R (m)

α: angle of the arc at the base of sediment slice in S_R (°)

β: bottom slope (°)

γ: saturated unit weight of sediment ($N\ m^{-3}$)

γ_w: unit weight of sea water ($N\ m^{-3}$)

γ': buoyant unit weight of sediment ($N\ m^{-3}$)

η_b: Bingham viscosity ($m^2\ s^{-1}$)

λ: meander wavelength (m)

ϕ: friction angle or grain size scale (°)

ϕ': effective friction angle (°)

σ: normal stress (Pa)

q_I: grain size standard deviation (ϕ)

CHAPTER 7

FRAMEWORK

7.1 Introduction

Section III discusses North Bentinck Arm and the delta front and prodelta portions of the delta. Data for the subaqueous delta - North Bentinck Arm analysis is provided by echograms and grab samples obtained from a small boat, and by seismic profiles side-scan sonar runs, gravity cores and bottom grabs obtained during a 1982 cruise in the study area aboard the C.S.S. Parizeau. This section consists of four chapters. Chapter 7 provides the framework for the subsequent data analysis, with reviews of seismic stratigraphy, of mass transport processes and of sediment instability forms and processes. Chapter 8 outlines the seismic stratigraphy for North Bentinck Arm. The delta front zone is examined in chapter 9 and the prodelta zone in chapter 10. Seismic facies, morphology, geotechnical characteristics and sediment instabilities are discussed for each zone. The rationale for division of the subaqueous delta into delta front and prodelta sections is discussed in chapter 9.

A Raytheon Fathometer, type DE719B, was used to provide echograms in shallow (<120 m) water investigations and bottom samples were obtained with an Eckman bottom grab. Parizeau-based seismic profiling

consisted of two types: air gun and pinger. The air gun source was a 5 in 3 Bolt Model 600 B chamber, the hydrophone array a Geospace 19 M17 and the recorder an EPC Model 4100. The pinger transducer array consisted of 5 hull-mounted Raytheon TR109 transducers and the transceiver was an ORE Model 140. A Klein Hydroscan with a Model 422 S towfish and Model 531 recorder were used for the side-scan sonar investigation. Sediment samples were obtained with a Shipek bottom grab and a 20 kg gravity corer. Grain size distributions were determined using standard sieve and hydrometer techniques (Folk, 1974), unconsolidated undrained sediment shear strength assessed with a Torvane and bulk density evaluated by finding the weight of a saturated sample in a given volume. Additional details of the equipment used in this investigation and a brief summary of principles of operation is provided in Appendix A. The locations of fathometer, seismic and side scan lines and grab sample and core sites are presented on Figures 43-45.

In order to provide a systematic analysis of the data from the seismic investigations, the seismic stratigraphy approach has been chosen and is summarized below. A brief summary of the main subaqueous mass transport processes follows. Next is a review of the forms and processes of sediment instabilities, as determined from sidescan and shallow seismic data and the application of various models.

7.2 Seismic Stratigraphy

The seismic stratigraphy approach to the analysis of seismic data is reviewed and discussed in detail by Sheriff (1980), Vail et al.,

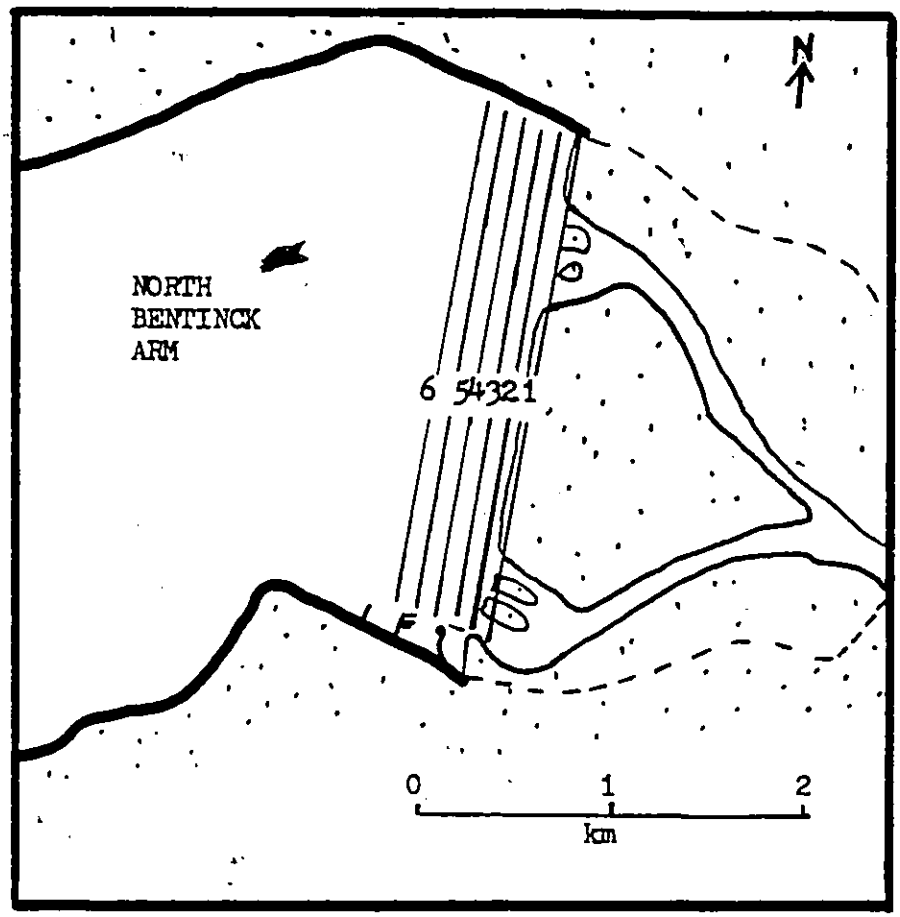

Figure 43. Location of echo-sounding lines.

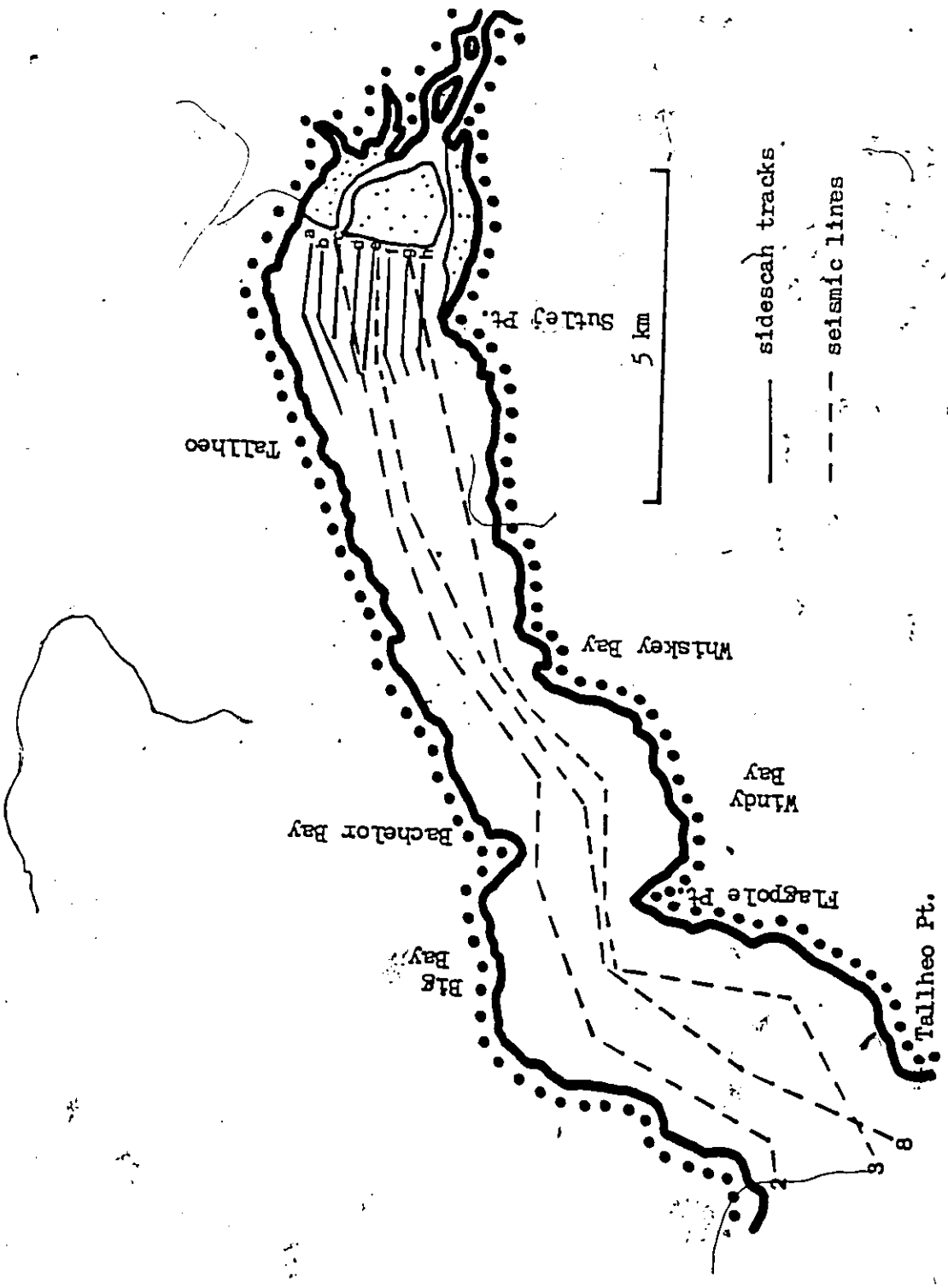

Figure 44. Location of seismic lines and sidescan tracks.

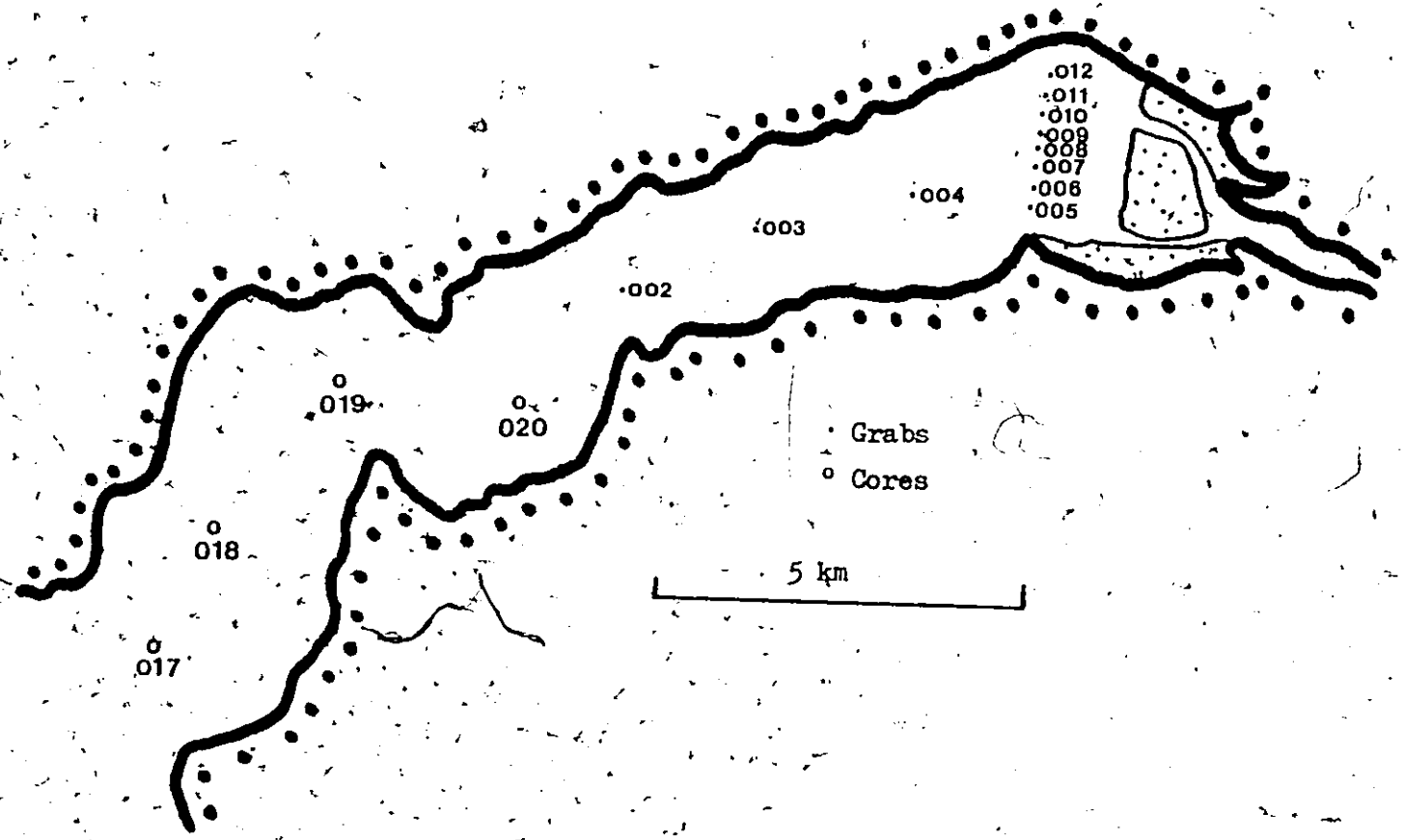

Figure 45. Location of Parizeau grab samples and cores.

(1977) and Brown and Fisher (1979) and the following summary draws largely from these sources. The approach involves: (1) seismic sequence analysis - subdividing the seismic section into packages of concordant reflections separated by surfaces of discontinuity and interpreting them as depositional sequences; and (2) seismic facies analysis - analyzing the configuration, continuity, amplitude frequency and interval velocity of seismic reflection patterns within seismic sequences, and interpreting these patterns in terms of environmental setting and estimates of lithology (Table 4) (Mitchum et al., 1977).

7.2.1 Seismic Sequences

A seismic sequence is a depositional sequence or time-stratigraphic unit recognized and interpreted from seismic data (Sheriff, 1980; Mitchum et al., 1977). The succession is bounded at the top and base by surfaces of discontinuity marked by reflection terminations and interpreted as unconformities (Mitchum et al., 1977). Unconformities represent a hiatus in deposition during which conditions are apt to have changed (Sheriff, 1980).

The key to isolating sequences is the angular pattern of reflections at sequence boundaries (Sheriff, 1980). The relations of reflections within a sequence unit to the unit boundaries are summarized on Figure 46 and include erosion truncation, toplap, onlap, downlap and concordance (Mitchum et al., 1977; Sheriff, 1980).

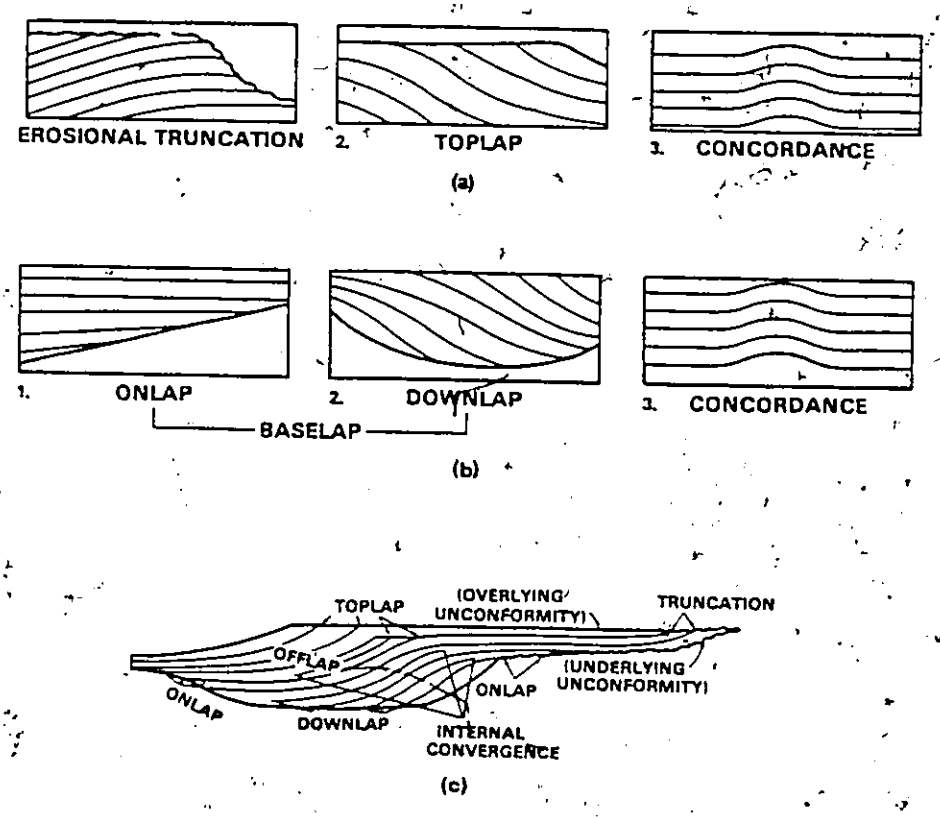

Figure 46. Relations of reflections within a sequence unit to the unit boundaries (from Sheriff, 1980).

7.2.2 Seismic Facies Units

A seismic facies unit is defined by Sheriff (1980) as: "a mappable, three-dimensional unit of reflections whose characteristics differ from that of the adjacent facies". The main characteristics to be considered include configuration, continuity, amplitude and external form. Reflection configuration reveals the gross stratification patterns, reflection continuity is closely associated with the continuity of strata and reflection amplitude contains information on the velocity and density contrasts of individual interfaces and their spacing (Mitchum et al., 1977). The following discussion examines the two components of the overall geometry of a seismic facies unit: reflection configuration and external form.

7.2.2.1 Reflection Configuration

The main types of reflection configuration patterns are parallel, subparallel, divergent, progradational, chaotic and reflection free. Various modifying terms may be added to these configurations (Table 4). Parallel, subparallel and divergent configurations are summarized on Figure 47a. Prograding configurations tend to be more complex and include sigmoid, oblique, complex sigmoid-oblique, shingled and hummocky clinoforms (Figure 47b). Figure 47c summarizes the chaotic and reflection-free configurations and Figure 47d shows some modifying terms that might be applied to configurations (Mitchum et al., 1977).

Reflection Terminations (at sequence boundaries)	Reflection Configurations (within sequences)	External Form (of sequences and seismic facies units)
Baselap	Parallel	Sheet
onlap	Subparallel	Sheet drape
downlap	Divergent	Wedge
Toplap	Progradational	Bank
Truncation	sigmoid	Lens
erosional	oblique	Mound
structural	complex sigmoid-oblique	Fill
Concordance	shingled	
no termination	hummocky clinoform	
	Chaotic	
	Reflection-free	
	Modifying terms	
	even / hummocky	
	wavy / lenticular	
	regular / disrupted	
	irregular / contorted	
	uniform	
	variable	

Table 4. Geologic Interpretation of Seismic Facies Parameters (from Mitchum et al., 1977).

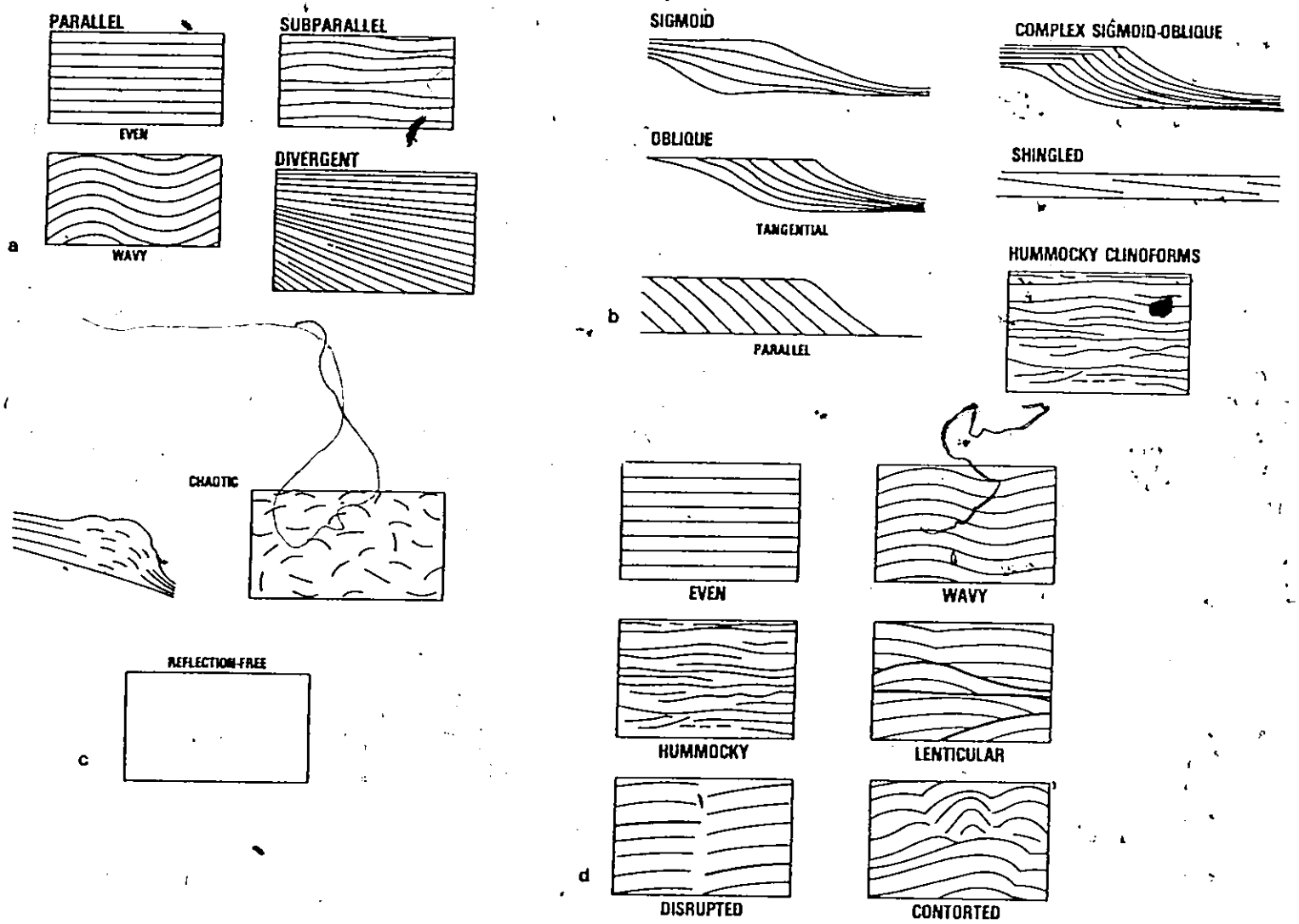

Figure 47. Seismic reflection configurations (from Mitchum et al., 1977).

7.2.2.2 External Forms

An understanding of three-dimensional external forms and areal associations of seismic facies units is important in their analysis. Table 5 and Figure 48 show important external forms: sheet, sheet drape, wedge, bank, lens, mound and fill. Mound and fill types can be divided into subtypes (Figure 49) (Mitchum et al., 1977).

7.3 Mass Transport Processes

Mass transport processes can be classified descriptively (e.g. Bouma, 1962; Walker, 1975, 1978) or genetically (e.g. Dott, 1963; Middleton and Hampton, 1976; Nardin et al., 1979). The scheme used here is the genetic one summarized by Nardin et al., (1979), which is based on a combination of mass movement, mechanical behaviour and sediment support mechanism. Three major processes are recognized: rockfalls, slides, and sediment gravity flows. Table 5 summarizes the mechanical behaviour, sediment support mechanisms, sedimentary structures and seismic characteristics of these types of mass transport. Figure 50 shows the sedimentary structures of gravity flow deposits.

7.4 Subaqueous Sediment Instabilities

In recent years considerable research has gone into the examination of the types and processes of sediment instability on subaqueous portions of deltas and in other submarine environments. The development of side-scan sonar and high resolution seismic techniques has led to

MASS TRANSPORT PROCESSES			MECHANICAL BEHAVIOUR	TRANSPORT MECHANISM AND SEDIMENT TRANSPORT	SEDIMENTARY STRUCTURES	ACOUSTIC RECORD CHARACTERISTICS
Rockfall				Freefall and rolling of clasts	Grain supported conglomerates, disorganized	Opaque, hyperbolae
Sediment gravity flow	Slide	Glide	Elastic	Failure along shear plane, little internal deformation	Essentially undeformed bedding, some deformation at base Flow structures, folds, faults	Reflectors continuous, undeformed, some contortion Humnocky surface Strong basal shear reflector
		Slump		Shear failure with rotation, little internal deformation		
	Mass flow	Debris flow	Plastic limit	Shear distributed through sediment mass, strength due to cohesion buoyant support	Matrix supported, random fabric, rip ups, inverse grading	Reflectors hyperbolic, irregular or smooth Few internal reflectors Mound or lens form
			Plastic			
		Grain flow	Liquid limit	Cohesionless sediment supported by dispersive pressure	Massive, a-axis parallel to flow, inverse grading	Unknown
	Fluidal flow	Liquified flow	Viscous fluid	Cohesionless sediment supported by upward displacement of fluid (dilitance) as structure collapses	Dewatering structures, sandstone dykes, flame -load structures	
		Fluidized flow		Cohesionless sediment supported by escaping pore fluid		
		Turbidity currents		Supported by fluid turbulence	Bouma series	Even layered, continuous onlapping reflectors Discontinuous reflector if channels present

Table 5. Mass Transport Processes with Associated Sedimentary Structures and Seismic Characteristics (from Nardin et al., 1979).

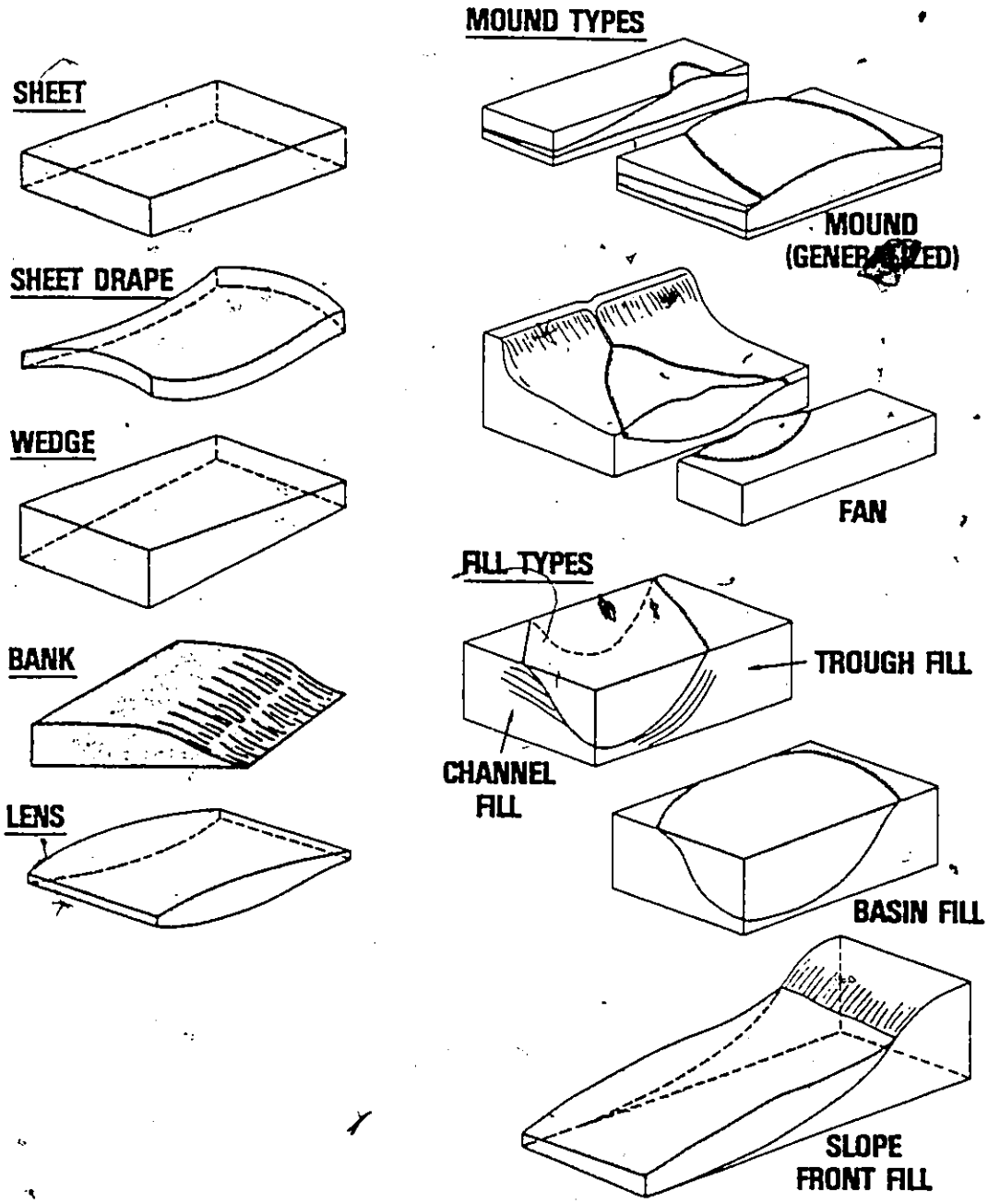

Figure 48. External forms of some seismic facies units (from Mitchum et al., 1977).

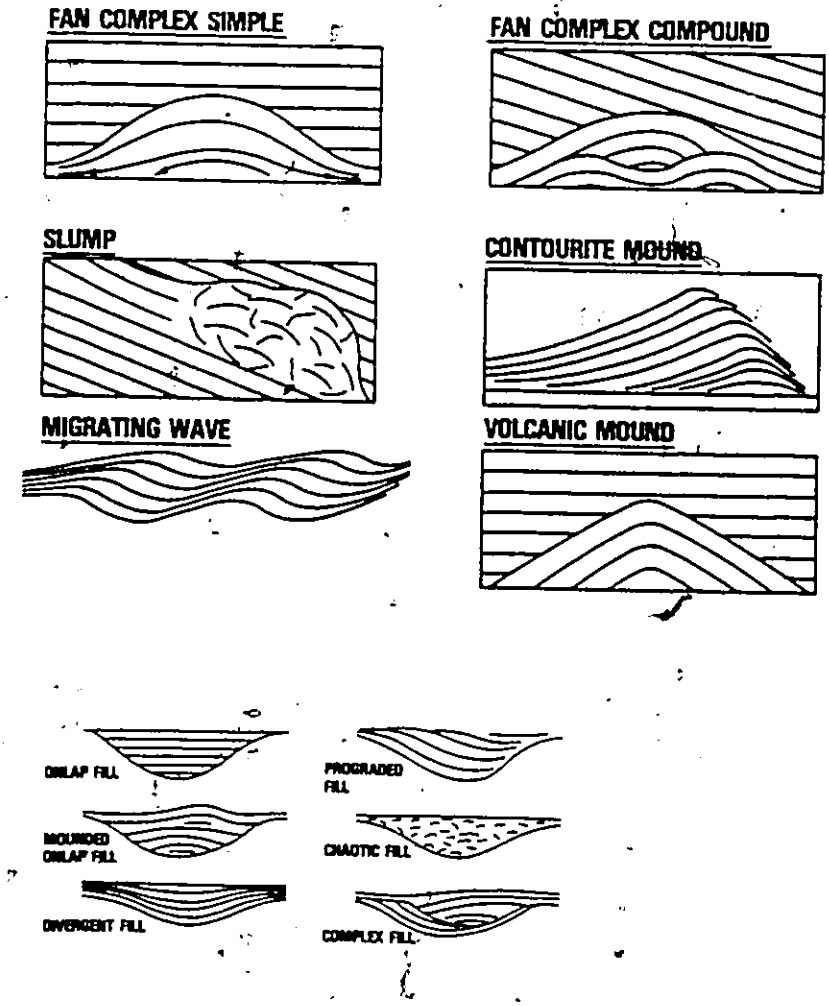

Figure 49. Some mounded and fill seismic facies units (from Mitchum et al., 1977).

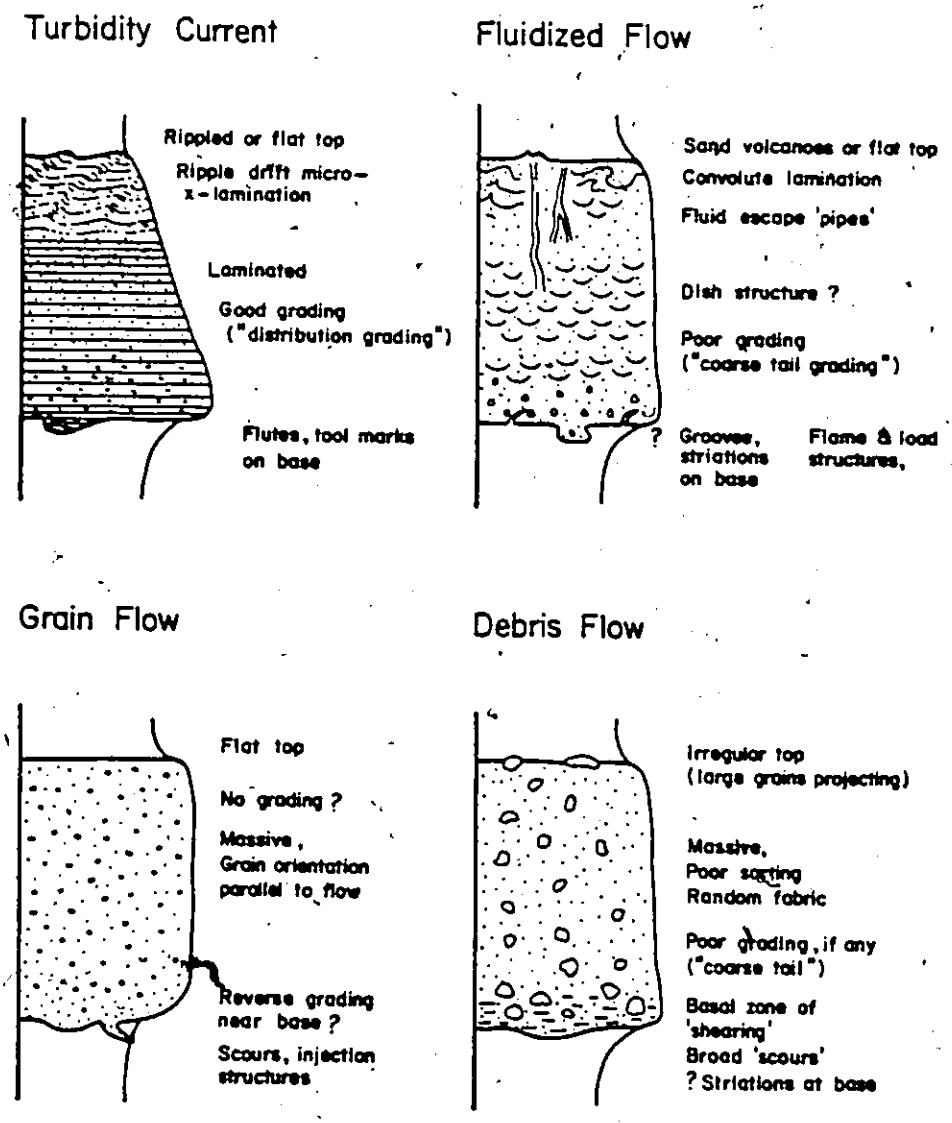

Figure 50. Sedimentary structures in gravity flow deposits (from Middleton and Hampton, 1976).

improved knowledge of the morphology and processes associated with subaqueous deformation (e.g. Prior and Coleman, 1978a, b, 1979; Prior et al., 1981). Recent reviews of delta instabilities can be found in Wright (1978) and Coleman and Prior (1980, 1981).

The discussion of sediment instabilities begins with a brief review of methods of determining sediment grain size and strength characteristics. A discussion of surface and shallow subsurface features and the factors involved in the generation of these features follows.

7.4.1 Sediment Characteristics

Grain size distributions can be described in a number of ways. The most common method is the determination of the mean (M_z) median (M_d) and standard deviation or sorting (σ_I) of the distribution using equations provided by Folk and Ward (1957). Sizes are expressed using the ϕ scale (Blatt et al., 1980).

The resistance to shear or the strength (s) of sediment can be expressed using the Coulomb equation for total stresses:

$$s = C + \sigma \tan \phi \qquad (30)$$

where C is cohesion, σ is the normal stress and ϕ is the friction angle. Cohesion can be produced by cementation of soils or, in clays, by electromagnetic forces between clay particles and water molecules. The normal stress is imposed by the weight of solids and water above a

point. Frictional strength is the resistance due to mineral particles in contact and is influenced by factors such as the number of point contacts in a volume of soil and by grain arrangement, size and shape (Selby, 1982).

In a saturated soil most cohesion is lost because there are no surface tension forces and part of the normal stress of the overburden is transferred from the soil fabric to the soil water. Thus for saturated soils the Coulomb equation for effective stresses is written as:

$$s = C' + (\sigma - u) \tan \phi' \qquad (31)$$

where C' and ϕ' are effective cohesion and the effective angle of friction respectively, and u is the pore water pressure.

A number of geotechnical testing methods can be used to determine the values of the Coulomb parameters. The shear vane method, for example, provides a total stress value of unconsolidated undrained shear strength, C_u, and the triaxial test can be used to determine values of cohesion and internal friction.

7.4.2 Surface Features

The three main types of surface features discussed below are translational slides (glides) rotational slides (slumps) and gullies (chutes). Some of the factors involved in the initiation and expansion of these features include gravity, retrogression, earthquake loading,

depositional loading, gas generation, rapid tidal drawdown, wave loading and creep.

7.4.2.1 Translational Slides

Most marine slides are translational in character, that is they have a geometry with the failure surface parallel to the sea bottom (Richards and Chaney, 1982) (Figure 51).

Translational slides can be considered in terms of effective stresses on an infinite slope, with the factor of safety, S, given by:

$$S = \frac{\text{resisting forces}}{\text{driving forces}} = \frac{C' + (\gamma Z \cos^2\beta - u) \tan \phi'}{\gamma' Z \sin \beta \cos \beta} \qquad (32)$$

where Z is the thickness of sediment above the slip surface, β is bottom slope, and γ' is the buoyant unit weight of the sediment: $\gamma' = (\gamma - \gamma_w)$ where γ is the saturated unit weight of sediment and γ_w is the unit weight of sea water. On the assumption that S = 1 (failure condition), it is possible to calculate the value of u needed for failure:

$$u = \frac{C' - S(\gamma' Z \sin \beta \cos \beta)}{\tan \phi'} + \gamma Z \cos^2\beta \qquad (33)$$

Retrogression

Retrogression refers to the upslope expansion of a slide as a slide block removes the lateral support of the sediment upslope of it

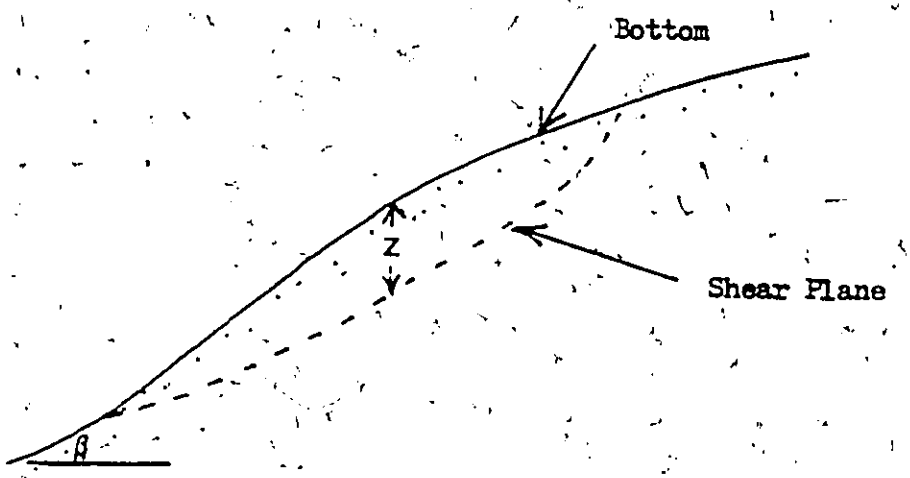

Figure 51. Geometry of a translational slide (from Selby, 1982).

(Selby, 1982). The criteria for retrogression of a slide can be expressed in terms of a subsidence ratio, $\Delta h/Z_1$, where Δh is the thickness of sediment in the back scarps above the slide surface (Figure 52) (Carson, 1977). When the observed ratio is greater than a critical value, then Carson (1977) concludes retrogression has taken place. The critical subsidence ratio is given by:

$$\frac{\Delta h}{Z_1} = 1 - \left(1 - \frac{4s}{\gamma Z_1}\right)^{1/2} \qquad (34)$$

where: Z_1 is the thickness of sediment from the top of the scarp to the slip surface.

Earthquake Loading

Cyclic loading associated with earthquakes can have two major effects in the reduction of slope stability: (i) potential for high pore water pressures or even liquefaction of sands as the abruptness of the earthquake shock renders impossible the drainage of pore water from the sediments, and (ii) introduction of a horizontal body force, a_x, expressed as some percentage of gravity (Almagor and Wiseman, 1982; Lutternauer and Finn, 1983). Morgernstern (1967) and Almagor and Wiseman, (1982) discuss the effects of the introduction of a horizontal force a_x, resulting from earthquakes, on slope stability. The factor of safety S_E for translational slides effected by earthquakes can be determined by adding the term $a_x \gamma \cos \beta$ to the denominator of Equation 32. Busch and Keller (1983) suggest that the resisting forces may be

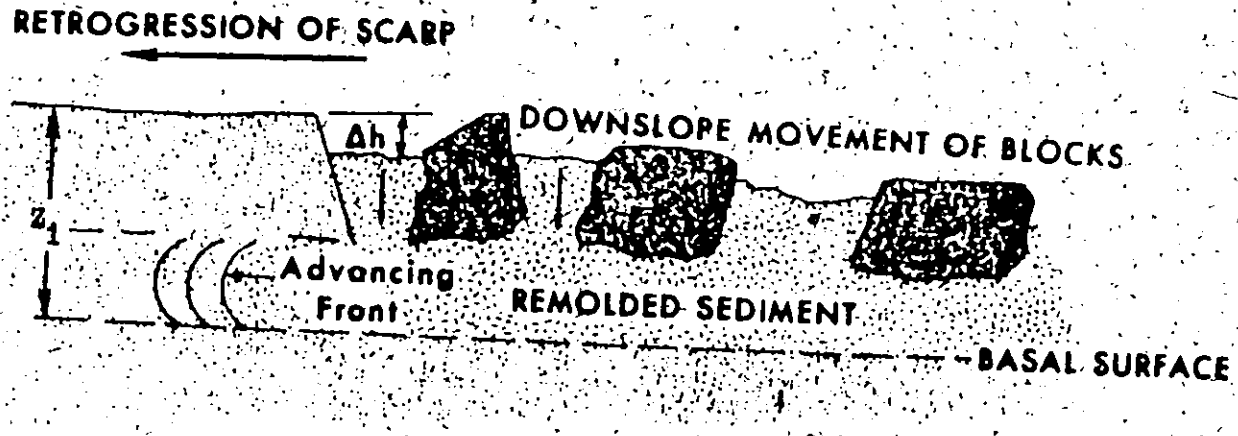

Figure 52. Upslope retrogression of a flow slide (from Prior et al., 1981).

decreased by earthquake loading, but this effect is not accounted for here.

Rapid Depositional Loading

Rapid depositional loading on a surface can increase pore water pressures in underlying sediments and reduce the factor of safety. Rapid loading is likely to be a result of debtis flows or slides (Prior and Suhayda, 1981). After loading the initial factor of safety, S, is reduced to S_L:

$$S_L = S\left(\frac{A}{A + 1}\right) \quad (35)$$

where A = Z/h, h being the thickness of the load.

Methane Gas Generation

Rapid biochemical and bacterial action on organic matter in sediments results in the generation of methane gas. At saturation levels the gas enters the bubble phase and may act to increase pore pressure in the sediments and reduce effective stress (Prior et al., 1981; Esrig and Kirby, 1977).

Rapid Tidal Drawdown

In areas affected by high tidal ranges, excess pore pressures

can be generated as the tide falls. If the sediment has low permeability, the movement of the water table is retarded as the tide drops. As a result excess pore pressures occur in the sediment at low tides (Terzaghi, 1956).

7.4.2.2 Rotational Slides

There appear to be two types of rotational slides (slumps) found in deltas, the difference between the two being largely that of scale. On the Mississippi delta small peripheral rotational slides are found near distributary mouths on bottom slopes of 0.2 to 1.0° (Figure 53). The surface of the slump block normally has extensive hummocky and irregular topography. The scarps of shear planes are not entirely linear features, but are composed of small arcuate slides reminiscent of subaerial rotational land slumps (Coleman and Prior, 1981).

Extremely large, deep seated rotational slides have been noted near the shelf edge of the Mississippi Delta (Figure 54). These are morphologically similar to the smaller arcuate slumps but are of a much larger scale.

The factor of safety for rotational slides, S_R, can be expressed using Bishops's (1955) method of vertical slices:

$$S_R = \frac{\Sigma[c'b + (\gamma \bar{Z} b - ub) \tan \phi']/M\alpha}{\Sigma \gamma' Z b \sin \alpha} \qquad (36)$$

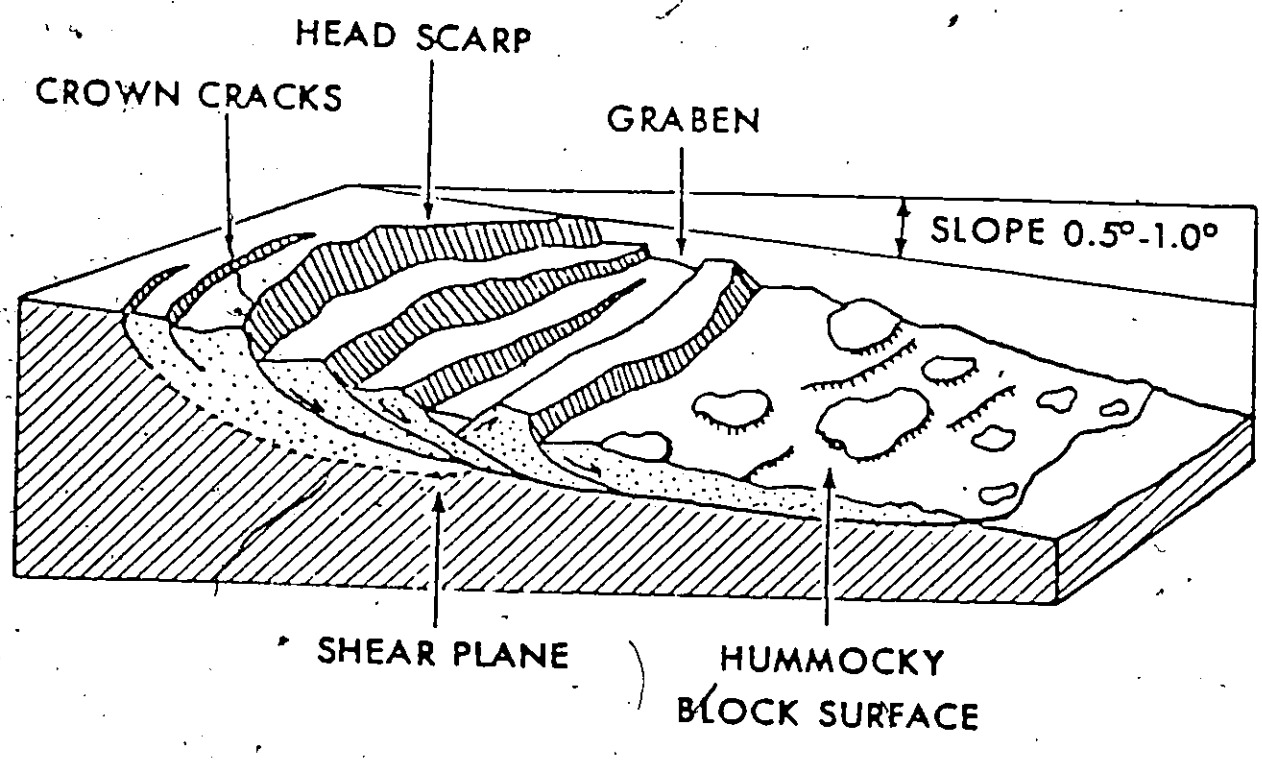

Figure 53. Morphology of a shallow rotational slide (from Coleman and Prior, 1981).

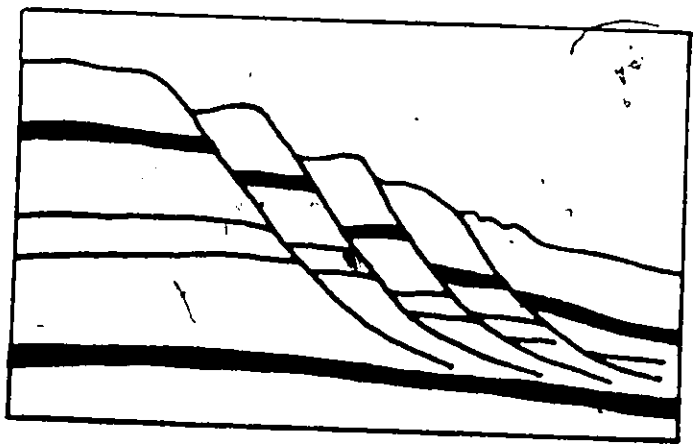

Figure 54. Large, deep-seated rotational slide (from Coleman, 1976).

in which: $M_\alpha = (1 + \frac{\tan \alpha \tan \phi'}{S_R}) \cos \alpha$

where b is the width of the vertical slice, $\bar{Z}$ is the average vertical thickness of the slice and α is the angle of the arc at the base of the slice. Earthquake effects resulting from horizontal accelerations can be determined by adding: $\Sigma\, a_x(\gamma \bar{Z} b) \cos \alpha$ to the denominator of equation (36). Other factors promoting instability, such as retrogression, depositional loading, gas generation and rapid drawdown likely effect rotational slides in a similar manner to translational slides.

Wave Loading

One of the effects of waves on delta sediments is to exert pressures on the surface of the sediment. Henkel (1970) provides a total stress analysis for the effects of wave pressure on slope stability. The magnitude of this pressure change, Δp, depends on the wavelength, L, the wave height, H, and the water depth, d. The sediment surface is assumed to be rigid and sliding along a circular arc with a maximum thickness Z_{max}. Wave pressures required to initiate failure can be determined from Figure 55. The term B is defined as:

$$B = \frac{s}{\gamma' Z_{max}} \qquad (37)$$

Values of Δp calculated for local waves can be placed on Figure 55 to determine if failure will occur.

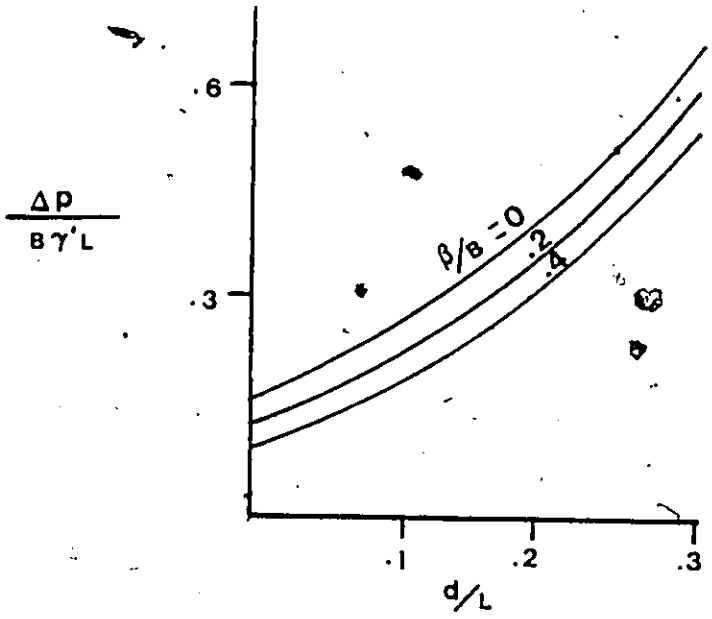

Figure 55. Relationship between minimum values of $\Delta p/B\ L$ and d/L for various values of β/B. The term Δp is the pressure change due to waves, γ' is the buoyant unit weight of sediment, L is wavelength, d is water depth, β is bottom slope and the ratio B is given in the text (from Henkel, 1970).

7.4.2.3 Gullies

Delta front gullies (chutes, sea valleys) have been described from many modern deltas such as the Mississippi (Prior and Coleman, 1978a, b); Fraser (Luternauer and Finn, 1983) and a number of fjord-deltas (e.g., Prior et al., 1981, 1983; Syvitski and Farrow, 1983). Each gully system typically consists of a narrow chute or channel that links a source area to depositional lobes on the seaward end. Prior and Suhayda (1981) suggest that each of these gully components can be examined and modelled separately. The source areas are commonly bowl shaped and appear to initiate as flow-slides that enlarge by retrogression. Carson's (1977) retrogression model (discussed earlier) appears to be applicable to these areas.

Chutes tend to be bound by sharp escarpments parallel or sub-parallel to one another. Chutes are often sinuous in form, may have adjacent gullies forming tributary systems, display natural levees and may experience sidewall slumping. Suhayda and Prior (1978) believe that debris flows are the primary mechanism of transport and that individual flows can be expressed in terms of Johnson's (1970) 'rigid-plug' model (Figure 56). Plug width, $2\,x_o$, thickness, y_o, and velocity, $\dot{w}$, are given by:

$$x_o = \frac{k}{\gamma \sin \beta} \left[\frac{a^2}{b_c^2} + 1\right] \qquad (38)$$

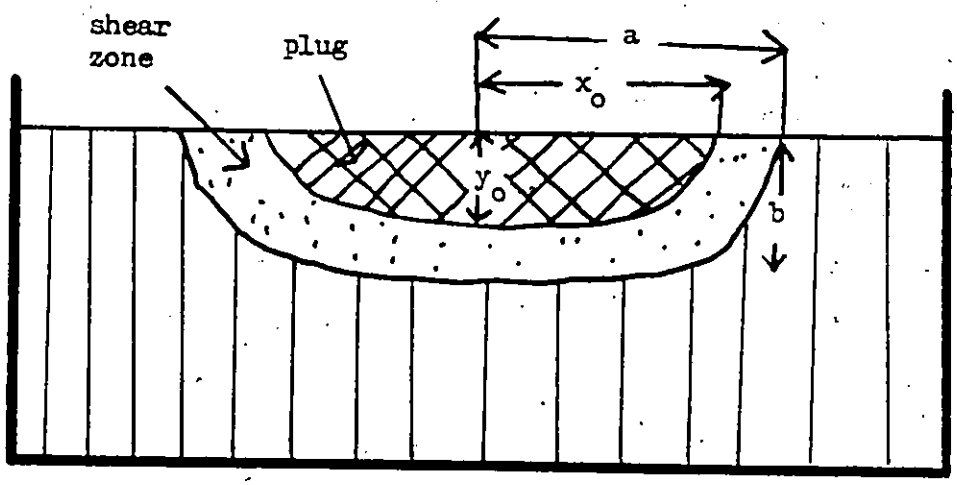

Figure 56. Parameters for debris flow plug geometry (from Prior and Suhayda, 1981).

$$y_o = \frac{k}{\gamma \sin \beta}\left[\frac{b_c^2}{a^2} + 1\right] \qquad (39)$$

$$\dot{w} = \frac{w^*(\gamma \sin \beta)(b_c^2)}{\eta_b} \qquad (40)$$

where k is debris strength, γ is the unit weight of sediment, β is slope angle, a is the half width of the chute, b_c is chute depth, w^* is a velocity variable and η_b is the Bingham viscosity (viscosity with a yield strength). The value of k can be determined from:

$$k = k'(a)(\gamma \sin \beta) \qquad (41)$$

where k' is estimated from Figure 57. Values of w^* can be determined from Figure 58, as a function of the strength variable k^*, where:

$$k^* = k'(a/b_c) \qquad (42)$$

Karlsrud and Edgars (1982) suggest that there are two major limitations of Johnson's solutions to submarine problems: (1) hydrodynamic forces on the top boundary are not included, which might be important if large velocities are generated, and (2) considerable time is needed to accelerate a flow to steady state and if slope geometry is not constant over large distances steady state velocities might never be reached.

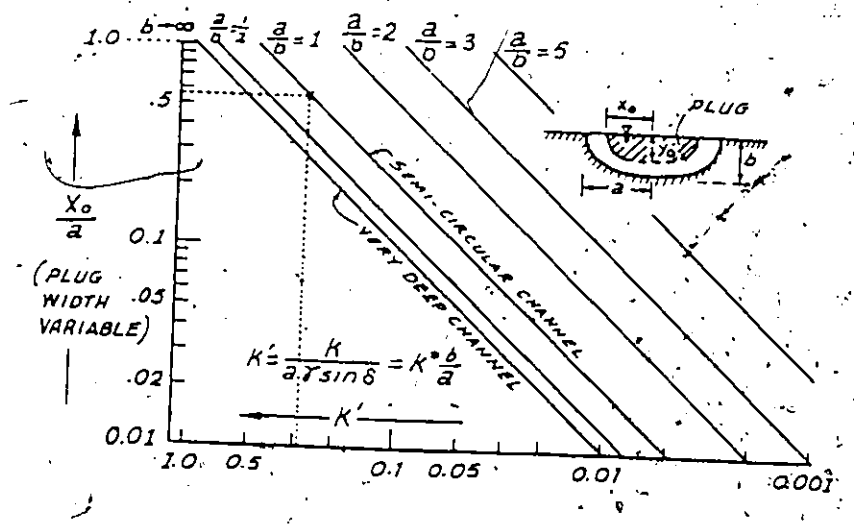

Figure 57. Graph relating debris flow properties to width of plug and shape of channel (from Johnson, 1970).

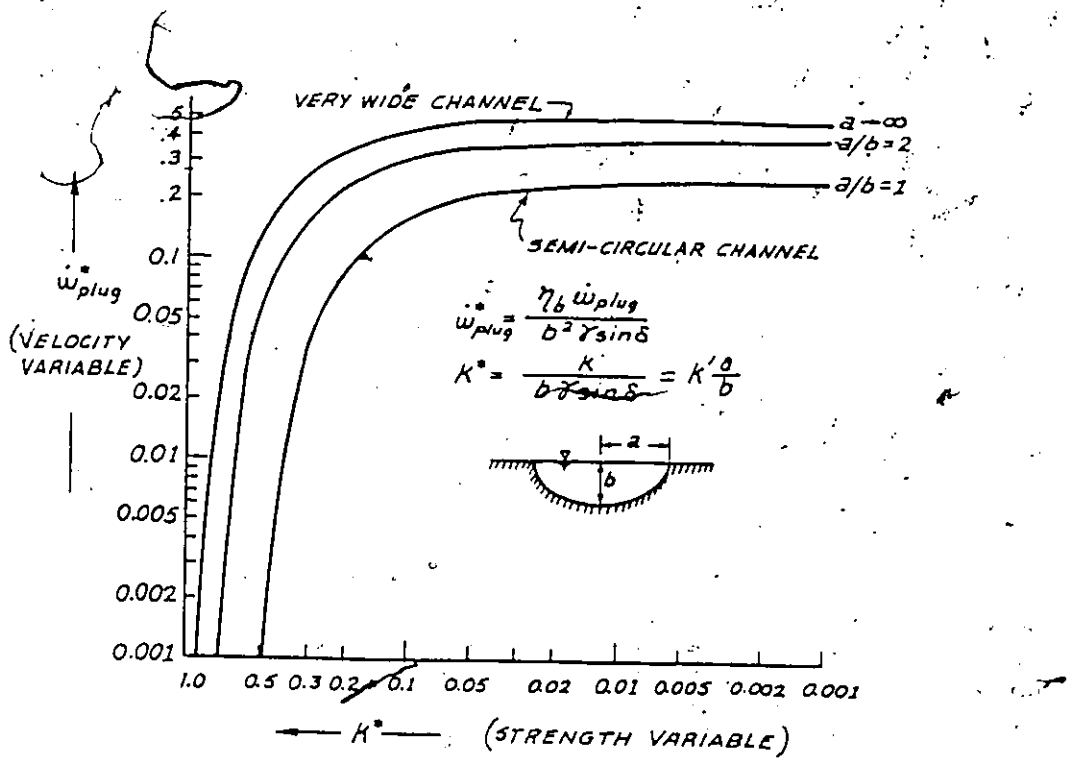

Figure 58. Graph relating debris flow properties to width of plug and shape of channel (from Johnson, 1970).

7.4.3 Shallow Subsurface Features

Three types of shallow subsurface features are discussed: faults, folds and mud diapirs.

7.4.3.1 Faults

A variety of fault types have been described on subaqueous deltas, including graben faults, growth faults and normal faults (Figure 59). In addition, more complex fault types have also been noted (Figure 60). Watkins and Kraft (1978) suggest that a number of forces may produce faulting, such as tectonic activity, hydraulic forces and gravity.

7.4.3.2 Folds

Folds have been noted on the Mississippi delta (Coleman and Prior, 1981) and are characterized by broad anticlines and tight synclinal troughs. Compressional forces associated with growth faults and downslope creep of sediments are probably important in fold formation (Coleman and Prior, 1981; Hill et al., 1982).

Hill et al., (1982) suggest that creep processes associated with folding can be modelled using Euler's column buckling theory and a Bingham model. Fold wavelength, F_L, can be determined from:

Graben Faults

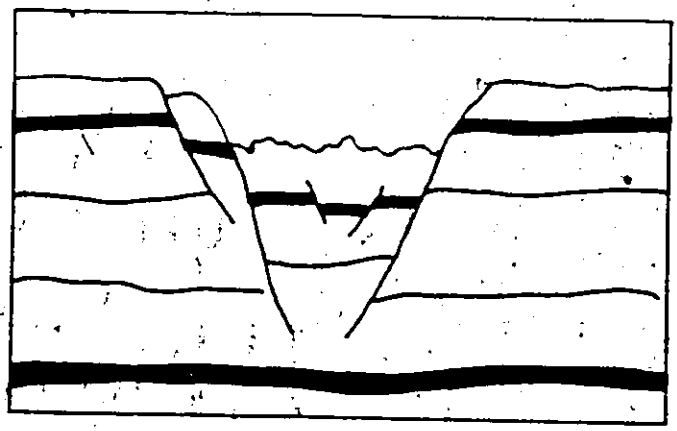

Normal Fault

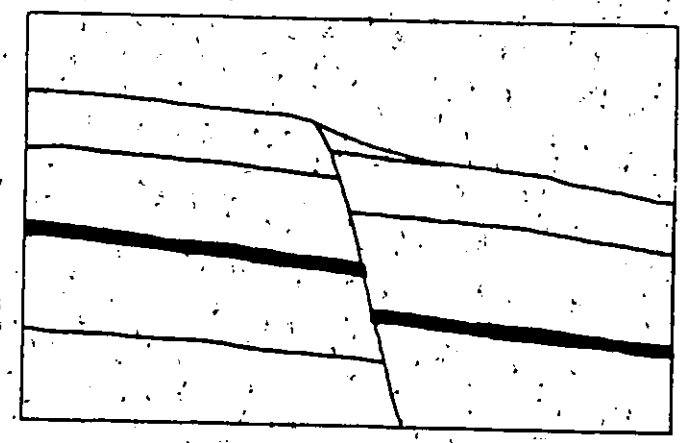

Growth Fault

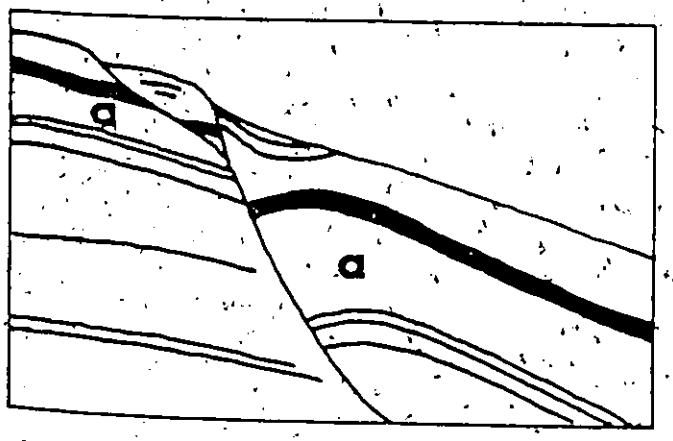

Figure 59. Fault types (from Coleman, 1976).

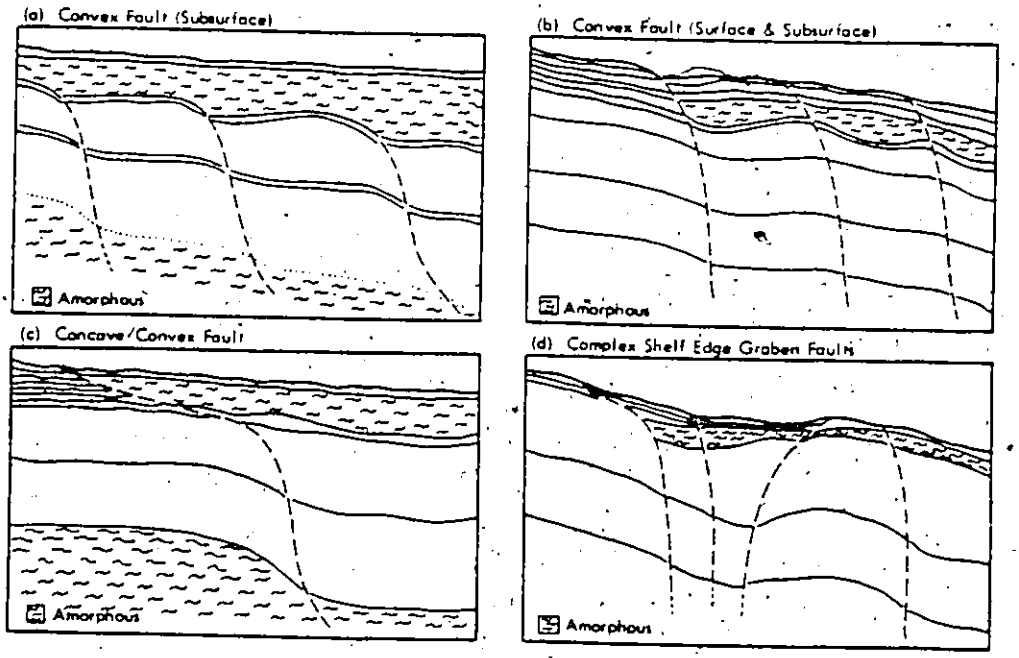

Figure 60. Fault types (from Watkins and Kraft, 1978).

$$F_L = \frac{\pi^2 Ee^2}{3\gamma' Z \cos \beta \sin \beta} \qquad (43)$$

where e is layer thickness, γ' is the buoyant unit weight of sediment, Z is the distance from the sea bottom to the layer and E is Young's modulus.

7.4.3.3 Mud Diapirs

Diapiric structures in deltas can intrude to near surface positions, arching overlying sediments (Figure 61a). Diapirs are common on the Mississippi delta and appear to be a result of distributary mouth bar sediments creating pressure on underlying clays, causing the latter to flow toward positions of least pressure (Coleman, 1976). In addition, diapirs may result at the base or seaward termination of large rotational slumps (Figure 61b) (Watkins and Kraft, 1978).

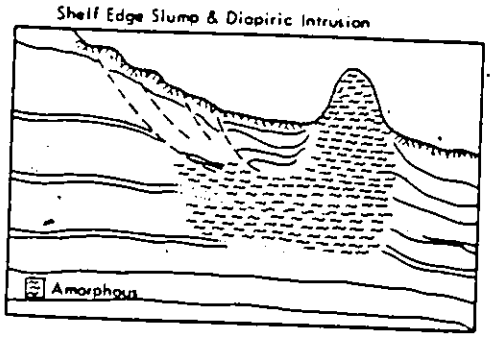

Figure 61. Diapiric intrusions (from Coleman, 1976; Watkins and Kraft, 1978).

CHAPTER 8

SEISMIC SEQUENCES

8.1 Introduction

This chapter examines the seismic sequences identified on lines 2, 3 and 8 (Figure 44) in North Bentinck Arm. On the basis of reflection terminations and seismic facies changes, two seismic sequences are proposed: the upper sequence is delta-related (examined in the following chapter) and the lower, which consists of 2 facies, is probably Pleistocene. This chapter begins with brief discussion of seismic velocities, followed by the proposed sequence boundaries and a description of the seismic facies associated with the lower sequence. Finally, the lower sequence is interpreted with respect to composition and history.

8.2 Seismic Velocities

Seismic refraction data (e.g. Bornhold, 1983) is not available for the North Bentinck Arm sediments. A velocity of 1500 m s^{-1} for the subbottom sediments (Bornhold, 1983; D'Olier, 1979) was chosen (Appendix 1) as being representative of glaciomarine and recent sediments.

8.3 Sequence Boundaries

The proposed sequence boundaries are presented on Figure 62, 63 and 64 which show the air-gun and pinger profiles for lines 8, 2 and 3 respectively. The deepest penetration is achieved on the air-gun record which is therefore more useful in determining sequence boundaries. Side wall reflections on lines 2 (Figure 63) and 3 (Figure 64), make the air-gun records of little interpretive value. The pinger records are better suited to near-surface detailed descriptions of seismic facies.

The lower sequence outcrops near the mouth of the fjord near Tallheo Point and in the central reaches in the Whiskey Bay area (Figure 44) on lines 8 and line 2. On line 3 this sequence appears to outcrop in the Bachelor Point and possibly Big Bay areas (Figure 44). In the Tallheo Point area, the upper sequence terminates rather indistinctly on the inclined eastern and western slopes of the outcropped lower sequence as an onlap.

In subsurface areas near Tallheo Point, the boundary is defined by a strongly reflective surface, indicating an unconformity and possible velocity-density contrast, and a facies change at a subottom depth of around 50 m. Towards the east on lines 8, 2 and 3, this reflective surface is obscured by sidewall reflections. The surface is picked up again as an erosional (?) unconformity truncating underlying lower sequence beds as a toplap at a subbottom depth of 50-55 m on line 8.

In the Whiskey Bay area the position of the subsurface boundary

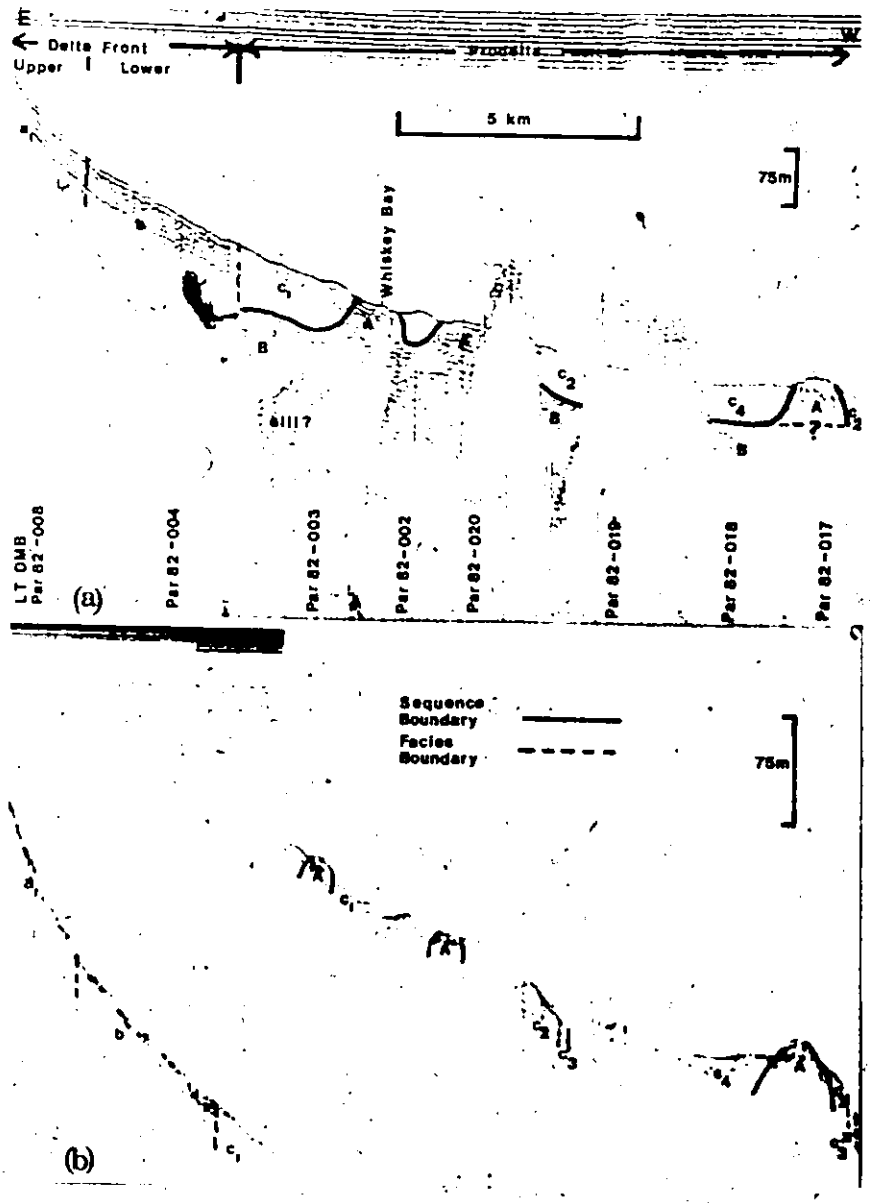

Figure 62. Seismic line 8: a airgun, b pinger.

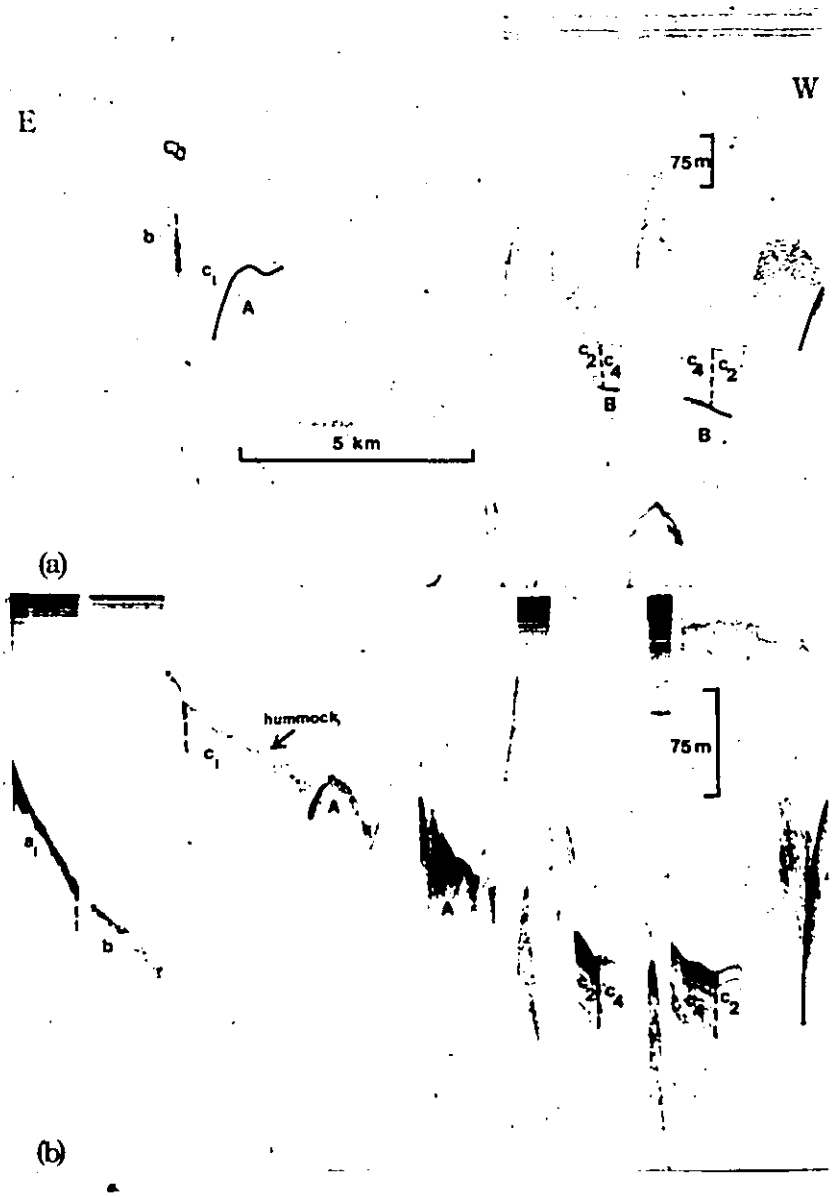

Figure 63. Seismic line 2: a airgun, b pinger.

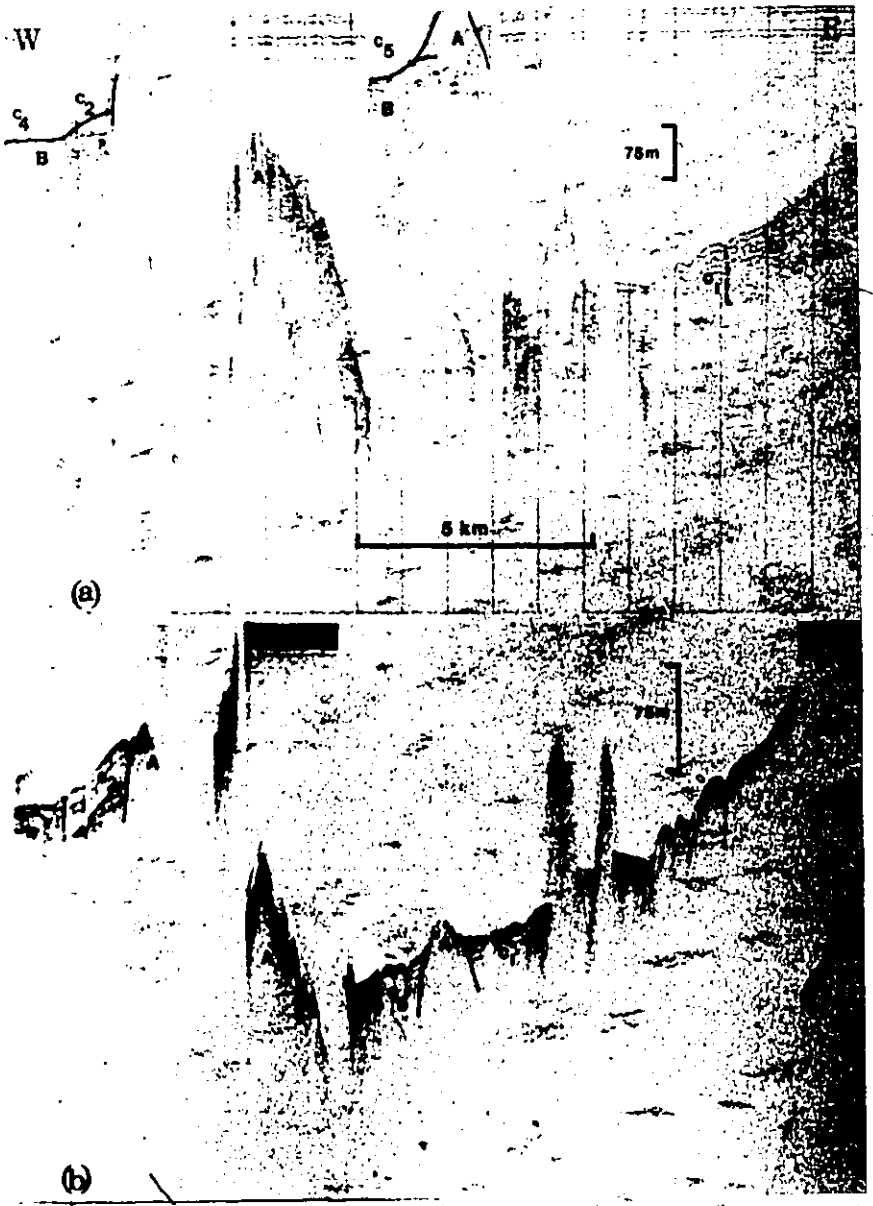

Figure 64. Seismic line 3: a airgun, b pinger.

is unclear, and on lines 2 and 3 considerably confused by sidewall reflection. On line 8 the most probable boundary in this area is as shown, and this interpretation is supported by facies evidence (discussed below). The air-gun record shows that the upper sequence terminates against inclined surfaces of the lower sequence as an indistinct baselap and is roughly concordant with the more horizontal surface of the lower sequence.

The lower sequence in the Whiskey Bay area may be subdivided into two sequences. The uppermost sequence boundary was just discussed. Another boundary may exist at 100-130 m beneath the sea floor (the 'sill' surface on Figure 62a). This surface is a strong reflector and is associated with a distinct facies change. The overlying sediment appears to onlaps with this boundary surface.

8.4 Lower Sequence Seismic Facies

Two distinct lower sequence seismic facies can be identified on lines 8, 2 and 3: Facies A and Facies B. Due to intense sidewall reflection on lines 2 and 3, only portions of the air-gun records are available for interpretation.

8.4.1 Facies A: Mounded Hummocky-Chaotic

This facies constitutes the outcrops at Tallheo Point and Whiskey Bay and perhaps the more deeply buried (sill) surface at Whiskey Bay (Figures 62, 63, 64). On individual lines this facies has a distinct

mounded external form in two-dimensions. The mounds appear on both lines 8 and 2, at Tallheo Point and on all three lines at Whiskey Bay, suggesting that these 'mounds' may in fact be parts of two continuous mounds or ridges that extend across the fjord.

Facies A is opaque to 3.5 kHz energy and produces a black to grey reflection on these records. The air-gun, however, penetrates these surfaces and reveals some of the reflection configuration (Figure 65). The reflectors are strong (black), with a hummocky, chaotic configuration with poor continuity and amplitudes of 2 to 2.5 m. The reflectors terminate with mound sides as a toplap and are generally concordant with the upper surface of the mound. Facies A is bounded to the east and west by upper sequence facies and possibly laterally (N-S) and below Facies B.

8.4.2 Facies B: Trough Fill Subparallel/Hummocky

Since Facies B is entirely subsurface, it is apparent only on the air-gun records. This facies has a trough fill external form with a relatively flat to gently westward dipping uneven surface (Figures 62, 63, 64). Reflectors vary from strong (black) to weak (grey) with a roughly subparallel, slightly hummocky, configuration. Reflection amplitude is variable (2-6 m) and continuity moderate (Figure 66). Reflectors are generally concordant with the upper surface of Facies B, except on line 8 where there appears to be an erosional truncation. This facies is overlain by upper sequence sediments and possibly grades laterally or is overlain by Facies A.

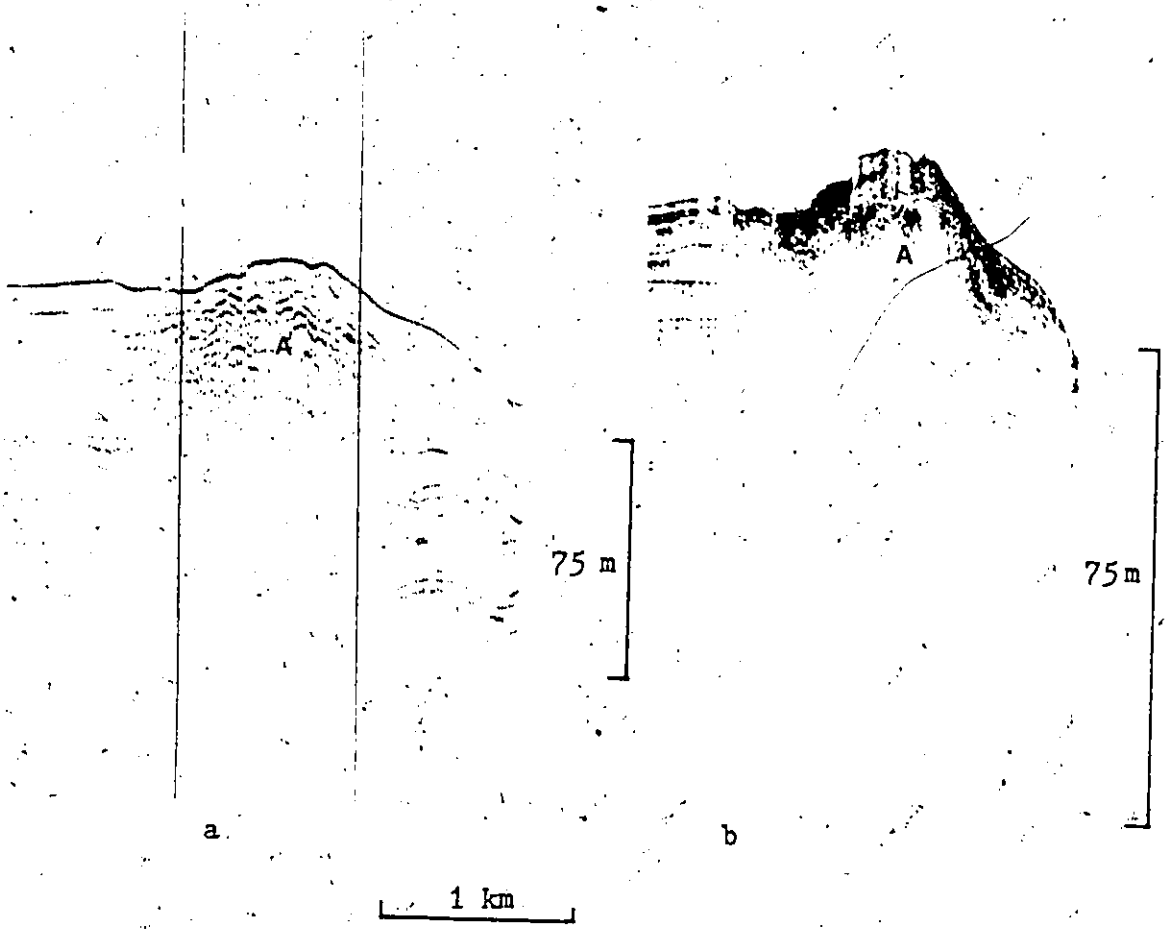

Figure 65. Facies A: a airgun, b pinger.

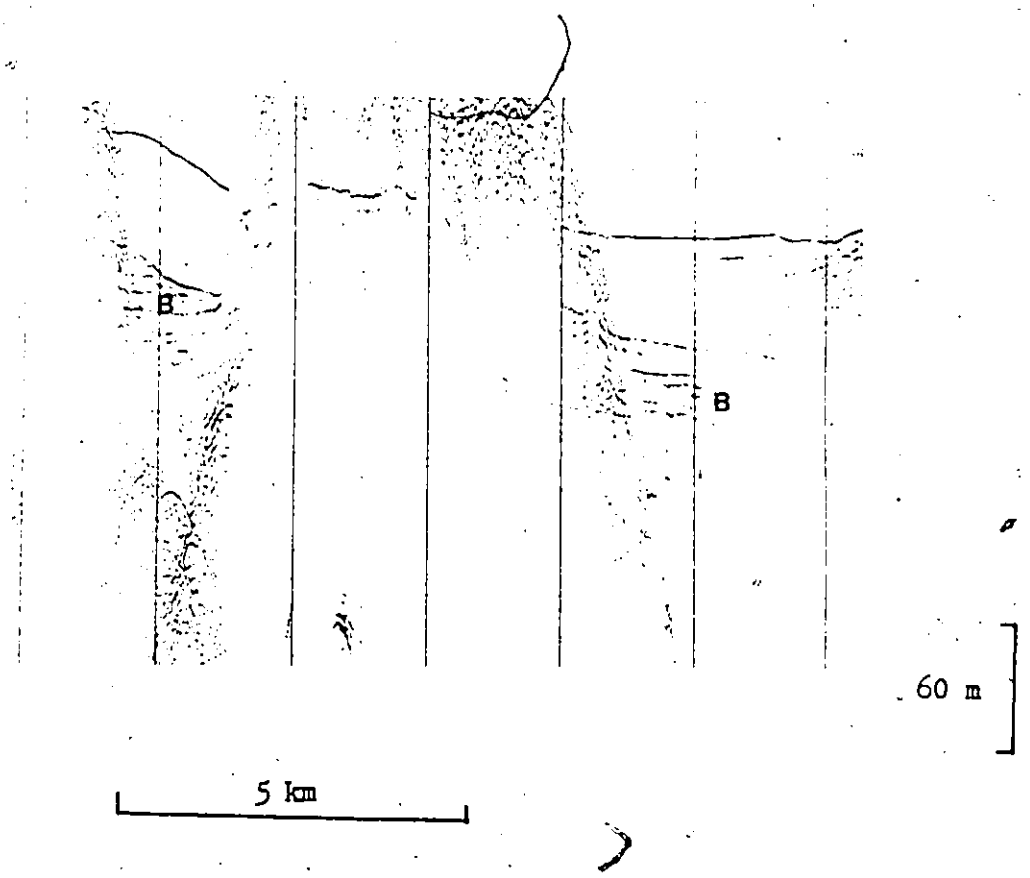

Figure 66. Facies B from airgun record.

8.5 Interpretation

Although no samples were recovered from the outcrops of the lower sequence in North Bentinck Arm, surface grabs were obtained from similar features in nearby Dean Channel. The Dean samples consist of very stiff, massive inorganic grey clay with fragments of granule-sized particles supported by the matrix.

Two distinct possibilities exist for the origin and hence history of the lower sequence: (1) that Facies A and B are Pleistocene features associated with the retreat of Late Wisconsin (Fraser Glaciation) ice; (2) that the sediment composing the lower sequence is glaciomarine in origin, but that Facies A is of diapiric origin and is forming contemporaneously with progradation of the delta.

8.5.1 Pleistocene Hypothesis

It seems clear from the stratigraphic position, sequence boundary and facies characteristics that Facies B predates the upper, delta- related sequence and as such is likely Late Wisconsin (Fraser Glaciation) in origin. The good penetration achieved by the air-gun indicates fine-grained material, the amplitudes suggest relatively thick bedding and the moderate continuity suggests relatively continuous strata. The subparallel component of the reflection configuration indicates relatively uniform deposition laterally (E. to W.) and the hummocky component may suggest some variation in depositional process

(deposition from suspension and gravity flows?), ice contact or deformation.

Based on the above considerations, Facies B is interpreted as being glaciomarine in origin, perhaps 'aquatill' (Edwards, 1980). The most likely mode of deposition would be from a floating ice shelf, although deposition from grounding ice is also a possibility.

Air-gun penetration into Facies A is somewhat less than Facies B, perhaps suggesting denser or coarser material in the former. The fact that there is penetration, however, points to a relatively fine-grained texture. The amplitudes of reflectors in Facies A suggests thinner bedding than in Facies B, and the poor continuity indicates discontinuous strata. The hummocky, chaotic configuration is an indication of highly variable depositional processes, ice contact, or extensive deformation and contortion of beds. The mounded-ridged external form, rising as a prominence above the sea floor, indicates a higher rate of deposition than in the adjacent or underlying Facies B units.

Facies A can be interpreted as an end moraine, associated with the retreat of Fraser Glaciation ice towards the east. The mode of moraine formation might be similar to that proposed by Edwards (1980) for submarine ridges, with debris accumulating at the grounding margin of floating glaciers. Similar features interpreted as moraines have been described in Douglas Arm (Bornhold, 1983).

8.5.2 Diapiric Origin of Facies A

In this hypothesis, the interpretation of Facies B is essentially the same as in the Pleistocene hypothesis, that it is glaciomarine in origin. Facies A, however, is now interpreted as a diapiric intrusion rather than as an end moraine. Mud diapirs described elsewhere (e.g. Hill et. al., 1983; Coleman, 1976) have similar chaotic internal characteristics.

The main evidence suggesting a diapiric origin is that there is little upper sequence sediment on the surface of these features. One would expect a sediment drape over a relict Pleistocene feature, especially since core evidence from prodelta areas (discussed below) indicates that recent sedimentation is dominated by deposition from suspension rather than by bottom-hugging gravity flows. An active diapir would not necessarily have a sediment cap.

If we assume a diapiric origin for Facies A, the implication is that Facies B sediments are mobile and have been 'squeezed' and migrated to form the diapirs. The necessary pressures required to mobilize the sediment would be provided by the weight of overlying delta sediments (Coleman, 1976) or by slumping of prodelta sediments (Watkins and Kraft, 1978).

8.5.3 Discussion

As mentioned earlier, there are arguments favouring both the

morainic and diapiric origins for Facies A. The morainal interpretation seems most likely, primarily because of similar interpretations from other sites and the across fjord extent of the mound or ridge. The lack of an upper sequence sediment cap is problematic, although similar 'capless' features have been interpreted as moraines by others (e.g. Bornhold, 1983). It may be that tidal currents are accelerated over the morainic ridges, restricting deposition on these features.

CHAPTER 9

DELTA FRONT

9.1 Introduction

As mentioned earlier, the subaqueous portion of the delta is divided into two main components: the delta front and the prodelta. This distinction is made primarily on the basis of grain size trends and seismic penetration. Wright (1978) suggests that delta-front areas should be composed primarily of bedload (sand and larger) and the prodelta primarily of material deposited from suspension (silts and clays). Figure 67 shows the seaward trends in grain size on the delta, along seismic line 8, with sample locations presented on Figure 62b. The exact values of the grain size parameters for the silt and clay sized sediments are somewhat in error because, for unknown reasons, the hydrometer analyses overestimated the % remaining in suspension. However, there is a clear correspondence between the sudden decrease in mean grain size from sand at Par 82-004 to silt at Par 82-003 and the sudden increase in seismic penetration between these samples on line 8. Thus the delta front, characterized by sandy sediment and little seismic penetration, extends to a distance of approximately 4,000 m seaward of the delta plain (Figure 67) and to a water depth of 275 m. The prodelta extends from 4,000 m to the moraine at the end of the fjord and to water

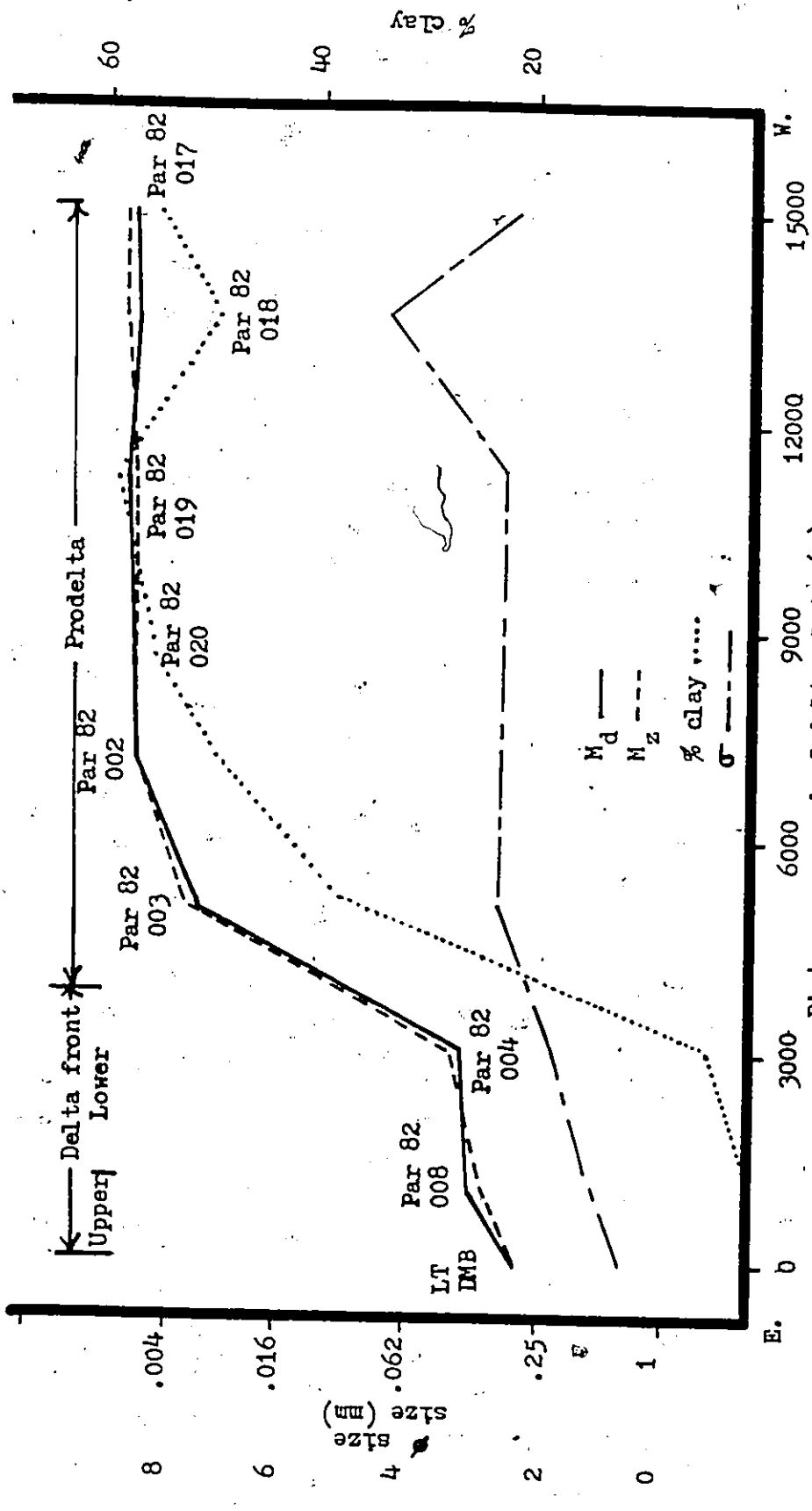

Figure 67. Grain size trends along delta on seismic line 8.

depths in excess of 400 m. This chapter examines the delta front and chapter 10 examines the prodelta. Seismic facies, morphology, grain size characteristics, geotechnical characteristics and sediment instabilities are discussed for each zone.

The delta front can be subdivided into two areas, the upper delta front and the lower delta front, on the basis of seismic facies and morphology. The upper delta front extends to depths of 80 to 125 m and the lower delta front occupies the remainder of the delta front area. The following discussion of the delta front is separated into two main parts, a sedimentologic-morphologic discussion and a geotechnical-stability analysis. The sedimentologic portion contains seismic facies, morphology and sediment grain size characteristics. The second portion includes the geotechnical characteristics of the sediment and instability analyses. Each part contains data from both the upper and lower delta front areas.

9.2 Sedimentology and Morphology

The seismic facies of the delta front were determined from lines 8, 2 and 3 and the 3.5 kHz records accompanying the sidescan tracks (Figure 44). Morphology was assessed primarily by echo-soundings (Figure 43) and sidescan records (Figure 44), and to a lesser degree from seismic records. Grain size distributions were determined from sieve and hydrometer tests of grab samples and calculation of Folk's (1957) statistical parameters.

9.2.1 Seismic Facies

Three seismic facies have been identified for the delta front (Figures 62, 63, 64). Facies a_1 - smooth/hyperbolic opaque and facies a_2 - hummocky/hyperbolic opaque apply to the upper delta front. The reason for the differences in these facies is that a_1 is found on downslope running lines and a_2 on across slope running lines. Facies b, - hummocky/hyperbolic opaque, applies to the lower delta front.

Facies a_1 - Smooth/hyperbolic opaque

The upper delta front varies in slope from oversteepened areas near the mouths of distributaries (15°) to average values of around 4° down to 80-125 m depths. The seismically opaque surface is generally smoothest and best defined (darkest) on the upper portions of slopes, becoming slightly hyperbolic and less well defined (lighter) lower on the slope (Figure 68). The hyperbolae in this zone are generally small-scale, low amplitude (~2 m) features. This facies is noted on all profiles on the delta front and usually grades subtly into delta front facies a_2.

Facies a_2 - Hummocky/hyperbolic opaque

The 3.5 record associated with sidescan track I (Figure 44) across the delta front shows a very irregular, hummocky opaque record with some large hyperbolic reflectors (Figure 69). Single hummocks-hyperbolae may be as much as 11 m in height. Individual gullies (dis-

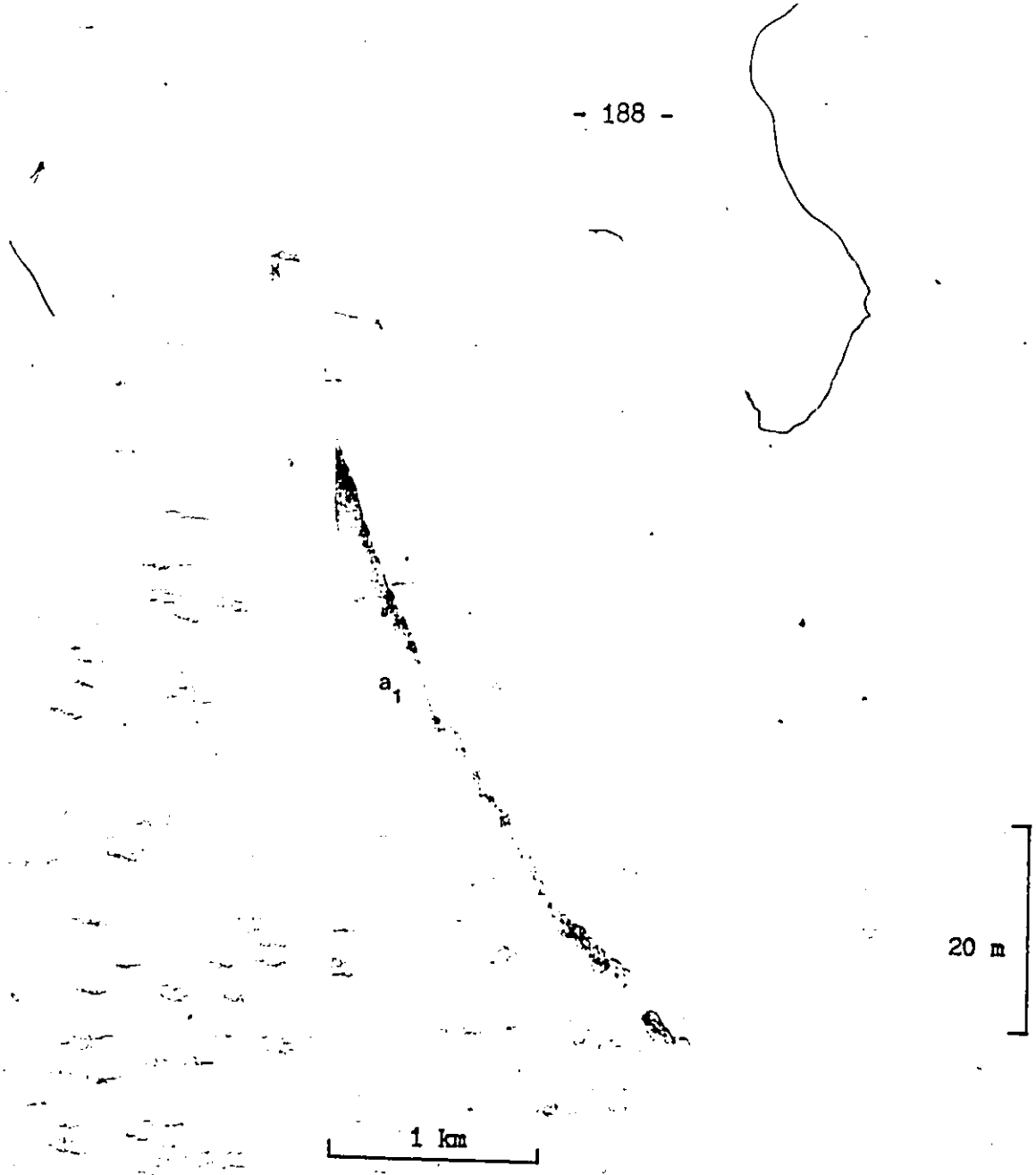

Figure 68. Seismic facies a_1 from line 8 pinger record.

Figure 69. Seismic facies a_2 from pinger record along sidescan track I.

cussed below) are not apparent at the 80 m depths recorded by this profile, because the gullies become less well defined at these depths. Facies a_2 is bounded downslope by lower delta front facies.

Facies b - Hummocky/hyperbolic opaque

Both the downslope (lines 2, 3, 8, and the 3.5 kHz record associated with tracks A-H) and the across slope (3.5 kHz with sidescan track J) seismic records have a similar seismic facies, facies b. Slopes in the lower delta front tend to be lower than those in the upper delta front, with typical values of 2.2-4°.

This facies is opaque to both air-gun and 3.5 kHz frequencies, has a surface with well developed hummocks and large scale (5-10 m) hyperbolic reflectors (Figure 70), and is similar to upper delta front facies a_2. In general, the hyperbolae tend to disappear and individual hummocks become more distinct farther downslope. On some profiles a small amount of subbottom penetration occurs in downslope areas of this zone. Facies b terminates abruptly with prodelta facies c_1 downslope.

Interpretation

The opaque nature of the delta front seismic records is a reflection of the sandy nature of the sediment. The smooth reflectors of facies a_1 indicate an even sediment surface in a downslope direction on the upper delta front. The hyperbolic reflectors of facies a_2 and b are suggestive of a very rugged, uneven surface across the slope on the

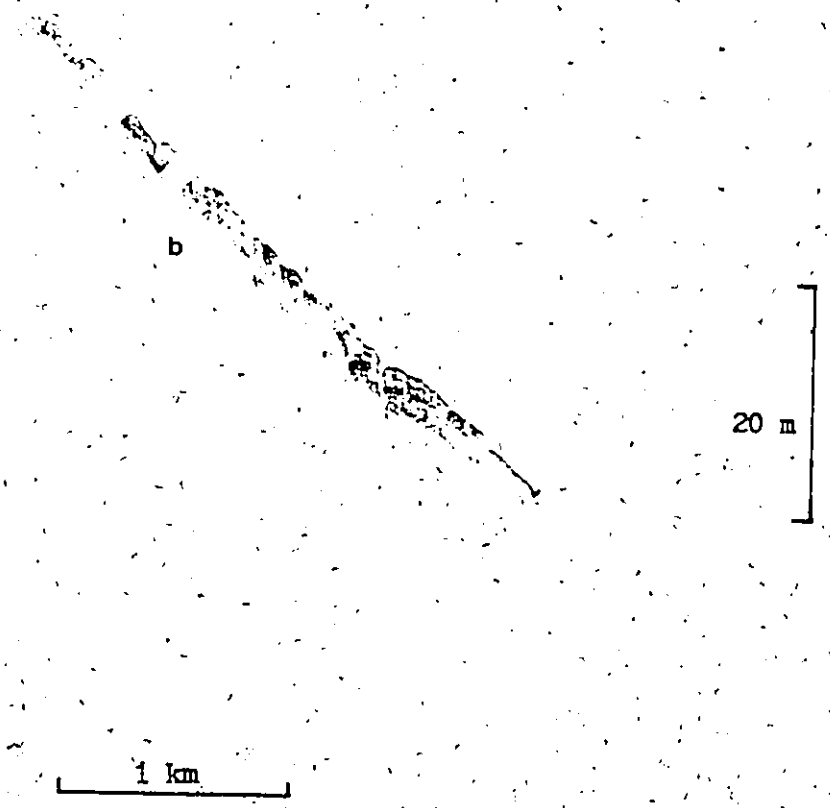

Figure 70. Seismic facies b from line 8 pinger record.

upper delta front and downslope on the lower delta front. As discussed below, these irregularities are related to slides and gullies. The hummocks of facies a_2 and b indicate a larger-scale hummocky surface, again related to slides and gullies.

9.2.2 Morphology

There are three sources of morphologic information for the delta front. A bathymetric contour map (Figure 71), based on detailed soundings taken in 1954-56 of the delta front and proximal prodelta zones, shows subaqueous slopes and the positions and extents of slope gullies. Six across slope echograms (Figure 43) provide the most detailed information of the upper delta front. The sidescan sonar (Figure 44) tracks are primarily from the lower delta front. The following description of delta front morphology is divided into upper delta front and lower delta front zones.

Upper Delta Front

The dominant features apparent on the echograms (Figure 72) are downslope trending gullies or chutes, as they have been termed by Prior et al (1981). The chutes originate on the upper delta front near the break in slope between delta plain and delta front as V-shaped notches eroded into the active distributary mouth bar of the North Channel, or as bowl-shaped depressions to the south of the North Channel. On the extreme northern edge of the delta, away from active distributaries, the chutes are narrow (40 m), shallow (3-5 m deep), and terminate at approx-

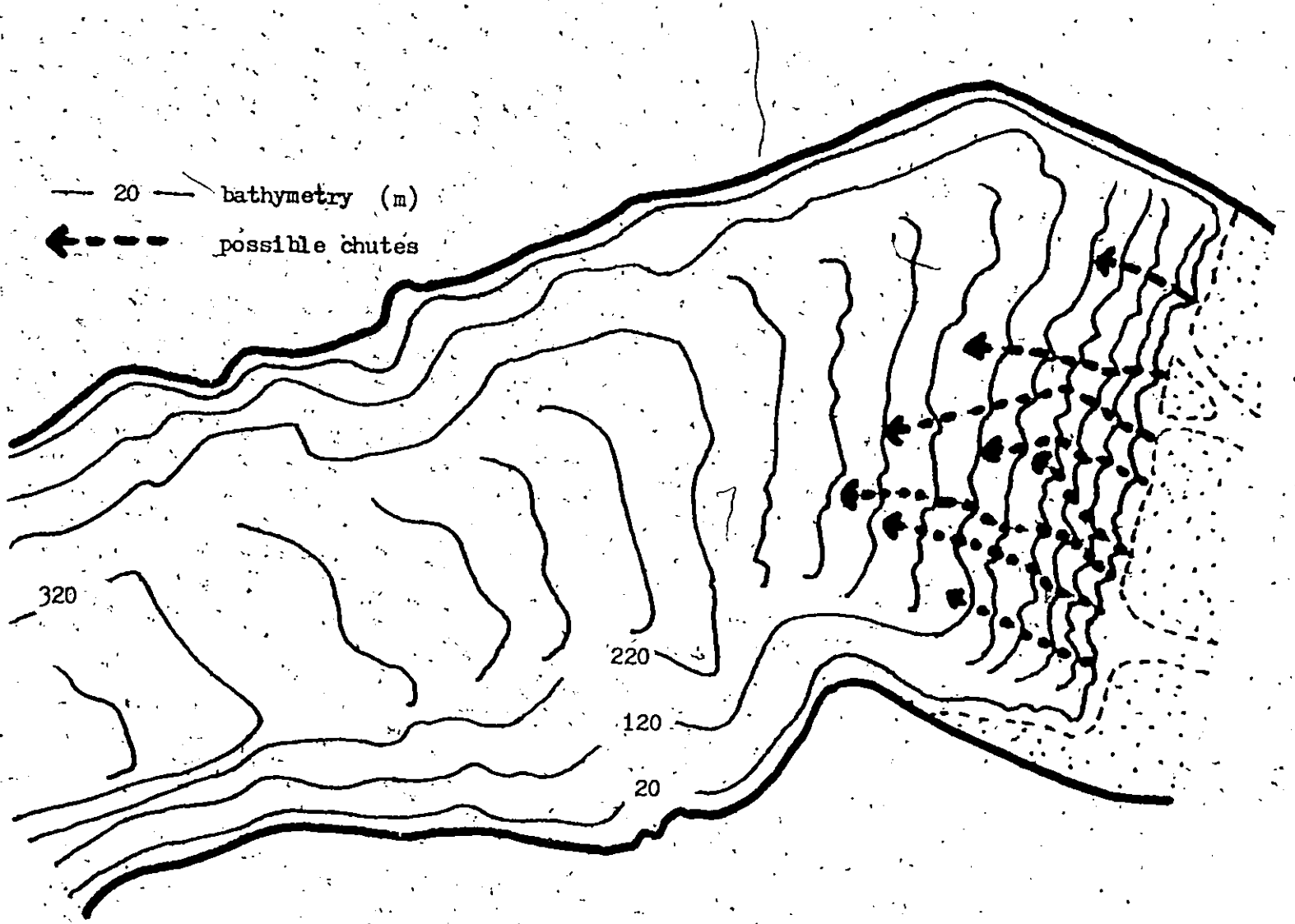

Figure 71. Bathymetric contour map of subaqueous delta, based on 1954-56 soundings.

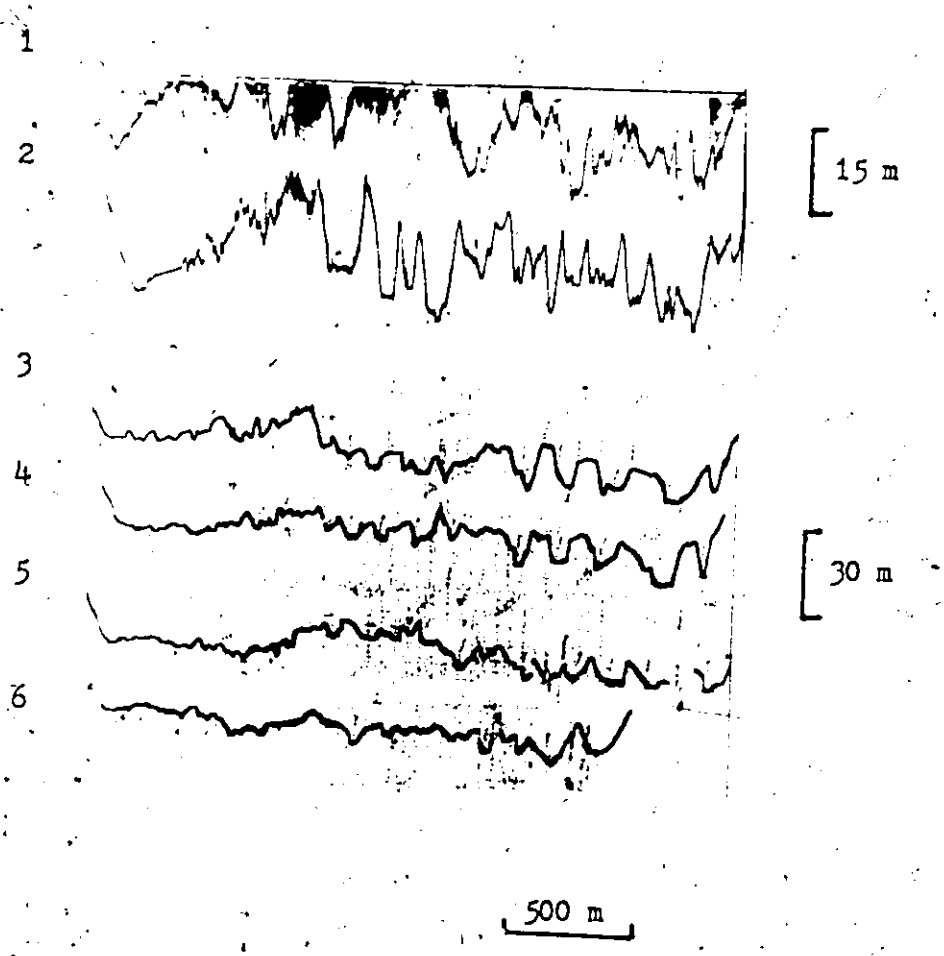

Figure 72. Echograms 1 to 6.

imately 80 m depths. On the rest of the upper delta front the chutes are wider (maximum of 180 m, profile 2) and eroded up to 20 m into the upper delta front surface. The chutes become shallower (8-10 m maximum, profile 5), narrower (150 m maximum, profile 5) and less well defined farther downslope and the surface becomes more hummocky (profiles 5 and 6). Chute bottoms are typically flat to slightly assymetrical in cross-section and in upslope areas commonly display a hummocky morphology with two distinct mounds (levees?) flanking a lower area (Figure 73). Inter-chute zones of the upslope reaches (profiles 1 and 2) tend to be sharp-crested, indicating the chute walls have migrated into one another. Farther downslope (profiles 3-6) interchute areas are more round-crested to flat and hummocky.

Lower Delta Front

Sidescan sonar tracks were run downslope (A-H) and across slope (I and J) on the lower delta front (Figure 44). The records of tracks I and J are of very poor quality and of little interpretive value. The track A to H records also suffer from some quality problems, but provide a good, if somewhat incomplete, indication of bottom features.

Figure 74 is a 'mosaic' produced from identical scale photographs of the A to H sonagraphs. It must be stressed that this is not a scale-corrected mosaic. Lateral overlap along the edge is assumed to be 25 m on each channel. The down slope scale is assumed equal to the cross slope scale and similar for all tracks. From this 'mosaic' at least three types of features can be identified: (1) gullies or chutes,

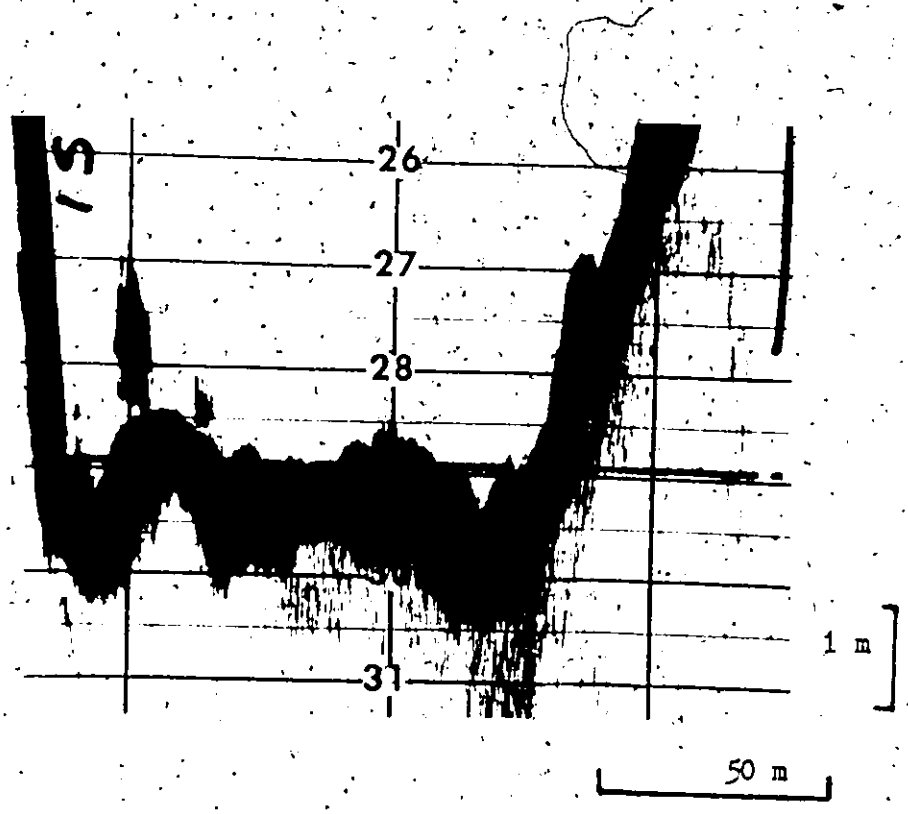

Figure 73. Chute bed from echogram 2.

(2) depositional zones and (3) arcuate rotational slides.

There are at least 3 distinct types of gully or chute features apparent on the sonagraphs: (1) side wall fan delta chutes (2) small, local chutes, and (3) large, sinuous chutes.

A series of deeply incised chutes associated with the Nieumiamus Creek fan delta at Tallheo appear near the downslope end of track A and may extend as far south as the right channel of track B (Figure 74). The chutes occur as dark streaks trending in a N.W. - S.E. direction down the fan-delta slope (Figure 75). The dark tone of these chutes may reflect the probable coarse (sand and gravel) composition of the chute beds.

Individual fan-delta chutes are on the order of 50 m wide near the centre of track A and may become narrower upslope. Chute length is difficult to determine because of the unclear nature of the record on the left channel of track A. Chute depths in the centre of track A are 20 to 25 m. Again, the poor quality of the record makes difficult the delineation of source and depositional areas related to the chutes.

The best examples of the small chutes are from tracks E and G. The track E chute originates rather indistinctly in the left channel, appearing as a distinct feature on the right channel and terminating around 400 m downslope in an abrupt manner with no apparent depositional zone or lobe (Figure 76). The feature, then, is oriented in a downslope or E. to W. direction.

a: fan-delta chutes

b: small chutes

c: large chutes

d: depositional zones

e: arcuate rotational slides

Figure 74. Sidescan 'mosaic' of lower delta front.

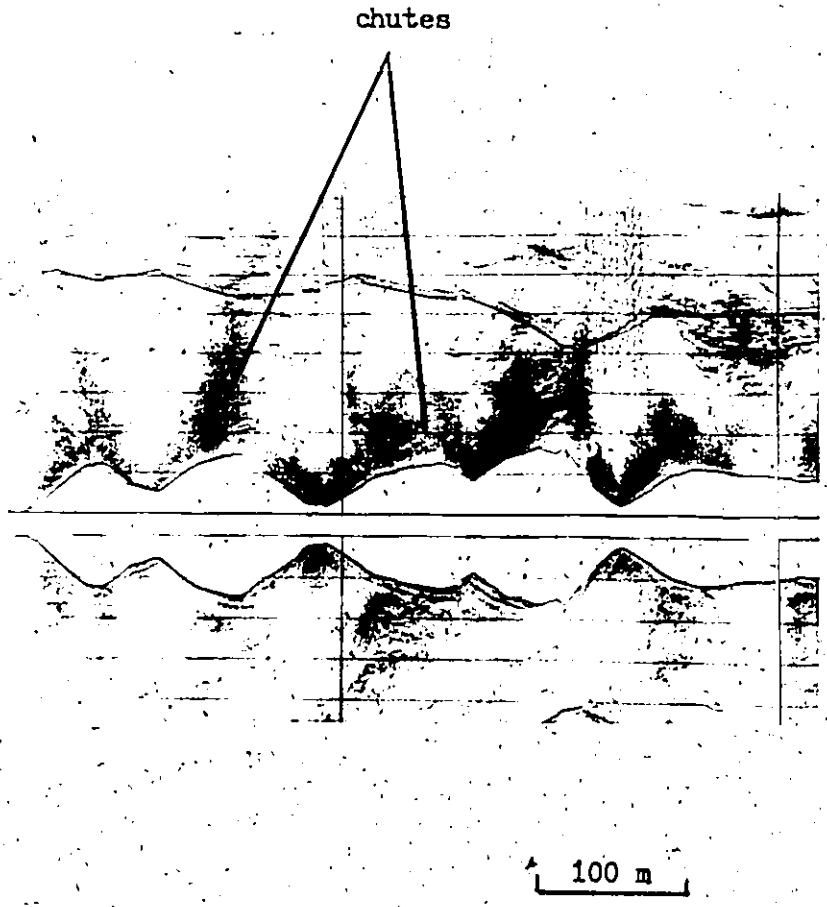

Figure 75. Fan delta chutes on the right channel of track A.

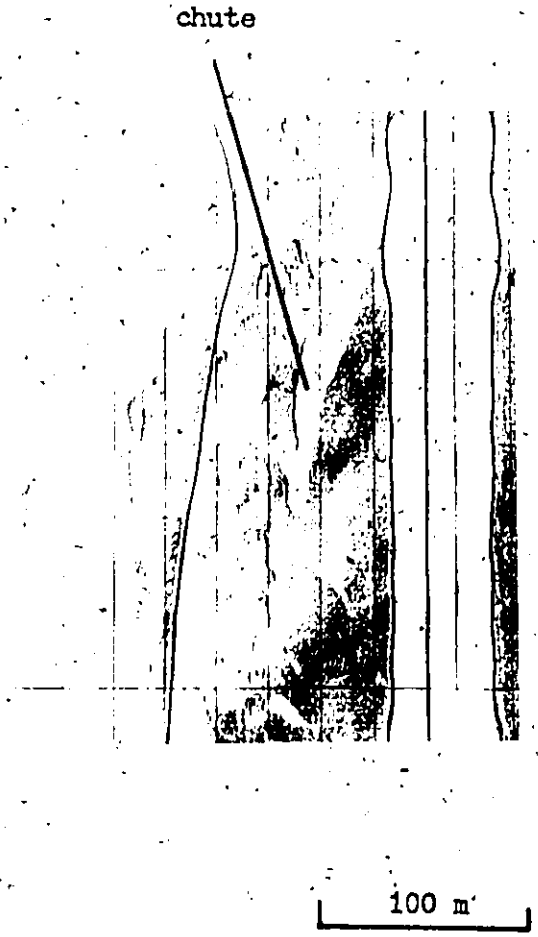

Figure 76. Small track E chute.

The track E chute channel is widest, 30 m, at the upslope end, narrowing to 15 m at the terminus. The southern edge of the chute is straight, but the northern edge widens in a number of places in response to the confluence of a series of small, short, tributaries. The wide zones range from 14 to 18 m, the narrow areas 3 to 5 m. These variations in width cause the chute to have a sinuous north bank and a straight south bank. The depth of the chute at the centre of track E is approximately 3 m. A close examination of the north bank of the track E chute shows that the bank casts an acoustic shadow into the off-channel area. This shadow indicates that the bank near the channel is elevated, suggesting the presence of a subaqueous levee.

The track G small chute (Figure 74) may not be an isolated feature but may in fact be situated within a much larger chute, which is discussed below. The track G chute is formed by the confluence of two main tributary channels (Figure 77). The northern tributary is 90 m in length and approximately 5 m in width. This tributary is rather indistinct on the record but appears to be straight to very mildly sinuous with constrictions in width.

The southern track G tributary is 60 m long, 7 m wide in proximal reaches and 10 m wide near where it joins the northern tributary. The northern bank is relatively straight, the southern bank having a sinuous form, reducing the width slightly to 5 m in the central area. The southern bank also displays well developed acoustic shadows interpreted as levees. A small chute 30 m long and 3 m wide can be seen running in a parallel direction south of this tributary.

Figure 77. Small track G chute.

Where the tributaries meet the resulting chute widens to 20 m for a short distance then constricts to 6 m and becomes indistinct and disappears within a 20 m distance downslope. The southern bank of the 20 m wide section of this chute is also sinuous and leveed.

The track G small chute appears abruptly in its upslope reaches and does not have a distinct source area. Downslope the chute disappears gradually, perhaps suggesting the chute has spread out in a depositional lobe. The chute then loses its topographic expression except for a small, shallow inner channel. As with the track E chute, the bottom of this chute is featureless.

In contrast to the small and relatively straight fan delta and local chutes are the large, sinuous chutes. The best example of these large features occurs on track H, with less distinct chutes apparent on tracks E, F and G (Figure 74).

The track H chute is first visible on the sonagraph on the upper left channel, meandering downslope to the lower limit of the right channel (Figure 78). The gully bed usually has a lighter tone than the interchute areas, and where the sidescan fish is within the chute, a rugged, hummocky surface is revealed. In some areas arcuate rotational slides are located on the bed and along banks.

Gully width varies along the length of the record. At the upper end in a relatively straight reach, chute width is 120 m. In the first meander bend downslope, definition of the outside of the bend is lost

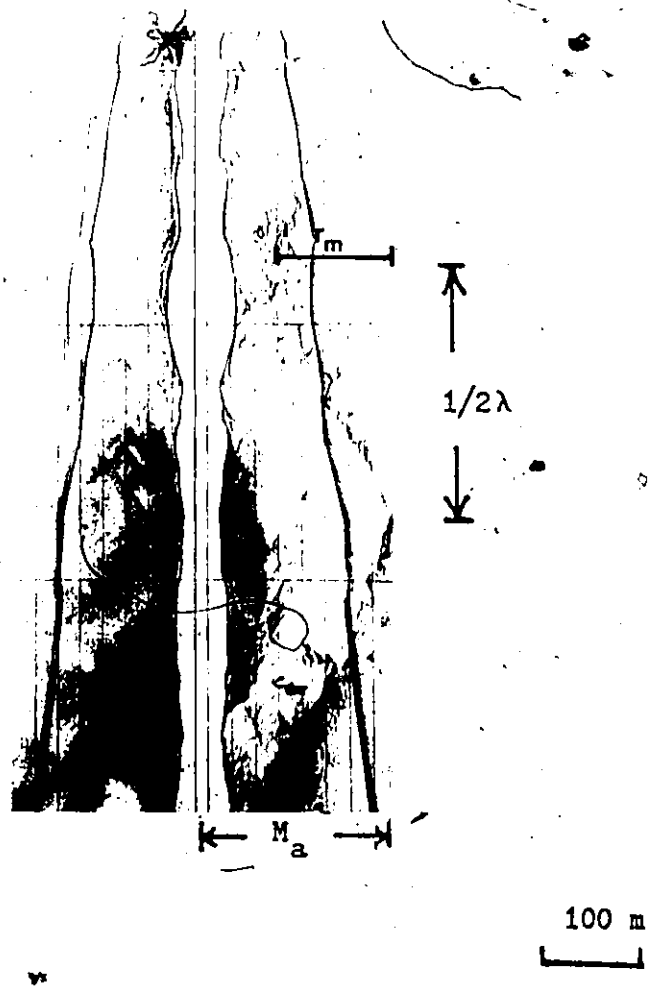

Figure 78. Large sinuous track H chute, showing half the meander wavelength, $\lambda/2\lambda$, meander amplitude, M_a, and radius of curvature, r_m.

and width is impossible to determine. Across the upslope end of the next meander the chute is approximately 100 m in width, expanding to 135 m along the meander axis. The gully abruptly narrows to 65 m downslope and is straight to the end of the record.

Other aspects of chute geometry include depth, and meander wavelength (λ), amplitude (M_a) and radius of curvature (r_m). The lower, narrow portion of the chute has a depth in the range of 10-15 m, and it seems likely that the wider portions are shallower. Meander wavelength is on the order of 500 m, amplitude approximately 200 m and radius of curvature around 300 m. Sinuousity for the total length of gully visible on the record is 1.13. Chute slope for this and other large chutes is 2-4°.

Portions of chutes are apparent on tracks E, F and G (Figure 74). In each case the record is unclear and interpretations uncertain. On track G the northern bank of a chute appears at the top of the right channel and a possible southern bank is situated somewhat downslope on the left channel. The small track G chute may be located within this larger chute. Farther downslope the gully disappears into a possible depositional lobe. Chute geometry is difficult to determine, but width is approximately 50 m and depth 5-8 m. The gully appears to be mildly sinuous.

On track F, the southern bank of a long, low sinuousity chute can be seen on the right channel. The location of the northern bank is unclear, but may be situated on the left channel of track E. On the

upslope portion of the record the width of this chute may approach 250 m, depending on the amount of overlap between tracks. The gully bed in this area has a hummocky, uneven appearance. Farther downslope on track F the chute narrows into a clearly defined gully 30 m in width that terminates against a possible depositional lobe.

A small segment of a chute is visible on the upper portion of the right channel of track E. The southern bank of this feature may be associated with the small track E chute. The large chute appears mildly sinuous with a dark, uneven bed. The gully is approximately 75 m in width and ends a short distance downslope in a possible depositional lobe.

As mentioned above, a number of chutes appear to have depositional zones or lobes associated with their downslope ends. The most distinct depositional zones are related to the large chutes, although both the fan-delta and small chutes must have similar features.

On tracks E, F and G the depositional zones are characterized by hummocky and very irregular topography (Figure 79). Dark-toned prominences are surrounded by irregular light-toned depressions. The prominences may represent transported blocks of sediment or, as suggested in the discussion of rotational slides, may represent residual areas produced by the merging of slides. Indeed, there are remnants of arcuate form in both the blocks and depressions. In addition, given the fact that depositional loading reduces slope stability and may aid in the initiation of rotational slides, depositional zones are likely to be associated with slides.

Figure 79. Depositional zone on track F.

The downslope and across slope extents of the depositional zones cannot be resolved on the sidescan records. It would be expected, however, that they would be somewhat wider than the chutes that feed them.

Arcuate rotational slides are extremely common on the lower delta front and are identifiable on all the sonagraphs except track A on the extreme northern edge of the delta (Figure 74). The slumps are best defined on the northern and central portions of the delta front (tracks B, C, D and E), becoming less distinct on the southern delta front (tracks F, G and H).

Slumps morphology consists of a series of arcuate features that are either isolated from one another (track C, left channel), or, more likely, are individual scarp-blocks in a larger rotational slide (Figure 80). Each arcuate feature is composed of 2 distinct morphologic zones: (1) a scarp and (2) a block. The scarp can appear as a bright acoustic shadow or as a darker zone on the record, depending on scarp orientation with respect to the signal. In the latter case, the scarp is seen as an irregular dark face composed of small-scale linear ridges that are oriented downslope. It is not possible to determine the height or slope of the scarp from the sidescan or associated 3.5 kHz records. The upslope portions of blocks are often obscured in acoustic shadow, but the downslope portion is an elevated area with an uneven surface and characterized by linear ridges and smaller blocks.

Individual scarp-blocks have an across-slope extent of 50-75 m. The exact down-slope extent of these features is unknown but appears to

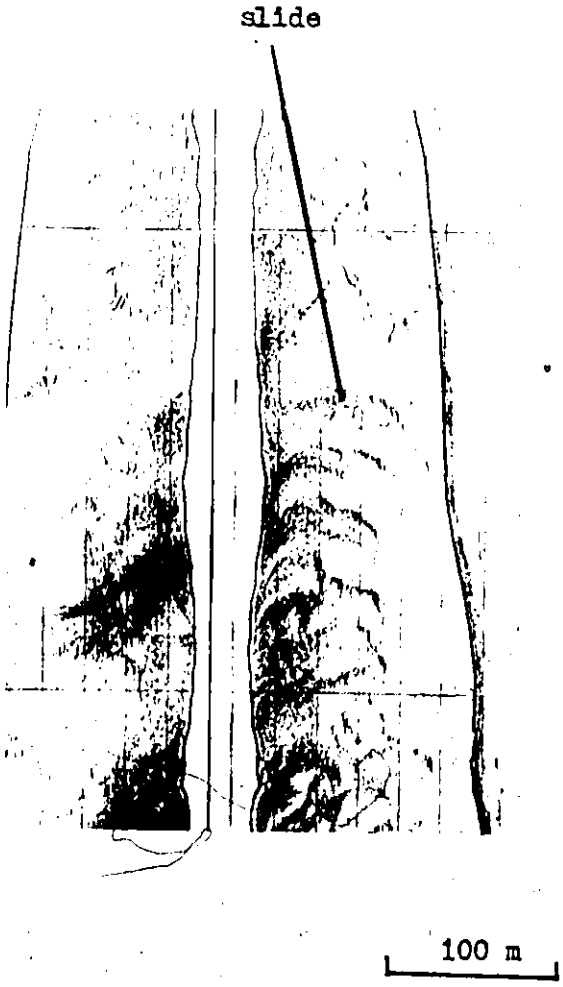

Figure 80. Rotational slide from the left channel of sidescan track C.

be in the 25 m range. The scarp to scarp distance between features (assuming a constant scale along each track) can be very regular and generally decreases in a downslope direction as bottom slope decreases. Due to the overall poor quality of the sidescan records, it is very difficult to identify other morphologic features, such as depositional lobes, that have been noted elsewhere in association with rotational slides (e.g. Prior et al., 1983).

9.2.3 Sediment Grain Size Characteristics

On the upper delta front samples were obtained from chute bottoms and interchute areas along echogram line 2 (Figure 43) and downslope from the North Channel distributary mouth bar (sample LT OMB) on seismic line 8 (Figure 62). Lower delta front samples include a line across the fjord from south to north (Par 82 005-012) and a sample downslope along seismic line 8 (Par 82-004) (Figure 45). Unlike the upper delta front samples, there is no morphologic control over lower delta front sample sites. As a result, the samples may come from any of the morphologic areas associated with rotational slides, chutes, or depositional zones.

Figure 81 shows the trends in mean grain size (M_2), median (M_d), standard deviation (σ_I) and % clay for the chute bottoms and interchute areas of the upper delta front. Chute bottom samples 5 to 8 are based on visual estimates of grain size because the coarse nature of the sediment prevented recovery of samples large enough for sieve analysis. Chute bottom samples on the south side of the delta (1-4) are poorly

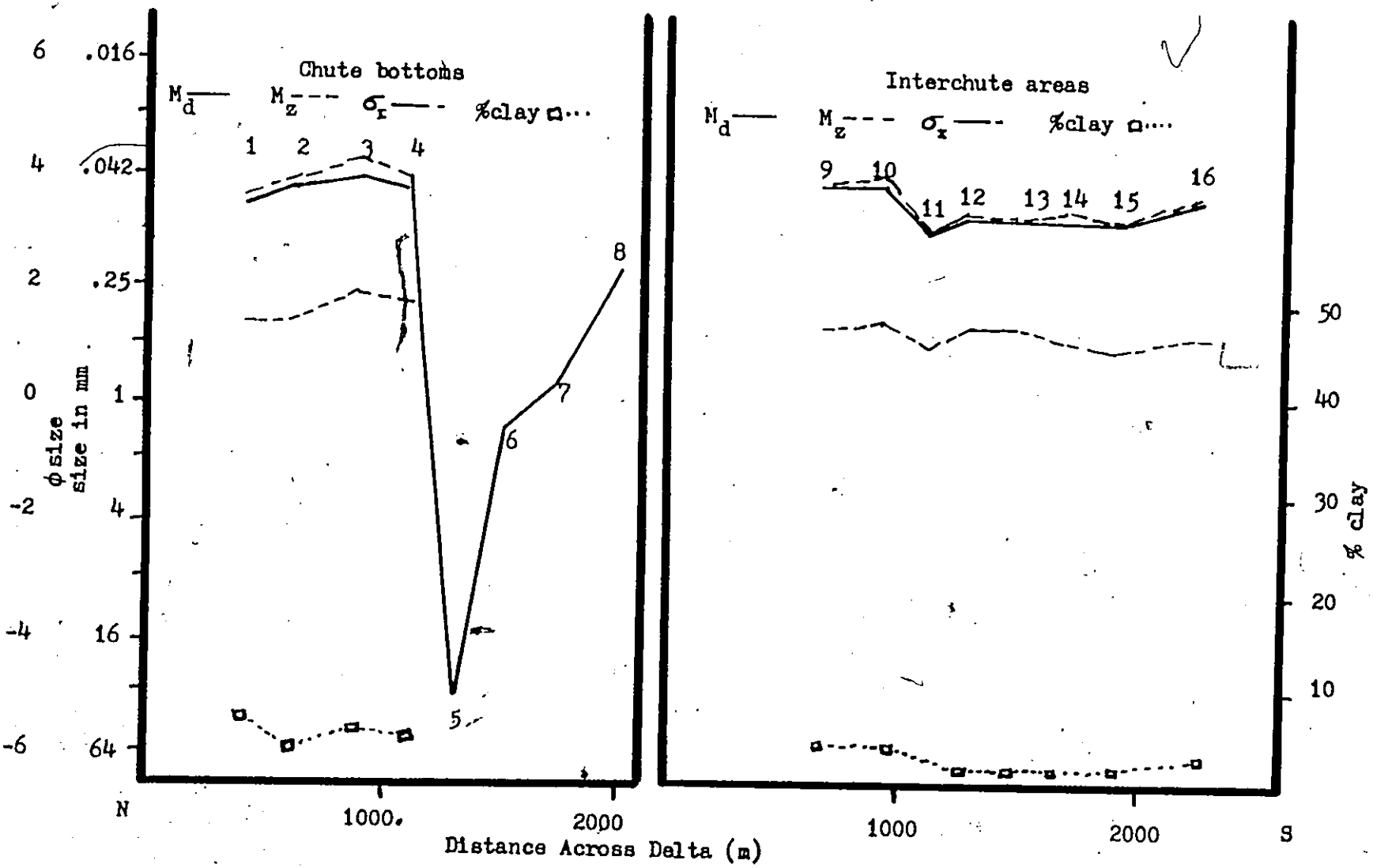

Figure 81. Grain size trends across delta along echogram 2.

sorted coarse silt, and clay content is relatively constant at 3-5 %. In contrast, samples in central and northern areas (5-8) are much coarser, with estimated means in the gravel and coarse to fine sand ranges.

Interchute samples are poorly sorted coarse silts on the southern edge of the delta (9 and 10), coarsening to poorly sorted very fine sand in central and northern areas (11-16). Clay content decreases somewhat across the delta (S. to N.) from 5% to 2-3%.

All of the samples from the lower delta front are in the sand size range. Very fine, poorly sorted sands occur on the southern and northern portions of the delta (Par 82-005, 010, 011, 012) (Figure 82). Sediments in central areas of the delta are somewhat coarser, poorly sorted, fine sands (Par 81-006, 007, 008, 009). Clay content is 0% in the central delta, increasing to 3-5% towards the north and south. In a downslope direction there appears to be a seaward-fining from poorly sorted fine sands with a 0% clay content at Par 82-008, to poorly sorted very fine sand with a 4% clay content at Par 82-004 (Figure 67).

9.3 Geotechnical Character and Sediment Stability

The only geotechnical parameter determined for the delta front samples is bulk density, assessed for samples LT DMB and Par 82-004 and 008 on seismic line 8. No triaxial tests were performed on these samples and as a result there are no actual values for the Coulomb strength parameters which could be used in stability analyses. However, probable values for these parameters can be obtained from the extensive

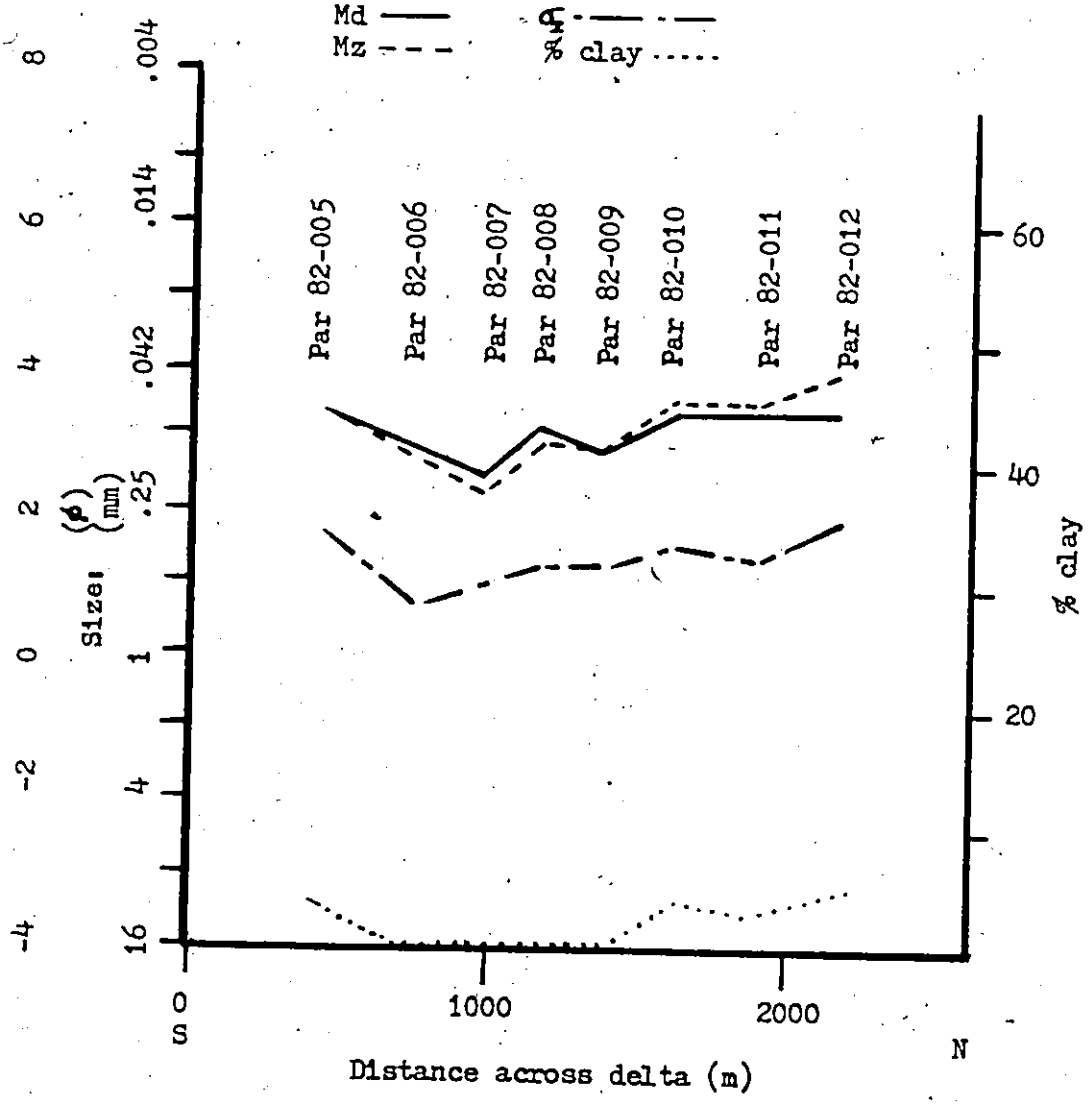

Figure 82. Grain size trends across lower delta front.

geotechnical data base on submarine sands. Values of cohesion (C') have been assumed equal to zero, an assumption considered valid for sands and normally consolidated clays in subaqueous conditions (Chowdhury, 1978; Henkel, 1970). Internal friction angles (ϕ') have been assigned values of 25 to 35° (Morgenstern, 1967). Values of unit weight of sediment (γ) depend on bulk density, the latter having values of 1488, 1518 and 1409 kg m^{-3} for LT DMB, Par 82-008 and Par 82-004 respectively. The following analysis of sediment stability on the delta front is based on assumed and actual values of geotechnical parameters from LT DMB and Par 82-004 and 008.

9.3.1 Sediment Stability

As indicated earlier, the three main morphologic components of the delta front are gullies or chutes, depositional zones and arcuate rotational slides. Slope stability with respect to each of these features can be modelled using methods outlined in chapter 7. Chutes and their associated depositional zones are analyzed in terms of translational and rotational slides and debris flows. Arcuate rotational slides are examined with respect to susceptibility to rotational sliding.

9.3.1.1 Chutes and Depositional Zones

Prior et al. (1981) suggest that chutes in fjord deltas are generated by slides or debris flows originating in distributary mouth bar sediments. Depositional zones result from sediment discharged at

the downstream ends of chutes. The potential for sliding in the distributary mouth bar and downslope chute beds, interchute areas and depositional zones can be assessed using infinite slope analysis. Debris flows can be modelled using Johnson's (1970) 'rigid-plug' model.

Translational Slides

On the upper delta front, near the break in slope between delta plain and delta front, slopes average 8.3° but in the vicinity of distributary mouths may reach 15°. Farther offshore, upper delta front slopes decrease to 4°. Lower delta front slopes are much gentler at 2.2 to 4°. The factor of safety, S, for gravitationally-induced translational slides on the delta front has been calculated using Equation (32) and is plotted against bottom slope on Figure 83. As bottom slope increases on the delta front, the value of S decreases but never reaches the critical value of 1 where sliding would occur. It may be that during river floods slopes on the seaward sides of distributary mouth bars exceed necessary values (25-35°) and sliding could result. Other factors responsible for translational slide initiation or expansion include excess pore pressure created by methane gas generation, rapid tidal drawdown and depositional loading, earthquake loading and retrogression. The effects of these factors on translational slides are examined below.

Pore pressures (u) required to initiate failure (S = 1) for each sample site have been determined from Equation (33). The ratios of u to hydrostatic pressure ($\gamma_w Z$) and to geostatic pressure (γZ) are summarized

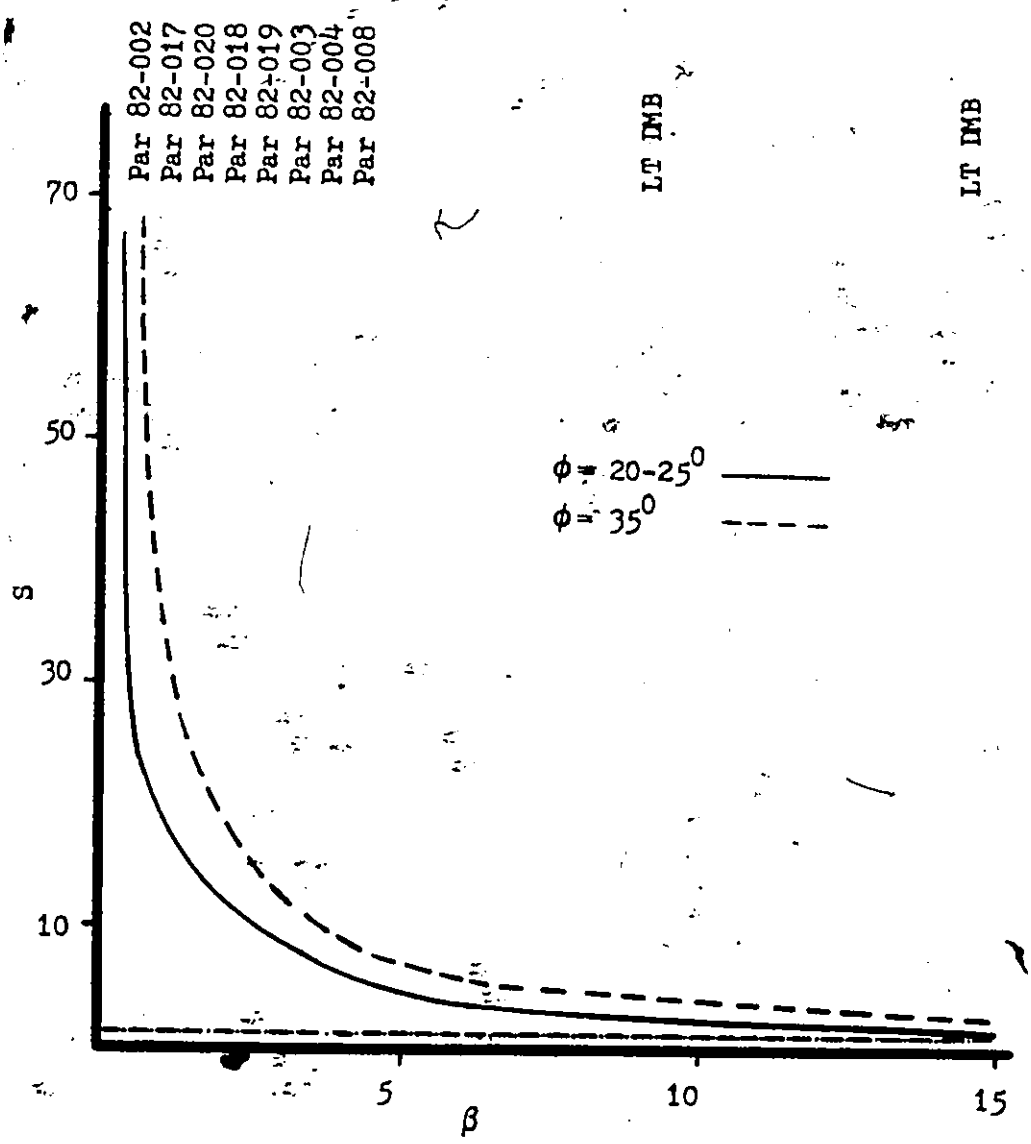

Figure 83. Factor of safety for translational slides (S) versus bottom slope (β).

on Figures 84 and 85. Values of u depend to a large degree on the unit weight of sediment (γ), a quantity which varies considerably amongst samples and as such causes some variablility in $u/\gamma_w Z$ ratios.

For the delta front values of $u/\gamma_w Z$ and $u/\gamma Z$ vary from 1.1 to 1.45 and 0.76 to 0.97 respectively. Thus as bottom slope increases and the unit weight of sediment decreases, the values of u required to initiate failure decrease. For the more gently sloping areas of the delta front the values of u required are very large, approaching geostatic values. Three factors that could create the necessary pressures are methane gas generation, rapid tidal drawdown and rapid depositional loading.

There is indirect evidence for methane gas generation in sediments on the upper delta front near the break in slope between delta plain and delta front. During extremely low tides small mud volcanoes appear on the intertidal zone (Figure 86). The sediment discharged from the volcanoes is dark and organic rich and the distinctive odour of methane gas emanates from the features. The volcanoes are interpreted as resulting from excess pore pressures generated in the upper delta front deposits. On the lower delta front, indirect evidence for gas generation, such as venting, is not apparent on the sonagraphs.

During a period of extremely low tide in 1982 a slope failure occurred at the seaward edge of the distributary mouth bar of the North Channel. The failure was characterized by the upward projection and then disappearance of a large log that was buried in the sediments.

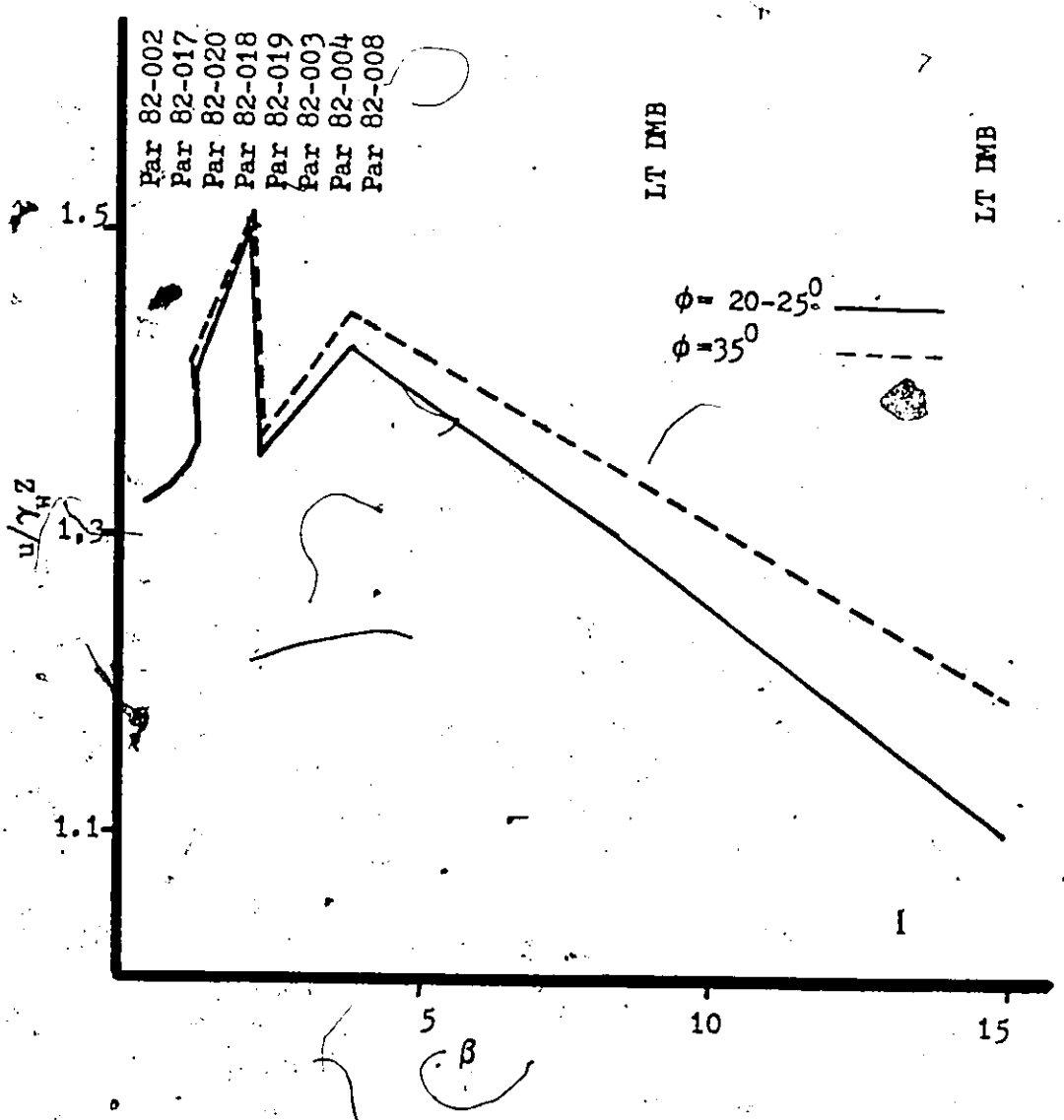

Figure 84. Ratio of pore pressure (u) needed to initiate failure to hydrostatic pressure ($\gamma_w Z$) versus bottom slope (β). The unit weight of water is γ_w and Z is the thickness of sediment above the slip surface.

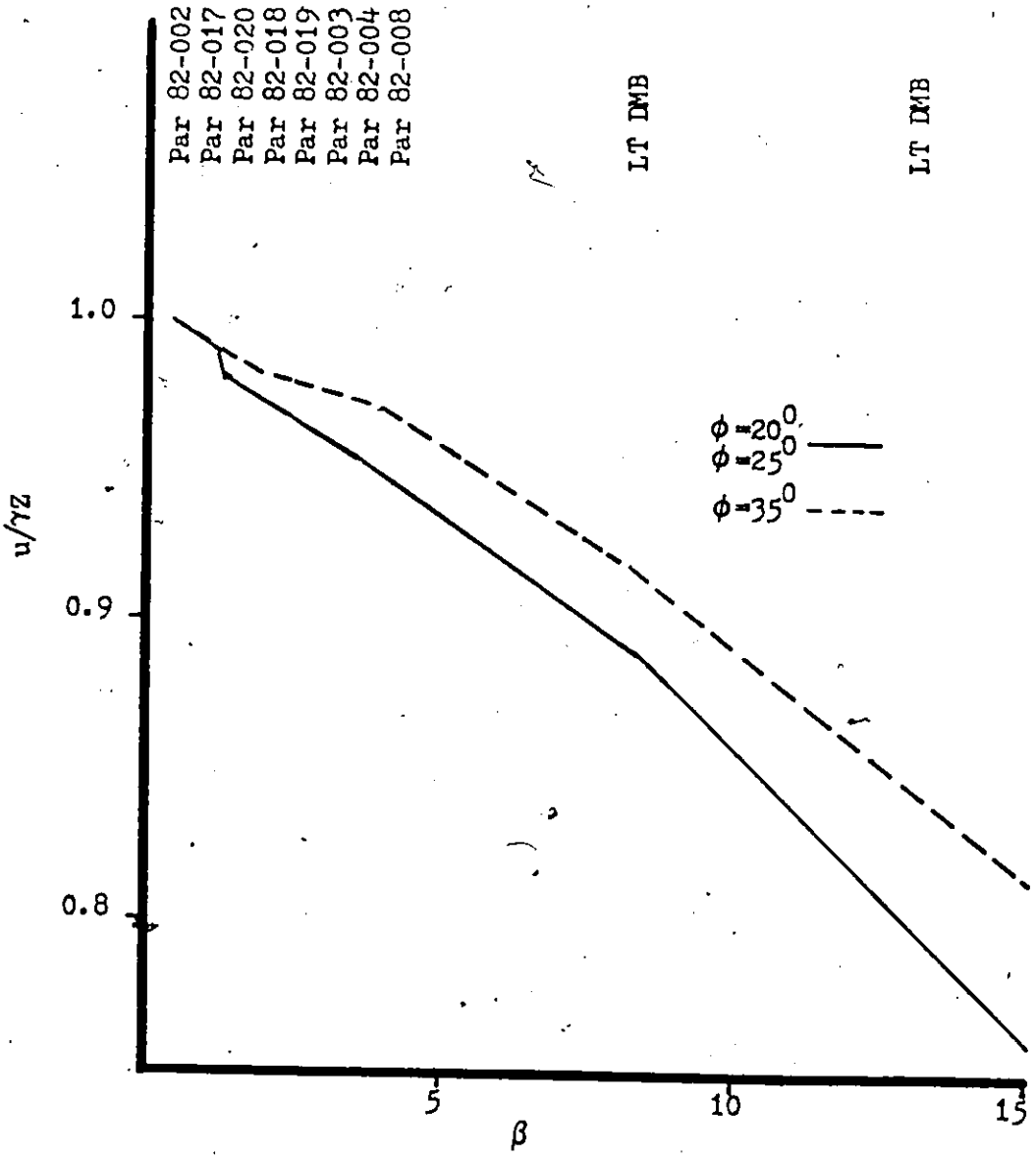

Figure 85. Ratio of pore pressure (u) needed to initiate failure to geostatic pressure (γZ) versus bottom slope (β). The saturated unit weight of sediment is γ and Z is the thickness of sediment above the slip surface.

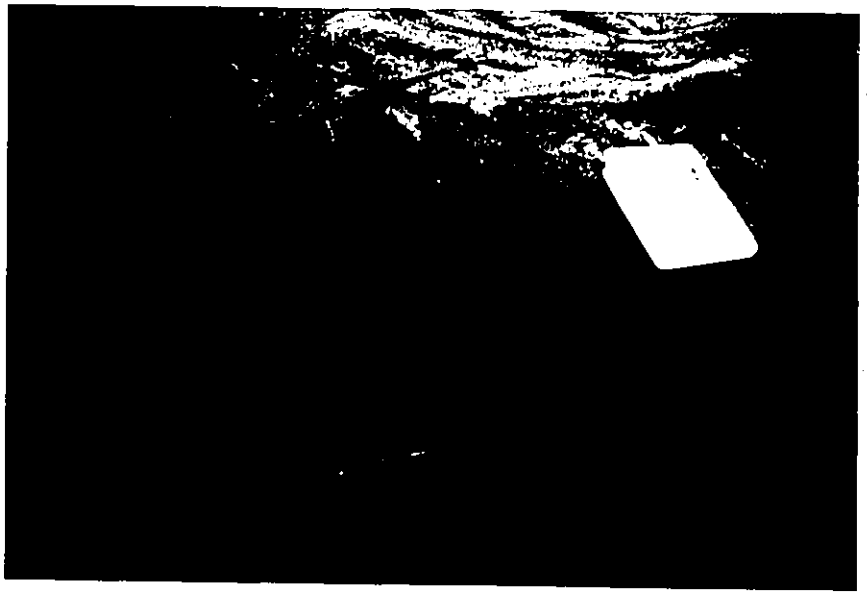

Figure 86. Mud volcano on sand flats.

Rapid tidal drawdown was likely a factor in creating the increase in pore pressure required to destabilize the slope.

Reduced factors of safety on the delta front due to depositional loading, S_L, can be determined from Equation (35) and are presented as functions of S and A on Figure 87. Depositional loading is probably most important in the depositional zones of the lower delta front. From Figure 87 it is possible to determine the thickness of depositional load, h, required to initiate failure ($S_L = 1$) (Figure 88). The assumption is made that the unit weight of the loaded sediment is identical to the underlying material. As is shown on Figure 88, values of h required for failure decrease with increasing slope and decreasing thickness of sediment above the slip surface (Z).

For the delta front, required values of h range from 3 to 16 m on slopes of 15° and 50 to over 100 m for slopes of 2.2°. For the steeper slopes, depositional loads of 3 to 16 m are reasonable for slides or debris flows (e.g. Prior et al., 1983; Suhayda and Prior, 1978). In addition, deposition on distributary mouth bars during extreme river floods might also provide the required load. For the gentler slopes, slide or debris flow loads of 50 to over 100 m are unlikely.

It seems probable that factors such as gas generation, rapid tidal drawdown, depositional loading and wave loading (discussed below) may act in concert to reduce the stability of slopes. The special case of combining earthquake acceleration and depositional loading is examined below.

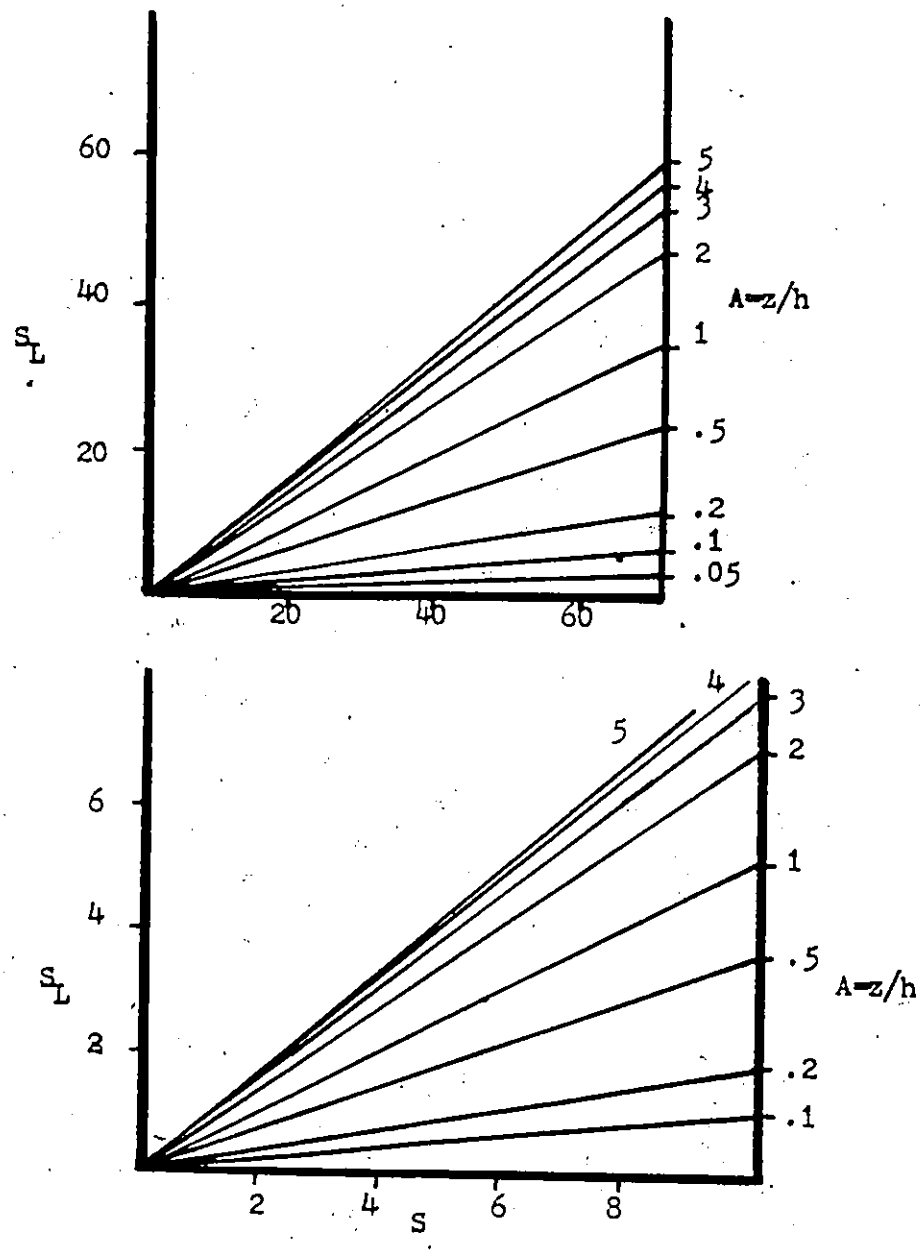

Figure 87. Reduced safety factors (S_L) due to depositional loading as a function of S and A. The initial safety factor is S, Z is the thickness of sediment and h is the thickness of depositional load.

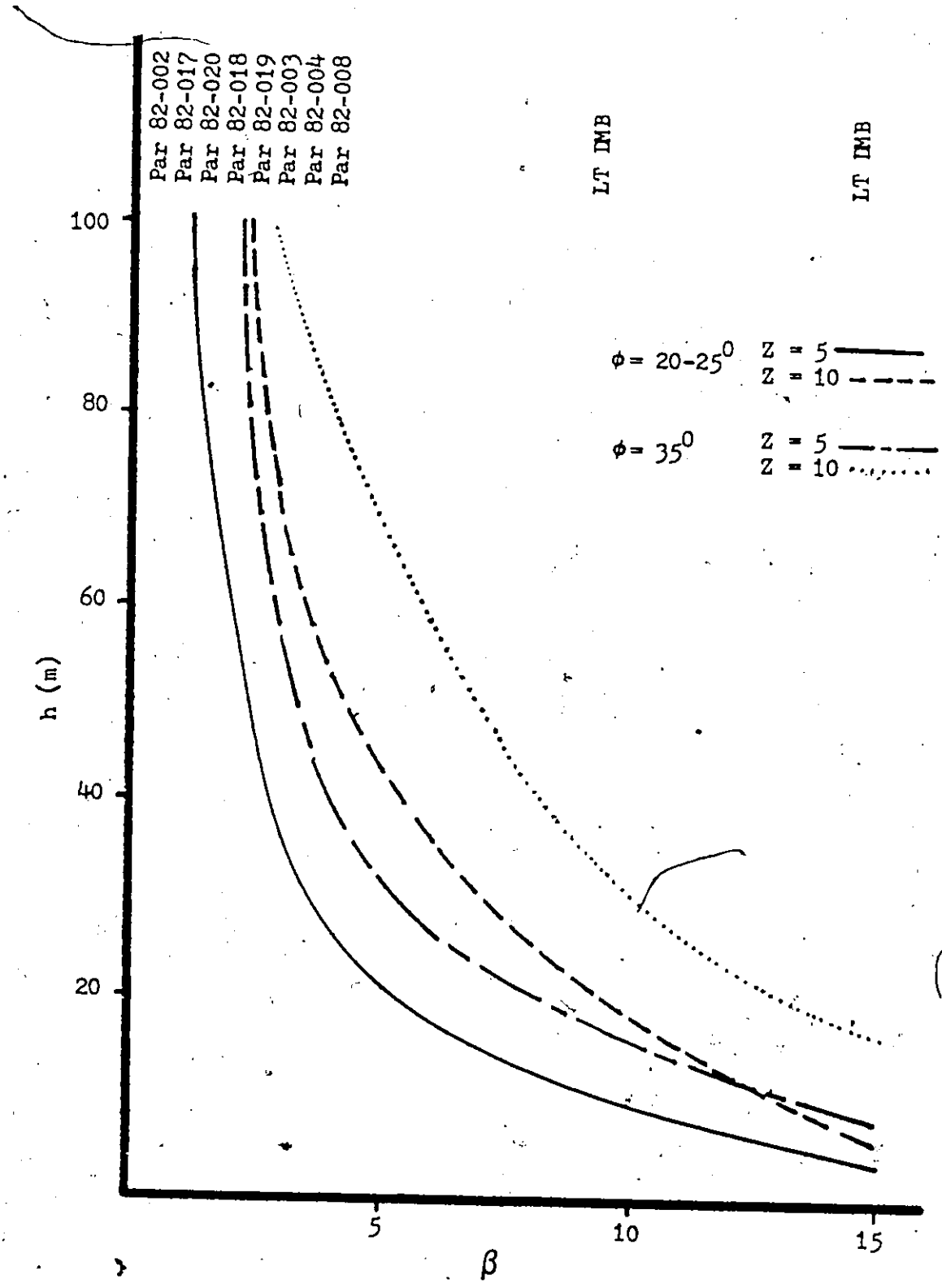

Figure 88. Thickness of depositional load (h) required to initiate failure ($S_L = 1$) versus bottom slope (β). The reduced safety factors is S_L.

A recent seismic risk map for Canada (Basham, 1983) indicates that peak horizontal accelerations (a_x) produced by earthquakes in the Bella Coola area range from 0.08 to 0.11. Using this information and Equation (32) modified to account for earthquake accelerations, factors of safety for translational slides effected by earthquakes (S_E) were calculated (Figure 89). Values of S_E are effected by the unit weight of sediment (γ) as well as bottom slope, and this causes some variation in S_E for areas of similar slope.

On the delta front, accelerations of $a_x = 0.08$ would cause slope failure ($S_E > 1$) only for the lowest sediment strengths ($\phi = 25°$) and slope angles greater than 13°. For larger accelerations of $a_x = 0.11$, slopes become unstable for lowest strengths ($\phi = 25°$) at bottom slopes of 8.5°. Clearly, then, earthquake effects are likely to be most important on steep slopes and during the largest accelerations.

Earthquake effects may act on sediments already weakened by gas generation or tidal drawdown. In addition, earthquake acceleration can combine with depositional loading to further reduce the factor of safety of the slope (Figure 90). This model assumes that an earthquake-generated slide or debris flow provides a depositional load which acts simultaneously with the earthquake acceleration. As is apparent on Figure 90, the addition of the earthquake component to the depositional loading model greatly reduces the value of h required to initiate failure. For the delta front slopes of 15° with $a_x = 0.08$ require h values from 0 to 3 m, and 2.2° slopes require h values of 1.7 to 11 m. When $a_x = 0.11$, h values are further reduced to 0 to 1 m for 15° slopes and 0.6

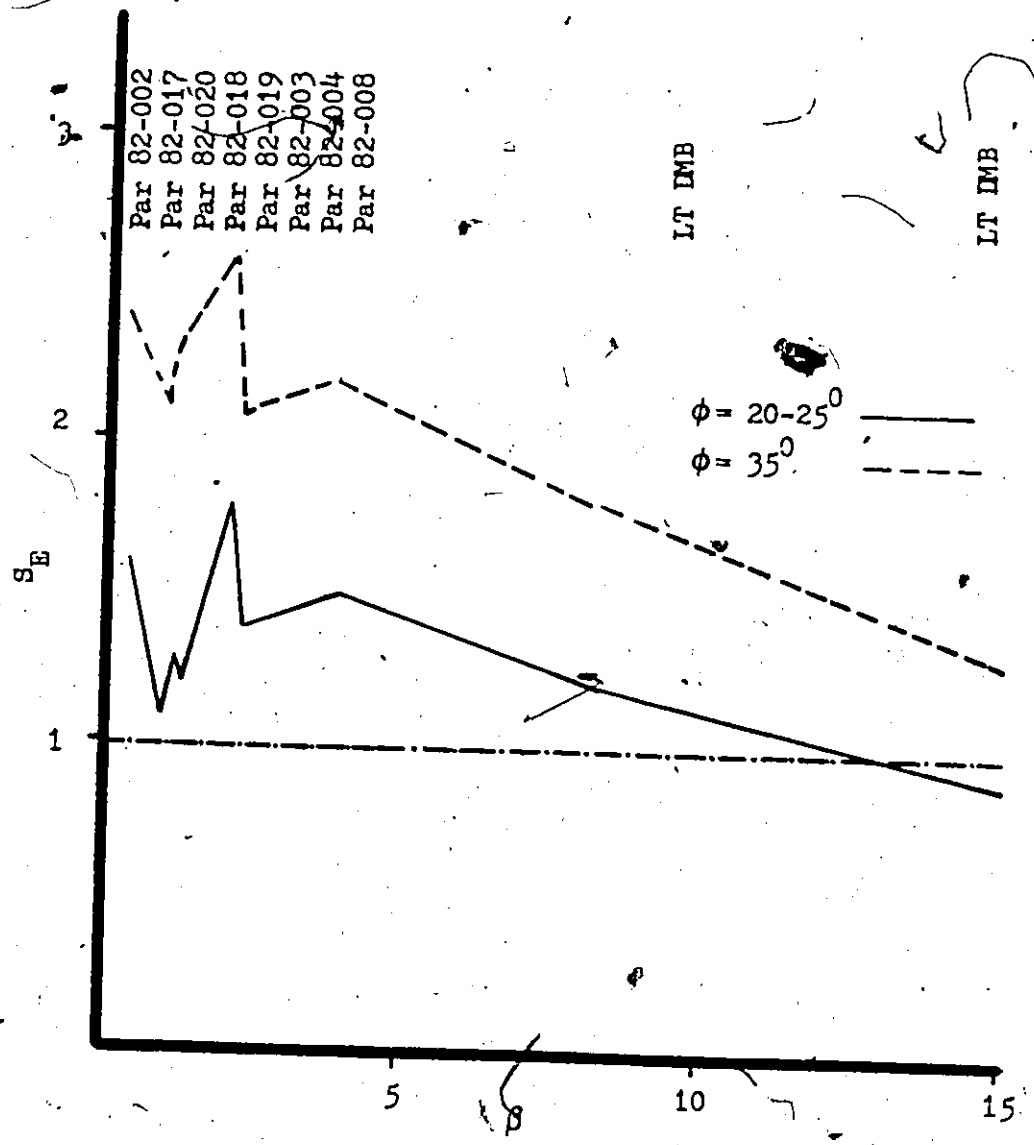

Figure 89a. Factor of safety (S_E) for earthquake acceleration (a_x) of 0.08 versus bottom slope (β).

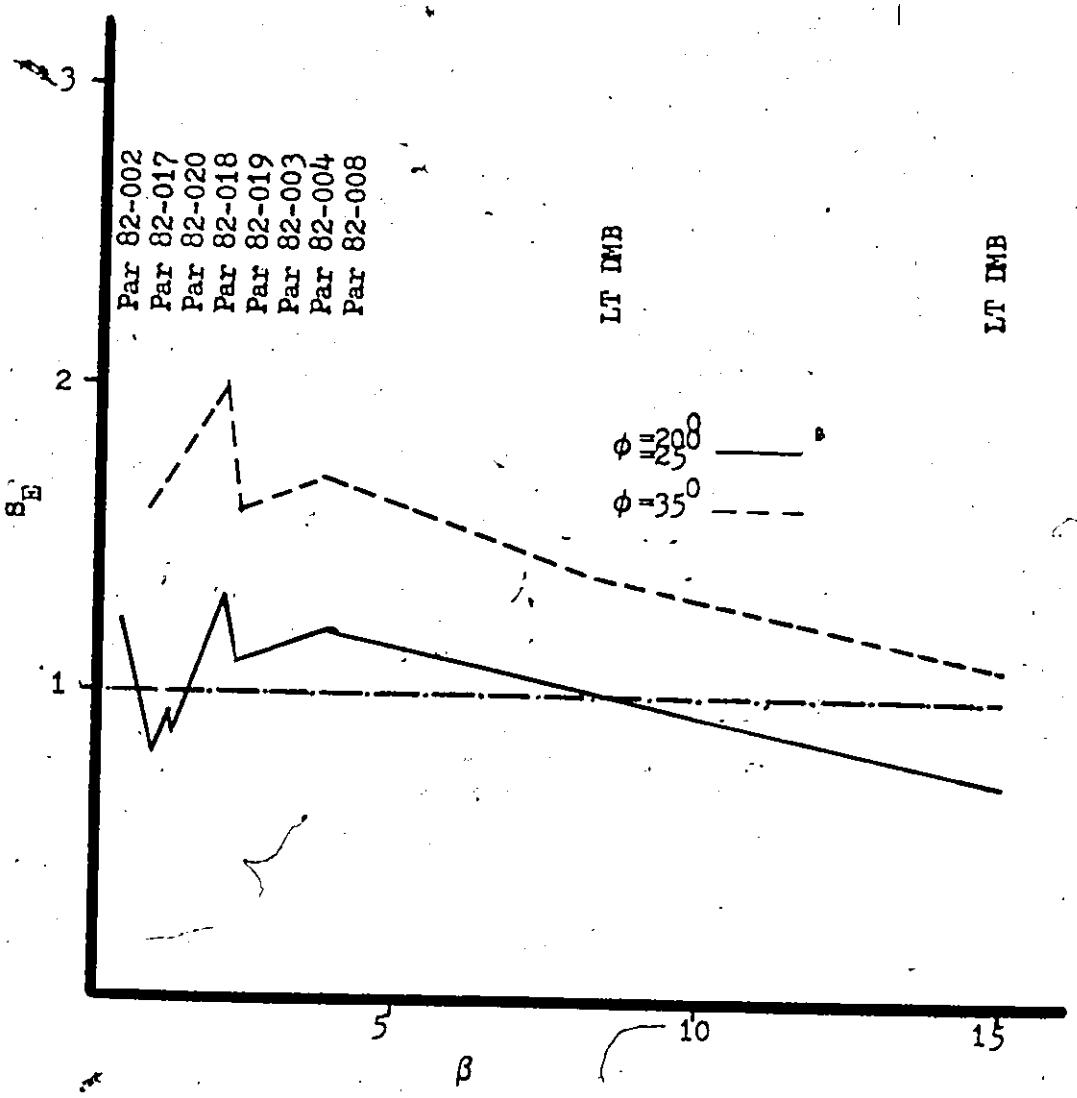

Figure 89b. Factors of safety (S_E) for earthquake acceleration (a_x) of 0.11, versus bottom slope (β).

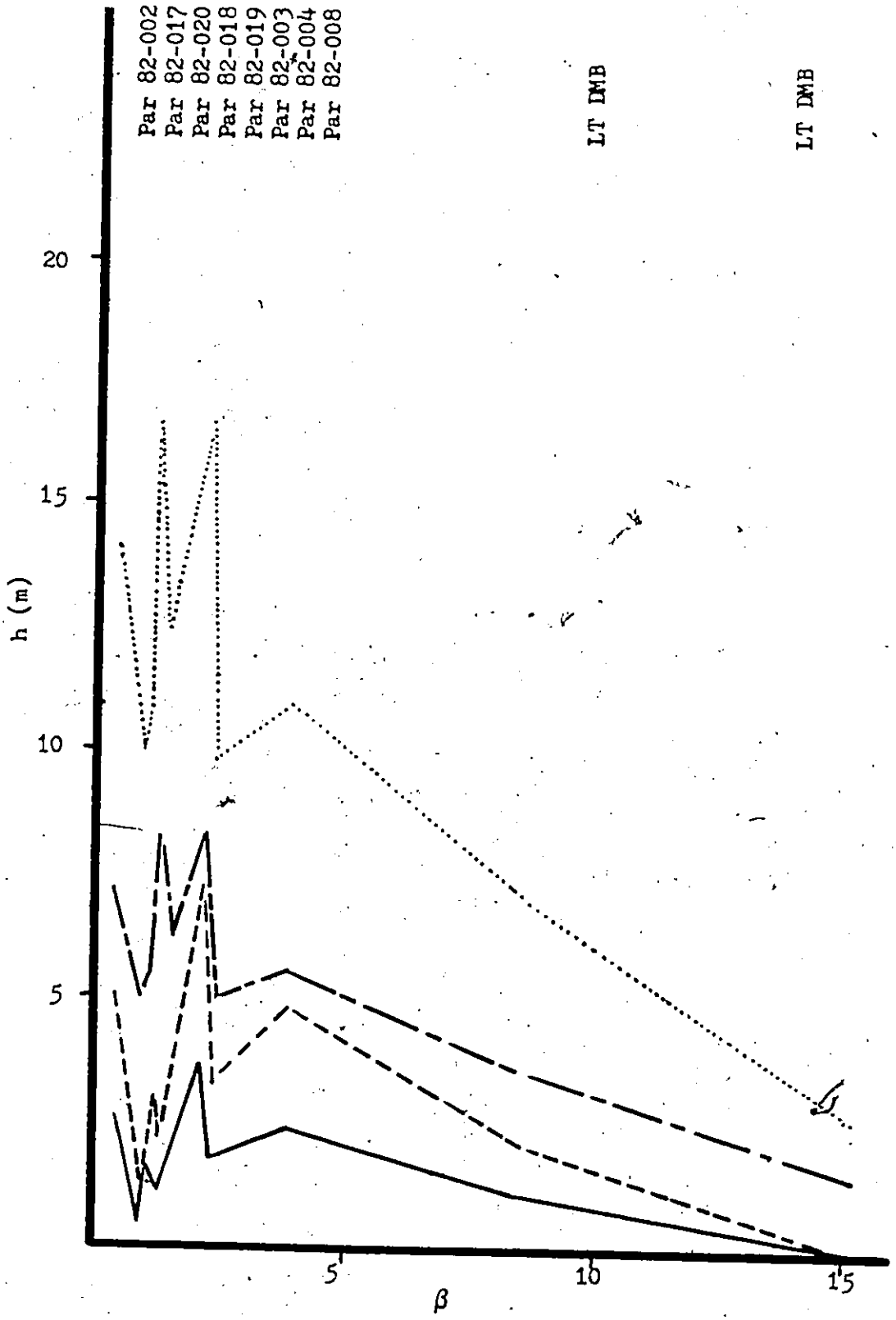

Figure 90a. Thickness of depositional load (h) required to initiate failure (S_E = 1) with an earthquake acceleration (a_x) of 0.08, versus bottom slope (β). The factor of safety due to earthquake is S_E.

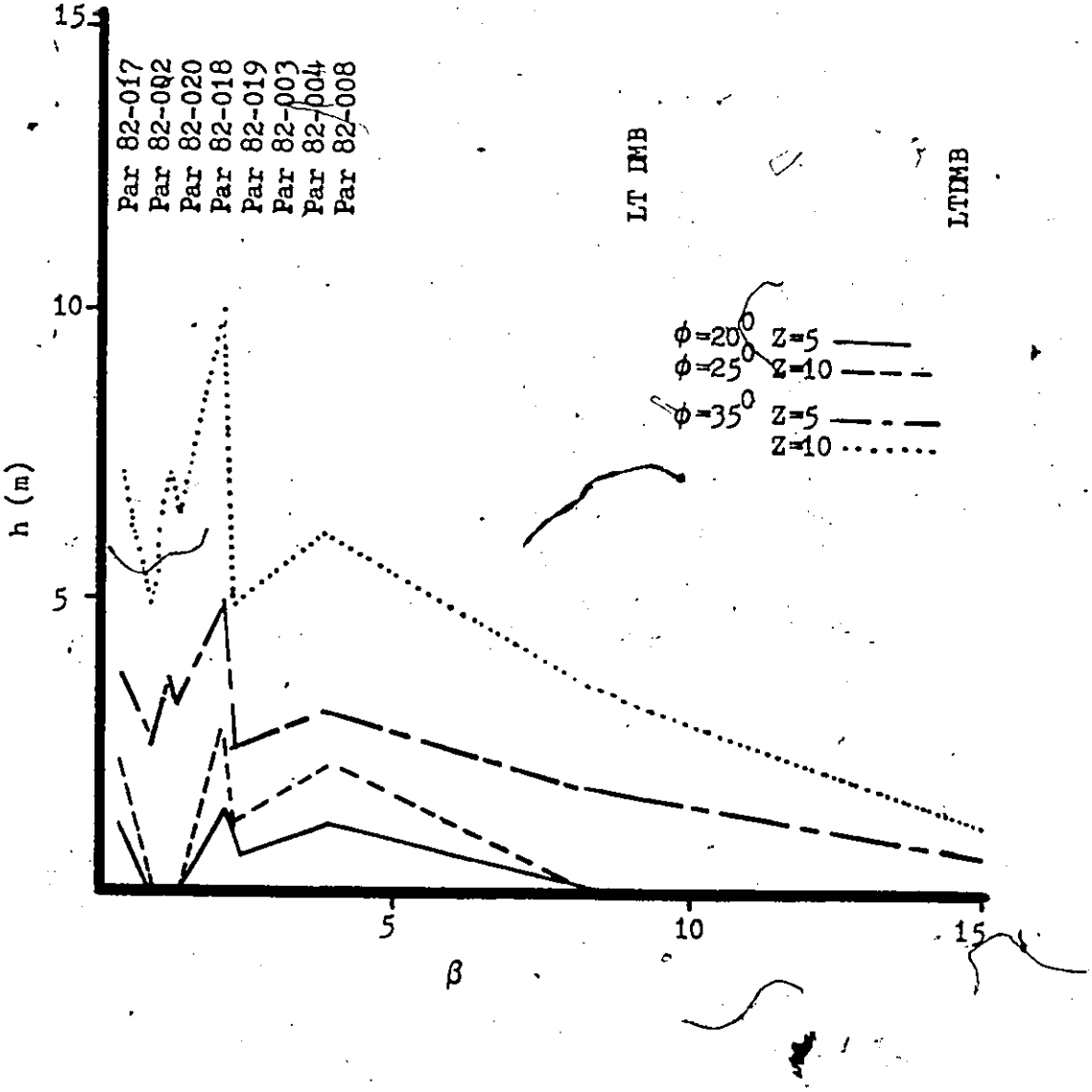

Figure 90b. Thickness of depositional load (h) required to initiate failure (S_E = 1) with an earthquake acceleration (a_x) of 0.11, versus bottom slope (β). The factor of safety due to earthquake is S_E.

to 6.0 m for 2.2° slopes. All of these h values are possible.

Equation (34) was used to determine the critical subsidence ratio ($\Delta h/Z_1$) for retrogression of translational slides in delta sediments. The ratio is plotted against unit weight of sediment (γ) on Figure 91. Values of $\Delta h/Z_1$ increase with both γ and ϕ' values. For the delta front the ratio ranges from a low of 0.31 to a high of 0.63. At present the data from the Bella Coola delta is insufficient to allow a comparison of these predictions to actual translational slide values.

Rotational Slides

The analysis of chute-related rotational slides is restricted to the effects of waves, using Henkel's (1970) method, on the upper delta front-distributary mouth bar area. The factors, such as excess pore pressure, depositional loading, earthquake loading and retrogression, that cause a decrease in slope stability for translational slides affect rotational slides as well.

The largest waves noted in North Bentinck Arm have heights (H) of 1.5 m, periods (T) of 4 S. and wavelengths (L) of 25 m. Using charts prepared by Henkel (1970) and Wiegel (1964), the pressure change (Δp) associated with the shoaling of a wave of this magnitude can be determined (Figure 92). A constant bottom slope, β, is assumed. As the wave begins to 'feel' bottom at a depth of around 12.4 m (L/2), L and H start to decrease and Δp increases. The maximum value of Δp = 4.124 kPa occurs as the wave breaks in 1.75 m water depth and H is at a maximum.

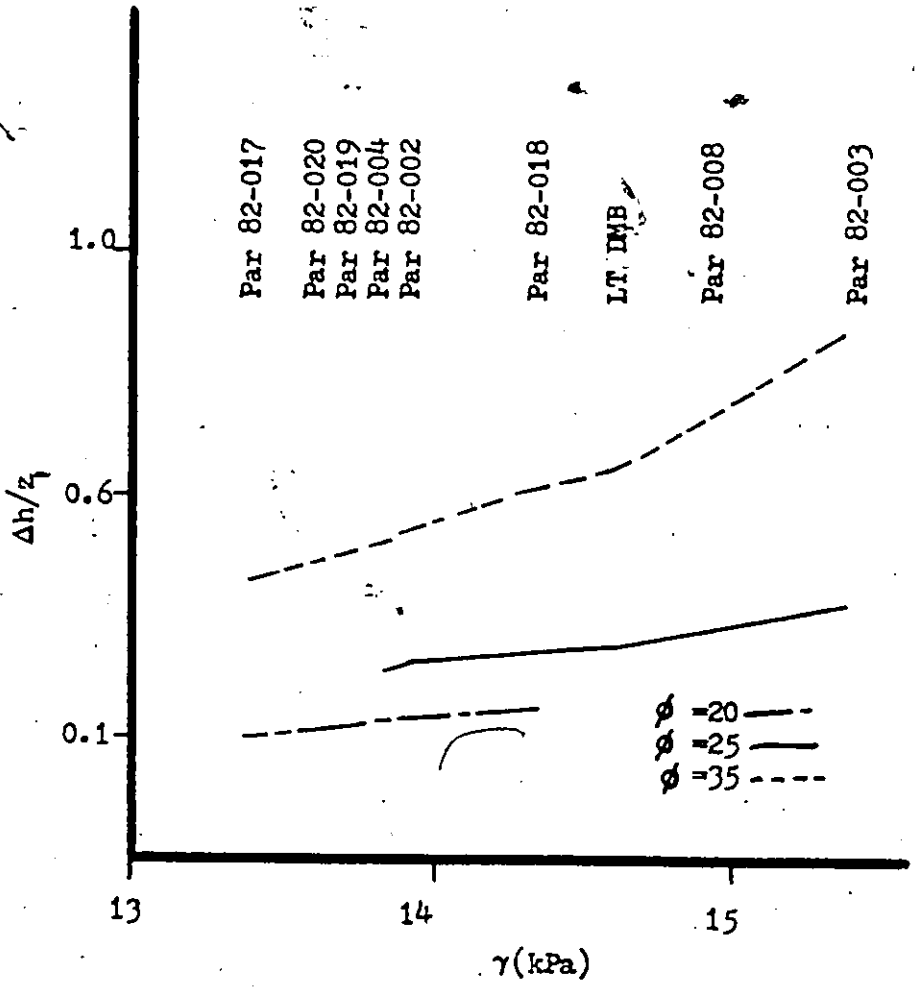

Figure 91. Retrogression criteria ($\Delta h/Z_1$) versus unit weight of sediment (γ). The thickness of scarp sediment is Δh and Z_1 is the thickness of sediment from scarp top to slip surface.

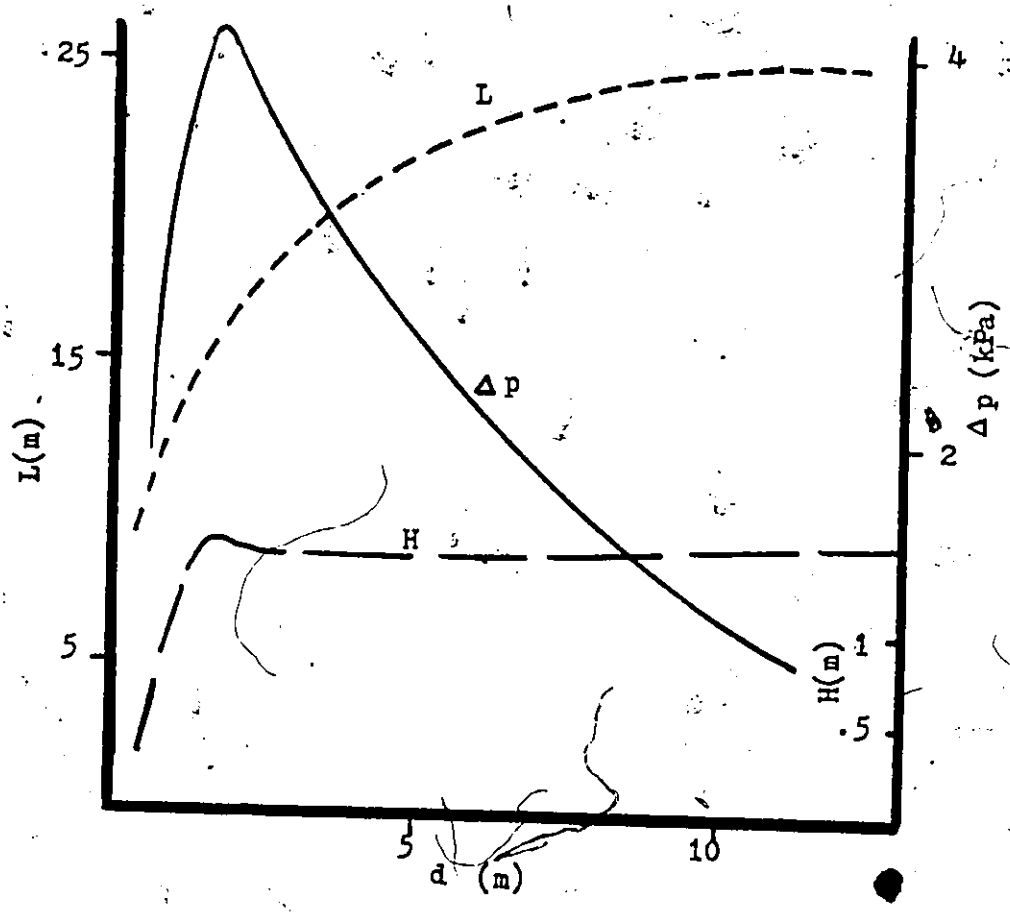

Figure 92. Variation in wavelength (L), height (H) and pressure change (Δp) with water depth (d).

As H declines rapidly after the wave breaks, so does Δp.

Figure 93 shows values of Δp required for failure for two values of β/B, where $\beta = 15°$ and B is determined from Equation (37) using LT DMB s and γ' values. As can be seen, the maximum Δp value of 4.124 kPa generated by the largest North Bentinck Arm wave would be capable of initiating only an extremely shallow slide ($Z_{max} = 0.25$ m) in the lower strength bound of the sediments. This analysis indicates that wave pressures exerted by the largest summer waves on the delta are unlikely to cause failure on the upper delta front. However, storms may generate larger waves with Δp values capable of inducing sliding. In addition, the impact of breaking waves on the upper delta front during extremely low tides may cause liquefaction of sediments and hence failure.

Debris Flows

The morphologic characteristics of the beds of large sinuous chutes on the upper and lower delta fronts, such as the well defined levees, suggests that debris flow processes (or possibly turbidity currents) are operational. Johnson's (1970) 'rigid plug' model was used to provide a debris-flow analysis of the delta front chutes. In addition, the morphometric characteristics of the track H chute are compared to results from subaerial meandering rivers.

For the upper delta front, chute A on echogram 2 (Figure 72) was chosen for analysis and the large track H chute chosen from the lower delta front. The half-width, a, of chute A is 41.3 m and the bottom

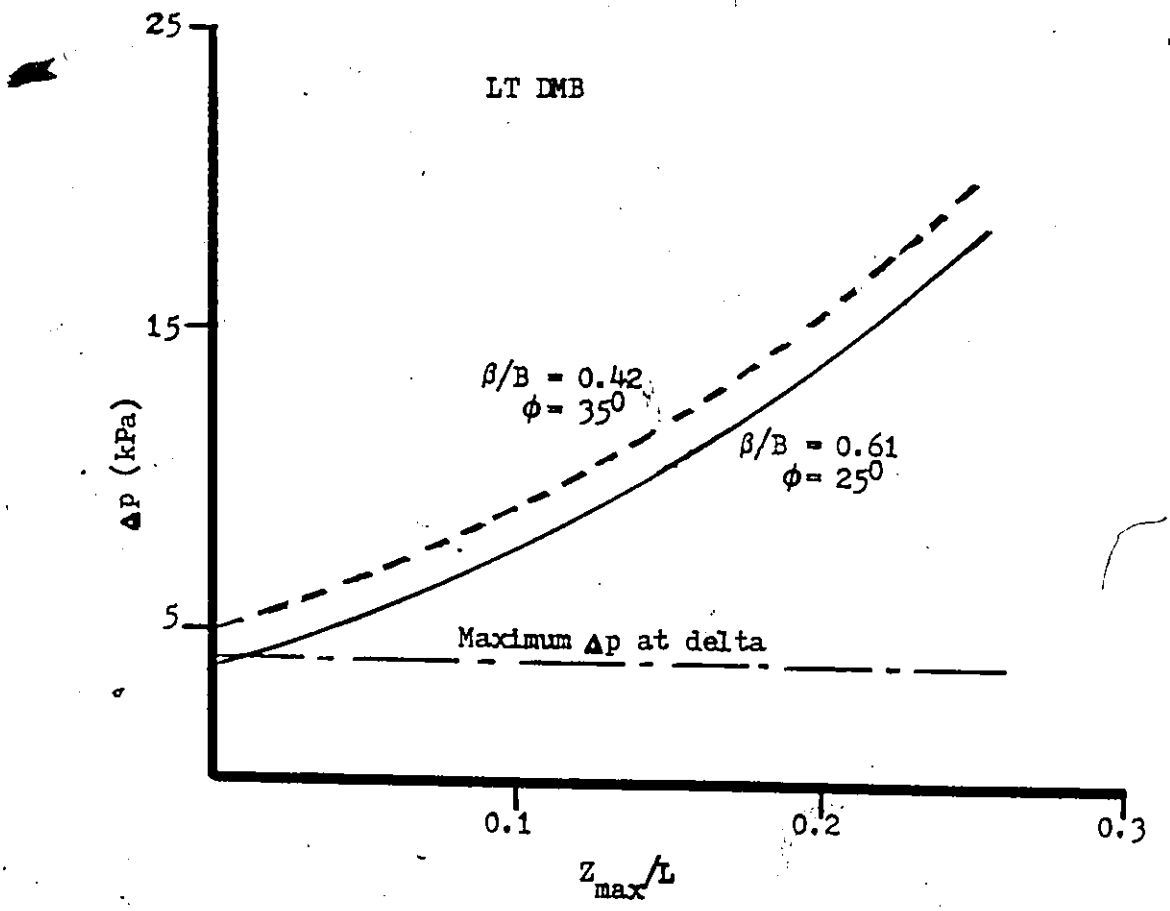

Figure 93. Relationship between pressure change due to waves (Δp) required for failure and maximum thickness of sediment (Z_{max}) over wavelength (L) for two values of β/B. The bottom slope is β and the term B is given in the text.

slope, $\beta = 8.3°$. For the track H chute, a is 61.3 m and $\beta = 3.8°$. Table 6 shows computed values of channel depth b, plug width x_o (Equation 38) and plug thickness y_o (Equation 39) for a/b ratios of 1, 2, 3 and 5. As can be seen on Table 6 and Figure 94, values of y_o and the ratio of y_o/b decrease as a/b increases. That is, the model implies that as the channel becomes shallower (a/b increases), plug thickness (y_o) and proportion of the channel depth occupied by the plug (y_o/b) decrease in non-linear manners. An interesting result of the application of Equation (38) is that plug width (x_o) decreases as a/b increases between 1 and 3, but increases as a/b increases between 3 and 5. The physical meaning (if any) of this result is unknown.

The determination of absolute values of plug velocity ($\dot{w}$) using Equation (40) required knowledge of the Bingham viscosity (η_b) of the flow. However, values of η_b for natural debris flows vary considerably (Johnson, 1970) and it is not possible to assign 'typical' η_b values to calculate $\dot{w}$. However it is possible to calculate relative velocities for $a/b = 1$ ($\dot{w}_1$) and $a/b = 2$, ($\dot{w}_2$), assuming η_b is constant. As shown on Figure 95, relative velocities increase markedly as the channel becomes shallower (a/b increases), with a constant ratio of $\dot{w}_1/\dot{w}_2$ of 0.24 that is independent of bottom slope. For both $a/b = 1$ and $a/b = 2$, the relative debris flow velocity ($\dot{w}/\dot{w}_o$) decreases as slope decreases (Figure 96). The value of $\dot{w}_o$ is the largest velocity for the flow, which occurs on the steepest slope (8.3°), and $\dot{w}$ values are velocities on progressively gentler slopes. The actual point that the flow stops, in this model, is a function of the thickness of the flow (Rodine and Johnson, 1976).

CHUTE	a/b =	1	2	3	5
A $\beta=8.3^0$	a(m)	41.3	41.3	41.3	41.3
	b(m)	41.3	20.6	13.8	8.3
	x_0(m)	34.0	31.9	29.8	33.2
	y_0(m)	34.0	8.0	3.3	1.3
H $\beta=3.8^0$	a(m)	62.5	62.5	62.5	62.5
	b(m)	62.5	31.3	20.8	12.5
	x_0(m)	50.0	46.8	43.7	48.7
	y_0(m)	50.0	11.7	4.8	1.9

Table 6. Morphologic Characteristics of Chutes.

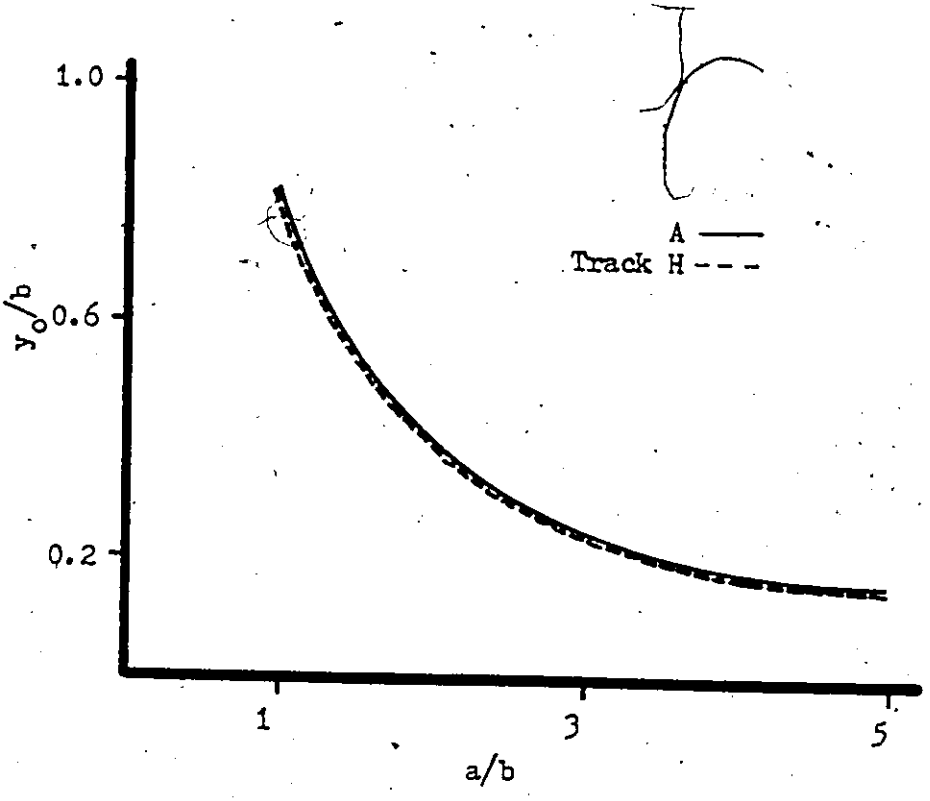

Figure 94. Variation in the relative proporation of debris flow channel depth occupied by the rigid plug (y_o/b) with channel half width to depth ratio (a/b).

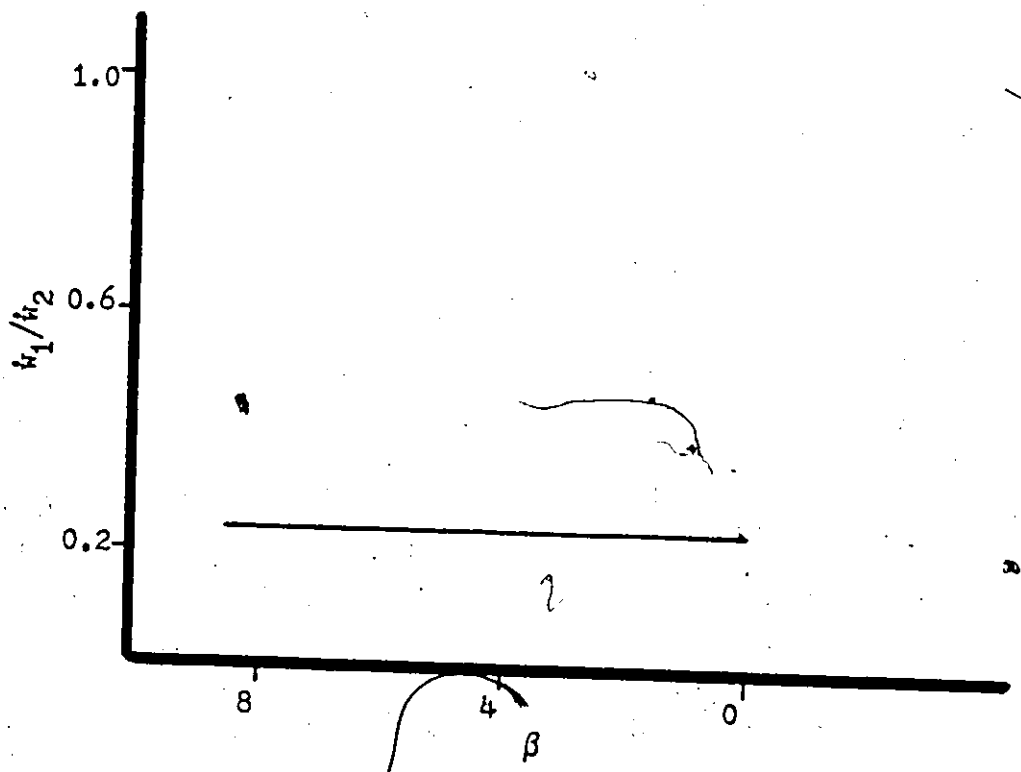

Figure 95. Ratio of debris flow plug velocity when a/b = 1 (V_1) to velocity when a/b = 2 (V_2) versus bottom slope (β).

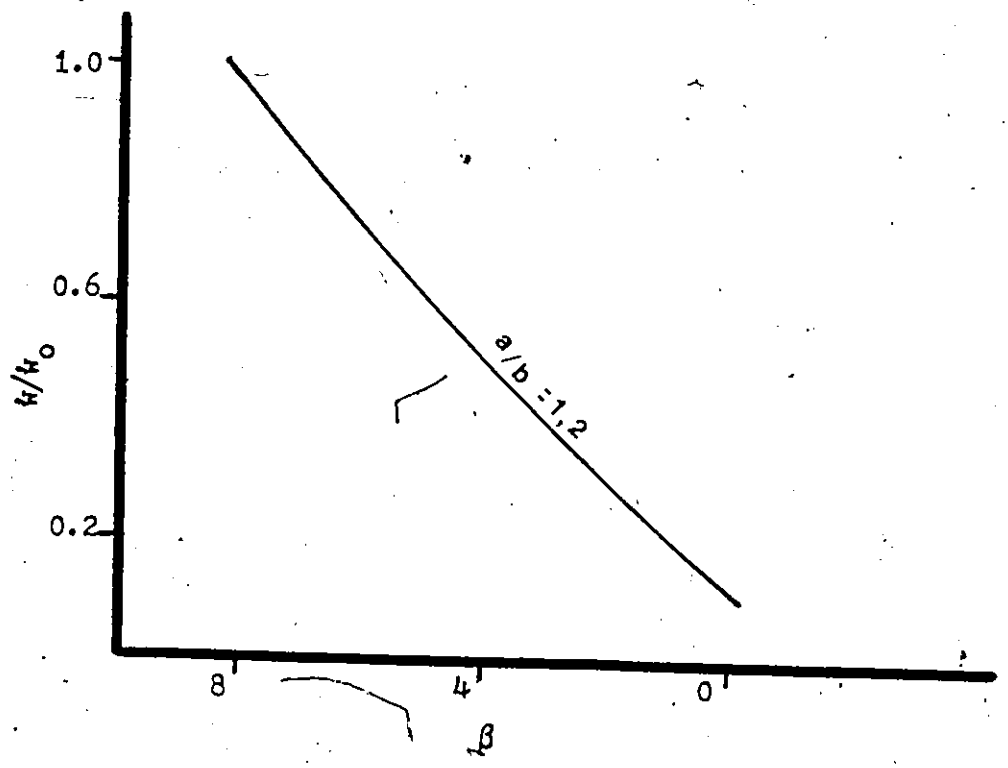

Figure 96. Debris flow deceleration ($\dot{w}/\dot{w}_o$) versus bottom slope (β). The velocity $\dot{w}_o$ is the highest velocity of the flow and $\dot{w}$ are lower velocities on gentler slopes.

Leopold and Wolman (1957, 1960) have shown empirically that for subaerial meandering streams, meander wavelength (λ) tends to be related to channel width (w) and radius of curvature (r_m) by:

$$\lambda = 10.9\ w \tag{44}$$

$$\lambda = 4.7\ r_m \tag{45}$$

while Inglis (1949) found that :

$$\lambda = 6.6\ w. \tag{46}$$

Relationships between meander amplitude (M_a) and width were determined by Leopold and Wolman (1957, 1960) to be

$$M_a = 2.7\ w^{1.1} \tag{47}$$

Table 7 shows predicted λ and M_a values from Equations (44) to (47) and estimated actual values for the track H chute. Two values of channel width, w, were used in the predictions, a minimum value of 65 m and a mean of 100 m. The results show 'ballpark' agreement for estimated actual values of λ and M_a using Equations (46) and (47) respectively, but less agreement for λ determined from Equations (44) and (45). However, as mentioned earlier, the downslope scale of the sidescan tracks is uncertain and measured values of λ and M_a may be considerably in error. These results, then, are somewhat inconclusive and comparisons of this

Empirical Relationship	Predicted (m) λ and M_a		Estimated (m) λ and M_a
	w=65m	w=100m	
$\lambda = 10.9\ w$	709	1090	500
$\lambda = 6.6\ w$	429	660	500
$M_a = 2.7\ w^{1.1}$	266	428	200
$\lambda = 4.7\ r_m$	1410		500

Table 7. Predicted Values of Meander Wavelengths (λ) and Amplitude (M_a) and Estimated Track H Values.

type would require accurate downslope measurements to determine if the subaerial relationships hold for submarine channels.

9.3.1.2 Arcuate Rotational Slides

As suggested earlier, the arcuate features described on the lower delta front sonagraphs are either individual scarp-blocks in a larger rotational slide, or are small, isolated rotational slides. The former explanation is the most likely, with the arcuate features resulting from upslope retrogression of the slide. However, in order to assess the stability of the slope to rotational slides, the slides must be treated as isolated features with circular slip faces.

Factors of safety for gravitationally induced rotational slides (S_R) and earthquake induced rotational slides (S_{R_E}) were determined for the isolated arcuate features at Par 82-008. Slide geometries with maximum depths to the slip surface from the sea bottom (Z_{max}) of 5 and 2.5 m were used for the analysis (Figure 97). Each slide was divided into 5 slices and the safety factor determined from Equation (36). Values of S_R range from 8.8 to 13 for a Z_{max} of 5 m, and from 5.8 to 8.7 for Z_{max} = 2.5 m. For earthquake accelerations of 0.08, S_{R_E} varies from 2.8 to 4.0 for Z_{max} = 5 m., and 2.3 to 3.3 for Z_{max} = 2.5 m. Accelerations of 0.11 further reduce S_{R_E} to 2.2 to 3.3 for Z_{max} = 5 m and to 1.8 to 2.8 for Z_{max} = 2.5 m. These results indicate that the factor of safety for rotational slides is reduced by decreasing distance to the slip face (Z_{max}) and by increasing earthquake accelerations. However, all safety factors are greater than 1. As suggested for translational

Par 82-008 $\beta = 3.8°$

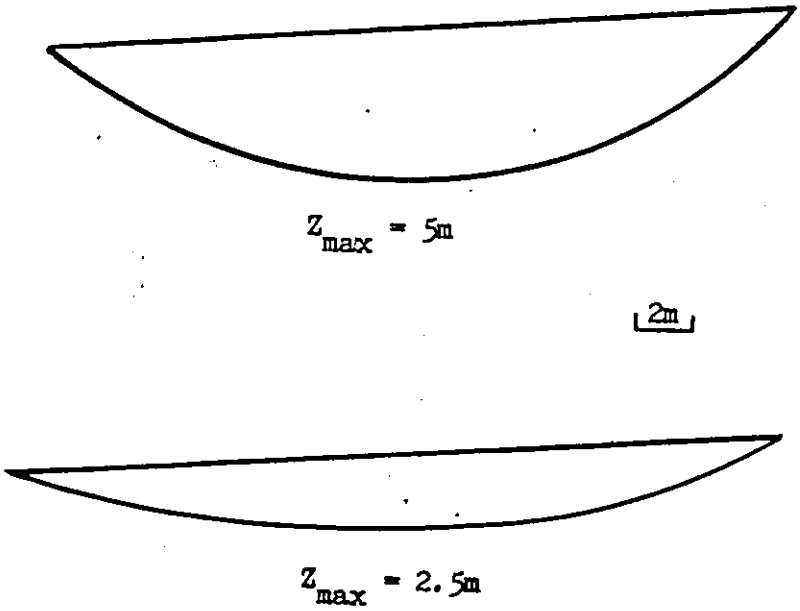

Figure 97. Slide geometry for arcuate rotational slides. The maximum depth to the slip surface is Z_{max}.

slides, gas generation and depositional loading may also reduce the slope stability.

Slide morphology indicates that upslope retrogression is occurring. The critical subsidence ratios ($\Delta h/Z_1$) for translational slides in this area range from 0.31 to 0.63. Assuming that these ratios also apply to rotational slides, then these values must have been exceeded for retrogression to occur.

9.4 Summary

On the basis of grain size trends and seismic characteristics, the subaqueous delta is divided into the delta front and prodelta. The sandy delta front is in turn partitioned into upper and lower zones.

The upper delta front is characterized by smooth/hyperbolic opaque and hummocky/hyperbolic opaque seismic facies, and the lower delta front by a hummocky/hyperbolic opaque facies. The opaque character of the facies reflects the sandy nature of bottom sediments, the hyperbolae represent a rugged, uneven surface resulting from slides and chutes and the hummocks represent large slides and chutes.

As suggested by the seismic records and confirmed by echograms and sonagraphs, the main morphologic components of the delta front are chutes and their associated depositional zones, and arcuate rotational slides. Three chute types occur: fan delta, small and large and sinuous. The beds of large chutes are coarser than interchute areas and may

display subaqueous levees. Depositional zones are characterized by a hummocky and very irregular topography. Arcuate rotational slides consist of a series of scarp-block features oriented across the slope.

Chutes are likely a result of slides and/or debris flow processes. Slopes on the delta front are too gentle for gravitationally-induced sliding to occur, and as such instability must result from excess pore pressures due to gas generation, rapid tidal drawdown and depositional loading, or from earthquake effects and wave loading. Debris flow plug thickness and the proportion of the channel width occupied by the plug both decrease as the chute becomes shallower. Debris flow velocities increase as chutes become shallower and decrease as slopes become gentler. A comparison of chute meander geometery with subaerial stream geometry is inconclusive.

Depositional zones are composed of remolded debris discharged at the seaward ends of large chutes. Depositional loading, possibly combined with earthquake loading, is a major source of sediment instability in these zones. The arcuate rotational slides are probably shallow and retrogressive and stable with respect to gravitational forces. Excess pore pressures and earthquake loading are essential in arcuate rotational slide initiation.

CHAPTER 10

PRODELTA

10.1 Introduction

The prodelta zone consists of the gently sloping (0.5° to 2.2°) portion of the subaqueous delta between the delta front and the moraine at the western end of the fjord. Seismic lines 2, 3 and 8 (Figures 44, and 62, 63, 64), grab samples Par 82-003 and 002 and cores Par 82-020, 019, 018 and 017 (Figure 45) provide the data base for this zone.

To this point, seismic facies A and B have been described for the (Pleistocene) lower sequence and facies a_1, a_2 and b have been described for the Holocene delta front. Five seismic facies are proposed for the prodelta, c_1 to c_5.

Grain size characteristics, using sieve and hydrometer techniques, were determined for the grab samples and for the top 10 cm. of each core. The cores were logged and measurements made of undrained peak shear strength, remolded shear strength and bulk density. A Torvane was used to determine the shear strength parameters (C_u) and as such the results are suitable for a total stress approach rather the effective stress analysis used in this study. The Torvane results,

then, are used only to show vertical strength variations in the cores.

The following discussion of the prodelta is divided into two parts. The first part is the sedimentologic-morphologic character of the prodelta and consists of descriptions of the five seismic facies and grain size and core log results. The second part examines the geotechnical properties of prodelta sediments and slope stability. This portion focuses on facies c_1 and c_4 because grabs and cores were available for these facies, providing geotechnical data for the stability analysis.

10.2 Sedimentology and Morphology

The following description of the sedimentologic-morphologic character of the prodelta begins with a description of the five seismic facies, followed by grain size data and core logs.

10.2.1 Seismic Facies

The five seismic facies determined for the prodelta are: facies c_1 - subparallel/hummocky, facies c_2 - even/wavy parallel/convergent, facies c_3 - reflection free, facies c_4 - even/wavy parallel, and facies c_5 - wavy parallel.

Facies c_1 - subparallel/hummocky

The surface of this unit has a hummocky appearance, with near-

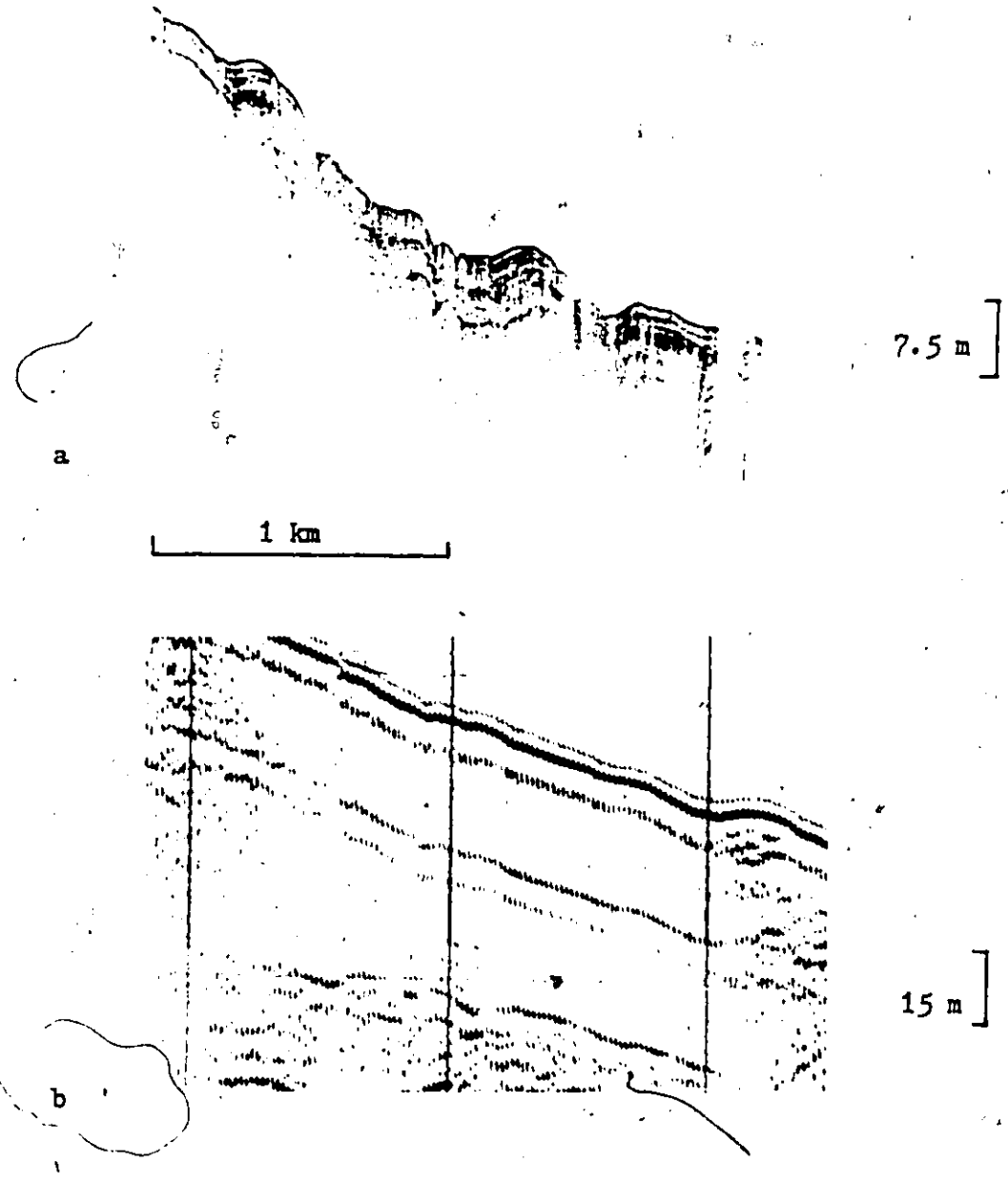

Figure 98. Seismic facies c_1 : a pinger, b airgun; from line 2.

surface reflectors parallel to subparallel and slightly wavy on the 3.5 kHz record (Figure 98a). On the air-gun record reflectors are poorly defined (light) and hummocky (Figure 98b). Reflector amplitude is variable, ranging from 1.5 to 2.5 m on the 3.5 kHz record and 8-13 m on the air-gun record, and continuity is moderate. The unit has a wedge external form E to W along the fjord with a proximal thickness of approximately 75 m and a distal thickness of 60 m. The across-delta (N. to S.) extent of this unit is difficult to determine because of the intense sidewall reflection on lines 2 and 3, but it does appear to be laterally continuous.

Upslope, facies c_1 is bounded by lower delta front facies b and downslope by facies A or c_2. The nature of the upslope boundary is difficult to discern. The contact with facies A is also indistinct but appears to be an onlap. Facies C_1 overlies facies B.

Facies c_2 - even/wavy parallel/convergent

Facies c_2 is found on lines 2, 3 and 8 (Figures 62, 63, ~~64~~), at two separate sites on lines 2 and 8 and one site on line 3. The surface of this facies is smooth to slightly crenulate or wavy, and there is considerable penetration by pinger energy (Figure 99a). The 3.5 kHz reflectors are well-defined and range from strong to weak. Reflection configuration ranges from even to wavy and parallel in upslope areas of the unit to even and convergent in downslope areas. On the air-gun record this facies shows roughly parallel moderately defined reflectors (Figure 99b). Amplitudes on the 3.5 kHz record are on the order of

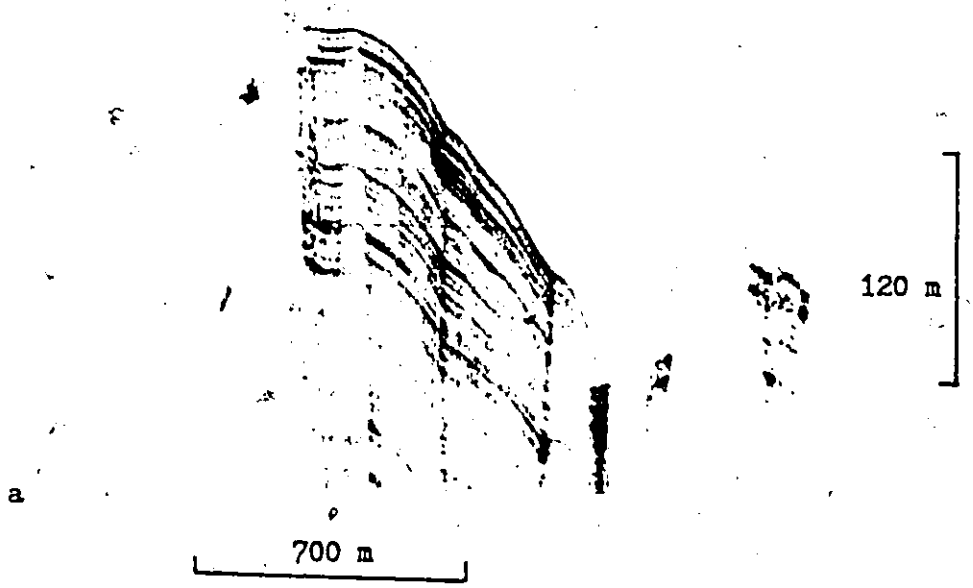

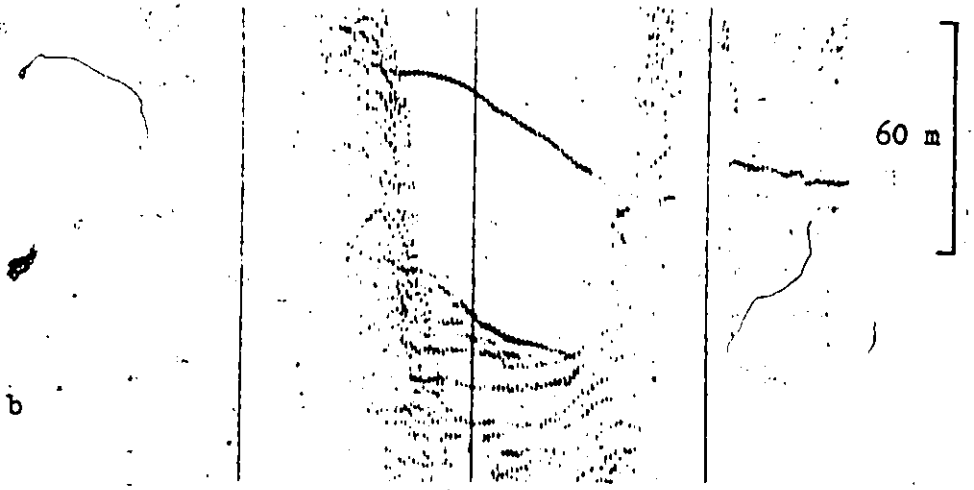

Figure 99. Seismic facies c_2 : a pinger, b airgun; from line 8.

4 m in a upslope areas and 0.7 m where the reflectors converge. Continuity of reflectors is high. Air-gun amplitudes are from 1.6 to 10 m and continuity good. The external form of the facies is difficult to determine because of side-wall reflections, but on line 8 appears to be a sheet approximately 50 m thick.

Facies c_2 is bounded upslope by either facies c_1 or facies A and downslope by facies c_3 or c_4. The contact with c_1 is obscured by side-wall effects and the contact with A is an onlap. The contacts with c_3 and c_4 are of special interest because they occur as onlaps along well developed faults. The faults and their effects on prodelta facies are discussed below. Facies c_2 overlies facies B.

Facies c_3 - reflection free

This facies is found on line 8 at two sites (Figure 62). The surface of this facies is smooth and anticlinal in form (Figure 100). Internally, reflections are very weak to absent on the 3.5 kHz record. Facies c_3 appears to be limited in lateral extent and extends to sub-ottom depths of around 50 m. The upslope and downslope boundaries are marked by well defined fault contacts with facies c_1 and c_4 respectively. Facies B underlies c_3.

Facies c_4 - even/wavy parallel

Facies c_4 is located near the western ends of lines 2, 3 and 8, to the east of the morainic feature (Figures 62, 63, 64). The surface

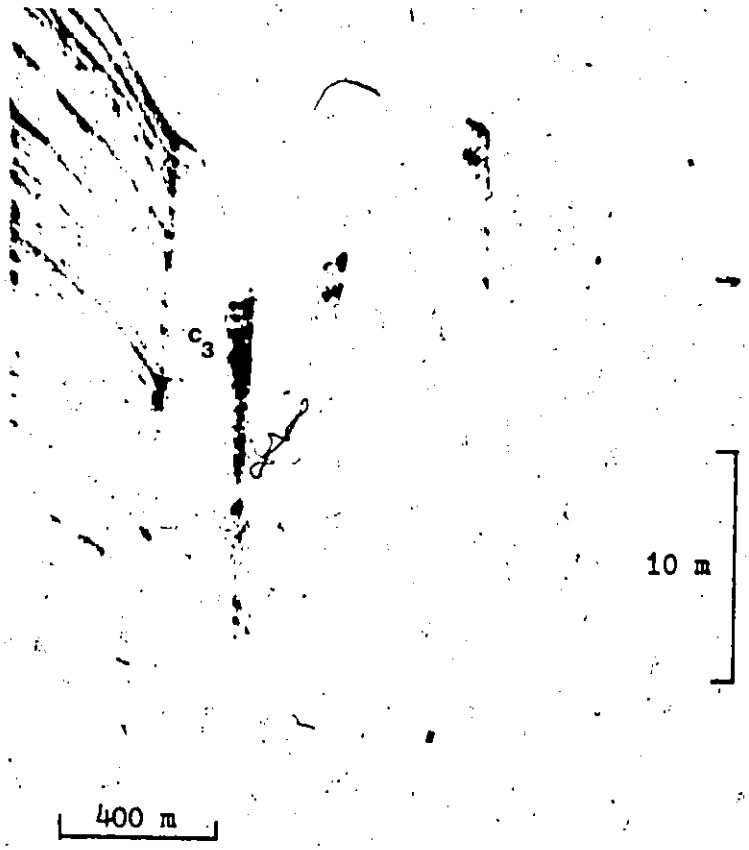

Figure 100. Seismic facies c_3 from pinger record of line 8.

of the unit varies from smooth to slightly wavy, with reflectors even to wavy, parallel and well-defined (Figure 101a). On the air-gun record reflectors are even, parallel and moderately-defined (Figure 101b). Reflector amplitude ranges from 1-2 m on the 3.5 kHz record and 5-8 m on the air-gun record, and continuity is good. The unit has a 'double' wedge form, becoming thicker (40 to 75 m) along (E to W) and across (S to N) the fjord.

Upslope, facies c_4 is bounded by facies c_2 or c_3 and downslope by c_2 or A. The contacts with c_2 and c_3 occur as onlaps against faults, and the contact with facies A as an onlap against the inclined moraine surface. Facies c_4 overlies facies B.

Facies c_5 - wavy parallel

Facies c_5 is found on line 3 (Figure 64) and is characterized by a wavy surface and wavy internal reflectors which are better defined on the 3.5 kHz record (Figure 102). The waves consist of broad anticlines separated by tight synclinal troughs. Reflection configuration is wavy and parallel with slight downslope convergence. Reflector amplitudes are 1.5 to 3 m on the 3.5 kHz record and 2 to 10 m on the air-gun, and 3.5 kHz reflector continuity is high. The external form of facies c_5 is difficult to determine but appears to be a 2-dimensional sheet on the E. to W. direction. Upslope and downslope this facies contacts facies A as an onlap and overlies facies B.

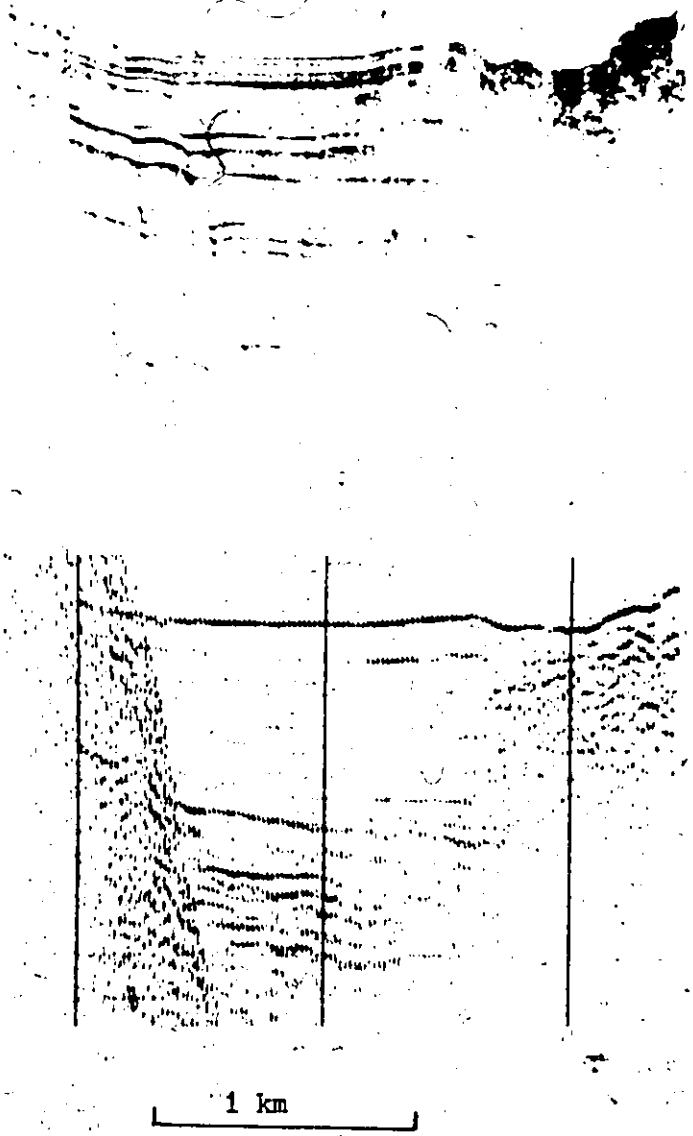

Figure 101. Seismic facies c_4: a pinger, b airgun; from line 8.

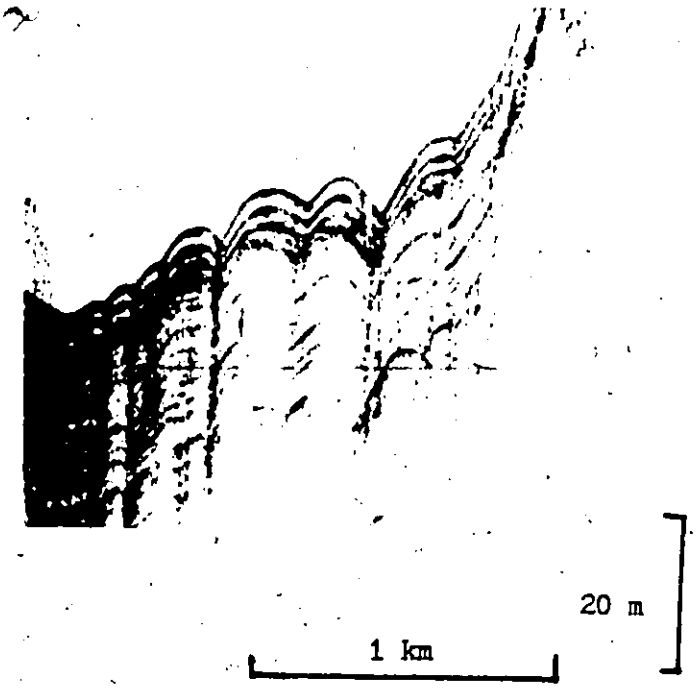

Figure 102. Seismic facies c_5 from the pinger record of line 3.

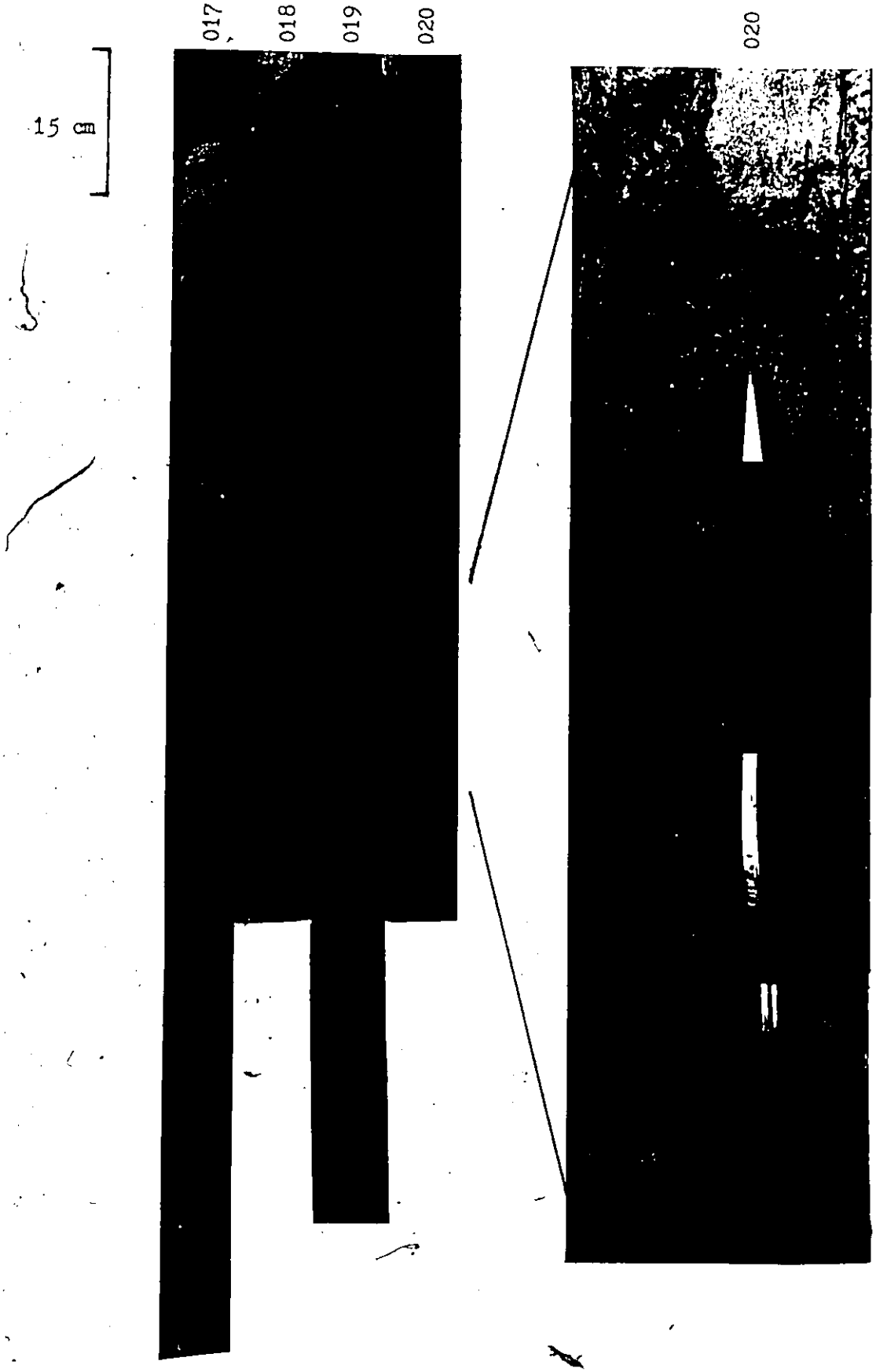

Figure 103. Cores Par 82-020 to 017.

10.2.2 Sediment Characteristics

The sediment characteristics of the prodelta are described in terms of grain size trends and core logs. There is little variation in grain size characteristics proximally to distally across the prodelta (Figure 67). Par 82-003 consists of very poorly sorted silt (M_z) with a clay content of 38%. Samples from Par 81-002 to Par 82-017 are composed of very poorly sorted clay with clay (M_z) contents of 55 to 58%. Par 82-020 is composed of very poorly sorted clay with 56% clay. There is somewhat of a decrease in grain size, little change in sorting and an increase in clay content seaward along facies C_1 from Par 82-003 to 002.

As with grain sizes, there is little variability in core logs from the prodelta. Typically the short cores are dominated by homogenous grey mud punctuated by sand and silt laminations (Figure 103). The mud is massive to weakly-laminated grey (5 Y 5/1) clay with indistinct darker grey (5 Y 4/1) bands and black organic specks. Contacts between the darker and lighter muds are gradational.

The coarser sand and silt laminations are usually dark grey (5 Y 4/1), graded and appear to fine in a seaward (E to W) direction. Basal contacts are sharp and regular and upper contacts sharp to gradational. The laminations often contain peat and fragments of wood and shell. Individual logs for cores Par 82-020, 019, 018 and 017 are presented on Figures 104-107 respectively, with a core log key on Figure 104.

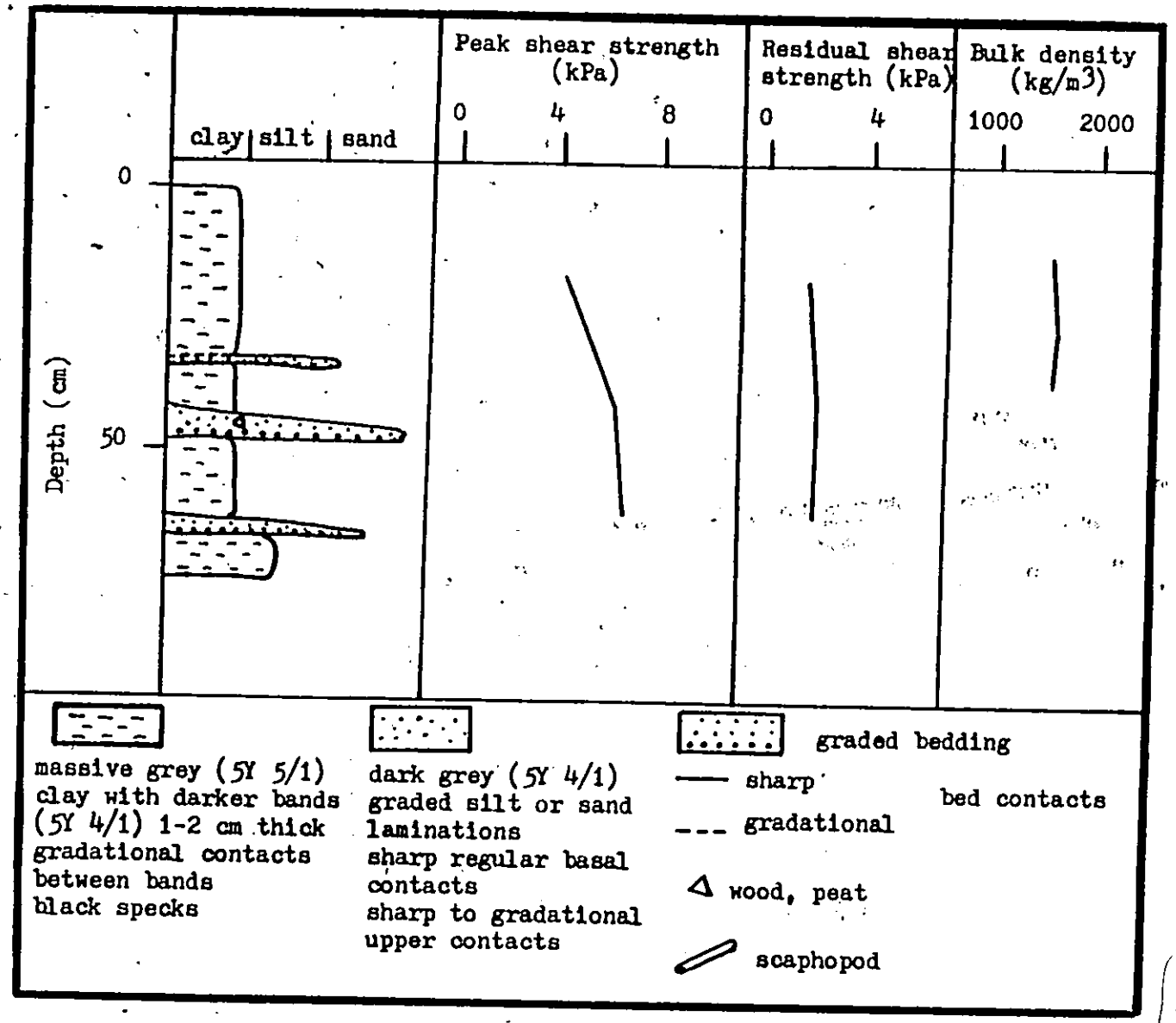

Figure 104. Core log and geotechnical properties of Par 82-020.

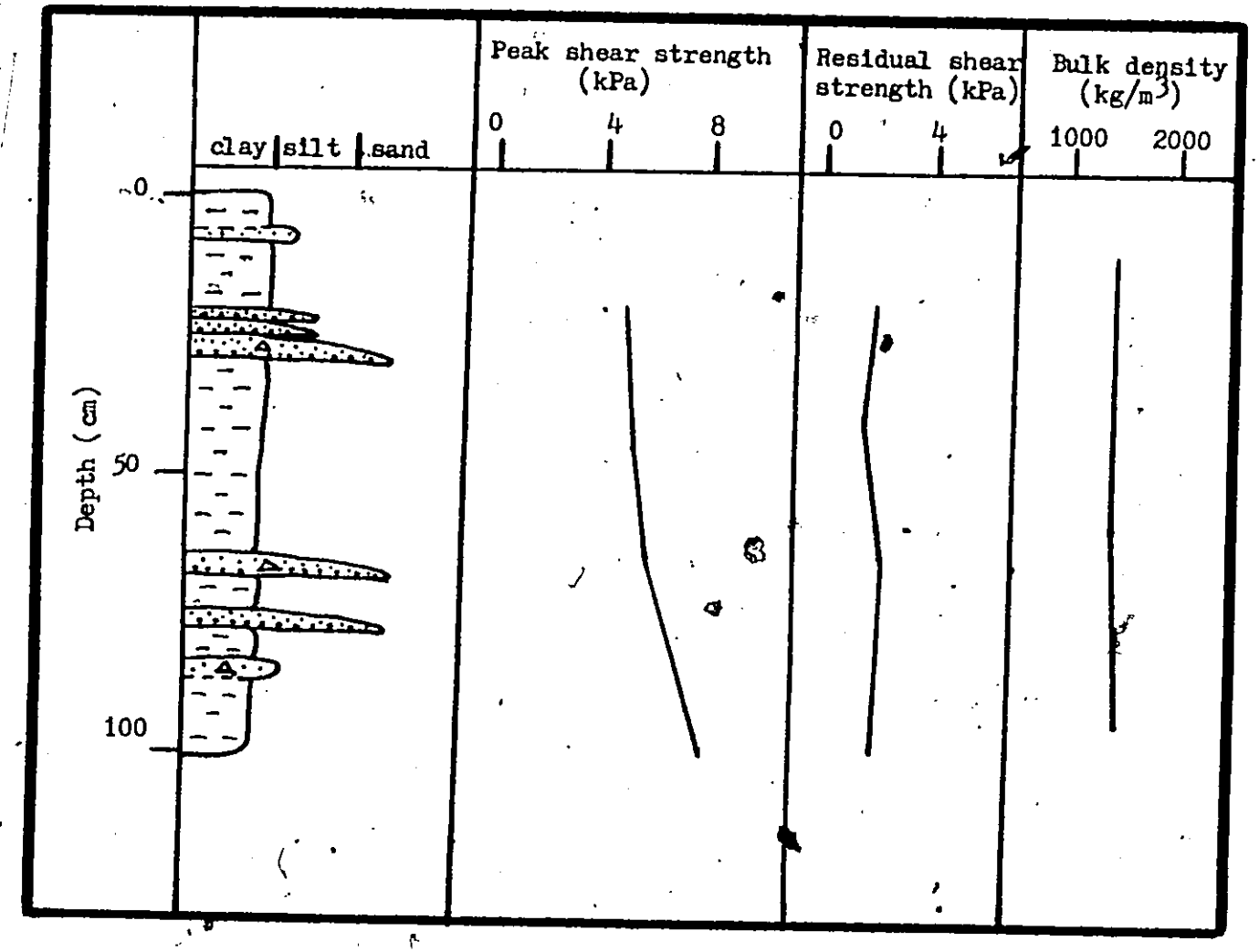

Figure 105. Core log and geotechnical properties of Par 82-019.

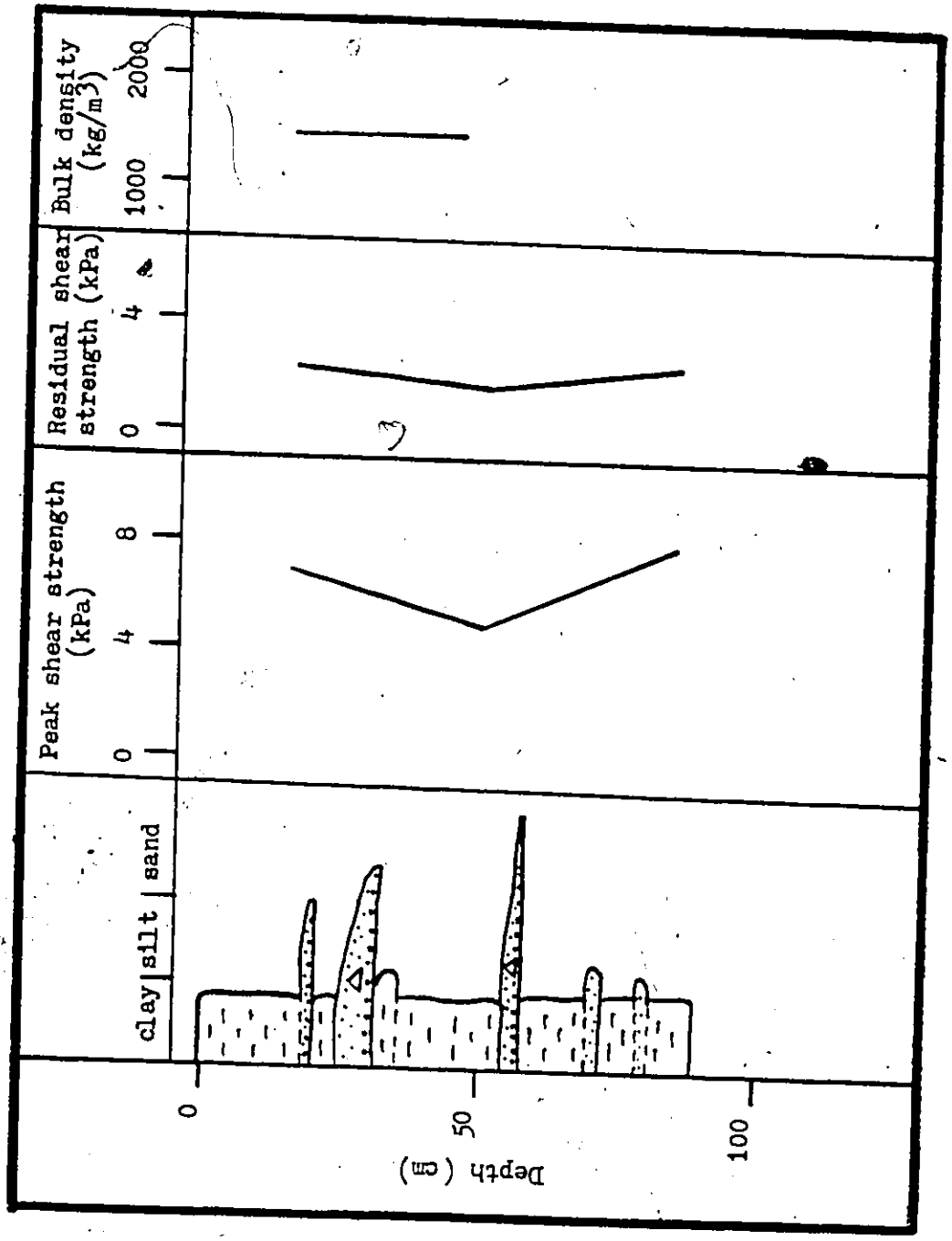

Figure 106. Core log and geotechnical properties of Par 82-018.

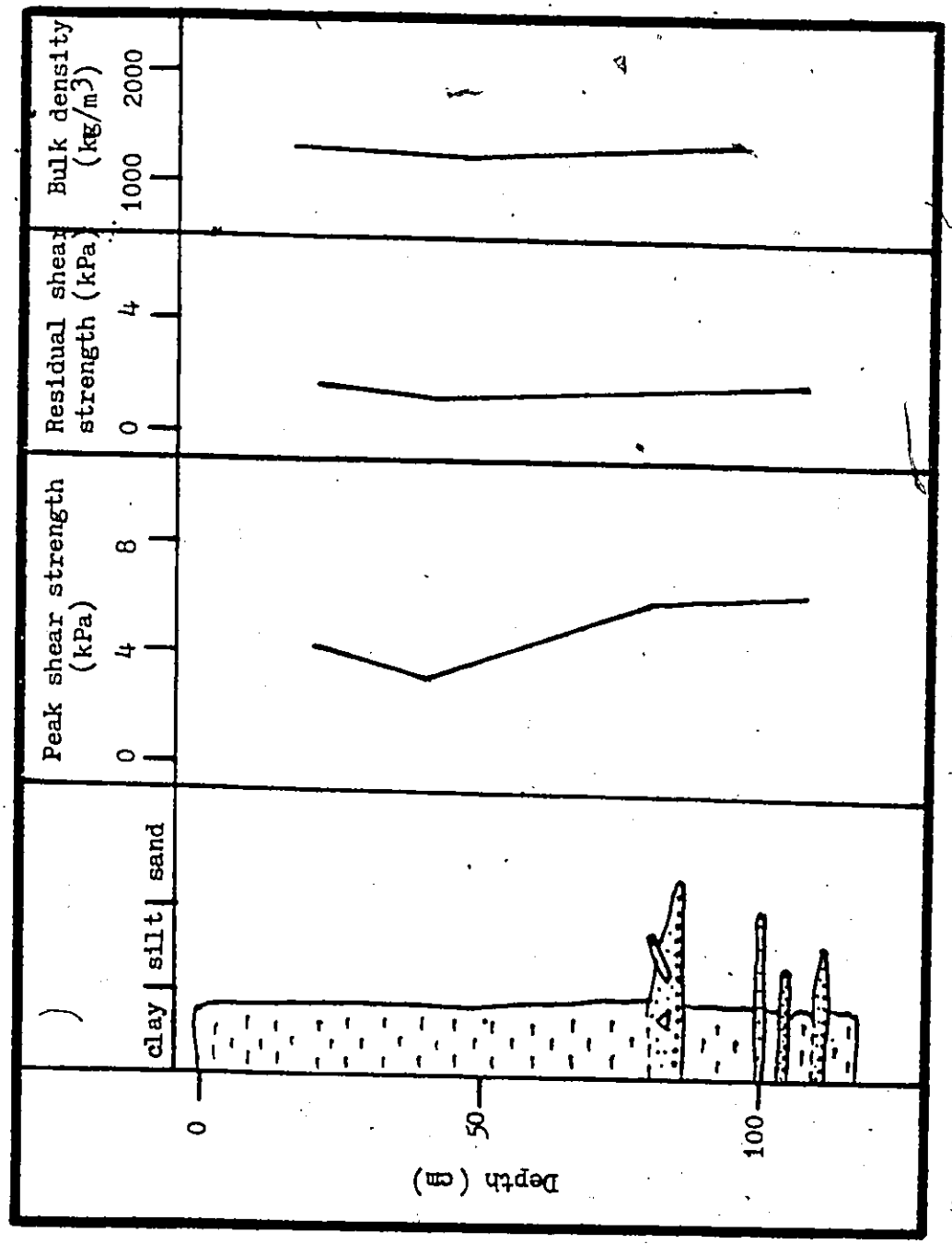

Figure 107. Core log and geotechnical properties of Par 82-017.

The core sediments can be interpreted in terms of two major depositional processes. The silt to clay size, massive to weakly-laminated structure and gradational contacts of the mud indicate it has settled from suspension from the surface. The coarser size, internal grading and sharp basal contacts of the silt and sand laminations suggest deposition by sediment gravity flows, most likely turbidity currents, generated on the delta front or along fjord walls.

10.3 Geotechnical Character and Sediment Stability

10.3.1 Geotechnical

Bulk density values were determined for the prodelta grab samples and cores. For the cores, peak undrained shear strength and remolded shear strength were measured with the Torvane. The bulk density and Torvane results are discussed below. For the effective stress analysis of sediment stability that follows, cohesion (C') is assumed equal to zero and the internal friction angle (ϕ') assigned values of 20-35° (Chowdhury, 1978; Morgenstern, 1967).

Grab samples Par 82-002 and 003, and cores Par 81-020 are located on facies c_1, and cores Par 82-019, 018 and 017 on facies c_4. Bulk density values for the grab samples are 1,568 and 1,419 for Par 82-003 and 002 respectively. The cores show little vertical variation or trends in bulk density (Figures 104 to 107), with mean values ranging from 1,300 to 1,600.

Vane-determined values of peak shear strength generally increase with depth in the cores, from values of 4 to 5 kPa at the top to 6 to 8 kPa near the bottom (Figures 104 to 107). Values for Par 82-107 are somewhat lower than the other cores.

Remoulded shear strengths vary from 1.6 to 2.4 kPa and show little variation with depth in cores. The sensitivity of clays can be expressed by the ratio of the peak undrained shear strength over the remoulded shear strength. Sensitivities are low (2.4 to 3.9) for the prodelta cores, typical of normally consolidated clays (Selby, 1982).

10.3.2 Sediment Stability

Sediment stability with respect to translational slides is discussed below for grab sample and core sites from seismic facies c_1 and c_4, and a rotational slide analysis prepared for facies c_1. Following this is a discussion of the causes and effects of faulting in the prodelta, and finally a creep analysis is provided for the folds on facies c_5.

Translational Slides

Values of the factor of safety, S, for prodelta sample and core sites vary from a low of 12 to over 70 (Figure 83), indicating that gravitationally-induced stresses are insufficient to cause failure. Pore pressures required to initiate failure have $u/\gamma_w Z$ ratios of 1.3 to 1.5 (Figure 84) and $u/\gamma Z$ ratios 0.8 to 1.0 (Figure 85). These results

suggest that pore pressures in excess of hydrostatic and approaching geostatic would be required to produce translational slides. Excess pore pressures in the prodelta would most likely result from gas generation or depositional loading. Gas bubbles and the distinctive odour of gas were noted in prodelta cores, indicating that the first of these mechanisms is operational. Depositional loading effects are examined below.

Factors of safety, S_E, for earthquake accelerations of 0.08 range from 1.1 to 2.6 (Figure 89a) and for accelerations of 0.11 from 0.8 to 2.0 (Figure 89b). The values of less than 1 for the lower bounds of the cores indicate that earthquakes may be capable of initiating shallow translational slides on the prodelta.

Depositional load thicknesses required to initiate failure are on the order of 60 m to greater than 100 m (Figure 88), values that are virtually impossible. The addition of earthquake accelerations of 0.08 and 0.11 reduce load thicknesses to 0.5 to 16.5 and 0 to 10 m respectively (Figure 90). Debris flow or slide loads of these thicknesses are reasonable.

Critical subsidence ratios for slide retrogression, $\Delta h/z$, for the prodelta sites range from 0.1 to 0.9 (Figure 91). As with the delta front, the data are not available to compare these results with actual values.

Rotational Slides

The large hummocks on the lower delta front and facies c_1 of the prodelta can be interpreted in at least 3 ways: (1) as conformable drapes over underlying (facies B) features, (2) as depositional zones associated with chutes, or (3) as slump blocks related to large, deep-seated rotational slides. As can be seen on Figure 98a, some hummocks are separated by faults, suggesting that the slump block interpretation is the most likely one. Using Bishops's method (Equation 36) a 'post-mortem' analysis of a rotational slide with dimensions determined from facies c_1 can be attempted.

The downslope length of the large hummock on Figure 98a is 350m. The slip surface is assumed to be the surface of facies B, with a maximum distance below the sea bottom (Z_{max}) of 75 m. The geometry of the slide is presented on Figure 108 and the geotechnical properties used are from Par 82-003. Factors of safety for gravitationally-induced slides range from 15.6 ($\phi' = 25°$) to 28.3 ($\phi = 3.5°$). These are reduced to 3.2 to 6.3 for earthquake acceleration of 0.08 and 2.5 to 4.9 for acceleration of 0.11. These values are all greater than 1, suggesting that excess pore pressures would be required to reduce sediment strength and cause a large, deep-seated rotational slide.

Faults

The large, deep-seated faults in the prodelta sediments have a major impact on seismic facies and morphology. The faults are inter-

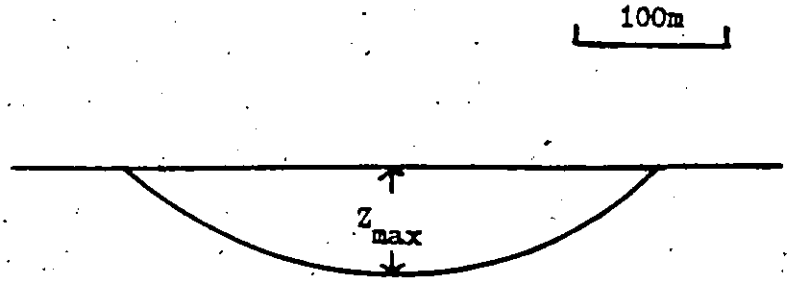

Figure 108. Geometry of deep-seated rotational slide in facies c_1 of prodelta.

preted as linear growth faults. This interpretation is based on the somewhat thicker strata and roll-over anticlines on the downthrown sides of the faults.

Growth faulting has at least three effects on seismic facies. First, the convergent reflectors of facies c_1 (Figure 98) appear to be a result of compression produced as the strata plunge into the fault. Second, the generation of roll-over anticlines produces some of the wavy configuration of prodelta reflectors. Third, the reflection-free configuration of facies c_3 may be a result of the faults that bound the facies upslope and downslope.

The reflection-free configuration of facies c_3 may be apparent or real. In the first case the strong reflective surfaces provided by the fault lines may cause acoustic interference across this facies (perhaps in a similar manner to side-wall reflections) producing an apparent lack of stratification on the record. In addition, Coleman (1976) suggests that mudflow or slide deposits with high water and gas contents may accumulate on the downthrown sides of growth faults and that dewatering and degassing of these sediments may occur along the fault plane. This could produce a gas accumulation and an acoustic 'bright spot' or reflection-free configuration. There is, however, no morphologic information which suggests that such processes (mudflows or slides) are occurring on the Bella Coola faults. A possible 'real' explanation is that stratification in c_3 has been broken down by intense deformation of the sediments related to the fault movements, producing a true reflection-free configuration. There is, however, no morphologic information which suggested that such processes (mudflows or slides) are

occurring on the Bella Coola faults.

The factors responsible for faulting are probably similar to those that cause other deformational processes such as sliding and folding. For the prodelta these factors would include gravity, excess pore pressure, earthquakes, differential consolidation, depositional loading and possibly diapirism (Watkins and Kraft, 1978).

Folds

At least three mechanisms could be responsible for the waves apparent on facies c_5. First, the waves may be conformable drapes over an underlying (facies B) surface. Second, a series of growth faults could produce waves through the generation of roll-over anticlines. Third, soil creep may generate regular folds. The first hypothesis is unlikely as the facies B surface does not appear to undulate in a regular manner. The second hypothesis is a distinct possibility because the synclinal troughs are associated with faults which may be growth faults. If creep processes are important, then the actual wavelengths should conform to predicted wavelengths using Hill et al.'s (1983) model (Equation 43).

Five wavelengths (F_L) were measured from Figure 102. These fall into two groups. The larger wavelengths of 187,206 and 146 m occur at the upper end of facies c_5 with bottom slopes of 0.5°. Farther downslope, as the bottom slope increases to 1.8°, the wavelengths decrease to 63 and 75 m.

Wavelengths were calculated from Equation (43) for bottom slopes

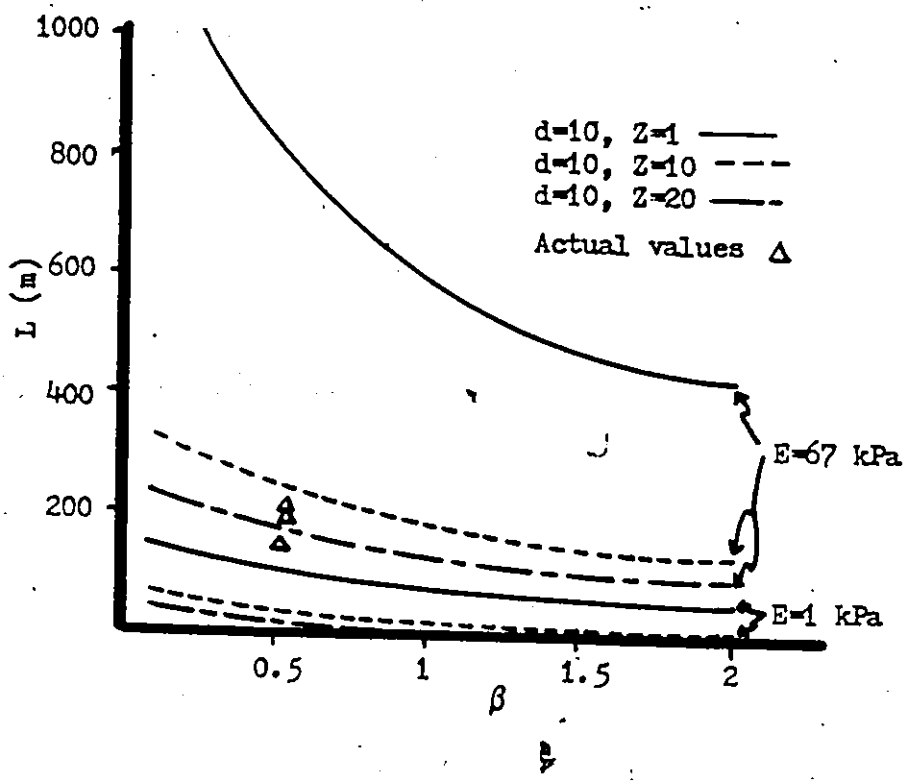

Figure 109. Predicted and actual fold wavelengths (F_L) from facies c_5 versus bottom slope (β). The layer thickness is given by d, Z is the distance from the sea bottom to the layer and E is Young's Modulus.

of 0.1 to 2.0°, a layer thickness (d) of 10 m and distances from the sea bottom to the layer (Z) of 1, 10 and 20 m. The critical geotechnical parameter in this analysis is Young's Modulus, E. Hill et al. (1983) used E = 1 kPa in their study of Beaufort Sea folds. However, Lambe and Whitman (1969) note that E can vary greatly between 50 to 1,000 times the value of the shear strength of the sediment. For Par 82-020, using $\phi = 20°$ and E = 50 s, a value of E of 67 kPa results. The predictions on Figure 109 use E values of 1 kPa and 67 kPa.

For slopes of 0.5 and 1.8°, the predicted wavelengths using E = 1 kPa are an underestimate of actual values, and using E = 67 kPa predictions are an over estimate. These results are somewhat inconclusive, but suggest that creep processes may be responsible for folding on facies c_5. More suitable results would require laboratory determination of E from on site cores and a more sophisticated layer model.

10.4 Summary

Prodelta sediments consist of massive, grey, poorly sorted clays deposited from suspension punctuated by graded sand and silt laminations deposited by turbidity currents. A variety of deformational processes have acted on the sediments and have produced five seismic facies.

Large-scale and deep-seated rotational slides have resulted in the occurrence of a subparallel/hummocky facies (C_1) just seaward of the lower delta front. Growth faults are associated with an even/wavy parallel/convergent facies (C_2) and a reflection free facies (c_3).

Faulting, or folding due to creep, has produced the degree of waviness and disruption in an even/wavy parallel facies (c_4). Creep is likely responsible for folding in the intensely folded wavy parallel facies (c_5).

A variety of factors have contributed to sediment instability and deformation in the prodelta zone. Included are gravitational forces, excess pore pressures generated by gas production or depositional loading, earthquake loading and tectonic activity, slide retrogression, differential consolidation of sediments and possibly diapiric activity.

SECTION IV - SUMMARY

CHAPTER 11

SEDIMENTATION IN THE BELLA COOLA DELTA AND NORTH BENTINCK ARM

Fjord-head deltas are a special kind of delta controlled by:

a) a contributing basin situation in steep, mountainous terrain that is often partly glacierized

b) a high energy fluvial system transporting sand and gravel bedload

c) a long, narrow and deep receiving basin

d) a Holocene history.

The objective of this thesis was to examine sedimentation in the Bella Coola delta, a fjord-head delta situated within the Coast Mountains of British Columbia. This has been accomplished by focussing on three themes:

A River Mouth Processes and Responses. Data collection for the analysis of river mouth morphodynamics consisted of effluent deceleration and expansion measurements and

distributary mouth mapping. The results were then compared with proposed morphodynamic models. Analyses of river mouth processes are vital because river mouths are the dynamic dispersal points of river-derived sediments and as such are the most fundamental elements of deltaic systems.

B Subaqueous Delta Morphology and Stability. The morphologic information for the subaqueous delta, obtained from echograms, seismic profiles and sidescan sonar tracks, was assessed for stability using effective stress methods. Subaqueous deformation is an important delta-forming process in steeply-sloping and earthquake-prone fjord-deltas in British Columbia.

C Sediment Package. The characteristics of the North Bentinck Arm - Bella Coola delta sediment package were determined from seismic stratigraphy and sample data. Such information is always relevant because 'the present is the key to the past'.

The principle conclusions relating to each theme are summarized below. More detailed summaries are provided in individual chapters.

A. 1. The large tidal range (3.9 m. mean range and 5.9 m large range) does not generate strong currents at river mouths. The main influence of the tide is to change the location and nature of the zone of marine - riverine interaction, producing a high tide and a low tide outlet for each distributary.

2. During high tides, frictional forces dominate as the efflu-

ent disperses as a plane jet over the delta plain (Figure 41). Four morphodynamic zones have been defined for the North Channel. Zone 0 is situated within the distributary channel and as such is dominated by channel processes. Zone 1 is friction dominated, composed of gravel and cobbles and is characterized by rapid effluent deceleration and restricted lateral expansion of 5 to 8°. Zone 2 is also friction controlled, with rapid deceleration and lateral expansion of 16-18°. A large radial distributary mouth bar that is gravel proximally and sand distally is related to Zone 2. The gravel portion of the bar features algal-covered gravel and cobbles and flow-parallel lobes surfaced by transverse ribs. Current ripples, sand waves, combined wave-current ripples, and wave-formed bars and ripples characterize the sandy portion of the bar. Zone 3, seaward of the break in slope between the subaerial and subaqueous delta, is a zone of turbulent diffusion, internal hydraulic jump and some deceleration. Seaward of Zone 3 is Zone 4, which is buoyancy dominated with little effluent deceleration. The high tide outlet best corresponds with Wright's (1977) friction dominated morphodynamic model.

3. At low tide, forces related to inertia, friction, buoyancy and an internal hydraulic jump are all important as the effluent disperses over saline basin water (Figure 42). Five morphodynamic zones define the low tide outlet. Zone 0 is landward of the outlet and controlled by channel proces-

ses. Zone 1 is friction dominated, with a confined lateral spreading of 5-8°, and functions only when the outlet is located on the subaerial delta. A gently landward-sloping, gravel-covered distributary mouth bar back and a horizontal sand and gravel bar crest are associated with these zones. Seaward of the break in slope between the subaerial and subaqueous delta is Zone 3, an area of extremely rapid deceleration due to an internal hydraulic jump; and of lateral expansion of 11-12°. The bar front in Zone 3 experiences rapid deposition of sand and gravel and is inclined at slopes up to 15°. Zones 3, 4 and 5 are dominated by buoyant forces, expand laterally at 13° and display minor decleration or acceleration. The low tide outlet effluent dynamics are qualitatively best approximated by Bate's (1953) plane jet model. Morphologically, the low-tide outlet is a combination of middle ground and lunate patterns.

B. 1. The subaqueous delta consists of a proximal sandy delta front and a distal silt-clay prodelta. The delta front extends 4 km offshore to depths of 275 m and slopes at 2.2 to 15°. The prodelta occupies an area 4 to 15 km offshore with maximum depths of 550 m and slopes of 0.5 to 2.2°.

2. The main morphologic components of the delta front are chutes and their depositional zones, and arcuate rotational slides. Chutes are erosional gullies, produced by debris flows or turbidity currents, that are situated on the steeper slopes of the upper delta front. As slopes decrease

downslope, the chutes deposit sediment lobes. Small, shallow, retrogressive, arcuate rotational slides occur between and within chutes. Large, deep-seated rotational slides are found in distal delta front and proximal prodelta areas and the distal prodelta is dominated by growth faults and folds.

3. Sediment instability and deformation on the subaqueous delta is a result of a number of forces. Gravitational forces, earthquake loading and excess pore pressures produced by gas generation are important in all subaqueous areas. On the delta front, additional factors include oversteepening of distributary mouth bar fronts, rapid tidal drawdown, wave loading, depositional loading and retrogression. Differential consolidation of sediments and diapiric activity may also produce instability.

C. 1. The North Bentinck Arm - Bella Coola Delta sediment package is defined in terms of two seismic sequence units, an upper and a lower (Figure 110). The sequence boundary is indicated by a highly reflective surface, an erosional truncation of lower sequence reflectors and facies changes.

2. The lower, probably Pleistocene sequence is composed of two facies. One facies is interpreted as glacial moraines associated with grounded ice, and the other as being glaciomarine in origin.

3. The upper sequence is the Bella Coola delta. The detailed stratigraphy beneath the delta plain and delta front is

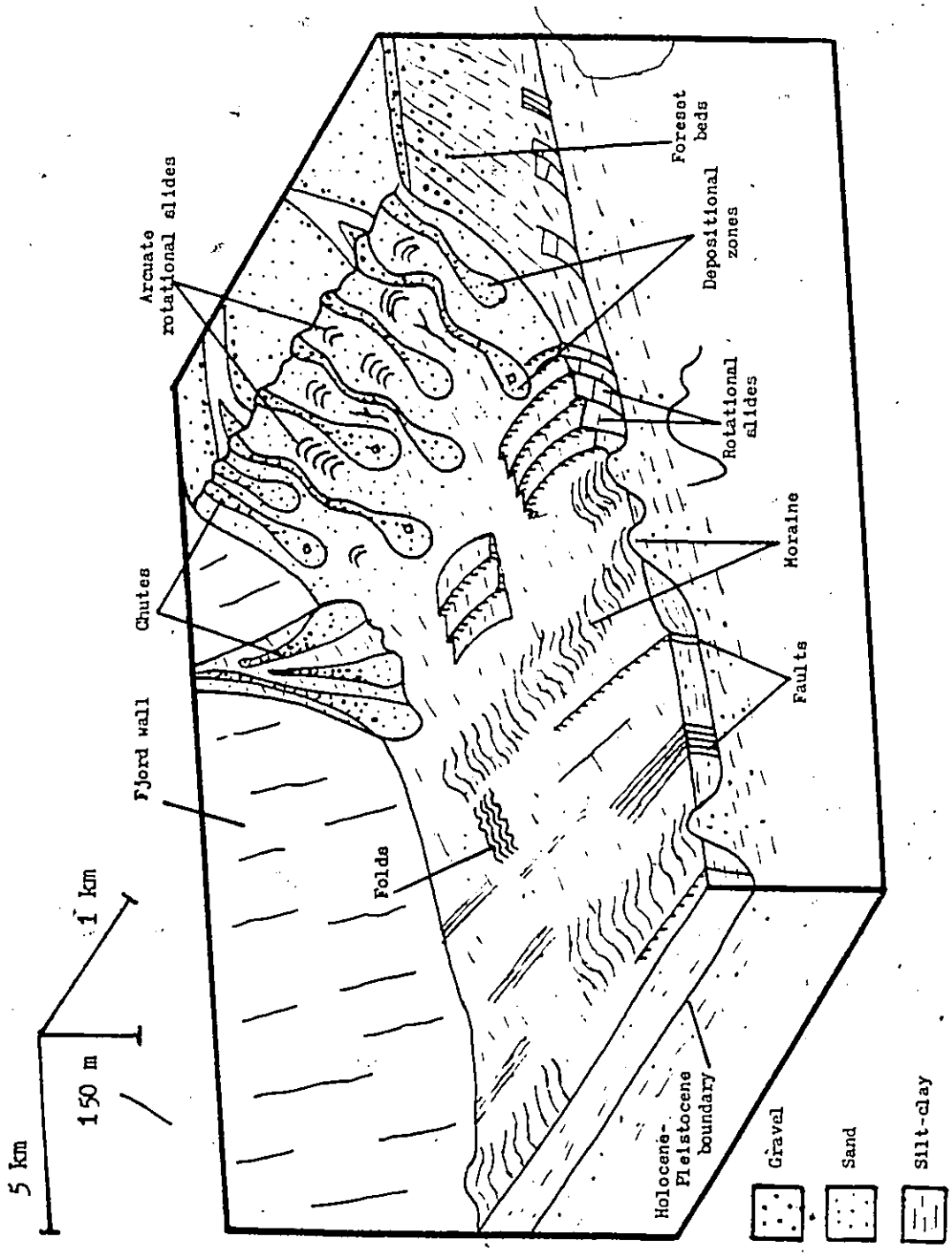

Figure 110. Block diagram summarizing the stratigraphy and morphology of the subaqueous delta and North Bentinck Arm.

largely unknown, but likely consists of topset and foreset beds of the Gilbert delta model. The delta plain stratigraphy is probably well stratified sands and gravels related to distributary channel migration, along with minor laminations of rippled sand and peat associated with the sand flats. Steeply sloping delta front (foreset) beds would be composed of sand and mud laminations resulting from deposition from suspension, matrix-supported sands and gravels related to debris flow deposition in chutes and depositional zones, graded sand laminations from turbidity currents and deep or shallow rotational slide features containing a zone of deformed (slip-surface) beds between undisturbed beds. Prodelta (bottomset) sediments are composed of massive silts and clays deposited from suspension and graded sand and silt laminations from turbidity currents. Large deep-seated rotational slide features occur in proximal prodelta areas. Further offshore, growth faults have displaced beds and produced roll-over anticlines on downthrown sides. Soft sediment folding, probably associated with creep processes, has produced a series of broad anticlines and tight, faulted synclines.

BIBLIOGRAPHY

Albertson, M.L., Dai, Y.B. Jenson, R.A. and Rouse H. (1950). Diffusion of submerged jets. Trans. Am. Soc. Civ. Eng., Vol. 115, pp. 693-697.

Almagor, G. and Wiseman, G. (1982). Submarine slumping and mass movements on the continental slope of Israel. In: Saxov, S. and Nieuwenhuis, J.K. (Editors), Marine Slides and Other Mass Movements. Plenum Press, New York, pp. 95-128.

Axelson, V. (1967). Laitaure Delta. Geografiska Annaler, Vol. 49, pp. 1-27.

Basham, P.W. (1983). New seismic zoning maps for Canada. GEOS, Vol. 72, No. 3, pp. 10-12.

Bates, C.C. (1953). Rational theory of delta formation. Am. Assoc. Petrol. Geol. Bull., Vol. 37, pp. 2119-2161.

Bell, L.M. (1975). Factors influencing the sedimentary environments of the Squamish River delta in South Western Britsh Columbia. Unpubl. M.A.Sc., thesis, University of British Columbia, Vancouver, 145 p.

Bell, L.M. and Kallman, R.J. (1976). The Kitimat River estuary, status of environmental knowledge to 1976. Canada Department of Environment, Regional Board, Pacific Region, Estuary Working Group, Special Estuary Series, no. 6, 296 p.

Bishop, A.W. (1955). The use of slip circles in the stability analysis of earth slopes. Geotechnique, Vol. 5, pp. 7-17.

Blatt, H., Middleton, G.V., and Murray, R.G. (1980). Origin of Sedimentary Rocks. Prentice-Hall Inc., New Jersey, 782 p.

Bondar, C. (1970). Considerations theoreques sur la dispersion d'un courant liquide de densite redruite et a reveau libre, dans un massin contenant un liquide d'une plus grand desnite. Symposium on the Hydrology of Deltas, UNESCO, Vol. 11, pp. 246-256.

Bonham-Carter, G.F. and Sutherland A.I. (1966). Diffusion and settling of sediments at river mouths: A Computer Simulation Model. Gulf Coast Assoc. Geol. Soc. Trans., Vol. 17, pp. 236-238.

Borichansky, L.S. and Mikhailov, V.N. (1966). Interaction of river and sea water in the absence of tides. In: Scientific Problems of the Humid Tropical Deltas and their Implications. UNESCO, pp. 175-180.

Bornhold, B.D. (1983). Sedimentation in Douglas Channel and Kitimat Arm. Can. Tech. Rep. Hydrogr. and Ocean Sci., Vol. 18, pp. 88-114.

Bouma, A.H. (1962). Sedimentology of Some Flysh Deposits. Elsevier, Amsterdam, 168 p.

Brown, L.F. and Fisher, W.L. (1979). Principles of Seismic Stratigraphic Interpretation. Austin, Texas, 125 p.

Buller, A.T. and McManus, J. (1979). Sediment sampling and analysis. In: Dyer, K.R. (Editor), Esturaine Hydrography and Sedimentation, Cambridge University Press, Cambridge, pp. 87-431.

Busch, W.H. and Keller, G.H. (1983). Analysis of sediment stability on the Peru-Chile continental slope. Mar. Geotech., Vol. 5, No. 2, pp. 181-211.

Carson, M.A. (1971). The Mechanics of Erosion. Pion Limited, London, 174 p.

Carson, M.A. (1977). On the retrogression of landslides in sensitive muddy sediments. Can. Geotech. Journal, Vol. 14, pp. 582-602.

Chowdhury, R.N. (1978). Slope Analysis. Elsevier Scientific, Amsterdam, 423 p.

Church, M.A. (1981). Pattern of instability in a wandering gravel channel. In: Modern and Ancient Fluvial Systems: Sedimentology and Processes, Abstracts. University of Keele, U.K.

Church, M.A., and Russell, S.O. (1977). The characteristics and management of the Bella Coola River and tributaries at the Bella Coola Indian Reserve. Canada Department of Indian and Northern Affairs, 39 p.

Coleman, J.M. (1976). Deltas: Processes of Deposition and Models for Exploration. Continuing Education Publication Co. Ltd., Champaign, Il., 102 p.

Coleman, J.M. and S.M. Gagliano (1964). Cyclic sediments in the Mississippi deltaic plain. Trans. Gulf. Coast Assoc. Geol. Socs., Vol 14, pp. 67-80.

Coleman, J.M., Gagliano S.M. and Webb, J.E. (1964). Minor sedimentary structures in a prograding distributary. Marine Geol., Vol. 1, pp. 240-258.

Coleman, J.M. and Prior, D.B. (1980). Deltaic Sand Bodies. A.A.P.G. Short Course Education Course Note Series No. 15, Tulsa, Okla.

Coleman, J.M. and Prior, D.G. (1981). Subaqueous sediment instabilities in the offshore Mississippi River delta. In: Bourma et al. (Editors), Offshore Geologic Hazards, A.A.P.G. Education Course Note Series No. 18, pp. 5-1 to 5-47.

Coleman, J.M. and Wright, L.D. (1975). Modern River Deltas: Variability of process and sand bodies. In: Broussard, M.L. (Editor), Deltas: Models for Exploration. Houston Geol. Soc., pp. 99-149.

Crickmay, C.H. and Bates, C.C. (1955). Discussion of delta formation. Am. Assoc. Petrol. Geologists Bull., Vol. 39, pp. 107-114.

Dodimead, A.J. and Herlinveaux, R.H. (1968). Some oceanographic features of the waters of the central British Columbia coast. Fish. Res. Board Can. Tech. Rept. No. 70, 26 p.

D'Olier, B. (1979). Side-scan sonar and reflection seismic profiling. In: Dyer, K.R. (Editor), Estuarine Hydrography and Sedimentation, Cambridge University Press, Cambridge, pp. 57-87.

Dott, R.H. (1963). Dynamics of subaqueous gravity depositional processes. A.A.P.G. Bull., Vol. 47, pp. 104-108.

Edwards, M.B. (1980). Glacial Environments. In: Reading, H.G. (Editor), Sedimentary Environments and Facies, Elsevier, New York, pp. 416-435.

Esrig, M.I. and Kirby, R.C. (1977). Implications of gas content for prediction of stability of submarine slopes. Marine Geotech., Vol. 2, pp. 753-766.

Fisher, W.L., Brown, L.F., Scott, S.J. and McGowen, J.H. (1969). Delta systems in the exploration for oil and gas: Bureau Econ. Geol. Texas.

Fisk, H.N. (1944). Geological investigation of the alluvial valley of the lower Mississippi River. U.S. Army Corps. of Engr. Mississippi River Commission, Vicksburg, Miss.

Fisk, H.N. (1947). Fine-grained alluvial deposits and their effects on Mississippi River activity. U.S. Army Corps. of Engr., Mississippi River Commission, Vicksburg, Miss.

Fisk, H.N. (1955). Sand facies of recent Mississippi delta deposits. Proc. 4th. World Petrol. Congr., Rome, Sec. 1, pp. 377-398.

Fisk, H.N. (1960). Recent Mississippi River Sedimentation. In: E. Aelst (Editor), 4th. Congress porer L'avancement etudes de stratigraphie et de geologie du Carbonifere, Heerlen, Compte Rednu, Vol. 1, pp. 187-199.

Fleming, B.W. (1976). Side-scan sonar, a practical guide. Int. Hydrographic Rev., Vol. 53, No. 1, pp. 65-92.

Folk, R. (1974). Petrology of Sedimentary Rocks. Hemphills, Austin, Texas, 170 p.

Folk, R. and Ward, W. (1957). Brazos River Bar, a study in the signifi-

cance of grain size parameters. Jour. Sed. Petrol., Vol. 27, pp. 3-27.

Galloway, W. (1975). Process framework for describing the morphological and stratigraphic evolution of deltaic depositional systems. In: M.L. Broussard, (Editor), Deltas, Models for Exploration, 2nd. ed., pp. 87-98.

Garvine, R.W. (1974). Physical features of the Connecticut River outflow during high discharge. Jour. of Geophys. Res., Vol. 79, pp. 831-846.

Garvine, R.W. (1975). The distributions of temperature and salinity in the Connecticut River estuary. Jour. Geophys. Res., Vol. 80, pp. 1176-1183.

Gilbert, G.K. (1884). The topographical features of lake shores. U.S. Geol. Surv. Annual Rept. 5, pp. 104-108.

Giles, R.V. (1977). Fluid Mechanics and Hydraulics. Schaumm's Outline Series, McGraw-Hill, 275 p.

Graf, W.H. and Acaroglu, E.R. (1966). Settling velocities of natural grains. Bull. Internat. Assn. Sci. Hydrology, Vol. 11, No. 4, pp. 27-43.

Gray, D.M. (1970). Principles of Hydrology. National Res. Coun. of Canada.

Hale, P.B., and McCann, S.B. (1982). Rhythmic topography in a mesotidal, low-wave-energy environment. Jour. of Sed. Petrol., Vol. 52, pp. 0415-0429.

Harms, J.C., Southard, J.B., Spearing, D.R., and Walker, R.G. (1975). Depositional Environments as Interpreted from Primary Sedimentary Structures and Stratification Sequences. Soc. Econ. Paleont. Mineralogists Short Course Lecture Notes, Vol. 2.

Hart, J.S. (1981). The physical environment of the Bella Coola valley. Hart-Mayal. Consultants, Tatla Lake, B.C., 46 p.

Hayashi, J. and Shuto N. (1967). Diffusion of warm water jets discharged horizontally at the water surface. Internat. Assoc. Hydraulic Res. 12th Congr. Proc. 4, pp. 47-59.

Hayashi, J. and Shuto, N. (1968). Diffusion of warm cooling water discharged from a power plant. Conf. Coastal Engr., Council Wave Res. 11th., Proc. London.

Henkel, D.J. (1970). The role of waves in causing submarine landslides. Geotechnique, Vol. 20, pp. 75-80.

Hill, P.R., Moran, K.M. and S.M. Blasco (1983). Creep deformation of slope sediments in the Canadian Beaufort Sea. Geomarine Let-

ters, Vol. 2, pp. 25-35.

Hooper, D.J. (1979). Hydrographic surveying. In: Dyer, K.R. (Editor), Estuarine Hydrography and Sedimentation, Cambridge University Press, Cambridge, pp. 41-57.

Inglis, C.C. (1949). The behaviour and control of rivers and canals. Research Pub., Poona (India), No. 13, 2 vols.

Johnson, A.V. (1970). Physical Processes in Geology. Freeman Cooper and Company, San Francisco, 577 p.

Johntson, W.A. (1921). Sedimentation of the Fraser River delta. Geological Survey of Canada, Memoir 125, 46 p.

Johnston, W.A. (1922). The character of the stratification of the sediments in the recent delta of Fraser River, British Columbia, Canada. Jour. of Geology, Vol. 30, No. 2, pp. 115-129.

Jopling, A.V. (1963). Hydraulic studies on the Origins of bedding. Sedimentology, Vol. 2, pp. 115-121.

Karlsrud, K. and Edgers, L. (1982). Some aspects of marine slope stability. In: Saxyov, S. and Nieuwenhuis, J.K. (Editors), Marine Slides and other Mass Movements. Plenum Press, New York, pp. 63-83.

Kashiwamura, M. and Yoshida S. (1967). Outflow pattern of fresh water issued from a river mouth. Coastal Engr. Japan, Vol. 10, pp. 109-115.

Kashiwamura, M. and Yoshida, S. (1969). Flow pattern of density current at a river mouth. Internat. Assoc. Hydraulic Res. 13th. Congr., Proc. 3, pp. 181-190.

Kashiwamura, M. and Yoshida, S. (1971). Transient acceleration of surface flow at a river mouth. Coastal Engr. Japan, Vol. 14, pp. 135-142.

King, C.A.M., and Williams, W.W. (1949). The formation and movement of sand bars by wave action. Geographical Journal, Vol. 12, pp. 70-85.

Komar, P.D. (1976). Beach Processes and Sedimentation. Prentice-Hall Inc., New Jersey, 429 p.

Lamke, T.W. and Whitman, R.V. (1969). Soil Mechanics. John Wiley, New York, 553 p.

Leaney, A.J., and Morris, S. (1981). The Bella Coola River Estuary Status of Knowledge to 1981. Special Series No. 10, Department of Fisheries and Oceans, West Vancouver, B.C., 226 p.

Leenhardt, O. (1974). Side-scan sonar - a theoretical study. Int.

Hydrographic Rev., Vol. 51, No. 1, pp. 61-80.

Leopold, L.B. and Wolman, M.G. (1957). River channel patterns, braided, meandering and straight. U.S. Geol. Survey Prof. Paper 282-B.

Leopold, L.B. and Wolman, M.G. (1960). River meanders. Geol. Soc. America Bull., Vol. 71, pp. 769-794.

Luternauer, J.L. and Finn, W.D.L. (1983). Stability of the Fraser River delta front. Can. Geotech. Jour. (in press).

Luternauer, J.L. and Swan, D. Kitimat submarine slump deposits: a preliminary report. In: Current Research, Part A; Geological Survey of Canada, Paper 78-1A, pp. 327-332.

McCann, S.B., Kostaschuk, R.A., Krawetz, M., and Matsushita, P. (in preparation). Sedimentation in a British Columbia fjord system.

McDonald, B.C. and Banarjee, I. (1971). Sediments and bedforms in a braided outwash plain. Can. J. Earth Sci., Vol. 8, pp. 1282-1301.

Middleton, G.V. and Hampton, M.A. (1976). Subaqueous sediment transport and deposition by gravity flows. In: Stanley, D.J. and Swift, D.J. (Editors), Maume Sediment Transport and Environmental Management, John Wiley and Sons, New York.

Middleton, G.V. and Southard, J.B. (1977). Mechanics of Sediment Movement. Tulsa, Okla.: Soc. Econ. Paleontologists and Mineral. Short Course Notes, No. 3.

Mikhailov, V.N. (1966). Hydrology and formation of river mouth bars. In: Scientific Problems of the Humid Tropical Zone Deltas and their implications. UNESCO, pp. 59-64.

Mitchum, R.M., Vail, P.R. and Sangree, J.G. (1977). Seismic stratigraphy and global changes of sea level, part 6: Stratigraphic interpretation of seismic reflection patterns in depositional sequences. In: C.E. Payton (Editor) Seismic Stratigraphy - Application to hydrocarbon exploration, A.A.P.G. Mem. 26, Tulsa Okla., 516 p.

Morgenstern, N. (1967). Submarine slumping and the initiations of turbidity currents. In: Richards, A.F. (Editor), Marine Geotechnique, pp. 189-220.

Nardin, T.R., Hein, F.J., Gorsline, D.S. and Edwards, B.P. (1979). A review of mass-movement processes, sediment and acoustic characteristics and contrasts in slope and base of slope systems versus canyon - fan, basin - floor systems. In: Doyle, L.J. and Pilkey, O.H., (Editors), Geology of Continental Slopes. S.E.P.M. Spec. Pub. No. 27.

Nelson, B.W. (1970). Hydrography, sediment dispersal, and recent historical development of the Po River Delta. Italy. In: Morgan J.P. (Editor), Deltaic Sedimentation: Modern and Ancient, Soc. Econ. Paleontologists and Mineralogists Spec. Publ. 15, pp. 152-184.

Pearce, A.F. (1966). Critical Reynolds Number for fully-developed turbulence in circular submerged water jets. Nat. Mech. Engr. Res. Inst. Council for Sci. and Indus. Res. (Pretoria, South Africa) CSIR Rept. MEG475.

Prior, D.B. and Coleman, J.M. (1978a). Disintegrating, retrogressive landslides on very low angle subaqueous slopes, Mississippi delta. Mar. Geotech. Vol. 3, No. 1, pp. 13-30.

Prior, D.B. and Coleman, J.M. (1978b). Submarine landslides on the Mississippi delta front slope. Geoscience and Man Series, Vol. 19, pp. 41-53. School of Geosciences, Louisiana State Univ., Baton Rouge, La.

Prior, D.B. and Coleman, J.M. (1979). Submarine landslides - geometry and nomenclature. Zeits. fur. Geomorphologie, Vol. 23, No. 4, pp. 415-426.

Prior, D.B., Coleman, J.M., Suhayda, J.N. and Garrison, L.E. (1981). Submarine land-slides as they affect bottom structures. In: Bouma et al., (Editors), Offshore Geologic Hazards, A.A.P.G. Education Course Note Series No. 18, pp. 5-112 to 5-125.

Prior, D.B., Coleman, J.M. and Bornhold, D.B. (1983). Results of a known seafloor instability event. Geomarine Letters, Vol. 2, pp. 117-122.

Prior, D.B., Wiseman, W.J., and Bryant, W.R. (1981). Submarine chutes on the slopes of fjord deltas. Nature, Vol. 290, pp. 326-328.

Prior, D.B., Wiseman, W.J. and Gilbert, R. (1981). Submarine slope processes on a fan delta. Howe Sound, British Columbia, Geomarine Letters, Vol. 1, pp. 85-90.

Prior, D.B. and Suhayda, J.N. (1981). Application of infinite slope analysis to subaqueous slope stability. In: Bouma et al., (Editors), Offshore Geologic Hazards, A.A.P.G. Education Course Notes Series No. 18, pp. 5-76 to 5-93.

Richards, A.F. and Chaney, R.C. (1982). Marine slope stability, a geological approach. In: Saxov, S. and Nieuwenhuis, J.K. (Editors), Marine Slides and other Mass Movements. Plenum Press, New York, pp. 163-173.

Rodine, J.D. and Johnson, A.V. (1976). The ability of debris, heavily freighted with coarse clastic materials, to flow on gentle slopes. Sedimentology, Vol. 23, pp. 213-234.

Rouse, H. (1937). Nomogram for the settling velocity of spheres. Div. Geol. Geo. Exhibit D, Rept., Comm. Sedimentation (1936-37) Natl. Res. Council, Washington, D.D., pp. 57-64.

Russel, R.C.H. and Macmillan, D.H. (1952). Waves and Tides. London, Hutchinson.

Selby, M.J. (1982). Hillslope Materials and Processes. Oxford University Press, Oxford 264 p.

Scruton, P.C. (1956). Oceanography of Mississippi delta sedimentary environments. Am. Assoc. Petrol. Geol. Bull., Vol. 40, pp. 2864-2952.

Scruton, P.C. (1960). Delta-building and the deltaic sequence. In: F.P. Shepard et al. (Editor), Recent sediments, northwest Gulf of Mexico, Am. Assoc. Petrol. Geologists, Tulsa, Okla., pp. 82-102.

Sheriff, R.E. (1980). Seismic Stratigraphy. Int. Human. Res. Development Corp. Boston.

Smith, N.D., Venol, M.A. and Kennedy, S.K. (1982). Comparison of sedimentation regimes in 4 glacier-fed lakes. In: Davidson Arnott, Nickling and Fahey (Editors), 6th. Guelph Symposium on Geomorphology.

Stolzenbach, K.D. and Harleman, D.R.F. (1971). An analytical and experimental investigation of surface discharges of heated water. Mass. Inst. Tech., Ralph M. Parsons Lab. Water Resources and Hydrodynamics, Dept. of Civil. Engr. Rept. 135, 212 p.

Streeter, V.L., and Wylie, E.B. (1979). Fluid Mechanics. McGraw-Hill Inc., New York.

Suhayda, J.N., and D.B. Prior (1978). Explanation of submarine landslide morphology by stability analysis and rheological models. Proc., 10th Offshore Tech. Conf., Paper No. 3171, pp. 1075-1082.

Syvitski, J.P.M. (1979). Flocculation, agglomeration and zooplankton pelletization of suspended sediment in a fjord receiving glacial meltwater. In: Freeland, H.J., Farmer, D.M. and Levings, C.D. (Editors), Fjord Oceanography, Plenum Press, New York, pp. 615-625.

Syvitski, J.P.M. and Farrow, G.E. (1983). Structures and processes in bayhead deltas: Knight and Bute Inlet, British Columbia. Sedimentary Geology, Vol. 36, pp. 217-244.

Tempest, W. (1974). Bella Coola River flood and erosion control. Water Investigations Branch, Department of Lands, Forests and Water Resources, Victoria, B.C., 83 p.

Terzaghi, K. (1956). Varieties of submarine slope failure. Proc. 8th Texas Oil Mech. and Engr. Conf., pp. 1-41.

Trowbridge, A.C. (1930). Building of the Mississippi delta. Am. Assoc. Petrol. Geologists Bull., Vol. 14, pp. 85-107.

Vail, P.R., Mitchum, R.M., Todd, R.G., Widmier, J.M., Thompson, S., Sangree, J.B., Bubb, J.N. and Hatfield, W.G. (listed in order of papers) (1977) Seismic stratigraphy and global changes in sea level. In: Payton, C.E. (Editor), A.A.P.G. Mem. 2, Tulsa, Okla, 516 p.

Walker, R.G., (1975). Generalized facies model for resedimentation conglomerates of turbidite association. Geol. Soc. Am. Bull., Vol. 86, pp. 737-748.

Walker, R.G. (1978). Deep water sandstone facies and ancient submarine fans: models for exploration and stratigraphic traps. A.A.P.G. Bull., Vol. 62, pp. 932-966.

Watkins, D.J. and Kraft, L.M. (1978). Stability of continental shelf and slope, Louisiana and Texas. In: Bouma et al. (Editors), Framework, Facies and Oil - Trapping characteristics of the Upper Continental Margin, A.A.P.G. Studies in Geology, No. 7, Tulsa, Okla.

Western Canada Hydraulic Laboratories Ltd. (1976). Potential sediment problem in the Bella Coola small boat harbour. Western Canada Hydraulic Lab., Port Coquitlam, B.C., 2 p.

Wright, L.D. (1970). Circulation, effluent diffusion and sediment transport, mouth of South Pass, Mississippi River Delta. Louisiana State Univ., Coastal Studies Inst. Tech. Rept. 84, 56 p.

Wright, L.D. (1971). Hydrography of South Pass, Mississippi River Delta. Am. Soc. Civil. Engrs. Proc. 1. Waterways Harbors and Coastal Eng. Div. Vol. 97, pp. 491-504.

Wright, L.D. (1977), Sediment transport and deposition at river mouths: a synthesis, Geological Society of America Bulletin, Vol. 88, pp. 857-868.

Wright, L.D. (1978). River Deltas. In: Davis, R.A. (Editor), Coastal Sedimentary Environments. Springer-Verlag, New York, pp. 1-64.

Wright, L.D., and Coleman, J.M. (1971). Effluent expansion and interfacial mixing in the presence of a salt wedge, Mississippi River Delta. Journal of Geophysical Research, Vol. 76, pp. 8649-8661.

Wright, L.D., and Coleman, J.M. (1973). Variations in morphology of major river deltas as functions of ocean wave and river discharge regimes. American Association of Petroleum Geologists Bulletin, Vol. 57, pp. 370-398.

Wright, L.D., and Coleman, J.M. (1974). Mississippi River mouth processes: effluent dynamics and morphologic development. Journal of Geology, Vol. 82, pp. 752-778.

Wright, L.D., Coleman, J.M. and Thom, B.G. (1973). Processes of channel development in a high-tide range environment. Cambridge Gulf-Ord River Delta. J. of Geology, Vol. 81, pp. 15-41.

Wright, L.D., Coleman, J.M., and Thom, B.G. (1975). Sediment transport and deposition in a macrotidal river channel, Ord River, Western Australia. In: Cronin, L.E., (Editor), Esturaine Research, Vol. II, Academic Press, New York, pp. 309-322.

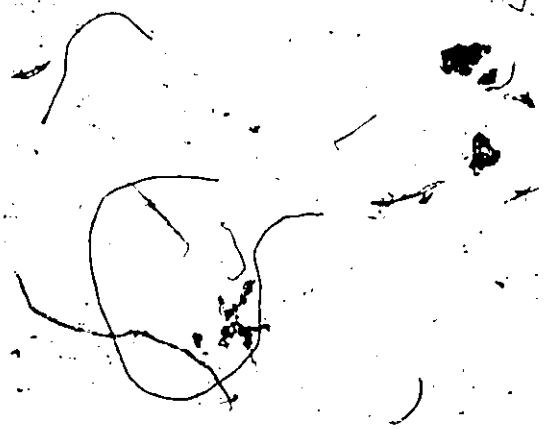

APPENDIX 1

EQUIPMENT SPECIFICATIONS AND OPERATION

Echo-sounding

A good review of the principles and applications of echo-sounding can be found in Hooper (1979). The echo-sounder utilized in this study was a Raytheon Fathometer, type DE719 B, with a frequency of 200 kHz, a beam width of 8° and a maximum range of 120 m. In addition to providing detailed bottom profiles with a large vertical exaggeration (19X) the sounder was used to aid in determination of the thickness of the surface freshwater layer and of suspended sediment concentrations. No obvious sub-bottom information was available from the fathometer record.

Seismic

Two types of continuous seismic reflection sub-bottom profiling were used in this study: air-gun and pinger. The air-gun source consists of a 5 in^3 Bolt Model 600 B chamber operated at 1950 lb. in^{-2} and fired at 2 second intervals. The frequency range was 70-400 Hz. The hydrophone array used was a Geospace 19 M 17 and the Graphic Recorder an EPC Model 4100. The pinger transducer array consisted of 5 hull mounted Raytheon TR109 transducers with a frequency of 3.5 kHz, and the

tranceiver was an Ocean Research Equipment Model 140. The graphic recorder for the pinger is the same model as that used for the air-gun. Ship speed for seismic operation was 5-6 knots.

The following discussion of the principles of operation of the seismic profiling systems is based largely on D'Olier (1979) and Leenhardt (1974). The basis of operation of these systems is a continuous series of sound pulses emitted from a source, which, after reflection from the sea floor and sub-bottom, are picked up by the receiver and recorded. The time taken for the pulses to travel to the horizons and return to the deflector after complete or partial reflection is recorded on a continuously running chart (Figure 111). The greater the depth of the reflector, the greater the two-way travel time. The propogation velocities of compressional waves produced by pulses vary according to the medium, with some examples given on Table 8.

Qualities of good sediment layer resolution and deep penetration are incompatible. The air-gun source, with a low frequency, provides good penetration but poor resolution (4-20 m), while the pinger source with a high frequency provides less penetration and good resolution (0.2-1.0 m). As the pulse length increases at lower frequencies, less attenuation of the sound pulse occurs and penetration increases. However the longer the pulse the poorer the resolution as the outgoing signal interferes with the one returning.

A major problem with an omnidirectional source such as the air-gun is reflection from other surfaces such as the air-water interface,

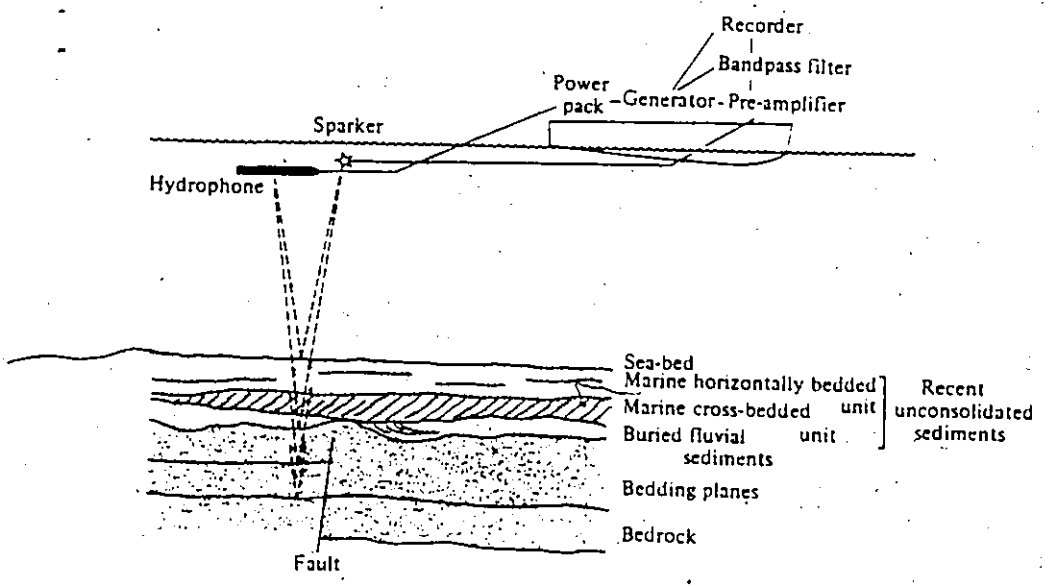

Figure 111. Diagram showing principle of operation of continuous sub-bottom profiling system (from D'Olier, 1979).

Material	Propagation Velocity
Air	330
Seawater	1450-1570
Recent estuarine sands and silts	1530-1600
Glacial till	1560-2500
London clay	1650-2100
Chalk	3000-4700
Granite	4500-6700

Table 8. Seismic Velocities (m s^{-1}) (from D'Olier, 1979).

or in a fjord situation, side-wall reflection. In the latter case the reflected signal from the wall of the fjord reaches the hydrophone before the reflection from the bottom or sub-bottom. This can lead to considerable problems in interpretation. The pinger, with a focussed beamwidth of 55°-30° is less prone to side-wall effects. Additional problems in interpretation may result from multiple reflections. These occur because some of the acoustic energy reflected from the sea-bed and sub-surface layers may reflect from the water surface and return to the sea-bed or sub-surface layer to be reflected again before being picked up by the receiver. Multiples may mask 'real' inyents received from sub-surface depths greater than water depths. Hyperbolic point sources can obscure the details of small-scale rugged uneven surfaces; the hyperbola resulting from the fact that the broken surface acts as an omnidirectional reflector, not allowing the signal to propogate vertically.

Sidescan Sonar

A Klein Hydroscan was used in this study. The towfish was a Model 422S with a frequency of 50 kHz and a horizontal beamwidth of 1°. The fish was towed with 450 m of cable at a distance of 20 m from the bottom. The recorder was a Model 531 T. Range was set at 200 m, i.e., each of the two channels covered a width of 200 m on both sides of the ships track. Ship's speed for sidescan operation was 2 knots.

D'Olier (1979) and Fleming (1976) discuss the principles of operation of sidescan systems. The principle of operation of sidescan

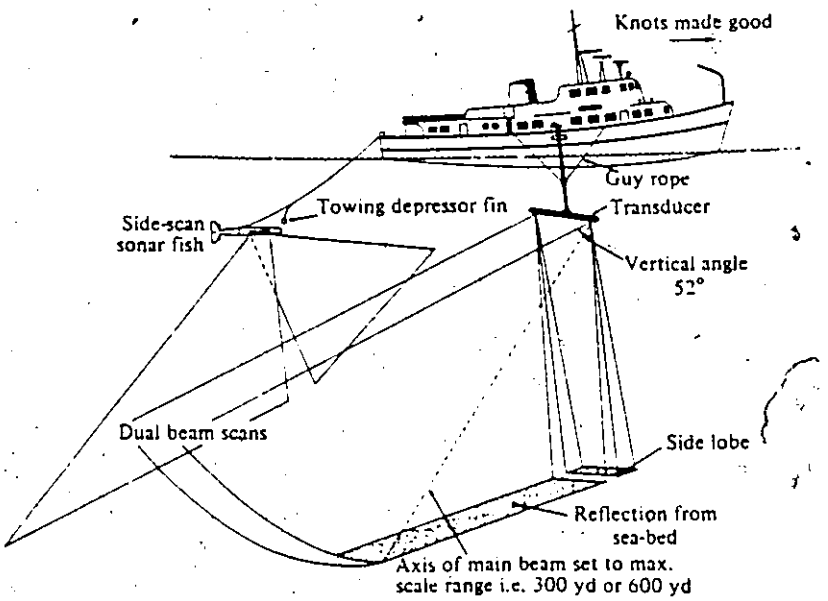

Figure 112. Diagram showing principle of operation of hull-mounted and towed dual-channel side-scan sonars (from D'Olier, 1979).

sonar is similar to that of an echo-sounder or seismic system. Pressure waves are projected into the water and reflections are picked up from the bed and recorded on the paper recorder (Figure 112). As with seismic apparatus, the choice of frequency is important in side-scanning. The higher the frequency the greater the attenuation in water as acoustic energy is absorbed; for example a high frequency of 300 kHz will have almost completely attenuated after travelling 100 m, while a wave of 50 kHz would have suffered only a 30% loss of power.

The resolution or clarity of the recorded signal depends on a variety of factors including directivity and beamwidth, pulse length and recording sensitivity. Directivity is determined in both horizontal and vertical dimensions (Figure 113). The acoustic beamwidth should be narrow in the horizontal dimension otherwise echoes might be received simultaneously from objects lying ahead, astern, or on either side of the vessel. The beamwidth should be wide in the vertical dimension so that scanning can be achieved from directly under the vessel to an adequate range on both sides. In order to distinguish two closely spaced objects the return signal from the first should not mask that from the second. As a result, targets should not be greater than half a pulse length apart, where pulse length is defined as pulse duration (a pulse of 50 kHz lasting one millisecond consists of 50 cycles) times the velocity of propagation (1520 ms^{-1} in seawater). The effectiveness of operation finally depends on recording sensitivity, i.e., the quality of the signal recording. Records can be made in 'dry' (graphite backed) or wet (chemically treated) paper. The wet paper (as used in the Klein system) is far more sensitive, but may distort or fade on drying.

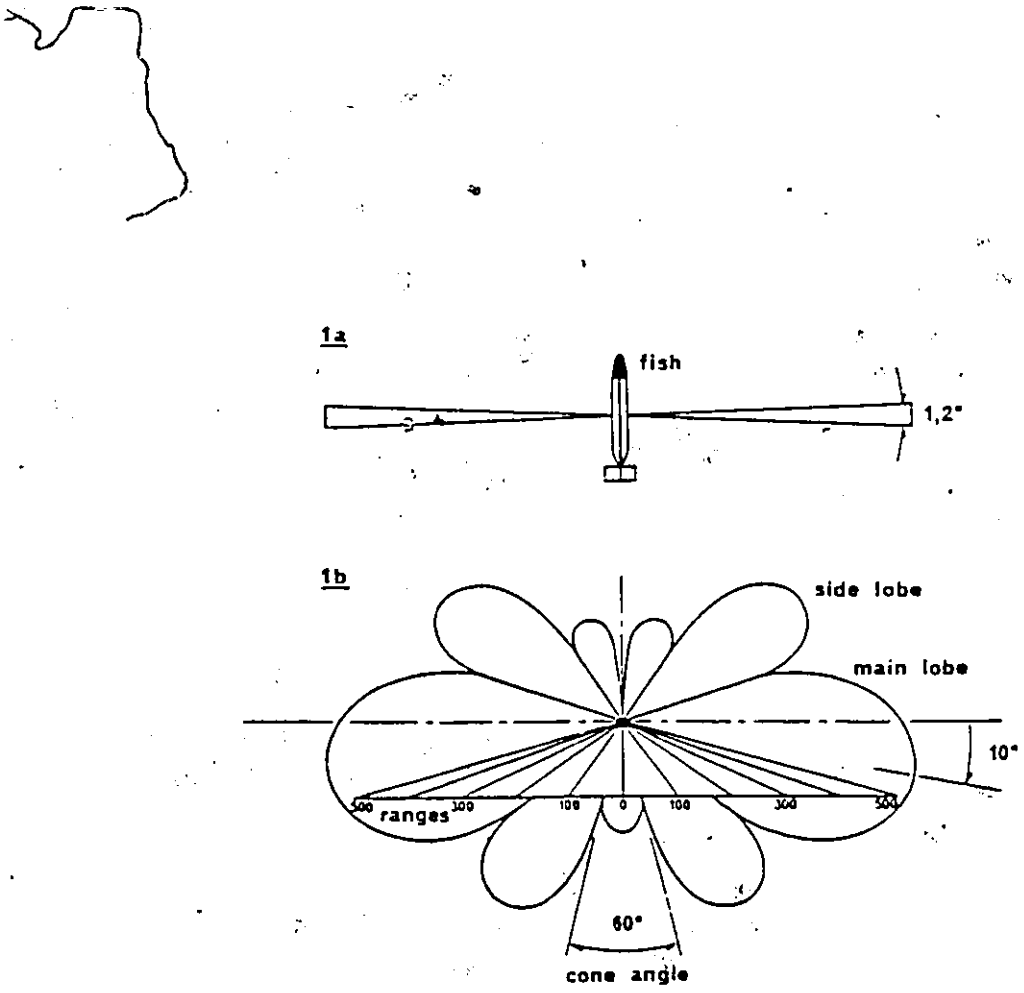

Figure 113. Sound lobes of the ultrasonic beam (exaggerated) a. Plan view; b. Vertical section (from Flemming, 1976).

Finally, distortion can occur parallel to the line of travel due to variable ship speeds, resulting in compression of sonographs in this direction (Figure 114). With the speed of 2 knots used in this study, distortion is virtually eliminated.

Sediment Sampling

Two types of sediment sampling programs were used in this study, bottom grabs and gravity cores (see Buller and McManus 1979, for discussion). Echman Model and Shipek Model grab samplers provided considerably disturbed surface samples suitable for grain size analysis, from sandy and coarser material that the gravity core was unable to penetrate. The Shipek was better able to penetrate coarser sediments and better sorted, compacted sand.

A 20 kg gravity corer, manufactured from a section of core barrel from an Alpine gravity corer, was used to provide short (maximum 1.5 m) cores from muddy prodelta areas. The corer penetrates the bed after free fall through the water, with the sample passing through a core cutter which has a diameter slightly less than the core barrel above. The barrel was lined with a clear plastic tube in which the core was removed, sealed and kept in cold storage until split, logged and sampled.

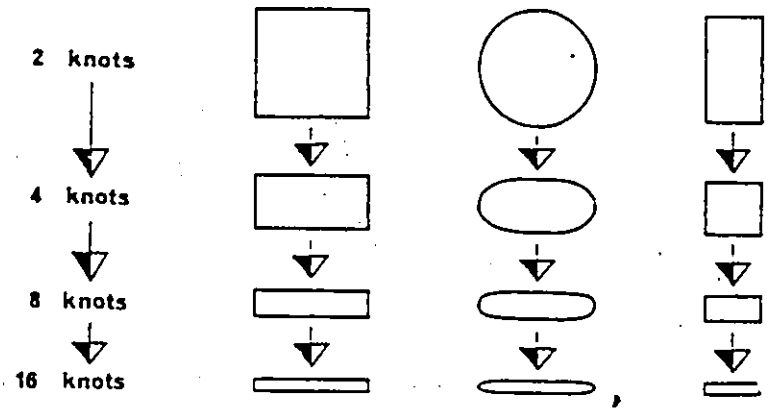

Figure 114. Distortion effects on some common shapes parallel to the line of travel caused by various ship speeds (from Flemming, 1976).

Shear Vane

A Torvane hand-held shear vane was used to estimate unconsolidated undrained shear strength (C_u) in prodelta cores. The vane was pushed into the core sediment and rotated slowly until failure occurred, the value at failure being the peak strength. Vane rotation was continued after failure until a stable strength value occurred, this being the remoulded strength. As shear vanes indicate total stress, they cannot be used to derive values of C' and ϕ' (Selby, 1982).